Radiotoxicity of 201Tl and its nanostructure-mediated delivery for potential cancer radiotherapy

Wulfmeier, Kasia

Awarding institution:
King's College London

Radiotoxicity of ^{201}Tl and its nanostructure-mediated delivery for potential cancer radiotherapy

Katarzyna Wulfmeier

School of Biomedical Engineering and Imaging Sciences
King's College London

2023

Abstract: Auger-electron emitting radionuclides have potential in targeted treatment of small tumours and micrometastases due to their high-LET (linear energy transfer) but short-range emissions. Thallium-201 (^{201}Tl, $t_{1/2}$ = 73 h), known for its previous use in myocardial perfusion scintigraphy, decays by electron capture releasing around 37 Auger and secondary electrons. However, its radiotoxic and cancer therapeutic effects remain unexplored. In addition, targeted therapy with ^{201}Tl is currently hindered by the lack of efficient chelators to incorporate ^{201}Tl into bioconjugates.

The main focus of this PhD thesis was to evaluate ^{201}Tl radiotoxicity to cancer cells, assess its subcellular localisation, as well as developing chemistry for incorporating this radionuclide into a radiopharmaceutical for cancer therapy. To achieve the main objectives, a variety of different methods were used, such as biological assays with radioactive ^{201}Tl, (e.g. cellular uptake and efflux, DNA damage and clonogenic survival assays), chemical synthesis and physicochemical analysis (e.g. thin layer chromatography, dynamic light scattering, infrared spectroscopy, X-ray diffraction analysis, thermogravimetric analysis, UV-Vis spectroscopy), confocal and electron microscopy, energy dispersive X-ray spectroscopy, ion beam analysis and inductively coupled plasma - mass spectrometry.

Firstly, the radiotoxicity of ^{201}Tl was evaluated by exploring its native cellular uptake via potassium channels in different cancer cell lines. It was demonstrated that ^{201}Tl has a significant radiotoxic effect in breast and prostate cancer cells but only when internalised. Secondly, the ion beam analysis appeared to be the most adequate technique for assessing ^{201}Tl subcellular localisation and revealed not only that thallium is present in the cell nucleus, but in an amount higher than in the cytoplasm. Lastly, three different types of nanoparticles were synthesised as a proposed delivery method for ^{201}Tl: nanotexaphyrins and Prussian blue nanoparticles coated either with citric acid or chitosan. Those nanoparticles were characterised, radiolabelled with [^{201}Tl]TlCl and their pharmacokinetics and radiotoxicity assessed by biological assays. Among them, Prussian blue nanoparticles coated with chitosan were the most promising, showing high radiolabelling efficiency with ^{201}Tl, very good stability in physiological conditions, as well as a high uptake and slow efflux when tested in lung cancer cells. More importantly, they showed significant radiotoxicity, increasing the number of DNA damage foci and reducing the clonogenic survival with estimated activity of 0.43 Bq/cell needed to achieve 90% reduction. Subsequently, these nanoparticles were tested *in vivo*, where they showcased significantly higher retention of ^{201}Tl in tumours compared to unbound ^{201}Tl 48 h after intratumoral injection.

In conclusion, this PhD thesis presents a radiobiological evaluation of unbound and nanoparticle-bound ^{201}Tl with an emphasis on the subcellular localisation of this potent Auger electron–emitter. Prussian blue nanoparticles coated with chitosan and radiolabelled with ^{201}Tl offer a solution for future ^{201}Tl targeted delivery and its potential use in cancer therapy.

Declaration

I, Katarzyna Wulfmeier, confirm that no part of this thesis has been submitted in support of any other application for a degree or qualification of King's College London, or any other university or institute of learning. I confirm that this work is my own. Where information has been derived from other sources, it has been indicated in this thesis.

This thesis was completed under the supervision of Prof Philip Blower and Dr Vincenzo Abbate.

List of abbreviations

A_{10} - activity bound per cell needed to reduce the clonogenic survival by at least 90%

A_{50} - activity bound per cell needed to reduce the clonogenic survival by at least 50%

AE - Auger electron(s)

ATP - adenosine triphosphate

BC - background count

BrdU - bromodeoxyuridine

BSA - bovine serum albumin

caPBNPs - citric acid-coated Prussian blue nanoparticles

CHL - cholesterol

chPBNPs - chitosan-coated Prussian blue nanoparticles

CPM - counts per minute

CPS - counts per second

DABCO - 1,4-diazabicyclo[2.2.2]octane

DAPI - 4',6-diamidino-2-phenylindole

DDC - diethyldithiocarbamate

DLS - dynamic light scattering

DMEM - Dulbecco's Modified Eagle Medium

DNA - deoxyribonucleic acid

DOTA - tetraazacyclododecanetetraacetic acid

DPPC - dipalmitoylphosphatidylcholine

DSB - double-strand break(s)

$DSPE\text{-}PEG_{2000}$ - distearoylphosphatidylcholine polyethylene glycol 2000

DTG - derivative thermogravimetry

DTIME% - dead time value (%)

DTPA - diethylenetriaminepentaacetic acid

EA - elemental analysis

EBRT - external beam radiotherapy

EBS - elastic backscattering spectrometry

EC - electron capture

EDC - 1-(3-dimethylaminopropyl)-3-ethylcarbodiimide hydrochloride

EDS - energy-dispersive X-ray spectroscopy

EDTA - ethylenediaminetetraacetic acid

EGF - epidermal growth factor

EGFR - epidermal growth factor receptor(s)

EPR - enhanced permeability and retention

FDG - fluorodeoxyglucose

FT-IR - Fourier transform-infrared spectroscopy

H&E - haematoxylin and eosin

HER - human epidermal growth factor receptor

IA - injected activity

IA/g - injected activity per gram of tumour

IC - internal conversion

ICP-MS - inductively coupled plasma-mass spectrometry

ICP-OES - inductively coupled plasma-optical emission spectroscopy

LA-ICP-MS - laser ablation-inductively coupled plasma-mass spectrometry

LET - linear energy transfer

mAb – monoclonal antibody

MIBG - metaiodobenzylguanidine

MIPs - maximum intensity projections

NC - negative control

NHS - N-hydroxysuccinimide

NLS - nuclear localising sequence

NOS - reactive nitrogen species

NP - nanoparticle(s)

NPCs - nuclear pore complexes

p.a. - post administration

PARP - poly-ADP ribose polymerase

PB - Prussian blue

PBNPs - Prussian blue nanoparticles

PBS - phosphate buffer saline

PDI - polydispersity index

PDT - photodynamic therapy

PEG - polyethylene glycol

PET/CT - positron emission tomography/computed tomography

PIXE - particle-induced X-ray emission

PSMA - prostate-specific membrane antigen

RE - radiolabelling efficiency

ROIs - regions of interest

ROS - reactive oxygen species

RPM - rotations per minute

RT - room temperature/radiotherapy

SAXS - small-angle X-ray scattering

SD - standard deviation

SIMS - secondary ion mass spectrometry

SPC - summary of product characteristics

SPECT - single photon emission computed tomography

SSB - single-strand break(s)

SUV - standardised uptake values (SUV)

TAT - transactivator of transcription

TEM - transmission electron microscopy

TGA - thermogravimetric analysis

TLC - thin layer chromatography

TRT - targeted radionuclide therapy

UHPLC-MS - ultra-high performance liquid chromatography-mass spectrometry

wt % - weight percentage

XFM - synchrotron-based X-ray fluorescent microscopy

XRD - X-ray diffraction

XRF - X-ray fluorescence

Table of contents

List of figures

List of tables

Chapter 1: Introduction

1.1 Standard approach to cancer treatment

Cancer remains a significant global health concern. It is estimated that one in two people born in the United Kingdom after 1960 will be diagnosed with cancer during their lifetime [1]. The current standard treatments for cancer, including surgery, chemotherapy and radiation therapy, form the baseline approach for the majority of patients [2]. The use of ionising radiation to eliminate cancer cells, known as radiotherapy (RT), has its origins in the late 19th century when Wilhelm Röntgen discovered X-rays, subsequently leading to their application in the treatment of cancer [3]. Over a century later, X-ray radiotherapy is administered to over 50% of cancer patients, either as a standalone treatment or in combination with other therapies [4]. External beam radiotherapy (EBRT) delivers high-energy (6–25 MeV) X-rays (i.e photons) generated by linear accelerators, which deposit energy deep in the tumour tissue [4]. Conventional EBRT, while well-established and effective, has limitations such as the lack of precise targeting and potential damage to the surrounding healthy tissue. More recently, highly energetic charged particles such as protons, α-particles and carbon ions are used for RT, called hadron therapy. Using a beam of charged particles instead of X-ray to irradiate cancer cells provides more precision and has demonstrated greater effectiveness in treating complex tumours located near critical structures (such as the brain and spinal cord), lung cancer, radioresistant or deep-seated tumours, and in paediatrics [5], albeit at an extensive monetary cost. Although external beam radiotherapy is highly efficient in treating solid tumours by delivering radiation to the main cancer site, it presents challenges when dealing with disseminated or metastatic disease. Despite considerable advancements in cancer treatment in recent years, metastases remain a leading cause of death in cancer patients [6]. The ability of cancerous cells to infiltrate and establish secondary tumours in different parts of the body not only diminishes the overall prognosis for patients but also complicates the therapeutic approach. As a result, understanding and developing strategies to prevent or target metastatic spread remain critical areas of focus in cancer research and treatment endeavours.

1.2 Targeted radionuclide therapy as an alternative to external beam radiotherapy

Targeted radionuclide therapy (TRT, also known as Molecular radionuclide therapy or Radionuclide therapy) is a therapeutic strategy that involves an internal administration of a radioactive compound, capable of delivering a high radiation dose selectively to the tumour cells by targeting their specific molecular or functional markers [5]. This precise delivery of radiation not only minimises toxicity to neighbouring healthy tissues but also enables the targeting of both primary tumours and disseminated cancer cells, including micrometastases. This targeted radiation dose can be delivered directly by

alpha particles, beta particles, and Auger electrons, or by inducing the bystander effect [7]. Furthermore, certain radionuclides, in addition to emitting particulate radiation that can damage tumour cells, produce gamma-rays. This property enables a theranostic approach, where the same radionuclide or the same radiopharmaceutical with a different radioisotope of the same element can be used for both radiotherapy and diagnostics [8].

Effective radionuclide therapy relies mostly on two strategies: specific binding of a targeting molecule conjugated with a radionuclide to a receptor that is overexpressed on the surface of tumour cells, or inherent properties of certain radionuclides that accumulate within cancer cells by imitating natural physiological processes (^{223}Ra, ^{89}Sr, ^{131}I) [9,10]. An illustrative example demonstrating various targeting approaches is iodine-131 (^{131}I), a beta particle-emitter which is currently in clinical use in cancer treatment either in the form of iodide, or in conjugation with a small molecule or an antibody (Fig. 1.1). Iodine-131 in the form of iodide [^{131}I]I^- stands as one of the oldest and most frequently used radioisotopes in targeted molecular radiotherapy. It has been extensively used for several decades in thyroid cancer to eliminate residual cells after thyroidectomy and tumour metastases [11]. [^{131}I]I^- is absorbed and accumulated within thyroid cells through physiological pathways. This is achieved through the sodium-iodide symporter located on the surface of thyroid follicular cells, which actively transport iodide (I^-) into the thyroid gland, serving as the initial step in the biosynthesis of thyroid hormones [12]. ^{131}I conjugated to a targeting vector, meta-benzylguanidine ([^{131}I]I-meta-iodobenzylguanidine or [^{131}I]I-MIBG), is used to treat specific types of neuroendocrine tumours, such as neuroblastomas, paragangliomas and pheochromocytomas. MIBG is structurally similar to noradrenaline, a neurotransmitter actively taken up by certain neuroendocrine cells through the noradrenaline transporter molecule [13,14]. [^{131}I]I-MIBG is able to detect and destroy neuroendocrine tumour cells as they overexpress the noradrenaline transporter. In addition to particulate radiation used to treat cancer, ^{131}I also emits γ-rays, detectable through SPECT imaging, making [^{131}I]I-MIBG suitable for both therapy and diagnostics [15]. Another iodine radioisotope, ^{123}I, offers superior imaging characteristics compared to ^{131}I when used with conventional gamma cameras and is the preferred radioisotope for diagnostic purposes, disease staging, and assessing treatment responses [16]. Hence, MIBG can be radiolabelled with either ^{123}I or ^{131}I and applied in clinical settings as a theranostic agent [13,17]. Iodine-131 can also be conjugated to an antibody. ^{131}I-tositumomab, commercially known as Bexxar, is an approved radiopharmaceutical designed for the treatment of refractory non-Hodgkin's lymphoma. This therapy targets CD20 antigens present on the surface of normal and malignant B lymphocytes. These conjugates enable a precise delivery of radiation therapy by the specific binding of the monoclonal antibody to antigens present on the surface of malignant cells [18].

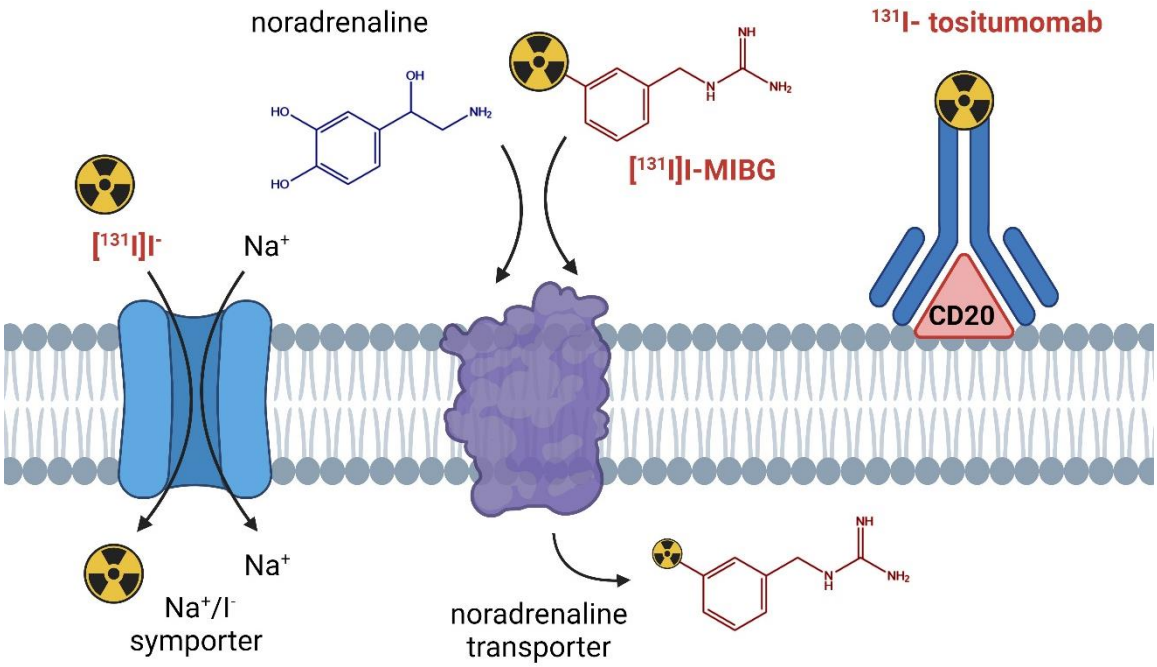

Figure 1.1 A diagram illustrating various targeting approaches using iodine-131 (^{131}I) in cancer therapy. ^{131}I is used in the form of iodide [^{131}I]I$^-$ for thyroid cancer, in conjugation with a targeting vector as [^{131}I]I-meta-iodobenzylguanidine ([^{131}I]I -MIBG) for neuroendocrine tumours and in combination with an antibody as ^{131}I-tositumomab for the treatment of refractory non-Hodgkin's lymphoma. Created with BioRender.com.

1.3 Developing a radiopharmaceutical for TRT - an overview

After identifying a promising molecular target, the development of an effective radiopharmaceutical necessitates careful consideration of various essential factors. This includes choosing a suitable targeting vector with a high binding affinity and specificity towards the targeted cancer cell, ultimately resulting in a substantial accumulation of the delivered radiation dose in the tumour [19]. The most commonly employed approach in the design of targeted radiopharmaceuticals containing radiometals involves the use a bifunctional chelator. The chelator is required to bind the radiometal with high affinity and kinetic stability, typically using a linker that is then attached to a targeting vector. This strategy has been used in the development of several targeted radiopharmaceuticals, some of which are in regular clinical use [20]. Among the most prevalent targeting vectors are small molecules, such as the prostate-specific membrane antigen (PSMA) ligands utilised in prostate cancer therapy, as seen in [^{177}Lu]Lu-vipivotide tetraxetan (Pluvicto). Additionally, peptides, like octreotide in [^{177}Lu]Lu-DOTATATE (Lutathera), are registered for the treatment of gastroenteropancreatic neuroendocrine tumours. Furthermore, antibodies, such as the anti-CD20 monoclonal antibody in ^{90}Y-ibritumomab tiuxetan (Zevalin), are employed for the treatment of non-Hodgkin's B-cell lymphomas.

Radiopharmaceuticals, when linked to various targeting vectors, exhibit distinct pharmacokinetics related to their uptake and clearance in both tumour and healthy tissues. The variable retention of

1.4 Nanoparticles as therapeutic agents for targeted radiotherapy

While using a bifunctional chelator is the most commonly employed strategy for targeting radiometals to cancer cells, an alternative approach involves conjugating the targeting vector to a nanoparticle that carries a therapeutic radionuclide, with or without help of the bifunctional chelator. Recently, there has been a growing interest in utilising nanotechnology to enhance targeted cancer radiotherapy [22,25]. Therapeutic radionuclides can be integrated into nanomaterials at high concentrations due to the high surface-to-volume ratio of nanoparticles, delivering their radioactive 'payload' directly to the tumour and sparing healthy tissue. To allow the radiation deposition in the tumour site, nanoparticles can be targeted through either active (nanoparticles displaying a targeting vector) or passive mechanism [26]. Small nanoparticles can take advantage of the enhanced permeability and retention effect (EPR effect), which facilitates their passive transport through the relatively porous vascular system (i.e. compared to healthy tissue vasculature) surrounding solid tumours and their accumulation inside the tumour cells (Fig. 1.3) [26,27].

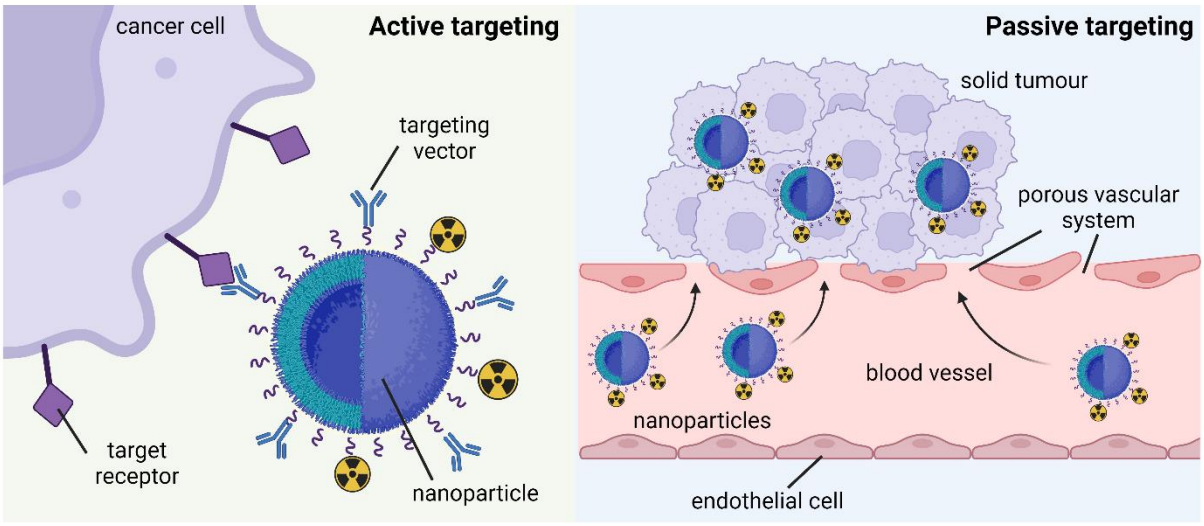

Figure 1.3 Illustration of active and passive targeting mechanisms. A) The nanoparticle is linked to a targeting vector (antibody) with high specificity and affinity for the biological target of interest within the cancer cell. Radionuclides may be attached with or without the assistance of a bifunctional chelator. **B)** Passive transport of nanoparticles through the porous vascular system, commonly referred to as the enhanced permeability and retention effect (EPR effect). Created with BioRender.com.

Nanoparticle delivery systems can be synthesised from inorganic and organic materials, such as Prussian blue (Prussian blue nanoparticles are described in more detail in chapter 3), gold, carbon (fullerenes, nanosheets and nanotubes), iron oxide (magnetic nanoparticles), titanium dioxide, silica, zinc sulfide (quantum dots), polymers (polymeric nanoparticles, micelles, dendrimers), phospholipid-based compounds (liposomes, exosomes, nanoporphyrins and nanotexaphyrins, which are described in chapter 5), proteins and viral components [26]. Each type of nanoparticle has distinct advantages and drawbacks associated with their material composition. These considerations include factors such

as solubility, chemical stability, thermal conductivity, capacity to bind biomolecules, as well as the ability to bind and release other substances [28]. Nanoparticle characteristics play a critical role in shaping particle-cell interactions, influencing cellular transport mechanisms, pharmacokinetics and biodistribution. Additionally, some nanoparticles possess magnetic, semiconducting and/or optical properties. For example, iron oxide nanoparticles, quantum dots and up-converting nanoparticles provide additional functions [26]. Nanoparticles serve as an optimal platform for enhancing radiotherapy as their chemical and physical properties can be easily modified, allowing the design of nanoparticles with different shapes and sizes, having various surface coatings and surface modifications to improve biocompatibility, change biological behaviour or actively target them to a tumour cell or a specific subcellular compartment [22]. Radionuclides can be conjugated directly on the nanoparticle surface, with or without a spacer; or they can be incorporated into the nanoparticle during chemical synthesis or encapsulated post-synthetically. In some cases, bifunctional chelators, such as DOTA (tetraazacyclododecanetetraacetic acid) and DTPA (diethylenetriaminepentaacetic acid), have to be used to attach the radiometal to the nanoparticle surface or ensure it is trapped inside a nanoparticle to achieve high radiolabelling stability [25,29]. Furthermore, the appropriate alignment between the biological half-life of the nanoparticle and the half-life of the radionuclide is a crucial consideration during the radiolabelling process. This synchronisation is necessary for the nanoparticle to effectively reach the target while minimising unnecessary radiation exposure [29]. The pre-targeting strategy explained earlier can also be applied to nanoparticles to achieve optimal results for targeted radiotherapy. Numerous passively and actively targeted nanoparticle therapies are under development, although the majority of radiolabelled nanoparticles for therapy are still in the preclinical phase of research. Examples of nanoparticle-mediated delivery of radiation for therapeutic purposes are trastuzumab-modified gold nanoparticles radiolabelled with β-emitter, ^{177}Lu, for HER2 (human epidermal growth factor receptor) positive breast cancer therapy [30] and ^{225}Ac-radiolabelled liposomal-based nanoparticles functionalised with peptides targeting NK1 receptors overexpressed on glioma cells for alpha-therapy of glioblastomas [31].

Radiolabelled nanoparticles have emerged as a versatile platform that enables a multimodal approach to cancer treatment and diagnostics. It is possible to integrate multiple radionuclides, various vector ligands, and additional non-radioactive therapeutics into a single nanodelivery system. This not only allows for the targeted delivery of radiation to tumour cells for therapeutic purposes but also facilitates multimodal applications, combining imaging, radiotherapy, chemotherapy or other types of cancer therapy. For instance, hybrid texaphyrin-based nanoparticles labelled with ^{111}In/Lu and targeted to PSMA-expressing prostate cancer cells have been specifically designed for theranostic purposes, involving SPECT imaging and photodynamic therapy [32].

1.5 Biological impact of different types of particulate radiation in TRT

Another important aspect to consider when designing a radiopharmaceutical for targeted cancer therapy is the choice of an appropriate radionuclide. Essential considerations should include the radionuclide's physical characteristics, such as mentioned earlier half-life, emission type, and decay products, along with biological aspects like the in vivo stability, toxicity, and biological half-life [22], and chemical factors, such as radiolabeling feasibility and efficiency. Radionuclides used in TRT are predominantly α- and β^--particle emitters, and to a lesser degree, Auger electron-emitters. All these types of particulate radiation can cause ionisation along the travelled distance, thereby influencing the surrounding biological environment. Ionising radiation can cause DNA damage directly - leading to ionisation or excitation of atoms - and indirectly via production of free radicals such as short-lived reactive oxygen species (ROS) and reactive nitrogen species (NOS). DNA damage has long been recognised as a significant factor contributing to the death of tumour cells. The toxic effects on DNA include DNA base damage (oxidised and abasic sites), single-strand breaks (SSB) and double-strand breaks (DSB), and DNA–DNA or DNA–protein crosslinks, which can accumulate and form cluster lesions (i.e. multiple damage sites) [33] (Fig. 1.4, Table 1.1).

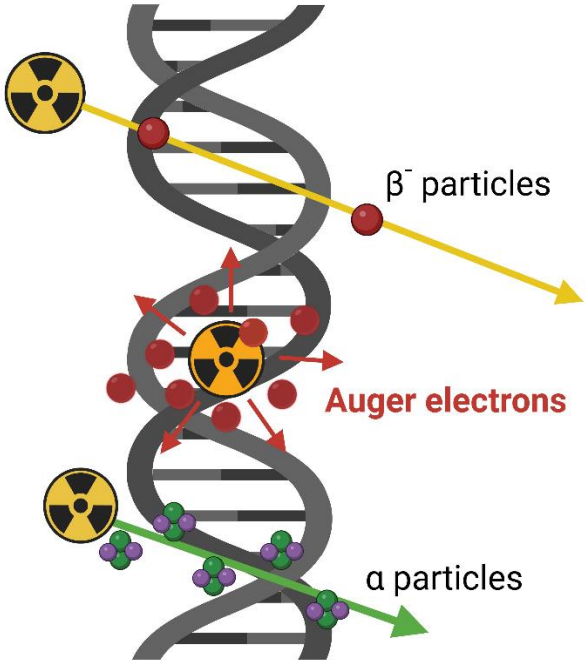

Figure 1.4 Schematic representation illustrating the potential impact of various types of particulate radiation on DNA, including α-particles, β^--particles and Auger electrons. Created with BioRender.com.

These various damaging effects, if not balanced by the DNA damage recognition and repair systems, can lead to cellular death or a cell cycle arrest [34]. However, apart from the DNA-centred approach, recent reports suggest that ionising radiation or generated free radicals can also oxidise cell membrane phospholipids [35] and damage mitochondrial membranes or mitochondrial DNA [36],

which in turn activates apoptotic signalling pathways. Furthermore, stress mediators can be transmitted between adjacent cells through intercellular communication via gap junctions or mitochondrial signalling, leading to death of non-irradiated cells by the 'bystander effect' [37,38].

	α-particles	β^--particles	Auger electrons
Particle type	two protons and two neutrons (^{4}He nucleus)	electron	electron
Energy	5 - 9 MeV	50 - 2300 keV	25 - 80 keV
Range in tissue	50 - 100 µm	0.05 - 12 mm	< 1 µm
Linear energy transfer	~ 230 keV/µm	~ 0.2 keV/ µm	4 - 26 keV/ µm
Bystander effect/'crossfire' effect	yes (low)	yes	yes
Tumour size	small/microtumours	higher volume solid tumours	microtumours

Table 1.1 Summary of physical and biological properties of α-particles, β^--particles and Auger electrons used in targeted radionuclide therapy.

Alpha emission occurs as a consequence of the radioactive decay of a large, unstable nucleus, which reduces its energy by releasing one or several α-particles composed of two protons and two neutrons (a nucleus of helium - ^{4}He). These particles are characterised as heavy, positively-charged particles with high energy (5-9 MeV), capable of traveling a distance of approximately 50-100 µm in tissue, equivalent to several cell lengths [39]. Linear energy transfer (LET) is a common parameter in radiobiology studies used to quantify the ability of the radionuclide to inflict damage in tissue and is defined as the average energy deposited per unit length of track of radiation expressed as keV/µm [39]. α-particle emitters are characterised by high LET, typically between 50 to 230 keV/µm, mostly causing direct ionisation effect which leads to double strand DNA breaks and clusters of difficult-to-repair DNA damage [18,39]. It is likely that the cytotoxic mechanism of α-particles also involves other types of damage, including damage induced by reactive oxygen species produced during the process. Examples of α-emitters used in targeted therapy include ^{213}Bi, ^{212}Bi, ^{212}Pb, ^{225}At, ^{211}At and ^{223}Ra [40].

β^--particles are typically emitted by unstable atoms that have fewer protons than neutrons. These particles are electrons with intermediate energy levels (0.05-2.30 MeV) and can penetrate long distances in tissue (0.05-12.0 mm) [41], damaging not only the targeted tumour cells but also the adjacent cells. This phenomenon, referred to as the 'crossfire' effect, can prove advantageous in targeted therapies, particularly in larger tumours or situations where not all tumour cells are accessible due to their heterogeneous expression of the targeted receptors. Nevertheless, when β^--particles impact neighbouring healthy cells, adverse effects may occur, such as bone marrow toxicity [39]. β^--particle emitters typically exhibit low LET emission, usually in the range of 0.2 keV/µm, which can result in multiple, individual DNA lesions, including DNA base damage, single and double DNA

strand breaks. The mechanism primarily involves indirect sparse ionisation and the production of free radicals. Sublethal damages caused by multiple β^-- particles can accumulate, and the inability of the irradiated cell to recognise damage and initiate repair mechanisms will ultimately lead to cellular death. The reduced effectiveness in hypoxic tumour tissue is associated with the indirect effect of β-radiation and the resistance to ROS in the absence of sufficient oxygen [22]. Several radionuclides with β^-- emission have been used for TRT, including ^{90}Y, ^{131}I, ^{177}Lu, ^{67}Cu and ^{186}Re, ^{188}Re [39].

Nuclei with an excessive ratio of protons to neutrons can decrease their energy either by positron emission or electron capture and/or internal conversion. The latter is typical for the elements with a higher atomic number. When a close orbital electron is drawn into the nucleus and converted into a neutron and neutrino, the atom's electron cloud becomes disrupted. The excess energy is either released as X-ray radiation or given to another electron, which in turn is emitted (Fig. 1.5) [42].

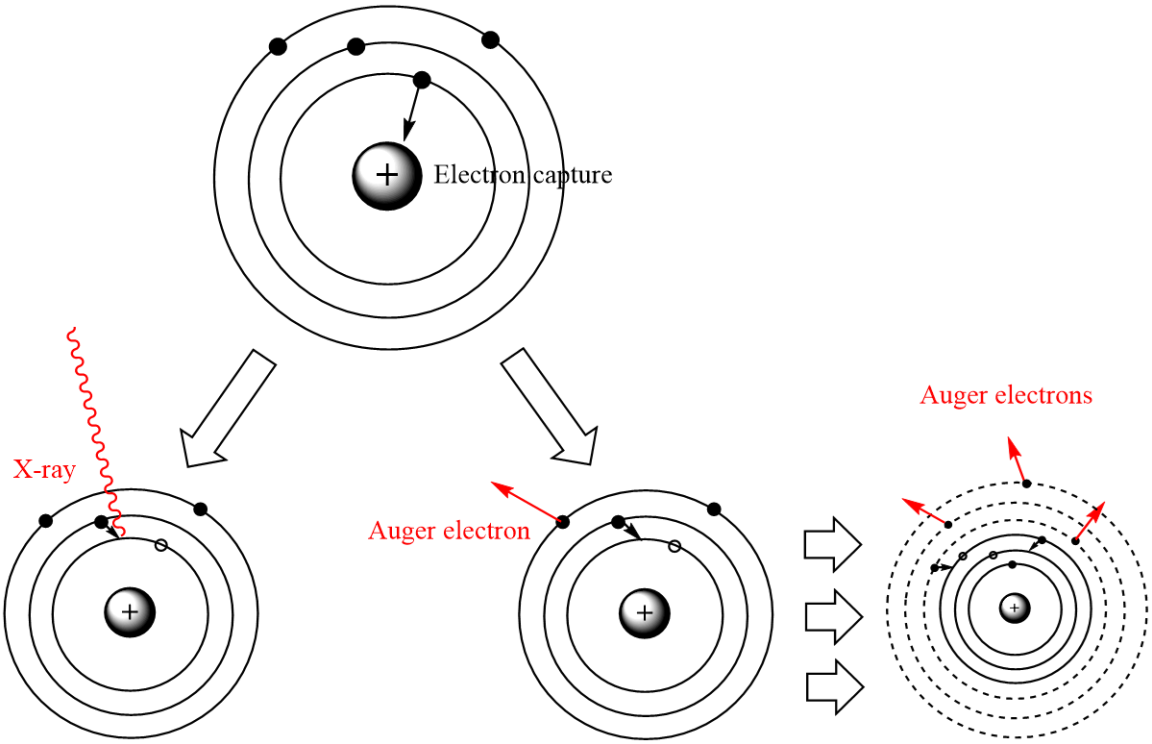

Figure 1.5 Schematic representation of the electron capture decay process. Nuclei with an excessive ratio of protons to neutrons may stabilise themselves by electron capture, when an orbital electron is 'captured' by the nucleus and a proton is converted into a neutron. The vacancy created in the inner shell is filled by a higher energy electron from an outer shell. The excess energy is either released as X-ray radiation or given to another electron, which in turn is emitted (called Auger electron) [42]. This process may be repeated causing a shower of Auger electrons released per decay.

The vacancy created in the inner shell leads to a subsequent cascade of vacancies and electron emissions. Depending on the relative position of the created orbital vacancy and the ejected electron, ejected electrons are called Auger, Coster-Kronig and super Coster-Kronig electrons [43], and collectively known as Auger electrons (AE).

The low energy levels carried by Auger electrons (< 80 keV) are typically deposited on a very short nanometre path length, which results in an intermediate LET (4-26 keV/µm) [44,45]. The highly localised energy deposition of Auger electrons, which avoids the 'crossfire' radiation typical for the long range β^-- particles, can cause a significant cytotoxicity at the subcellular level and therefore possibly find an application in targeting small tumours, micrometastases and isolated cancer cells. The most valuable Auger electron-emitters being considered for TRT include ^{125}I, ^{123}I, ^{111}In, ^{67}Ga, ^{195m}Pt, ^{201}Tl [39].

In addition to the toxicity of emitted low energy AE, direct ionisation events may occur at the point of decay. The release of orbital electrons and the subsequent disruption to the electron cloud lead to a transient, highly positive charge building up on the decaying atom [46]. The positive charge is either redistributed among atoms of the parental molecule or neutralised by electrons from molecules positioned in the immediate proximity. This process causes extensive ionisation and excitation around the site of the decaying atom, potentially leading to the destruction of these molecules [47]. While the radiobiological effects of AE are relatively well studied, the mechanism of charge neutralisation following the emission of the Auger cascade remains poorly understood. Iodine-125 (^{125}I) was employed as a model radionuclide to investigate ionisation processes and the biological outcomes resulting from its multistep decay by electron capture to an excited state of tellurium-125 (^{125}Te), followed by its internal conversion to stable ^{125}Te, producing around 25 AE (12.2 keV) and one internal conversion electron (7.2 keV) [43]. Early studies have shown that the decay of ^{125}I covalently bound to either methyl or ethyl groups ($CH_3[^{125}I]I$ and $[C_2H_5[^{125}I]I$) is highly disruptive, resulting in extensive ionisation and fragmentations of these simple molecules [48]. Excited ^{125}Te ions were observed to have an average charge of 9, with a maximum reaching as high as 18 [48]. The average potential energy of multiply charged ^{125}Te atoms was calculated to be approximately 0.9 keV and even though it constitutes a small fraction of the total energy released during the radioactive decay, dosimetric calculations suggest that, in volumes smaller than 100 nm in diameter, the energy delivered by the charged atom might be a dominant contributor to the local effective dose [47]. When ^{125}I was directly incorporated into the DNA of bacterial cells in the form of 5-iododeoxyuridine (an analogue of thymidine), it was observed to effectively damage DNA; specifically, one decaying atom was found to cause a single DNA DSB [49]. The substantial radiotoxic effect of ^{125}I on DNA was postulated to result from a combination of two key factors: the emission of low-energy electrons with high local energy deposition (radiation component) and the neutralisation process of multiply charged tellurium atoms (non-radiation component) [50]. An experimental study comparing the contribution of these two components to DNA strand breaks related to ^{125}I decay concluded that approximately 50% of the observed breakage in synthetic oligodeoxynucleotides can be attributed to the non-radiation

component [50,51]. Considering the limited range of Auger electrons in tissue and the destructive ionisation events occurring directly on the decay site, it has been hypothesised that the subcellular localisation of a radionuclide plays a crucial role in effective Auger electron therapy [52]. This concept is explored further in chapter 4.

A large variety of carrier molecules, combined with a range of available radionuclides exhibiting the appropriate type of particulate radiation and desired physicochemical characteristics, such as a suitable half-life, enables us to create a unique radiopharmaceutical tailored precisely for the specific clinical scenario [41].

1.6 ^{201}Tl as a tool in myocardial diagnostic imaging

Since the 1970s, ^{201}Tl has been recognised by scientists and clinicians as a crucial diagnostic tool for evaluating coronary perfusion and cellular viability. In the past, it played a significant role in myocardial imaging, helping to diagnose ischaemic heart disease and various cardiomyopathies. Its clinical use closely followed a series of studies involving radioactive potassium isotopes (^{42}K, ^{43}K) [53,54] and potassium analogues such as rubidium and caesium (^{81}Rb, ^{86}Rb, ^{129}Cs, ^{131}Cs) [55–58], which highlighted an inverse correlation between ischemic or infarcted myocardial tissue and regional potassium metabolism. These radioactive monovalent cations, when administered intravenously, accumulated in the myocardium, and their distribution patterns could be analysed. 'Cold spots' or areas with reduced accumulation were indicative of heart muscle abnormalities [59]. Among the investigated radioactive potassium analogues, ^{201}Tl emerged as the preferred radionuclide due to its unique biological similarity to potassium. In addition to this potassium mimicking behaviour, during its electron capture decay to stable ^{201}Hg, ^{201}Tl emits X-ray photons with energies around 67-82 keV (94% abundance) and gamma-ray photons at 135 and 167 keV (3% and 10% abundance, respectively) [60]. While the low-energy spectrum posed challenges in diagnostics related to tissue attenuation, it allowed for the efficient detection of myocardial abnormalities [61], initially through planar scintigraphy and later, since the mid-1980s, through single photon emission computed tomography (SPECT).

^{201}Tl shares similar pharmacokinetics with other potassium analogues. Following intravenous administration, the radionuclide is rapidly cleared from the bloodstream with approximately 4% of its activity accumulating in the myocardium [62]. ^{201}Tl can also be detected in various other organs, including the liver, kidneys, thyroid, skeletal muscles, salivary glands, colon, stomach, eyes, and testes [63]. Simple, monovalent cations like Tl^+ can rapidly transverse from the intravascular to the interstitial fluid space through small gaps and pores in the endothelial membranes of capillaries [64].

Approximately 60% of ^{201}Tl entering myocytes does so primarily via the active transport of the sodium-potassium pump (Na^+/K^+-ATPase), with the remainder transported through passive diffusion following electropotential gradients [65].

The initial biodistribution of ^{201}Tl is directly related to the regional blood flow in the myocardium and the tracer's extraction rate by the myocardium. Following a potassium-like pattern, ^{201}Tl continuously exchanges between intracellular and extracellular compartments for several hours until equilibrium is achieved, which is determined by the net balance between influx and efflux rates [66]. The prolonged retention of thallium in myocytes depends on the metabolic integrity of the cells and, consequently, reflects their viability (Fig. 1.6) [67]. The washout rate of the radionuclide is higher in healthy myocardium compared to abnormal tissue. Poorly perfused yet viable myocytes tend to retain ^{201}Tl, resulting in a smaller difference in the initial distribution between normal and ischemic myocardium, which subsequently normalises [60,67].

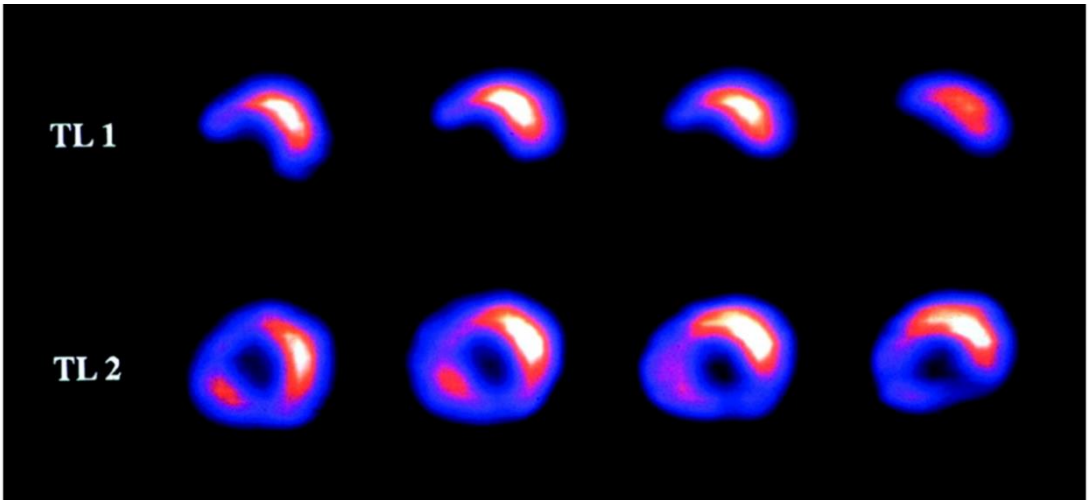

Figure 1.6 SPECT series images of ^{201}Tl rest-redistribution in short-axis cardiac slices. TL1 (top) represents early images showing a defect in the inferoseptal wall with ^{201}Tl redistribution evident in later images (TL2, bottom). This figure was originally published in the Journal of Nuclear Medicine by Schinkel A., et al. [67] ©SNMMI, and is reprinted in accordance with JNM policies.

Despite its initial success in myocardial diagnostics, ^{201}Tl had its limitations. These included a long physical and biological half-life, which ultimately led to a high radiation dose for patients; a low signal-to-noise ratio; and significant tissue attenuation due to its relatively low-energy emission. In response to these challenges, ^{201}Tl was eventually replaced by technetium-99m (^{99m}Tc)-labelled tracers like sestamibi and tetrofosmin, which do not mimic the behaviour of potassium. This transition offered improved image quality, reduced exposure of patients to radiation, and widespread availability facilitated by the ^{99}Mo/^{99m}Tc generator [60]. Furthermore, with the increasing availability of PET/CT scanners, a different potassium analogue - ^{82}Rb - emerged as a superior option for precise and high-

quality perfusion imaging while imposing a considerably lower radiation burden on patients [69]. Consequently, since the mid-1990s, the relevance of ^{201}Tl in myocardial imaging has gradually diminished. Nevertheless, efforts have been made to explore alternative applications of this radionuclide in diagnostic areas, such as tumour imaging.

1.7 The use of ^{201}Tl in cancer imaging

During routine myocardial scanning with ^{201}Tl in patients displaying symptoms indicative of coronary artery disease, an unexpected radionuclide uptake pattern was observed in the cardiac scintigrams (Fig. 1.7) [70]. It became apparent that, in addition to the anticipated normal biodistribution, ^{201}Tl had the capability to accumulate in tumours. This intriguing observation prompted further investigations, both in animal models and clinical settings [71–73]. Subsequent studies employed ^{201}Tl scintigraphy to explore the presence and location of various primary and metastatic tumours within the chest area, including the lungs, breasts, oesophagus, head and neck regions (such as the brain, thyroid, and parathyroids), lymphatic nodes, as well as bones and soft tissue sarcomas [63]. These investigations highlighted the potential of ^{201}Tl in tumour imaging.

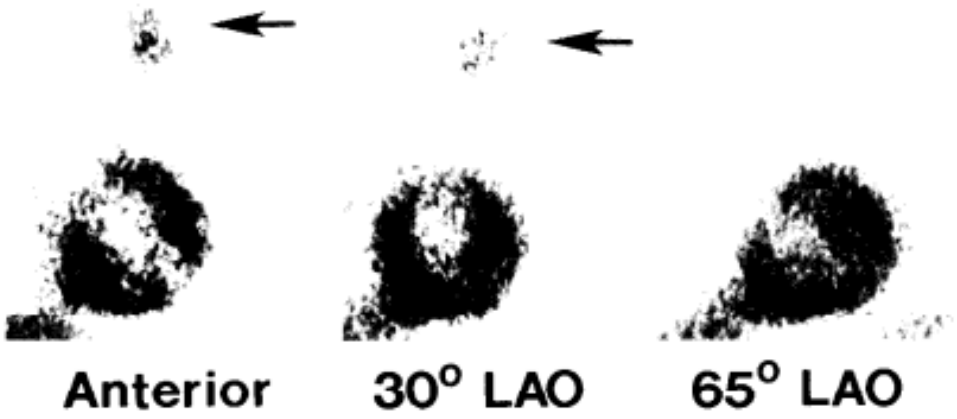

Figure 1.7 Extracardiac localisation of [^{201}Tl]TlCl in a patient with coronary heart disease showing rest scintigraphic images in 3 projections. Arrows indicate focal extracardiac accumulation of [^{201}Tl]TlCl subsequently confirmed as pulmonary carcinoma. LAO - left anterior oblique view. Figure was taken from Basara B., et al. [70] and reprinted with permission from Copyright Clearance Center.

Despite numerous studies conducted on the tumour-seeking properties of ^{201}Tl, the exact mechanism underlying its accumulation remains unknown. Generally, ^{201}Tl uptake appears to be associated with several factors, including cell viability, necrosis, the grade of malignancy, and the regional blood flow [74]. It has been reported that the rapid uptake and distribution of ^{201}Tl in tumours and other tissues

resemble those of ^{42}K, suggesting that thallium's affinity for malignancies may be linked to increased potassium metabolism [73]. The swift extraction of ^{201}Tl from the bloodstream by cancerous cells, resulting in peak tumour activity within just 10-15 minutes after injection, is reminiscent of the process observed in the myocardium [75]. Considering the rapid uptake kinetics of ^{201}Tl, it has been suggested that the tumour vasculature might also play a role in its accumulation. Tumour perfusion and vascularity are typically abnormal, with greater prominence in the tumour periphery and increased permeability of new vessels, leading to heterogeneous ^{201}Tl uptake [74,76]. Notably, it has been observed that necrotic areas within tumours do not accumulate thallium, which may be attributed to reduced perfusion at the tumour's centre and the absence of active transport across cellular membranes. It has been noted that Na^+/K^+ pump plays a crucial role in ^{201}Tl tumour uptake, reflecting the viability and metabolic state of the cells, similar to its role in myocardial imaging [77]. Importantly, the influx of ^{201}Tl is significantly reduced by cardiac glycosides such as ouabain and digoxin - known inhibitors of the Na^+/K^+-ATPase, particularly in lung carcinoma cells [77]. The effect of cardiac glycosides on ^{201}Tl kinetics in prostate cancer cells is reported in chapter 2.

While ^{201}Tl imaging showed promise for specific tumour types [78] and, in some cases, outperformed radioactive gallium (^{68}Ga) [79], it did not emerge as the definitive diagnostic tool that clinicians had hoped for. The same limitations that hindered the use of ^{201}Tl in myocardial disease diagnostics also posed challenges in tumour imaging. The advent of new PET radiotracers, particularly the fluorinated glucose analogue ^{18}F-FDG (fluorodeoxyglucose), marked a significant breakthrough. These newer tracers offered improved image resolution, biodistribution, and enhanced sensitivity [80]. Consequently, interest in ^{201}Tl began to disappear, persisting primarily in specific domains like brain tumour imaging, where the use of ^{18}F-FDG was constrained due to elevated background accumulation [81,82].

1.8 ^{201}Tl production methods and impurities

During the 'golden age' of thallium in the 1970s and 80s, commercial production of ^{201}Tl was established to meet the growing demand for diagnostic imaging. Several production methods were developed, involving proton-induced nuclear reactions using targets such as mercury, bismuth, lead, and thallium [83,84]. Among these methods, the most efficient route, considering production yield, radiochemical purity, and practical aspects, was to use a thallium-containing target [85]. Natural thallium is a mixture of two stable isotopes, ^{205}Tl (70.5%) and ^{203}Tl (29.5%), and can be found in low concentrations in the Earth's crust, especially in sulfide ores of various heavy metals [86]. Two indirect nuclear reactions have been explored for ^{201}Tl production: $^{205}Tl(p, 5n)^{201}Pb$ and $^{203}Tl(p, 3n)^{201}Pb$, with

the latter being the more commonly used method [83,87]. Lead-201 (^{201}Pb) is a precursor to ^{201}Tl and has a half-life of 9.4 hours (Fig. S2.2 A, in chapter 2 supplementary materials). During the target proton bombardment process, other competing nuclear reactions may occur, leading directly to a formation of radiochemical impurities, mainly ^{202}Tl and ^{200}Tl [88]. The maximum limits for the production radioimpurities, which can be identified by emission spectroscopy, are set by the European Pharmacopoeia. The most problematic, from the clinical perspective, is the contamination of the long-lived ^{202}Tl radioisotope (half-life of 12.3 days), which can result not only in increased signal-to-noise ratio and a degradation of contrast in SPECT imaging, but also an increased radiation dose to the patient [84]. The evaluation of the residual amounts of ^{205}Tl and ^{203}Tl in the stock material is described in chapter 2 supplementary materials (Table S2.1 and Fig. S2.2 B).

1.9 ^{201}Tl as a potent Auger electron-emitter

In addition to its clinically relevant gamma rays, ^{201}Tl also emits Auger and secondary electrons. ^{201}Tl decays by electron capture to a stable daughter – mercury-201 (^{201}Hg) with a half-life of 73 h. During this process ^{201}Tl produces a potent shower of 37 Auger electrons with short distance range of a few nanometres in tissue and average energy of 15.3 keV [43]. The low energy of emitted Auger electrons and their short range in tissue results in medium levels of linear energy transfer (LET). This characteristic makes ^{201}Tl an ideal candidate for delivering high levels of targeted radiation to specific cellular targets. When coupled with a targeting vector such as a small molecule, peptide, or an antibody, ^{201}Tl has a great potential for targeted delivery of high radiation doses to cancer cells while avoiding adverse radiotoxic effects in healthy tissue. Additionally, the short-range electrons may benefit from targeted delivery directed to sensitive subcellular target such as nucleus, cell membrane or mitochondria to achieve their best potential [52]. The investigation of subcellular localisation of unbound ^{201}Tl and nanoparticle-bound ^{201}Tl is presented in chapter 4.

Despite the potential, the radiotoxicity of ^{201}Tl has not been fully investigated, with only a handful of toxicity studies published over the last few decades. An assessment of ^{201}Tl kinetics and in vitro toxicity in breast and prostate cancer cells with references to the initial experiments published on ^{201}Tl toxicity is outlined in chapter 2.

1.10 Chemical properties of thallium

One of the challenging aspects of incorporating ^{201}Tl into a targeted radiopharmaceutical and evaluating its specific radiotoxicity is the limited availability of suitable chelating agents. Looking at Tl chemical properties, we can distinguish two important oxidation states: 1+ and 3+. The univalent ion

is more stable in aqueous solutions and forms compounds similar to those of the alkali metals, whereas the trivalent thallium compounds are more acidic and chemically resemble those of gallium and indium [86]. The high standard redox potential for Tl^{+}/Tl^{3+} pair (E° = +1.25 V) suggests that thallium is likely to exist predominantly in the Tl^{+} form in aqueous solutions, requiring strong oxidation conditions for the generation of Tl^{3+} [89]. Given the electrophilic nature of Tl^{3+}, it might be preferable to form complexes with electron-rich species, such as oxygen- and nitrogen-containing neutral molecules or anions, which may also contribute to stabilisation of the tripositive oxidation state. The increased ionic radius of Tl^{+} in comparison to Tl^{3+} (164 pm vs 103 pm) [89] and the greater polarisability have a huge impact on Tl^{+} becoming a 'softer' acceptor with enhanced affinity for donors like sulphur [86]. Despite thallium's discovery over 150 years ago, the challenges posed by its distinctive physicochemical properties have hindered the development of efficient and biologically stable chelators. Until recently, there has been minimal progress in thallium coordination chemistry, prompting a growing need for innovative approaches and research in this field.

One of the known substances with a remarkable ability to effectively bind thallium (I) is Prussian blue, which is registered by the US Food and Drug Administration for the use in acute, non-radioactive thallium poisoning or as an antidote in case of radioactive thallium or caesium ingestion. Its natural capacity to incorporate thallium ions within the interstitial spaces of its crystal structure is further elaborated in chapter 3. In an effort to eliminate thallium (I) from living organisms, a combination of desferrioxamine and deferiprone – both commercially utilised for iron overload (Fig. 1.9 A and B) - was investigated in rats, yielding limited success [90]. Using the unique property of thallium to mimic potassium in cells, lipophilic complexes of thallium (I) and diethyldithiocarbamate (DDC) (Fig. 1.9 C) were tested in rats for mapping the neuronal activity in the brain with an autometallographic technique. This method proved to be efficient in detecting Tl^{+}-fluxes across the blood-brain barrier [91,92]. Furthermore, a pilot study was conducted using [^{201}Tl]DDC in rabbits and also in humans to measure regional brain metabolism and perfusion by SPECT imaging. It was concluded that [^{201}Tl]DDC is taken up in the brain tissue and has a potential in detecting cerebral ischemia [93]. More recently, derivatives of kryptofix (4,7,13,16,21,24-hexaoxa-1,10-diaza-bicyclo[8.8.8]hexacosane) (Fig. 1.9 D) were synthesised in an attempt to chelate [^{201}Tl]TlCl and selectively deliver it to prostate cancer cells upon conjugation with a PSMA - targeting peptide. While kryptofix compounds, both alone and in conjugation with the targeting peptide, exhibited high radiolabelling yield and stability in serum, subsequent incubation with cells resulted in the release of Tl^{+} from the complex, and no PSMA-specific uptake was observed. It has been proposed that the instability of $^{201}Tl^{+}$ complexes with kryptofix derivatives could be attributed to the competition for Tl^{+} binding between kryptofix chelators and

other molecules present in the incubation medium or on a cell surface, such as potassium transporters [94].

Complexing Tl^{3+} is also not a straightforward task. There have been reports describing complexes of Tl^{3+} with modified porphyrins (Fig. 1.9 E), which are macrocycles with a large planar structure containing four modified pyrrole subunits [95–97]. This approach is further explored in chapter 5. Chelators like DOTA and DTPA (Fig. 1.9 F and G) have been examined for the purpose of Tl^{3+} complexation, aiming for potential applications in SPECT imaging [89]. In this study [^{201}Tl]Tl^{+} was oxidised to [^{201}Tl]Tl^{3+} with ozone in the presence of hydrochloric acid and complexed with DTPA and DOTA achieving high radiolabelling yield. Only the radiolabelled DOTA complexes demonstrated good stability in serum. However, when ^{201}Tl(III)-DOTA was tested in a mouse model, its biodistribution mirrored that of unchelated [^{201}Tl]Tl^{+} indicating the instability of the complex and the subsequent release of thallium(I) [89]. This observation was confirmed by another study assessing [^{201}Tl]Tl^{3+} chelation with DTPA, DOTA and EDTA (ethylenediaminetetraacetic acid), concluding that although all the chelators could rapidly and efficiently complex thallium(III), their stability in serum was limited [98].

Another category of potential Tl^{3+} chelators includes multidentate picolinic acid based chelators such as H_4pypa, H_5decapa, H_4neunpa-NH_2, and H_4noneunpa [99]. All these ligands were able to efficiently bind [^{201}Tl]Tl^{3+} and demonstrated improved serum stability compared to DOTA or DTPA. One of the chelators - H_4pypa (Fig. 1.9 H), underwent further conjugation with a PSMA-targeting peptide and the conjugate was subjected to in vitro and in vivo testing. Cellular uptake experiments revealed potential instability of the radiolabelled targeting conjugate ([^{201}Tl]Tl-pypa-PSMA), leading to a reduction of Tl^{3+} to Tl^{+} and its subsequent release. However, biodistribution and stability studies in healthy mice have shown that myocardial accumulation was lower compared to unchelated thallium. In mice with PSMA-positive and PSMA-negative prostate cancer xenografts, the uptake of [^{201}Tl]Tl-pypa-PSMA in PSMA-positive tumours was higher in PSMA-positive tumors compared to PSMA-negative tumors, but still insufficient for selective tumor delivery. Although radiolabelled H_4pypa conjugates demonstrated greater stability compared to previously tested chelators like DOTA or DTPA, the vulnerability of Tl^{3+} to reduction in a biological environment and its subsequent dissociation presented a significant challenge, prompting the need for further improvements [99].

1.11 Thesis aims

The primary aim of this project was to provide the groundwork for creation of a radiopharmaceutical that leverages the radiotoxic properties of ^{201}Tl for the use in the targeted treatment of small tumours and micrometastases in cancer therapy. There were several key objectives for this project (Fig. 1.9):

1. Evaluating the radiotoxicity of ^{201}Tl by investigating its native cellular uptake through potassium channels in various cancer cell lines and comparing this to the toxicity of non-radioactive Tl and ^{201}Hg, which is the stable product of ^{201}Tl radioactive decay. Chapter 2 provides evidence of ^{201}Tl radiotoxicity.

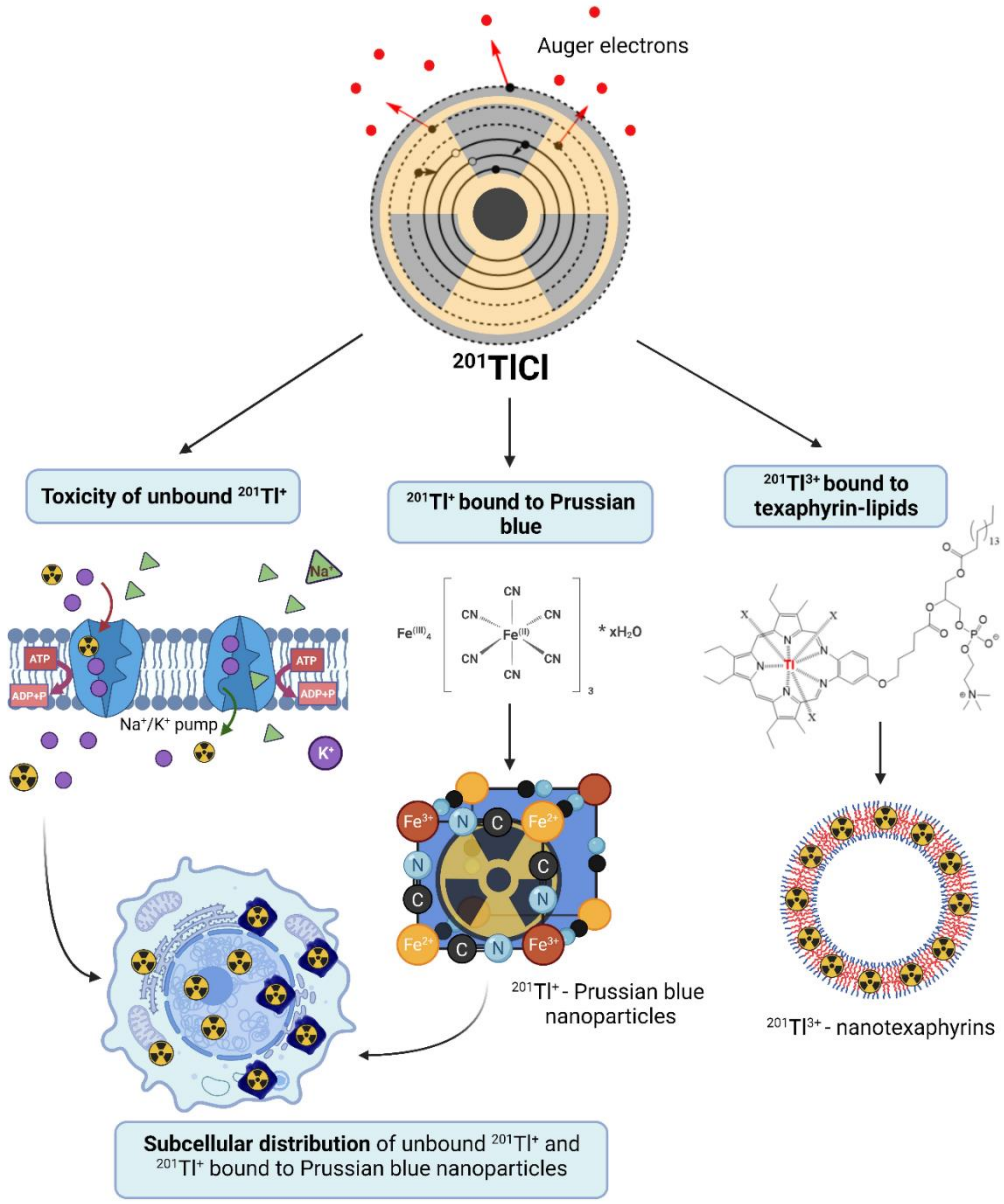

Figure 1.9 Schematic illustration outlining the primary objectives of this PhD thesis. Created with BioRender.com.

2. Developing nanoparticles that contain a Prussian blue core capable of binding $^{201}Tl^{+}$ within its crystal structure. This involves characterising the ^{201}Tl-labelled Prussian blue nanoparticles and assessing their kinetics and toxicity in both in vitro and in vivo settings. The impact of different surface coatings on the kinetics and toxicity is also examined. This work is described in chapter 3.
3. Investigating the subcellular distribution of unbound ^{201}Tl and ^{201}Tl bound to Prussian blue nanoparticles (PBNPs) using various methods, which is explored in chapter 4.
4. Assessing the feasibility of binding $^{201}Tl^{3+}$ to texaphyrin-lipids and nanoparticles based on their structure. This preliminary study is included in chapter 5.

Chapter 2: In vitro proof of concept studies of radiotoxicity from Auger electron-emitter thallium-201

The research included in this chapter was published on 5th July 2021 in the European Journal of Nuclear Medicine and Molecular Imaging Research (doi: 10.1186/s13550-021-00802-w) What is presented here is the approved final manuscript with the additional supplementary materials located at the end of this chapter. The journal-formatted version of the article can be found at the end of the PhD thesis.

Katarzyna M. Osytek[1], Philip J. Blower[1], Ines M. Costa[1], Gareth Smith[2], Vincenzo Abbate[3*] and Samantha Y. A. Terry[1*]

[1] King's College London, School of Biomedical Engineering and Imaging Sciences, London, United Kingdom

[2] Theragnostics Limited, 2 Arlington Square, Bracknell, RG12 1WA, United Kingdom

[3] King's College London, Department of Analytical, Environmental and Forensic Sciences, London, United Kingdom

Corresponding authors: Samantha Y. A. Terry, samantha.terry@kcl.ac.uk; Vincenzo Abbate, vincenzo.abbate@kcl.ac.uk. *contributed equally.

2.1 Abstract

Background: Auger electron-emitting radionuclides have potential in targeted treatment of small tumours. Thallium-201 (^{201}Tl), a gamma-emitting radionuclide used in myocardial perfusion scintigraphy, decays by electron capture, releasing around 37 Auger and Coster-Kronig electrons per decay. However, its therapeutic and toxic effects in cancer cells remain largely unexplored. Here, we assess ^{201}Tl in vitro kinetics, radiotoxicity and potential for targeted molecular radionuclide therapy, and aim to test the hypothesis that ^{201}Tl is radiotoxic only when internalised. **Methods:** Breast cancer MDA-MB-231 and prostate cancer DU145 cells were incubated with 200-8000 kBq/mL of [^{201}Tl]TlCl. Potassium concentration varied between 0-25 mM to modulate cellular uptake of ^{201}Tl. Cell uptake and efflux rates of ^{201}Tl were measured by gamma counting. Clonogenic assays were used to assess cell survival after 90 minutes incubation with ^{201}Tl. Nuclear DNA damage was measured with γH2AX

fluorescence imaging. Controls included untreated cells and cells treated with decayed [^{201}Tl]TlCl. **Results:** ^{201}Tl uptake in both cell lines reached equilibrium within 90 minutes and washed out exponentially ($t_{1/2}$ = 15 min) after the radioactive medium was exchanged for fresh medium. Cellular uptake of ^{201}Tl in DU145 cells ranged between 1.6% (25 mM potassium) and 25.9% (0 mM potassium). Colony formation by both cell lines decreased significantly as ^{201}Tl activity in cells increased, whereas ^{201}Tl excluded from cells by use of high potassium buffer caused no significant toxicity. Non-radioactive TlCl at comparable concentrations caused no toxicity. An estimated average ^{201}Tl intracellular activity of 0.29 Bq/cell (DU145 cells) and 0.18 Bq/cell (MDA-MB-231 cells) during 90 minutes exposure time caused 90% reduction in clonogenicity. ^{201}Tl at these levels caused on average 3.5-4.6 times more DNA damage per nucleus than control treatments. **Conclusions:** ^{201}Tl reduces clonogenic survival and increases nuclear DNA damage only when internalised. These findings justify further development and evaluation of ^{201}Tl therapeutic radiopharmaceuticals.

Key words: Auger electrons, ^{201}Tl, thallium-201, radiobiology, targeted molecular radionuclide therapy

2.2 Background

Thallium-201 (^{201}Tl, $t_{1/2}$ = 73 h) is well-known in diagnostic nuclear medicine. By mimicking the biological behavior of potassium, it has played a major role in myocardial perfusion scintigraphy [61], until it was largely replaced by ^{99m}Tc labelled complexes [68]. ^{201}Tl has also been used for tumour imaging [63,73], to evaluate chemotherapy responses [100] and tumour malignancy [101,102]. However, because of low signal-to-noise ratio, significant tissue attenuation and high radiation absorbed dose [60], diagnostic use of ^{201}Tl has substantially diminished in recent years.

Apart from its gamma rays (135 keV - 3%, 167 keV - 10%) and X-rays (67-83 keV - 94%) used in clinical imaging [103], ^{201}Tl decay by electron capture to stable mercury (^{201}Hg) also produces around 37 short-range Auger and Coster-Kronig electrons, one of the highest numbers among other Auger-electron emitters (Table 2.1) [104] with therapeutic potential.

	^{201}Tl	^{111}In	^{67}Ga	^{125}I
Half-life (days)	3.04	2.80	3.26	59.4
Number of Auger and Coster-Kronig electrons/decay	36.9	14.7	4.7	24.9
Auger and Coster-Kronig electrons energy per decay (keV)	15.3	6.8	6.3	12.2
Associated gamma emission (keV)	135.3; 167.4	171.3; 245.4	9.1; 9.3; 184; 209; 300; 393	35

Table 2.1 Characteristics of some of the Auger electron-emitters [104].

The average total energy of Auger and Coster-Kronig electrons per decay is calculated as 15.3 keV [104] and even though this is comparable to the energy of ^{125}I, its half-life is around 20 times shorter and hence more amenable to clinical use. Auger electron-emitters such as ^{111}In, ^{125}I and ^{67}Ga (Table 2.1) [104], have already shown potential for targeted radionuclide therapy of cancer [105–107], especially when delivered close to sensitive cellular targets such as DNA and plasma membrane [104] [108,109]. However, the therapeutic potential of ^{201}Tl has barely been studied, despite its potent shower of Auger electrons and good worldwide availability. Nearly 40 years ago, in the context of the safety of diagnostic use of ^{201}Tl, Rao et al. observed radiotoxic effects of ^{201}Tl in spermatogonial cells after intratesticular injection in a mouse model [110], and Kassis et al. compared the cellular kinetics and radiotoxicity of ^{201}Tl to those of β-emitters (^{42}K, ^{43}K and ^{86}Rb) in Chinese hamster lung fibroblasts [111]. Since then, there has been little interest in ^{201}Tl radiobiology or radionuclide therapy. In this preliminary evaluation of the potential of ^{201}Tl as a therapeutic radionuclide, we investigated the rate and extent of non-targeted ^{201}Tl uptake into cancer cells via potassium channels, such as the Na^+/K^+ pump (Fig. 2.1) and used this mechanism of accumulation to assess its radiotoxic effect in human cancer cells in vitro.

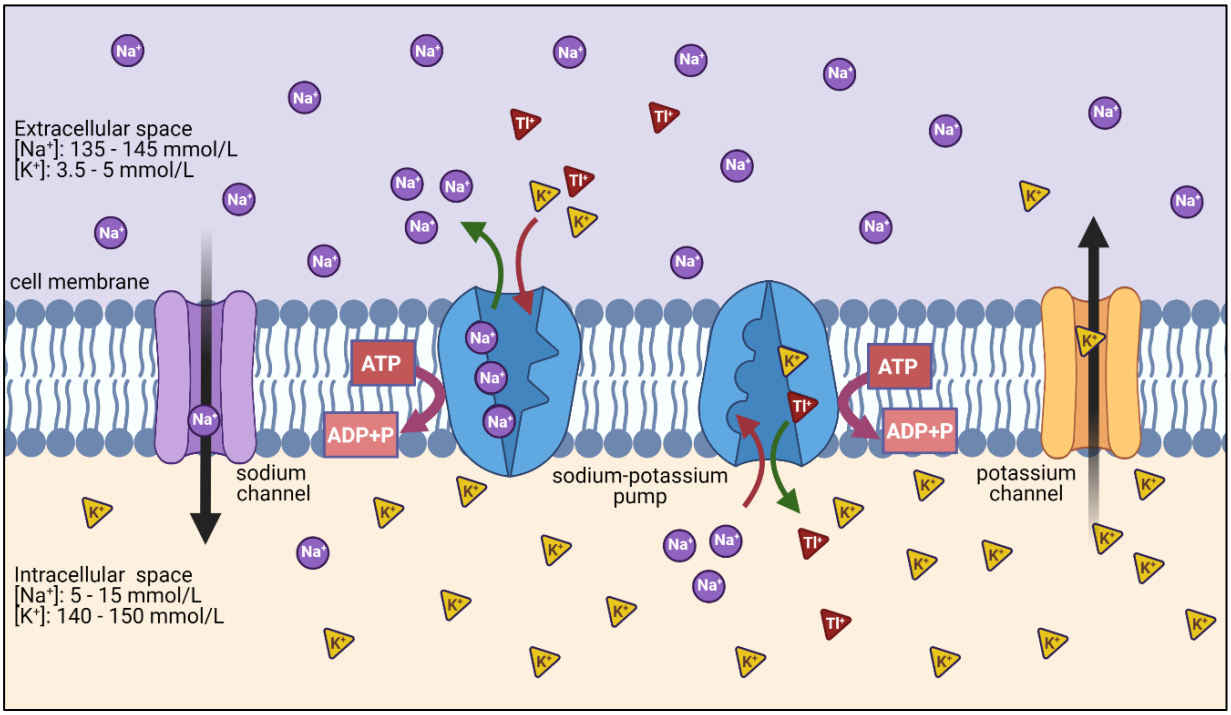

Figure 2.1 Schematic representation of K^+, Na^+ and Tl^+ transport across cellular membranes. Sodium-potassium pump (Na^+/K^+-ATPase) transports K^+ ions inside and Na^+ ions outside a cell against their concentration gradient using energy released by the hydrolysis of ATP. Tl^+ ions, which mimic K^+ physiological behaviour, can be transported inside the cell via potassium channels, such as the sodium-potassium pump. Tl^+ transport mechanism outside the cell is currently unknown.

2.3 Aim

The primary aim of this study was to measure the effect of internalised and non-internalised ^{201}Tl on clonogenic survival and DNA integrity in prostate and breast cancer cells. Non-targeted ^{201}TlCl was used in this study only to assess the radiotoxic potential of the radionuclide, and not to assess the potential of ^{201}TlCl itself. In contrast to other Auger electron-emitting radionuclides, such as ^{111}In or ^{67}Ga, no suitable chelators are available for ^{201}Tl and their development can be challenging due to its physical and chemical properties. A finding that ^{201}Tl has potential as a therapeutic radionuclide would stimulate development of effective thallium chelators for construction of targeted bioconjugates.

2.4 Methods

Cell culture consumables, unless specified, were purchased from Sigma-Aldrich, UK. [^{201}Tl]TlCl in sterile 0.9% NaCl solution (360 - 560 MBq/5.8 mL) was obtained from CIS Bio International, France; [^{201}Tl]TlCl specific radioactivity was greater than or equal to 3.7 MBq/µg of thallium and radiochemical purity was at least equal to 95% (as per [^{201}Tl]TlCl specification). [^{201}Tl]TlCl was used in all experiments without any preconditioning.

2.4.1 Cell culture: human breast adenocarcinoma cells MDA-MB-231 (ATCC® HTB-26™) were cultured in Dulbecco's Modified Eagle Medium (DMEM, low glucose 1000 mg/L) and human prostate carcinoma cells DU145 (ATCC® HTB-81™) in RPMI-1640 medium. Both media were supplemented with 10% fetal bovine serum, 5% L-glutamine, penicillin (100 units) and 100 µg/mL streptomycin. Cultured cells were trypsinised and seeded at 250,000 cells per well in 24-well plates 16 hours before each experiment and grown at 37°C in a humidified 5% CO_2 atmosphere. During experiments, cells were kept in full medium or phosphate buffered saline (PBS; D8537) supplemented with $MgCl_2$ and $CaCl_2$ in concentrations equivalent to those found in media, or PBS without potassium (Alfa Aesar, J60465) supplemented as described above for PBS. KCl solutions were prepared by dissolving KCl (BDH Laboratory) in 0.9% NaCl. Concentrations of K^+ and Na^+ in PBS, PBS without K^+, RPMI and DMEM media are shown in Table 2.2.

Incubation solution	Concentration of K^+ (mmol/L)	Concentration of Na^+ (mmol/L)
Dulbecco's Modified Eagle Medium (DMEM)	5.3	155.0
RPMI-1640 medium	5.3	138.5
Phosphate buffer saline (PBS)	4.2	153.0
Phosphate buffer saline (PBS) without K^+	0	157.0

Table 2.2 Concentration of potassium and sodium in incubation solutions used in experiments. To modulate ^{201}Tl uptake in cells, 0 mmol/L K^+ solutions were supplemented with KCl at a range of concentrations up to 25 mmol/L.

2.4.2 Uptake and efflux assays: fifteen minutes before each experiment the medium in each well was replaced by 200 µL fresh medium, PBS or PBS without K^+. Stock [^{201}Tl]TlCl was diluted with 0.9% NaCl to the required concentration (1-40 MBq/mL) and 50 µL (50-2000 kBq) was added to each well. Plates were incubated at 37°C for a specified period. Then, the radioactive incubation solution was collected. Adherent cells were briefly washed thrice with PBS and lysed with 1 M NaOH for 15 min at room temperature (RT). Unbound radioactivity (incubation medium and PBS washings) and cell-bound radioactivity (lysate) were measured (counts per minute, CPM) with a CompuGamma CS1282 gamma counter.

To measure the rate of ^{201}Tl washout, cells were incubated at 37°C for 90 minutes with 50 kBq (1 MBq/mL) ^{201}Tl in 250 µL medium, which was then removed. Adherent cells were washed briefly with 250 µL PBS and 250 µL of fresh non-radioactive medium was added to each well. Cells were incubated for various times (from 15-180 min) at 37°C, after which medium was collected and cells washed and lysed as described above. A second method, to assess continuous complete ^{201}Tl efflux, involved repeated medium changes on the same cells. In brief, after incubation with 50 kBq (1 MBq/mL) ^{201}Tl as above, replacing radioactive medium with fresh medium and allowing a further 15 minutes of efflux; medium was again removed, cells were washed once with PBS and fresh medium added. This process was repeated 4 times at intervals from 15-60 min. After 180 min cells were lysed and ^{201}Tl activity measured as described above, converting CPM to activity by means of a calibration curve (Supplementary materials: Fig. S2.1). A nominal average intracellular volume of 1.6 pL for individual DU145 cells (as measured by diffusion NMR spectroscopy [112]) was used for intracellular-to-extracellular concentration ratio calculations.

^{203}Tl is a stable isotope used as a target material in the ^{201}Tl manufacturing process [113] and despite a rigorous purification process, some ^{203}Tl is still present in [^{201}Tl]TlCl solution (Supplementary materials: Fig. S2.2 and Table S2.1). Inductively Coupled Plasma-Mass Spectrometry (ICP-MS) analysis was performed using a PerkinElmer NexION350D ICP-Mass Spectrometer to estimate ^{203}Tl concentrations in [^{201}Tl]TlCl decayed samples, using a calibration curve prepared as described in Supplementary Information.

2.4.3 DNA damage: γH2AX assays were used to quantify DNA double-strand breaks (DSBs). Cells were seeded on coverslips coated with poly-L-lysine (50 µg/mL) placed in each well of a 24-well plate. Following a 90-minute incubation with 50 µL (50-2000 kBq) of different ^{201}Tl activities (200-8,000 kBq/mL), ^{203}Tl/^{201}Hg in equivalent concentrations, or ^{201}Tl (1000 kBq, 4,000 kBq/mL) with added KCl (15 and 25 mM), medium was removed and coverslips were washed with PBS, fixed with 3.7% formalin in PBS, treated for 15 minutes with 0.5% Triton X-100® and 0.5% IGEPAL CA-630® solution, incubated

with 1% goat serum/2% bovine serum albumin (BSA) in PBS for 1 h, washed with PBS, incubated overnight at 4˚C with mouse antiphospho-histone H2A.X monoclonal antibody (Merck, 1:1600 in 3% BSA), washed with 3% BSA in PBS and incubated with goat anti-mouse secondary fluorescent antibody Alexa Fluor®488 (Invitrogen, 1:500 in PBS) for 2 h at 4˚C. Hoechst 33342 nuclei stain was added for 2 min at RT. Coverslips were washed twice with PBS and attached to microscope slides using 2.5% DABCO/Mowiol® (except for the experiment blocking ^{201}Tl uptake with KCl, where cells were stained and mounted with Prolong™ Gold Antifade Reagent with DAPI (Invitrogen)). Slides were stored at 4˚C. A TCS SP5 confocal microscope with Leica software was used to obtain fluorescent images and CellProfiler was used to quantify foci numbers per nucleus.

2.4.4 Cytotoxicity: ^{201}Tl (50-2000 kBq, 200-8,000 kBq/mL), ^{203}Tl/^{201}Hg in equivalent concentrations, or ^{201}Tl (1000 kBq, 4,000 kBq/mL) with KCl (15 and 25 mM) was added to MDA-MB-231 or DU145 cells in 200 µL medium or potassium-free PBS. After 90 minutes, the radioactive incubation solution was removed, cells were washed three times with PBS, trypsinised, re-suspended in non-radioactive medium, seeded at 1,000 cells/well in a 6-well plate and cultured for 8-10 days, changing medium every 2-3 days. Colonies were fixed and stained with 0.05% crystal violet in 50% methanol and counted manually with blinding, defining colonies as containing >50 cells. All clonogenic assays were done alongside uptake assays to relate activity per cell with the surviving fraction.

2.4.5 Statistical analysis: Data were analysed in Excel Microsoft 2016 and GraphPad Prism 8, and expressed as mean ± SD. A non-parametric Mann-Whitney test for unpaired data was used to determine significance ($P < 0.05$). Each experiment was performed in triplicate or quadruplicate. Error bars represent standard deviations among independent experiments, except when n=1 where the error is intra-experimental.

The intracellular activity was calculated comparing the gamma counter measurements (cpm) of the collected medium activity (with three PBS washes) to the lysate (NaOH) activity. The background count (BC) was subtracted from both values.

$$\text{Intracellular activity (\%)} = \frac{\text{lysate activity} - \text{BC}}{(\text{lysate activity} - \text{BC}) + (\text{collected medium activity} - \text{BC})} * 100$$

For the gamma counter measurements, fractions of the culture medium and lysate were taken (when needed) and then multiplied by the appropriate factor to obtain total values necessary for calculations.

The intracellular activity per cell was calculated by multiplying the activity added to each well (50-2000 kBq) by the measured intracellular activity (%) and divided by the number of cells per well counted right after the experiment.

Intracellular activity per cell (Bq/cell) $= \frac{\text{activity added per well (Bq)} * \text{intracellular activity (\%)}}{\text{number of cells per well} * 100}$. Figures were created with GraphPad Prism 8 and BioRender.com.

2.5 Results

2.5.1 ^{201}Tl kinetics – uptake and efflux

In preliminary experiments in RPMI or DMEM medium (Table 2.2), cellular uptake of ^{201}Tl in both DU145 and MDA-MB-231 cells rose sharply up to 60 min and then plateaued (Fig. 2.2 A and Supplementary materials: Fig. S2.3 A).

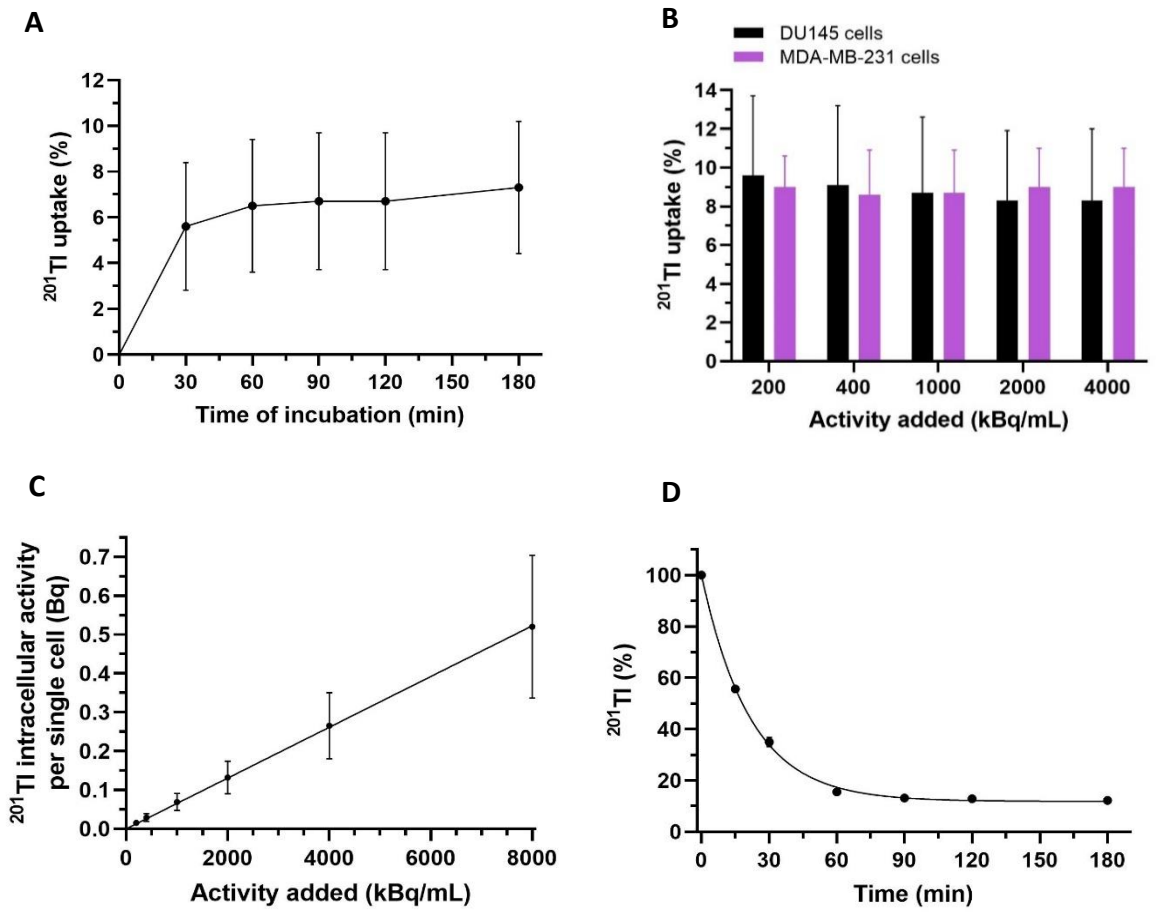

Figure 2.2 ^{201}Tl kinetics. A) Uptake of ^{201}Tl in DU145 cells (n=3) after incubation with 200 kBq/mL [^{201}Tl]TlCl in medium. These results were used to determine the best incubation time for subsequent radiobiological experiments. **B)** ^{201}Tl uptake in DU145 cells (n=3) and MDA-MD-231 cells (n=2) after 90 min incubation in medium with different activities of [^{201}Tl]TlCl. **C)** ^{201}Tl intracellular activity per single cell (Bq) versus activity added (kBq/mL) in DU145 cells (n=3) measured in medium. Graphs B and C show that the increasing activity of ^{201}Tl does not inhibit its cellular uptake, suggesting that saturation of uptake mechanisms is not reached at the activities used in this work. **D)** Efflux of ^{201}Tl in DU145 (n=3) cells. Plateau uptake from the preceding uptake assay is defined as 100% at time 0. Radioactive medium was replaced with non-radioactive and ^{201}Tl activity was measured over time. Data are presented as mean ± SD, done in triplicates; exponential regression line was fitted in D. Some error bars are smaller than the data symbols and hence not visible.

The % uptake was independent of the activity used within the range examined (Fig. 2.2 B and C) showing that the uptake mechanism was not saturable in this range. Based on these results, 90 min incubation time was chosen for radiobiological experiments.

Efflux rate measurements were performed after 90 min 'loading' with 200 kBq/mL of ^{201}Tl in RPMI or DMEM medium. In both cell lines, when the radioactive medium was replaced by non-radioactive medium, ^{201}Tl bound by cells decreased exponentially with a half-life of around 15 minutes reaching a new equilibrium (Fig. 2.2 D and Supplementary materials: Fig. S2.3 B) with the same intracellular-to-extracellular ratio of ^{201}Tl concentration. When medium was repeatedly refreshed, we again observed an exponential drop in the activity bound per cell, from 0.017-0.019 Bq at the beginning of the efflux experiment to approach 0 after 180 min (Supplementary materials: Fig. S2.3 C).

To modulate ^{201}Tl uptake into cells, cardiac glycosides digoxin and ouabain were evaluated but rejected because of their toxic effects on cells as described in Supplementary Material (Fig. S2.4 A and B) [114]. Instead, the effect of varying potassium concentration was evaluated. DU145 cells were incubated with 80 kBq/mL of ^{201}Tl for 90 minutes in PBS solution without potassium (Table 2.2) and supplemented with different concentrations of KCl rising to 50 mM. ^{201}Tl uptake decreased from 23.6 ± 0.6% in 0 mM potassium to 1.1 ± 0.1% in 50 mM potassium (Supplementary materials Fig. S2.4 C). The potassium concentrations used showed no measurable baseline effects as measured by clonogenic assay or γH2AX imaging (see below), therefore variation of potassium concentration was adopted as the method of choice to modulate ^{201}Tl uptake.

2.5.2 ^{201}Tl-induced nuclear DNA damage (γH2AX assay)

Results from three experiments on DU145 and MDA-MB-231 cells are shown in Table 2.3 and Figure 2.3 A. Cells treated with 4,000 kBq/mL of ^{201}Tl showed a significantly higher average number of foci per nucleus (3.5 and 4.6 times for DU145 and MDA-MB-231 cells, respectively) than in the 0.9% NaCl-treated control ($P<0.05$, Mann-Whitney test) (Supplementary materials: Fig. S2.5 A and B).

Activity of ^{201}Tl (kBq/mL)	Average number of foci per nucleus (± SD) DU145			Average number of foci per nucleus (± SD) MDA-MB-231		
0	3.5 ± 3.6	17.8 ± 18.3	11.9 ± 10.4	7.9 ± 10.3	8.6 ± 6.2	12.0 ± 10.9
100	5.2 ± 5	37.5 ± 25.2	13.3 ± 10.6	7.0 ± 5.3	9.4 ± 7.5	14.0 ± 13.1
200	4.4 ± 4.1	40.6 ± 33.7	12.0 ± 9.1	13.8 ± 8.0	9.5 ± 5.3	15.0 ± 7.2
400	16.2 ± 11.5	60.4 ± 34.9	19.9 ± 12.8	18.2 ± 9.4	22.7 ± 11.0	21.0 ± 12.2
1000	10.1 ± 6.2	71.2 ± 23.2	26.2 ± 18.1	30.9 ± 18.0	27.9 ± 17.0	38.8 ± 20.4
4000	28.6 ± 14.7	61.2 ± 27.8	25.3 ± 13.0	61.5 ± 28.0	29.6 ± 12.7	39.2 ± 21.5

Table 2.3 ^{201}Tl radiotoxicity – nuclear DNA damage. Average number of foci per nucleus in DU145 cells and MDA-MD-231 cells after 90 min incubation with various activities of [^{201}Tl]TlCl in medium, and with 0.9% NaCl (0 kBq/mL) measured in three independent experiments.

Comparing the nuclear DNA damage in DU145 cells caused by 4,000-8,000 kBq/mL of ^{201}Tl to that caused by an equivalent volume of decayed [^{201}Tl]TlCl sample, we observed that only the radioactive component of the samples significantly increased the average number of foci per nucleus ($P < 0.05$, Mann-Whitney test) (Fig. 2.3 B).

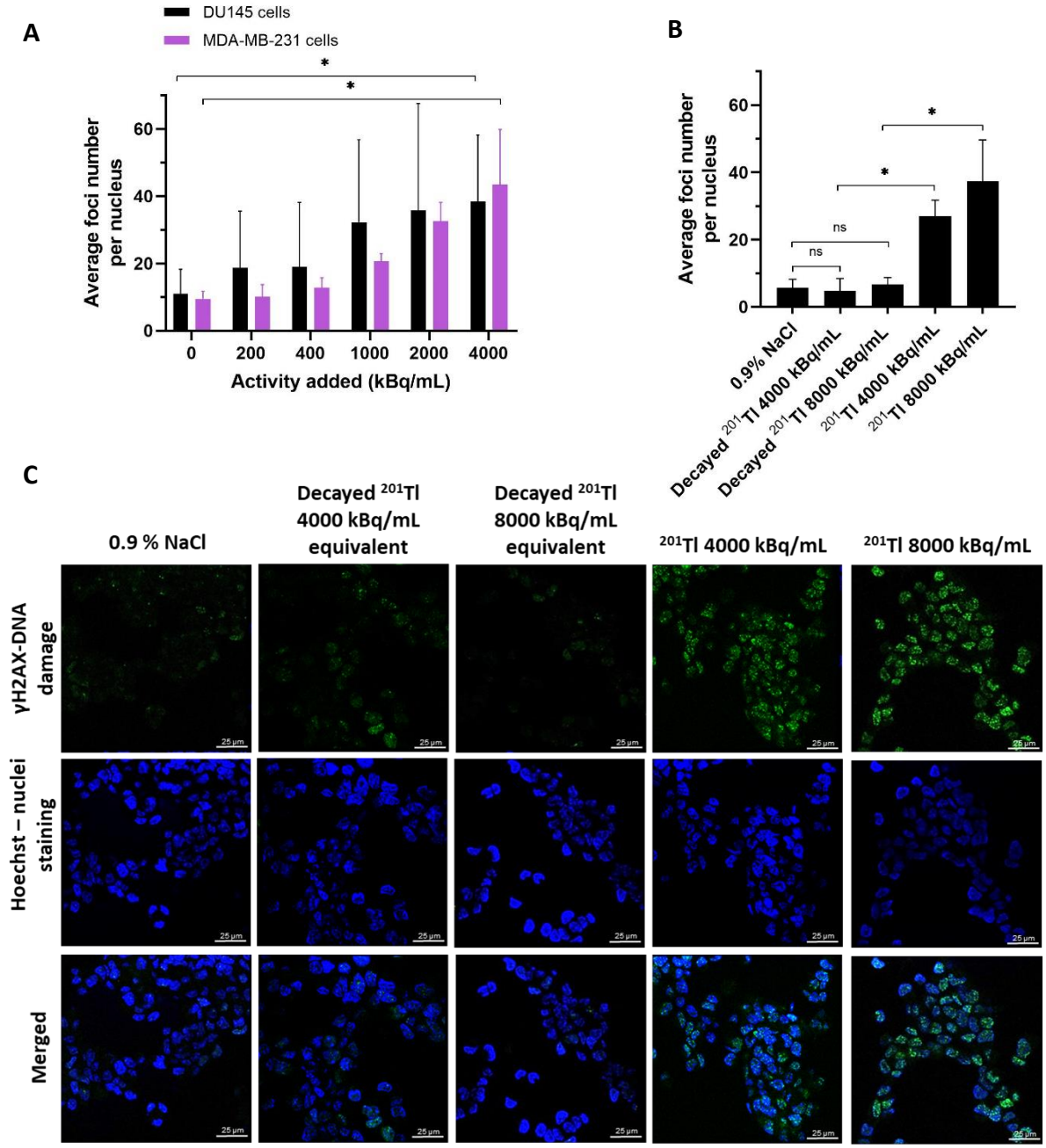

Figure 2.3 ^{201}Tl radiotoxicity – nuclear DNA damage. Average number of foci per nucleus in DU145 cells and MDA-MD-231 cells after 90 min incubation **A)** with [^{201}Tl]TlCl in medium **B)** with 0.9% NaCl (negative control), an equivalent volume of [^{201}Tl]TlCl-decayed sample or [^{201}Tl]TlCl. A range of 26 to 72 nuclei per condition were analysed across all experiments; same settings were kept within the experiment. 3-9 pixel units were set as a typical diameter of foci. Bars represent mean ± SD, n=3, * indicates $P < 0.05$, ns – not significant. **C)** Exemplar confocal microscopy images (100x, field contain minimum 25 nuclei) of DU145 cells incubated for 90 min with 0.9% NaCl (negative control), an equivalent volume of [^{201}Tl]TlCl-decayed sample or [^{201}Tl]TlCl followed by immunofluorescence staining with green fluorescence for γH2AX (smart gain (SG) and smart offset (SO) were kept constant for all conditions in the experiment). Nuclear DNA is stained with Hoechst (blue). Scale bar - 25 µm.

The decayed sample caused no visible DNA damage compared to untreated controls (Fig. 2.3 C) as expected, since thallium concentration is very low and other heavy metals (such as ^{201}Hg decay product) were not detectable by ICP-MS (Supplementary materials: Fig. S2.2 A and B and Table S2.1).

2.5.3 ^{201}Tl radiotoxicity - clonogenic survival

Figure 2.4 A presents clonogenic survival results for both cell lines incubated with various activities of ^{201}Tl for 90 min in RPMI or DMEM medium ([K^+] 5.3 mM). No reduction in surviving fractions was observed in cells treated with an equivalent volume of the decayed ^{201}Tl sample in DU145 cells (Fig. 2.4 B).

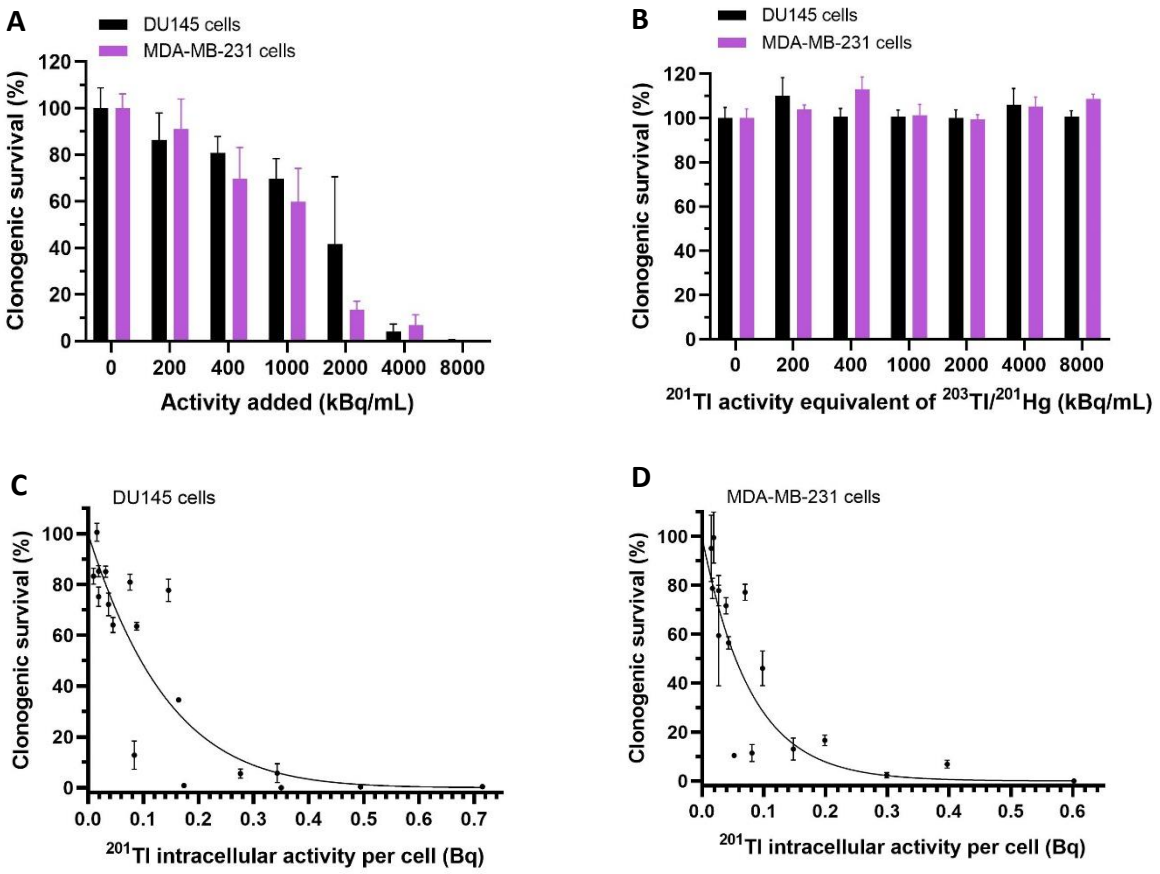

Figure 2.4 ^{201}Tl radiotoxicity – clonogenic survival. A) Clonogenic survival (%) in DU145 (n=3) and MDA-MD-231 cells (n=3 except 8000 kBq/mL where n=1) after 90 min incubation with [^{201}Tl]TlCl in medium. **B)** Clonogenic survival (%) measured in DU145 cells (n=3) and MDA-MB-231 cells (n=1) after 90 min incubation in medium with different concentrations of non-radioactive [^{201}Tl]TlCl decayed sample. **C)** Clonogenic survivals (%) versus ^{201}Tl intracellular activity per single cell in DU145 cells (n=3) and **D)** MDA-MB-231 cells (n=3). Linear quadratic survival model was fitted and calculated activity causing at least 90% reduction was 0.29 Bq for DU145 cells (95% CI: 0.18-0.49) and 0.18 Bq for MDA-MB-231 (95% CI: 0.10-0.39). Some error bars are smaller than the data points and not visible. Data are presented as mean ± SD, triplicates.

An estimated average ^{201}Tl intracellular activity per cell of 0.29 Bq (95% CI: 0.18-0.49 Bq) for DU145 cells and 0.18 Bq (95% CI: 0.10-0.39 Bq) for MDA-MB-231 cells (Fig. 2.4 C and D) reduced clonogenic survival by at least 90% compared to untreated cells.

2.5.4 The impact of ^{201}Tl internalisation on clonogenic survival and nuclear DNA damage in DU145 cells

Varying potassium concentrations in the incubation solution above and below the physiological level (3.5 - 5 mM [115]) was adopted as a method to modulate ^{201}Tl uptake in cells, for the purpose of comparing the radiotoxicity of intracellular and extracellular ^{201}Tl. Applying this method, we used the γH2AX assay to compare the average number of foci per nucleus in DU145 cells with high ^{201}Tl uptake ([K^+] 0 mM, 25.9 ± 1.7% uptake, 181:1 intra:extra ratio) and low ^{201}Tl uptake ([K^+] 15 and 25 mM, 1.6 ± 0.4 and 2.2 ± 0.2% uptake respectively, 8:1 and 12:1 intra:extra ratio) after incubation with the same radioactive concentration (4,000 kBq/mL) of ^{201}Tl (Fig. 2.5 A and B and Supplementary materials: Table S2.2).

We observed a significant reduction in the average number of foci per nucleus induced by ^{201}Tl – from 31.9 ± 5.2 at 0 mM K^+ to 8.8 ± 4.3 and 7.5 ± 5.0 at 15 and 25 mM potassium, respectively ($P < 0.05$, Mann-Whitney test). In cells incubated with these K^+ concentrations without ^{201}Tl or non-radioactive Tl (NC 1, 3-4), there was no increase in foci per nucleus compared to cells incubated in standard RPMI medium ([K^+] 5.3 mM) (NC 2). These results show that ^{201}Tl only induced DNA DSBs when internalised; extracellular ^{201}Tl showed no effect. A similar result emerged from clonogenic survival assays. Incubation of DU145 cells for 90 min with 4000 kBq/mL of ^{201}Tl (Fig. 2.5 C) was lethal (no clonogenic survival) in 0 mM potassium medium, but 94.7 ± 3.9% to 98.6 ± 4.4% survival was found when ^{201}Tl uptake was suppressed with 15 or 25 mM KCl. Both extremes of potassium concentration showed no clonogenic toxicity in the absence of ^{201}Tl. Thus, preventing or reducing cellular uptake of the ^{201}Tl by increasing potassium concentration in the medium prevented both the DNA damage and clonogenic toxicity of ^{201}Tl.

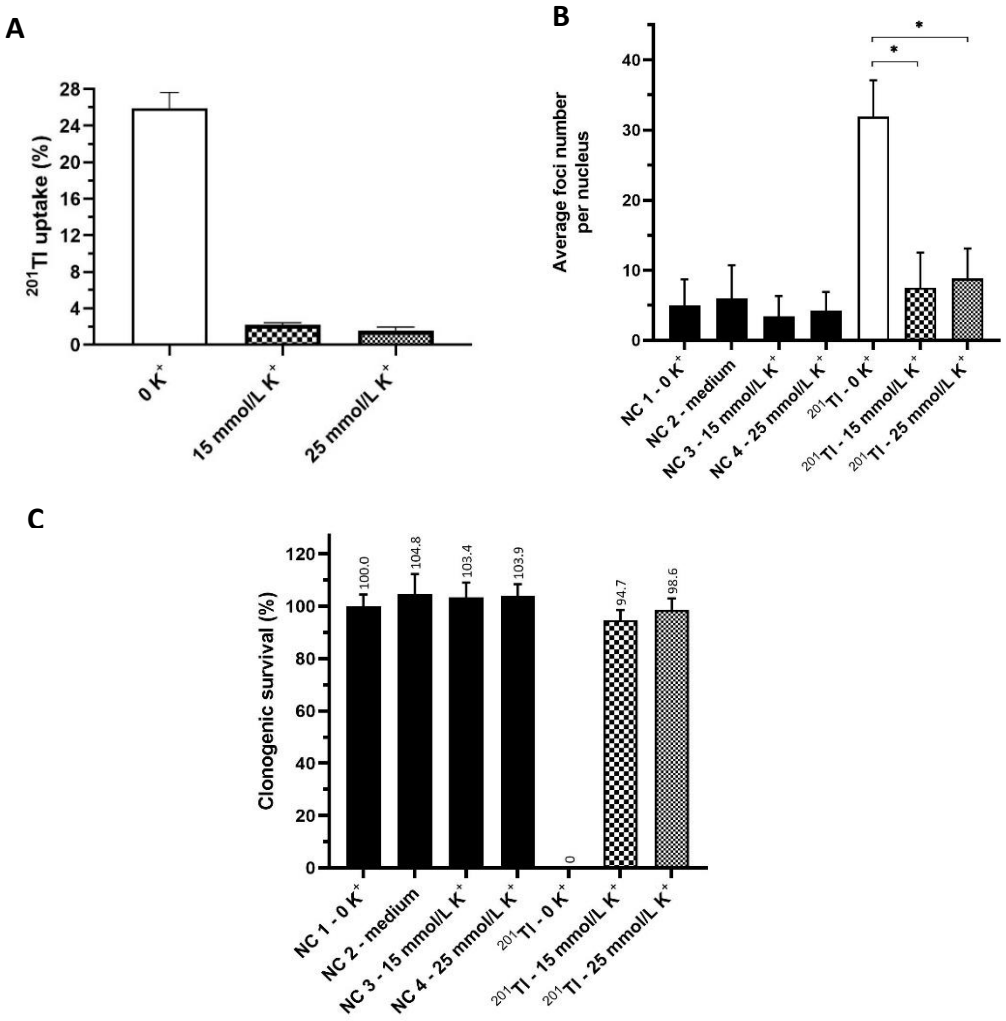

Figure 2.5 ^{201}Tl radiotoxicity – internal vs external ^{201}Tl. A) ^{201}Tl uptake in DU145 cells in PBS with different concentrations of K^+ (0 mM to 25 mM) after 90 min incubation with 4000 kBq/mL of [^{201}Tl]TlCl. **B)** Average number of foci per nucleus and **C)** clonogenic survival measured in DU145 cells after 90 min incubation with 4000 kBq/mL of [^{201}Tl]TlCl and 15 or 25 mmol/L KCl and various non-radioactive controls (NC 1-4). Data are presented as mean ± SD, n=3, triplicates, * indicates $P < 0.05$.

2.6 Discussion

^{201}Tl is efficiently taken up by MDA-MB-231 cells and DU145 cells in standard incubation media ([K^+] 4.2-5.3 mM), achieving equilibrium at around 90 minutes with an estimated intracellular to extracellular ^{201}Tl concentration ratio (in DU145 cells) in the range 40:1 to 53:1 (Supplementary materials: Table S2.2 A and B), very similar to literature estimates for K^+ ratios of 30:1 to 50:1 [110]. This ratio rises to 181:1 in potassium-free medium and collapses to 8:1 at elevated potassium levels (25 mM) (Supplementary materials: Table S2.2 C)**.** These findings are consistent with the assumption that Tl^+ mimics potassium in a biological environment. ^{201}Tl efflux results showed exponential time-dependent efflux when the incubation medium was replaced by ^{201}Tl-free medium, returning to a new

equilibrium with similar internal to external concentration ratio, suggesting that there is no significant irreversible binding mechanism for thallium ions inside cells in the short time scale of these experiments. The two efflux methods used confirmed that the chemical form of thallium is unchanged after entering the cell and the uptake mechanism is completely reversible, since the same ratios are preserved at every wash; and that only by the continuous efflux method can radioactivity be completely removed from the cells. Nevertheless, the high intracellular to extracellular concentration ratio achievable allowed evaluation of radiotoxicity of internalised ^{201}Tl without having a specific tumour-targeted uptake mechanism.

The radiotoxic effect of ^{201}Tl uptake in both cell lines was assessed by measuring clonogenic survival and the average number of DNA damage foci per nucleus. Treatment of both cell lines with ^{201}Tl in standard incubation media caused a substantial reduction in the surviving fraction compared to non-treated cells. Cells incubated with an equivalent volume of decayed [^{201}Tl]TlCl did not show this effect, indicating that the toxicity was solely due to the radioactivity. The average intracellular activity per cell required to achieve 90% reduction in clonogenicity over 90 min was estimated as 0.29 Bq (DU145) and 0.18 Bq (MDA-MB-231). These levels of exposure were accompanied by nuclear DNA damage measurable by the γH2AX assay, which showed a significant increase in the nuclear DNA DSBs caused by ^{201}Tl compared to negative controls. Larger standard deviations when measuring nuclear DNA damage could be linked to a heterogeneous uptake of ^{201}Tl among cells and/or its unequal subcellular distribution. Factors such as a different cell passage number or different cell cycle phases within the population, might explain large variation in results between experiments. Although nuclear DNA damage might be an important factor leading to a reduction in clonogenic survival, we cannot exclude ^{201}Tl impact on other susceptible cellular targets, such us cell membrane or mitochondria, both of which have been linked to the toxicity of other Auger electron-emitting radionuclides [52]. Currently, the precise subcellular localisation of ^{201}Tl in cancer cells remains unknown.

In clonogenic survival studies on MDA-MB-231 cells we used ^{201}Tl activity of 8000 kBq/mL in one experiment only as the lower activities used were considered high enough to cause at least 90% reduction in clonogenic survival necessary for the calculations and comparing with the other cell line. In toxicity control figures (Fig. 2.3 B and 2.4 B) showing that various components of decayed ^{201}Tl material are not affecting ^{201}Tl radiotoxicity, we aimed to use the maximum amount of the radioactive material (and its "cold" equivalent) to be able to observe the potential impact of non-radioactive thallium, if there was one. We therefore limited the number of experiments with higher ^{201}Tl activities (4000-8000 kBq/mL) to DU145 (n=3) only or n=1 for MDA-MB-231. This is justified by repeatedly observing no impact of low thallium concentrations on cell toxicity and our efforts to reduce radiation expose caused by the higher doses of gamma radiation.

Based on the subcellular range of Auger electrons (<1 μm) [105] and their typically low energy, we hypothesised that ^{201}Tl has to be internalised to exhibit its radiotoxic effect in cells and that the gamma and X-ray emissions do not contribute significantly to toxicity. To test this hypothesis, we needed a method to modulate ^{201}Tl cellular uptake from the medium. Na^+/K^+-pump inhibitors ouabain or digoxin, known to be effective in blocking potassium uptake [114], in our experiments caused substantial baseline cytotoxicity in tested cells. However, by varying the K^+ concentration in the incubation solution between 0 and 25 mM, we were able to achieve a range of ^{201}Tl uptake values from 25.9% (0.8 Bq/cell) to 1.6% (0.05 Bq/cell), corresponding to intracellular to extracellular concentration ratios in the range 8:1 to 181:1 – a wider range than could be achieved with the cardiac glycosides – without affecting baseline clonogenic survival. When ^{201}Tl uptake in cells was substantially suppressed by high K^+ concentration in the medium, both the loss in clonogenic survival and the increase in DNA DSB caused by ^{201}Tl were completely suppressed. This suggests that ^{201}Tl needs to be transported inside cells to cause significant radiotoxicity. In the future, if ^{201}Tl can be successfully incorporated into a targeted radiopharmaceutical, an optimal dose for the radionuclide administration can be established to achieve an effective therapeutic effect. Furthermore, an impact of low energy gamma and X-ray emission on patients and carers should be investigated to assess feasibility of this treatment. The same principle would apply to any other Auger electron-emitting radiopharmaceutical.

The average of 0.18 Bq/cell for MDA-MB-231 and 0.29 Bq/cell for DU145 of intracellular ^{201}Tl required to achieve 90% reduction in clonogenicity over 90 minutes is equivalent to around 1000-1600 decays per cell. This is less than half the number of decays per cell calculated for ^{111}In and ^{67}Ga-oxine complexes (3240 and 3600 decays per cell, respectively, over 60-minute incubation) required to obtain the same 90% reduction in clonogenicity in DU145 cells [116]. Although these experiments were not conducted under fully identical conditions, this result is consistent with the higher total energy and number of Auger and Coster-Kronig electrons per decay released by ^{201}Tl (15.3 keV, 37 electrons) compared to ^{111}In and ^{67}Ga (6.7 keV, 14.7 electrons and 6.3 keV, 4.7 electrons, respectively) [117]. Because ^{201}Tl effluxes quickly from the cell after the incubation period, whereas ^{111}In and ^{67}Ga do not, the nominal incubation time in the latter cases severely underestimates the actual exposure time, suggesting that ^{201}Tl has a much higher radiotoxic potential per Bq.

Our results are consistent with early work by Rao et al. and Kassis et al. [110,111] addressing potential radiobiological risk associated with diagnostic use of ^{201}Tl, showing that decay of intracellular ^{201}Tl is toxic, reducing clonogenicity and inducing DNA DSBs. At the same time, ^{201}Tl decay presents little hazard to bystander cells that have not taken up the radionuclide. Although we have not compared this potency directly with other Auger electron-emitting radionuclides under consideration as

radiotherapeutics, it appears that ^{201}Tl is more potent than ^{111}In and ^{67}Ga, consistent with the respective known number and energy of the emissions. Consequently, ^{201}Tl is an attractive candidate radionuclide for further research in targeted Auger electron-emitter therapy. In addressing this goal, it will be necessary to overcome several limitations of the present work. First, while we have shown that ^{201}Tl must be internalised to elicit significant radiotoxic effects, it is likely that different subcellular distributions will have greatly differing effects, since the range of the emitted electrons is much smaller than typical cell dimensions. Nothing is known about the subcellular distribution of ^{201}Tl in the cell lines investigated here, nor of ^{67}Ga and ^{111}In in similar studies [116]; indeed, in general the role of subcellular location of radionuclides in determining toxic effects is poorly understood. A radiopharmaceutical containing ^{201}Tl that is targeted both to cancer cells and to specific subcellular locations within them might be significantly more potent than [^{201}Tl]TlCl. Moreover, 'trapping' ^{201}Tl inside the cell will slow down its efflux and might further increase its radiotoxic potential. Despite the high potency, actualising therapeutic potential with ^{201}Tl is currently more challenging than with other potential Auger electron emitters (^{67}Ga, ^{111}In, ^{125}I etc.) because the chemistry required to incorporate ^{201}Tl into targeting molecules is underdeveloped - there are no satisfactory bifunctional chelators for thallium (I) or thallium (III). Here we have used physiological mimicry of potassium to achieve uptake in cells, but this has no specificity for cancer cells and probably has no specific targeting to subcellular structures.

2.7 Conclusions

^{201}Tl showed significant radiotoxicity, damaging nuclear DNA and reducing clonogenic survival when internalised in both cancer cell lines used in this study, and had no significant effect if not internalised. These results warrant further investigation of ^{201}Tl as a therapeutic radionuclide and the development of chelators to incorporate thallium into targeting molecules for specific delivery of ^{201}Tl to cancer cells.

2.8 Supplementary materials

2.8.1 Calibration line for [^{201}Tl]TlCl. A series of standards was prepared by diluting 600 kBq/mL of ^{201}Tl (measured by a dose calibrator - Capintec) in phosphate buffer solution (PBS) and their radioactivity was monitored by a gamma counter (CompuGamma, CS1282). All activities (0.3 - 600 kBq/mL) were measured in four technical replicates. Measurements with a dead time (DTIME%) value over 20% (marked red) were discarded as unreliable. The gamma counter result (as mean CPM – counts per minute) was plotted against known activity (kBq/mL) and a linear regression line was fitted with R^2 value of 0.9991. ^{201}Tl calibration line was used to convert CPM into ^{201}Tl activity required for the efflux assays calculations.

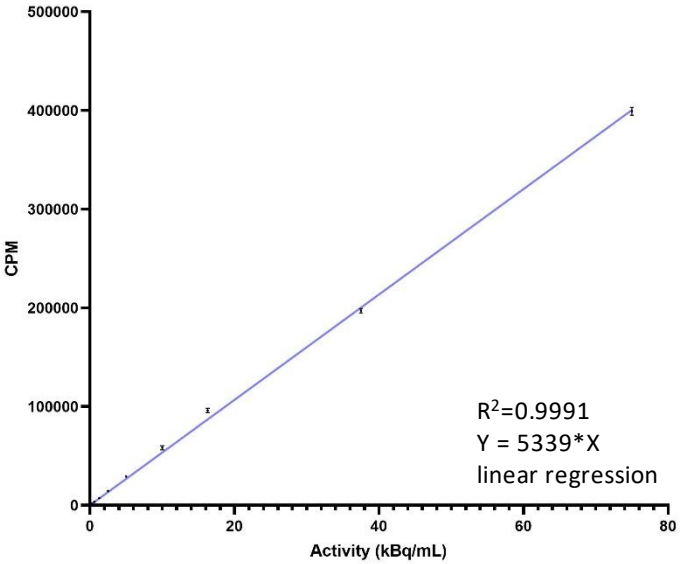

Activity (kBq/mL)	Mean CPM	SD	DTIME%
600.0	2892485	67050	73.2
300.0	1567760	28284	51.4
150.0	801556	26553	29.2
75.0	399118	3934	16
37.5	197121	2164	8.5
16.3	96128	2228	4.5
10.0	58327	2095	2.9
5.0	29156	249	1.7
2.5	14423	872	1.1
1.3	7276	299	0.8
0.6	3481	334	0.6
0.3	1757	89	0.6

Figure S2.1 Calibration line for [^{201}Tl]TlCl. Average value of CPM (counts per minute) measured by a gamma counter is plotted against activity checked by a dose calibrator (kBq/mL).

2.8.2 ^{203}Tl in [^{201}Tl]TlCl supplied (molar activity)

Natural thallium is a mixture of two stable isotopes: ^{205}Tl and ^{203}Tl (natural abundance: 70.5% and 29.5%, respectively). ^{201}Tl is produced in a cyclotron from a solid target of natural thallium enriched in ^{203}Tl isotope [113] (Fig. S2.2 A). Inductively Coupled Plasma-Mass Spectrometry (ICP-MS) analysis of a decayed sample of [^{201}Tl]TlCl was performed to determine the presence of carrier ^{203}Tl and other potential heavy metal contaminants. It confirmed the presence of an isotope with a mass to charge ratio of 203 (Fig. S2.2 B) with concentration averaging 0.8 ± 0.4 µmol/L (n=5 x triplicates) (Table S 2.1), indicating a molar activity in the range 77 – 240 GBq/µmol at the time of experiments. Neither this level of thallium nor other heavy metals (adventitious lead and the decay product ^{201}Hg) were expected to cause toxic effects.

A calibration line for ^{203}Tl was prepared (Fig. S2.2 C) from a series of natural thallium standards (0.1-200 µg/L) using a thallium solution (100 ppm, Leeman Labs Inc., Teledyne) diluted with 2% HNO_3 and 0.1% HCl solution (Optima grade, Fisher Scientific). Decayed [^{201}Tl]TlCl solution (0.3 mL, in triplicate) was diluted with 2% HNO_3/0.1% HCl to 5 mL. Quality of the ICP-MS measurements was ensured through repeat measurements of blanks, an external calibrant and an external water reference material from High Purity Standards. The experiment was carried out at argon gas flow of 1 L/min and radiofrequency power of 1600W.

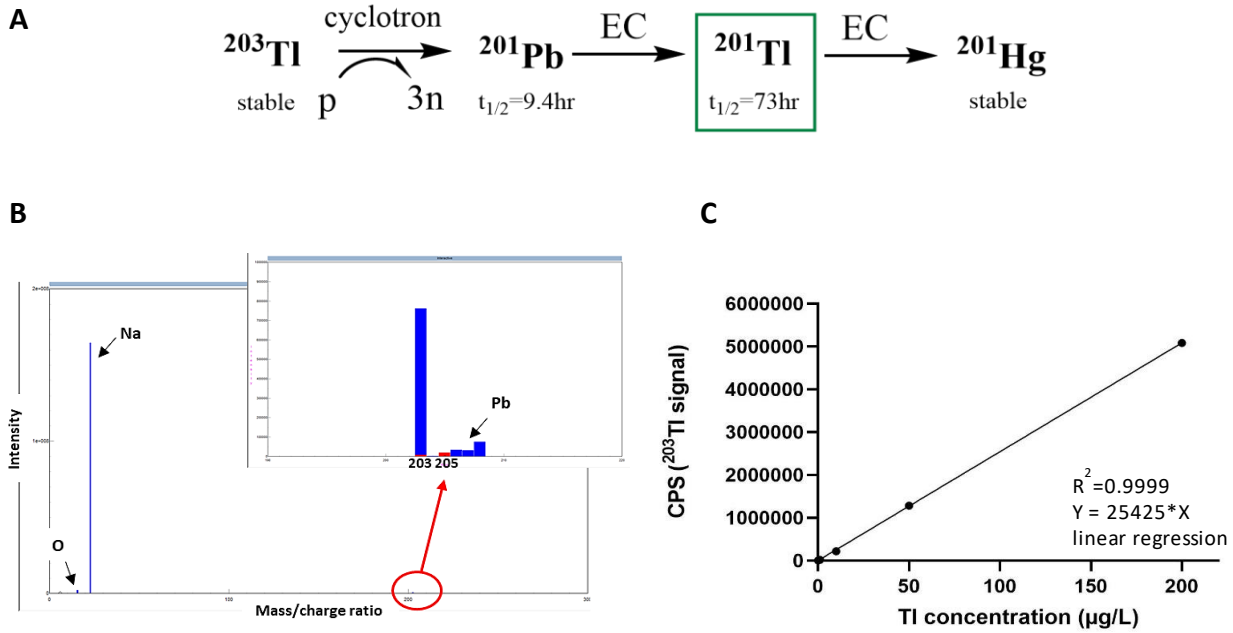

Figure S2.2 ^{203}Tl in [^{201}Tl]TlCl supplied. **A)** Schematic representation of ^{201}Tl production and decay process. ^{201}Tl is produced in a cyclotron, when the external beam of protons bombards a naturally occurring isotope of ^{203}Tl. This nuclear reaction leads to the creation of ^{201}Pb (half-life of 9.4 h), which decays by electron capture (EC) to ^{201}Tl (half-life of 73 h). ^{201}Hg is a stable daughter of ^{201}Tl. **B)** Inductively coupled plasma - mass spectrometry (ICP-MS) analysis showing signal intensity versus isotopic mass/charge (m/z) ratio. Oxygen and sodium were identified, as well as a smaller peak for mass to charge ratio (m/z) = 203 indicating ^{203}Tl - a cyclotron production process contaminant. Red colour for m/z 203 (^{203}Tl) and m/z 205 (^{205}Tl) indicate thallium natural abundance. Blue colour for m/z 203 shows non-natural abundance. Lead contamination was within the expected range. The amount of the isotope with m/z ratio of 201 (^{201}Hg) was below the detection limit for this method. **C)** A calibration line showing concentrations of prepared $TlNO_3$ standards (µg/L) plotted against ^{203}Tl signal intensity in counts per second (CPS). Linear regression was fitted with R^2 value of 0.9999.

Batch	Average concentration (µmol/L)	SD
1	0.75	0.02
2	1.14	0.03
3	0.45	0.003
4	0.35	0.06
5	1.29	0.02
Average	0.80	0.41

Table S2.1 Inductively coupled plasma - mass spectrometry (ICP-MS) quantification analysis of five different batches of decayed [^{201}Tl]TlCl solution showing concentrations (µmol/L) for isotopic mass/charge (m/z) ratio of 203, indicating the concentration of ^{203}Tl - a cyclotron production process contaminant. [^{201}Tl]TlCl was obtained as 0.9% NaCl solution; 360 - 560 MBq/5.8 mL.

2.8.3 ^{201}Tl kinetics in DU145 cells and MDA-MB-231 cells

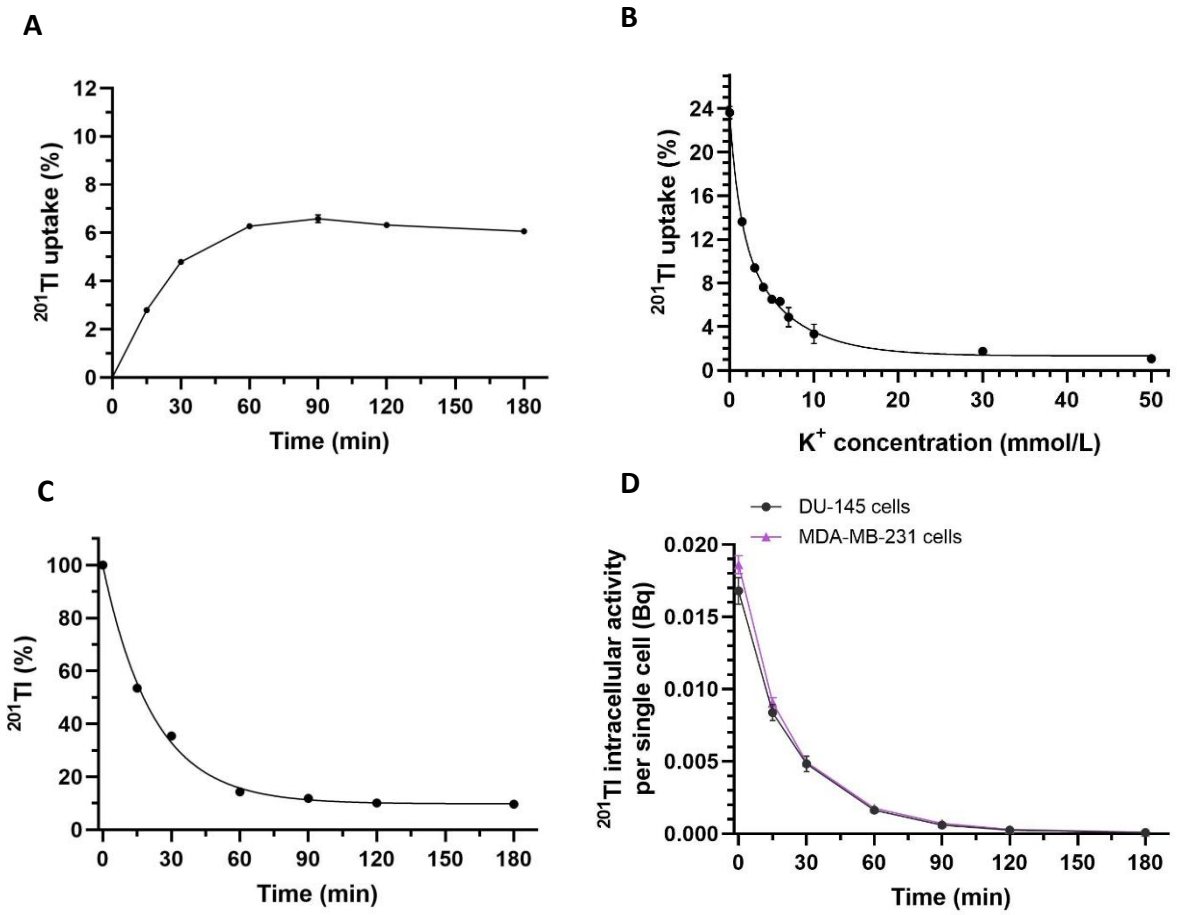

Figure S2.3 ^{201}Tl kinetics in DU145 cells and MDA-MB-231 cells. A) Uptake of ^{201}Tl in MDA-MD-231 cells (n=1) after incubation with 200 kBq/mL [^{201}Tl]TlCl in medium. These results were used to determine the best incubation time for subsequent radiobiological experiments. **B)** ^{201}Tl uptake in DU145 cells after 90 min incubation with 80 kBq/mL [^{201}Tl]TlCl and different concentrations of KCl in PBS without K^+ (n=1), showing that KCl solution can efficiently modulate ^{201}Tl uptake. **C)** Efflux of ^{201}Tl in MDA-MD-231 (n=1) cells. Plateau uptake from the preceding uptake assay is defined as 100% at time 0. Radioactive medium was replaced with non-radioactive and ^{201}Tl activity was measured over time. **D)** Activity (Bq) of ^{201}Tl bound per cell in DU145 cells (n=2) and MDA-MD-231 cells (n=1) after radioactive medium was replaced repeatedly with non-radioactive medium over time, performed on the same cells in quadruplicates. Activity bound per cell at 0 min is the activity bound in a preceding uptake assay.

A

Time of incubation (min) with 200 kBq/mL of ^{201}Tl in RPMI medium	Average ^{201}Tl concentration (kBq/µl) ± SD inside DU145 cells, n=3	Average ^{201}Tl concentration (kBq/µl) ± SD in external medium, n=3	Internal to external ^{201}Tl concentration ratio, n=3
30	7.59 ± 3.03	0.19 ± 0.01	40
60	8.86 ± 3.32	0.19 ± 0.01	47
90	9.16 ± 3.55	0.19 ± 0.01	49
120	9.09 ± 3.40	0.19 ± 0.01	49
180	9.89 ± 3.25	0.19 ± 0.01	53

B

Activity of ^{201}Tl (kBq/mL) added (90 min incubation) in RPMI medium	Average ^{201}Tl concentration (kBq/µl) ± SD inside DU145 cells, n=3	Average ^{201}Tl concentration (kBq/µl) ± SD in external medium, n=3	Internal to external ^{201}Tl concentration ratio, n=3
200	9.61 ± 2.87	0.18 ± 0.01	53
400	18.18 ± 5.94	0.36 ± 0.02	50
1000	43.43 ± 13.92	0.91 ± 0.04	48
2000	82.29 ± 26.16	1.83 ± 0.07	45
4000	165.32 ± 53.13	3.67 ± 0.15	45
8000	324.91 ± 114.75	7.35 ± 0.31	44

C

Concentration (mmol/L) of K^+ in the incubation solution (90 min incubation with 4000 kBq/mL ^{201}Tl)	Average ^{201}Tl concentration (kBq/µl) ± SD inside DU145 cells, n=3	Average ^{201}Tl concentration (kBq/µl) ± SD in external solution, n=3	Internal to external ^{201}Tl concentration ratio, n=3
0	537.75 ± 51.42	2.96 ± 0.07	181
15	45.62 ± 7.74	3.91 ± 0.01	12
25	32.76 ± 11.07	3.94 ± 0.02	8

Table S2.2 Average ratio of intracellular to extracellular concentrations of ^{201}Tl and K^+. Average ratio of intracellular to extracellular concentrations of ^{201}Tl and K^+ **A)** DU145 cells incubated for 30 – 180 min with 200 kBq/mL of [^{201}Tl]TlCl in RPMI medium. **B)** DU145 incubated with various ^{201}Tl activities ranging between 200 and 8000 kBq/mL for 90 min in RPMI medium. **C)** DU145 incubated for 90 min with 4000kBq/mL of [^{201}Tl]TlCl in PBS without K. The intracellular to extracellular concentrations ratio of ^{201}Tl was calculated using the uptake experiments results (n=3) in DU145 cells. Experimental DU145 intracellular volume, measured by diffusion NMR spectroscopy [112] was taken from literature as 1.6 pL.

2.8.4 Impact of cardiac glycosides on ^{201}Tl uptake and cell survival

To compare the radiotoxicity caused by ^{201}Tl present in the extracellular medium and those inside cells, ^{201}Tl uptake needed to be substantially reduced. Cardiac glycosides (ouabain, digoxin) are known to efficiently block the Na^+/K^+-ATPase pump [114] and were found to decrease the amount of internalised ^{201}Tl in DU145 cells by 59.5 - 83.9% (Fig. S2.4 A), but they also caused a 56.8 - 98.9% reduction in baseline clonogenic survival (Fig. S2.4 B), therefore alternative methods to control ^{201}Tl uptake were sought**.** Digoxin (0.5 mg/2 mL solution) for intravenous injection (Aspen) was diluted with 0.9% NaCl to the required concentration. Ouabain solutions were prepared by dissolving ouabain octahydrate in 0.9% NaCl.

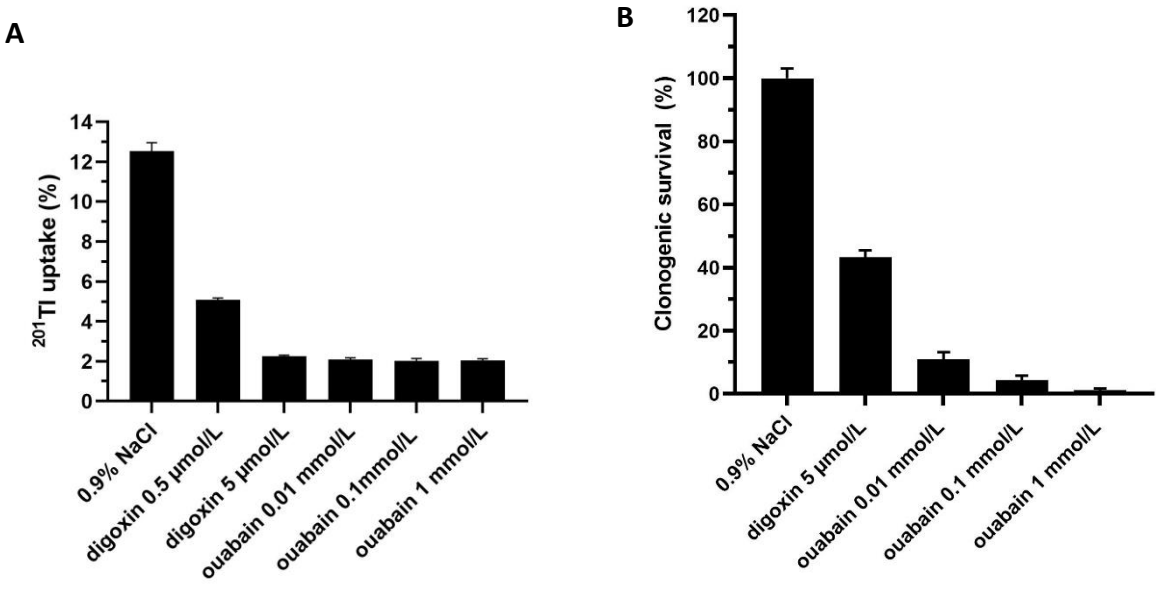

Figure S2.4 Impact of cardiac glycosides on ^{201}Tl uptake and cell survival. A) ^{201}Tl uptake in medium measured in DU145 cells after 90 min incubation with 80 kBq/mL of [^{201}Tl]TlCl and different concentrations of digoxin (0.5 - 5 µmol/L) or ouabain (0.01 – 1 mmol/L in 0.9% NaCl). **B)** Clonogenic toxicity of cardiac glycosides expressed as surviving percentage measured in DU145 cells after 90 min incubation with 5 µmol/L of digoxin or 0.01 - 1 mmol/L of ouabain in medium. Cells were not exposed to ^{201}Tl in these experiments. Data are presented as mean ± SD, n=1, experiments were performed in triplicates.

2.8.5 ^{201}Tl radiotoxicity – nuclear DNA damage

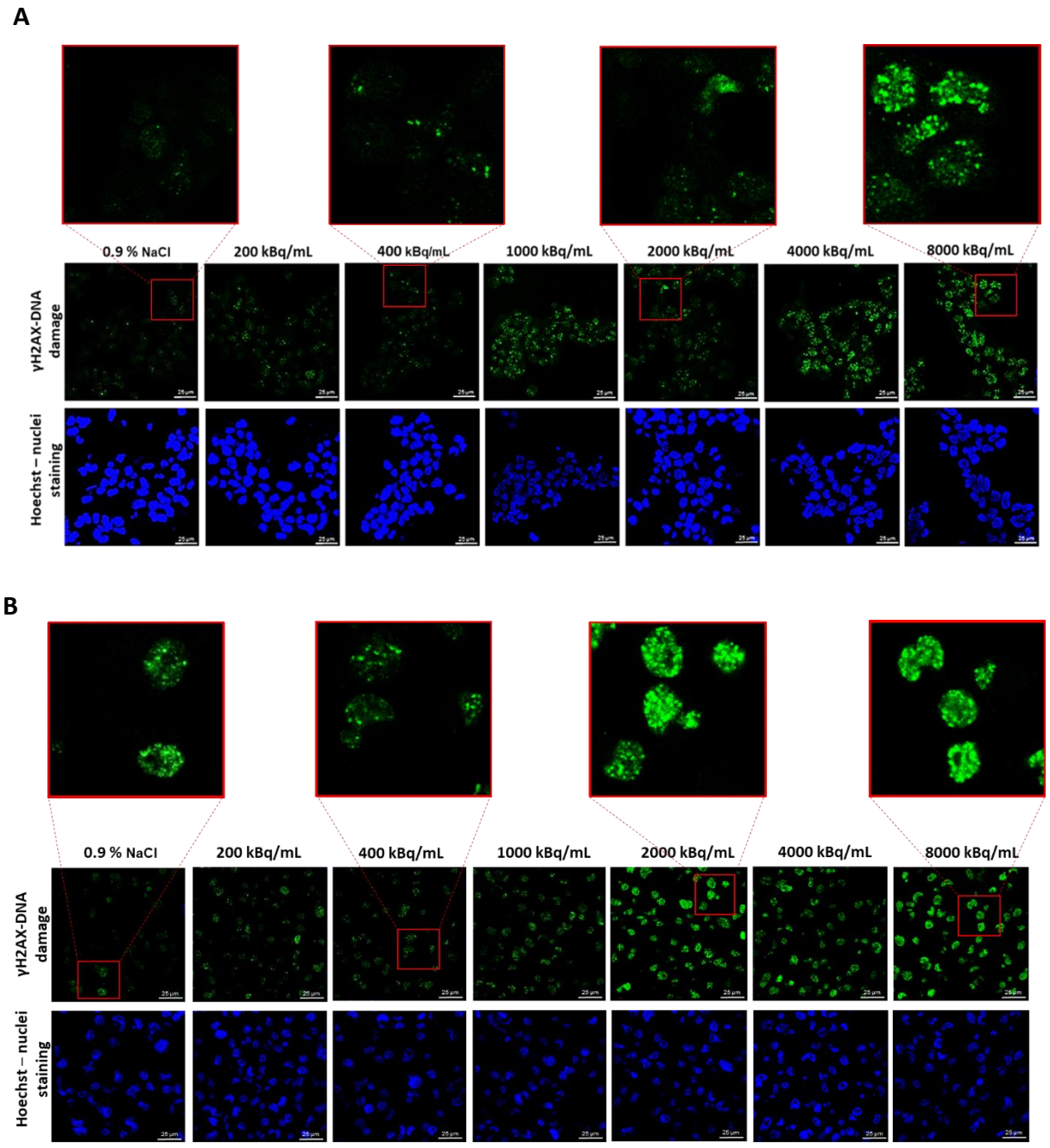

Figure S2.5 ^{201}Tl radiotoxicity – nuclear DNA damage. Exemplar confocal microscopy images (100x) of **A)** DU145 cells and **B)** MDA-MB-231 cells incubated for 90 min with 0.9% NaCl (negative control) or 200 – 8,000 kBq/mL [^{201}Tl]TlCl, followed by immunofluorescence staining for γH2AX (green). Nuclear DNA is stained with Hoechst (blue); minimum 25 cells visible, Z-stack size was kept constant throughout all experiments; for the AlexaFluor green fluorescence: smart gain (SG) and smart offset (SO) were kept constant for all conditions in the experiment. Scale bar – 25 µm.

2.9 Declaration

Acknowledgements: We acknowledge the support received from King's College London Metallomics Facility with ICP-MS analysis funded by a Wellcome Multi-User Equipment Grant**.** Authors would like to thank Prof Robert Hider, Dr Elise Verger, Dr Francis Man, Jordan Cheng, and Alex Rigby for help and advice related to the project.

Authors' contributions: KO contributed to the conception of the experiments, designed the study, acquired, analysed and interpreted the data, and has drafted and revised the work. PB, ST, GS and VA conceived the project and significantly contributed to the conception and design of the experiments, analysis and interpretation of the data, and has substantially revisited the drafted manuscript. IC helped with the design and data interpretation. All authors substantially revised drafts.

All authors have read and approved the final version of this manuscript, and have agreed both to be personally accountable for the author's own contributions and to ensure that questions related to the accuracy or integrity of any part of the work, even ones in which the author was not personally involved, are appropriately investigated, resolved, and the resolution documented in the literature.

Funding: This study received funding from UK Research and Innovation Medical Research Council Doctoral Training Partnership (MR/N013700/1), Theragnostics Ltd., Rosetrees Trust (M786), Engineering and Physical Sciences Research Council (EPSRC) (EP/S032789/1), Wellcome/EPSRC Centre for Medical Engineering (WT 203148/Z/16/Z), and Wellcome Trust. The research was also supported by the National Institute for Health Research (NIHR) Biomedical Research Centre at Guy's and St Thomas' NHS Foundation Trust and King's College London. The views expressed are those of the authors and not necessarily those of the NHS, the NIHR or the Department of Health.

Availability of data and material: The datasets generated and analysed during the current study are available from the corresponding authors on reasonable request.

Ethics approval and consent to participate: not applicable

Consent for publication: not applicable

Competing interests: GS was an employee of Theragnostics Ltd. at the time of this research. PJB is a member of the Theragnostics Advisory Board.

Chapter 3: Prussian Blue nanoparticles (PBNPs) for nanoscale-mediated delivery of ^{201}Tl to cancer cells

3.1 Introduction

Thallium salts are considered one of the most toxic substances, with lethal doses in adults typically ranging from 10 to 15 mg/kg [118]. Because both thallium (Tl^+) and potassium (K^+) ions have a single positive charge and similar ionic radii (Tl^+- 164 pm vs K^+ - 152 pm), thallium can disrupt potassium-dependent processes. Numerous studies on toxicity in animals and humans have shown that thallium can be rapidly absorbed through various routes such as the skin, gastrointestinal tract, and respiratory system. It then quickly distributes throughout the body, including the kidneys, liver, intestines, heart, and brain, before being excreted in urine and faeces [86]. Symptoms of thallium poisoning are diverse and often nonspecific, affecting multiple organs. The most common symptoms include gastrointestinal disorders, hypertension, arrhythmia, respiratory difficulties, encephalopathy, and hair loss. In severe cases, thallium poisoning can lead to fatal cardiac and respiratory failure [119].

A recognised antidote for thallium poisoning is Prussian blue (PB), which received approval from the US Food and Drug Administration in 2003 under the name Radiogardase for its application in patients with radioactive thallium and caesium poisoning. It is also used in medical settings to treat non-radioactive thallium intoxication [118]. PB was first synthesised in the 18th century to be used as a dye, and over the years, it has been known by different names such as Iron blue, Chinese blue and Paris blue. Depending on the conditions of preparations, PB is often categorised into two groups: insoluble PB and soluble PB, which can be dispersed in water. Chemically, insoluble PB can be described as ferric hexacyanoferrate (II) with an empirical formula of $Fe^{(III)}_4[Fe^{(II)}(CN)_6]_3 * xH_2O$, where x = 14 - 16. Its simplified crystal structure and formula are shown in Figure 3.1.

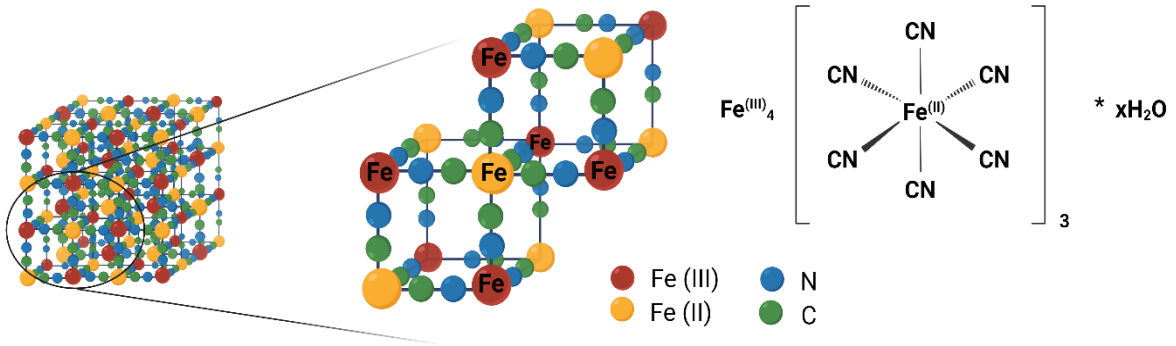

Figure 3.1 The crystal structure and structural formula of Prussian blue. For simplicity, water molecules coordinated to Fe (II) sites (coordinative water) and the water molecules inside interstitial cavities (zeolitic water) are not shown [120].

Soluble PB can form colloids in aqueous conditions and has a formula represented as $AFe^{(III)}_4[Fe^{(II)}(CN)_6]_3 * xH_2O$, where x = 1 - 5 and A is a monovalent cation, such as K^+, Na^+ or NH_4^+ [120]. PB molecules form a face-centred cubic crystal structure, in which Fe (II) and Fe (III) ions are connected via cyano bridges. The characteristic blue colour of PB arises from an intervalent charge transfer of an electron transferring from Fe (II) to Fe (III).

Prussian blue exhibits high affinity for thallium, effectively binding it through mechanisms that include ion-exchange, adsorption, and mechanical entrapment within its crystal lattice. In the ion-exchange mechanism, thallium may replace hydrogen ions from water molecules (H_3O^+), often referred to as hydronium ions, which are bound within the PB crystal structure [121]. Alternatively, in the presence of monovalent cations resulting from using specific reagents and synthetic methods, ion exchange may occur with alkali metal impurities like sodium, potassium or ammonium. It has been estimated that the maximum binding capacity of insoluble PB for thallium is approximately 1400 mg/g, depending upon factors such as particle size, pH and moisture content [122]. When administered orally for thallium poisoning, PB acts by binding to unabsorbed thallium within the intestines, thereby diminishing the concentration gradient and leading to a decrease in overall thallium accumulation within the body. It is worth noting that both the in vitro and in vivo binding of thallium to PB can be influenced not only by the specific chemical composition of PB but also the size and structure of the crystal lattice, with smaller size crystals having better binding properties [123].

Recently, PB has gained more attention in the scientific community as it can be easily assembled into a diverse range of nanoparticles of different shapes and sizes [124], which possess unique physicochemical properties, including porosity and ion-binding capability, a high redox potential, and the flexibility of structural modification through metal cation exchange and creating PB analogues. Consequently, Prussian blue nanoparticles (PBNPs) have found wide-ranging applications and have been studied extensively as ion exchange materials [125], ion batteries [126], photomagnets [127], electrochemical sensors and biosensors [128,129]. Moreover, their water-dispersibility and biocompatibility encouraged exploration in biomedical research, where PBNPs serve as drug carriers [130], contrast agents for techniques such as magnetic resonance imaging [131], photoacoustic imaging [132], nanoenzymes [133] and in photothermal therapy [134].

The use of nanoparticles as effective carriers for targeted delivery of radionuclides to tumour cells is a promising avenue in modern cancer therapy. The ability to create nanoparticles with precise control over their shape and size, surface charge or electromagnetic properties, coupled with the adjustability and functionalisation of the surface coating, enabled researchers to tailor nanoparticles (NPs) design for specific biomedical application. While active targeting strategies are frequently employed,

instances exist where passive accumulation through the enhanced permeability and retention (EPR) effect have proved very efficient [135]. Utilising nanoparticles for the delivery of radionuclides, whether for diagnostic or therapeutic applications, proves highly advantageous. This approach serves to improve the pharmacokinetics of the radionuclide, enhance its stability and solubility, control the release of the radionuclide or enable the creation of multimodal imaging or theranostic radiopharmaceuticals.

Prussian blue nanoparticles have been used for ^{201}Tl delivery for diagnostic purposes mostly to alter its biodistribution and imaging properties. It has been reported that ultrasmall PBNPs coated with aminopolyethylene glycol or glucose-functionalised aminotriethyleneglycol ligands can be successfully radiolabelled with ^{201}Tl and showed accumulation in lungs after 1 h 20 min and in liver after 3 h 20 min when tested in vivo, while typical biodistribution for unbound ^{201}Tl at these timepoints is in kidneys. This study has proved that the biodistribution of ^{201}Tl-PBNPs is significantly different from the unbound ^{201}Tl and depends on the surface coating [136]. ^{201}Tl-radiolabelled citric acid - coated PBNPs were investigated for a potential use as contrast agents for dual SPECT/MRI imaging. The radiolabelling yield for these nanoparticles was over 98% [137]. In another study, the impact of different coatings, including dextran and phospholipid bilayer, as well as variations in the nanoparticle core morphology, were explored in relation to the biodistribution of ^{201}Tl-PBNPs with a view towards their use as SPECT nanoprobes [138]. The in vivo biodistribution of ^{201}Tl can be significantly altered by modifying the size, composition, and surface characteristics of PBNPs. However, it is important to note that, up to this point, there have been no published studies examining the radiotoxic effects of ^{201}Tl when bound to PBNPs or proposing the use of ^{201}Tl-PBNPs as a potential strategy for cancer radiotherapy.

While stable isotopes of thallium can be highly toxic in biological systems when present in milligram quantities, it is crucial to recognise that thallium does not exhibit any toxicity when found in trace amounts, as is the case with [^{201}Tl]TlCl. As demonstrated in chapter 2, when prostate and breast cancer cells were exposed to concentrations of ^{203}TlCl equivalent to those found in the radioactive sample (on average: 0.8 ± 0.4 µmol/L), no clonogenic toxicity was observed.

3.2 Aims

The primary objective of the research presented in this chapter is twofold: firstly, in the absence of satisfactory chelation systems for conjugation of thallium to targeting molecules [99], to design nanoparticles with the capability to efficiently deliver radioactive thallium (I) (^{201}Tl^{+}) into cancer cells; and secondly, to increase the ^{201}Tl internal retention time (and hence, radiation dose delivered) within these cells in comparison to unbound thallium (I) chloride.

To achieve this, Prussian blue was selected based on its known affinity and capacity for adsorbing thallium (I) ions. Two types of Prussian blue nanoparticles (PBNPs) with different coatings were synthesised, fully characterised, radiolabelled with ^{201}Tl and examined to explore the impact on cellular uptake, intracellular retention, and most importantly, the radiotoxic effect. A comparative assessment between the radiotoxic effects induced by ^{201}Tl bound to nanoparticles and unbound thallium was performed, aiming to establish whether the nanoparticle formulation or its subcellular distribution have a significant impact on the radiotoxicity of ^{201}Tl. The subcellular localisation of the two types of synthesised PBNPs and unbound ^{201}Tl is explored in more detail in chapter 4.

Additionally, a pivotal aspect of this investigation encompassed an in vivo analysis to determine whether the PBNPs can enhance the retention of ^{201}Tl, considering its rapid efflux in the unbound form, and therefore increase the radiotoxicity of ^{201}Tl in tumours.

3.3 Materials and methods

Cell culture consumables and chemicals, unless otherwise specified, were purchased from Sigma-Aldrich, UK. [^{201}Tl]TlCl in sterile 0.9% NaCl solution (280 - 580 MBq/5.8 mL) was obtained from Curium Pharma, France.

3.3.1 Prussian blue nanoparticles' synthesis: The synthetic method and purification process of citric acid-coated Prussian blue nanoparticles (caPBNPs) were adapted and optimised from a previously published work [137]. In brief, 105 mg of citric acid (as monohydrate, 0.5 mmol) was added to 20 mL of 1 mM aqueous $FeCl_3$ solution, heated to 60 - 65°C and then 20 mL of 1 mM aqueous $K_4[Fe(CN)_6]$ (Alfa Aesar) with 105 mg citric acid was added dropwise over 10 min. The suspension was left for another minute stirring at 60 - 65°C and then cooled down to room temperature (RT). To purify the nanoparticles, 40 mL of caPBNPs suspension was moved to Amicon® filter tubes (15 mL, 30,000 MWCO) and centrifuged at 4,200 rpm for 10 min (Rotina 380R, Hettich). The filtrate solution was discarded and caPBNPs were resuspended with MilliQ water and centrifuged again. This process was repeated twice. CaPBNPs were re-suspended in 5 mL of MilliQ water (to a concentration approximately 1 mg/mL); pH: 6-7. To obtain dry powder, caPBNPs in aqueous suspensions were freeze-dried at -54°C, 0.1 mbar (LTE Scientific™ Freeze Dryer Lyotrap). The synthesis for chitosan-coated Prussian blue nanoparticles (chPBNPs), together with the purification process, was performed and optimised by Dr Juan Pellico, KCL, based on a previously published article [139]. Chitosan solution (0.1 mg/mL in 0.5 M HCl) was stirred for 1 h at RT and filtered through a 0.45 µm filter. Then, 5 mL of 1 mM $K_3Fe(CN)_6$ aqueous solution was added to 20 mL of chitosan solution in water at RT while stirring. After 30 min, 5 mL of 1 mM $FeCl_2*4H_2O$ was added dropwise to the above mixture and left stirring for

1 h at RT. Finally, 50 mL of acetone was added, and particles were collected by centrifugation at 4,000 rpm for 10 min. ChPBNPs were washed with a mixture of 0.5 M HCl and 0.5 M acetone (20:80 v/v) twice and collected by centrifugation.

3.3.2 Prussian blue nanoparticles incubation with non-radioactive thallium: 2.5 mL of either caPBNPs or chPBNPs suspension in water (typical concentration: 1 mg/mL and 0.5 mg/mL, respectively) was added to 2.5 mL TlCl aqueous solution (2000 mg/L), mixed and kept at RT for 3 h. Then, the suspension of Tl-PBNPs was moved to Amicon® filter tubes (0.5 mL, 10,000 MWCO), centrifuged at 12,000 rpm for 5 min, resuspended with MilliQ water and centrifuged again. This process was repeated three times. To obtain dry powder, the Tl-PBNPs aqueous suspension was freeze-dried at -54°C, 0.1 mbar (LTE Scientific™ Freeze Dryer Lyotrap) for a minimum of 16 h. A schematic representation of both types of synthesis, followed by the incubation of nanoparticles with TlCl or [^{201}Tl]TlCl, is presented in Figure 3.2.

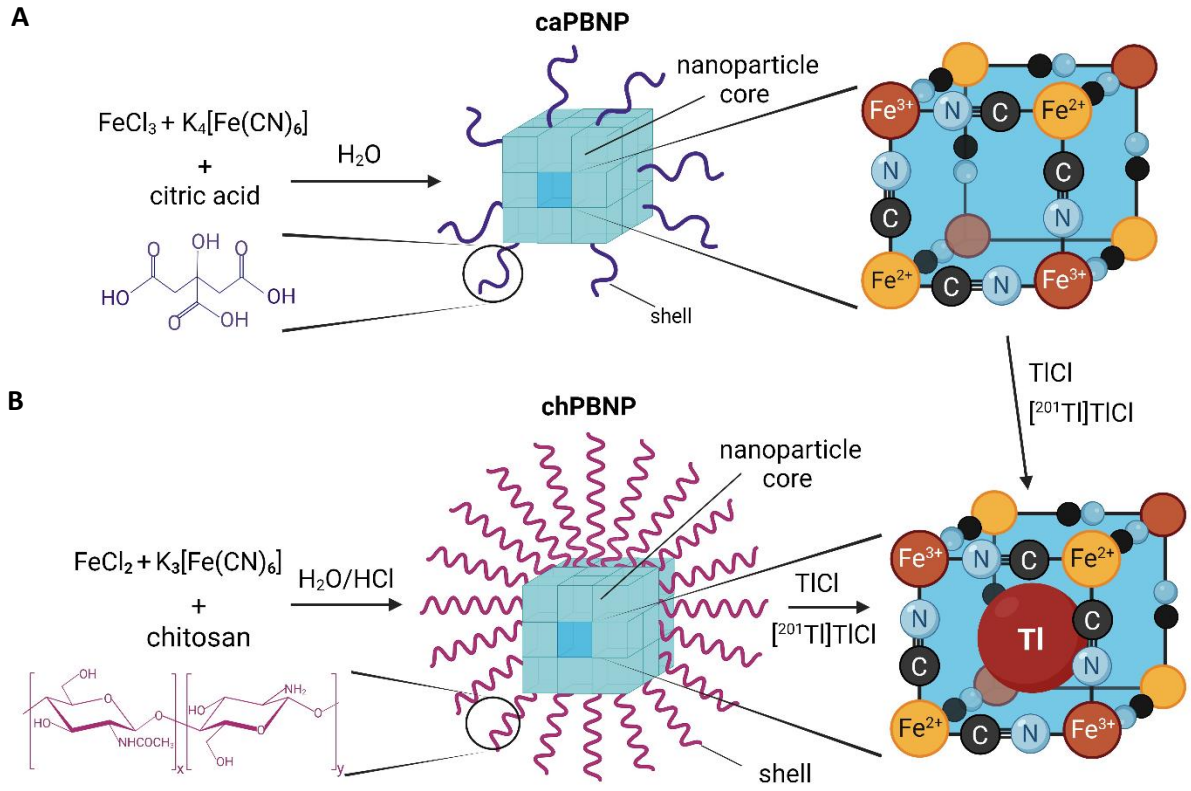

Figure 3.2 Schematic representation of the synthesis of PBNPs. A) caPBNPs and **B)** chPBNPs synthesis and the subsequent incubation with TlCl and [^{201}Tl]TlCl.

3.3.3 Physicochemical characterisation: surface charge (zeta potential) and dynamic light scattering **(DLS)** size measurements were carried out using a Zetasizer Nanoseries ZS90 instrument (Malvern Instrumentals Ltd) equipped with He-Ne laser (λ = 633 nm). Before the analysis, samples of caPBNPs and chPBNPs (concentration: 1 mg/mL and 0.5 mg/mL, respectively) were diluted 8 times with MilliQ water and sonicated for 10 min. Transmission electron microscopy (TEM) was performed to visualise the morphology of nanoparticles and assess their size, using a JOEL JEM 1400 Plus transmission electron microscope (Dr Pedro Machado, Centre for Ultrastructural Imaging, KCL, and Dr Saskia Bakker, Advanced Bioimaging Research Technology Platform, University of Warwick). Size distribution was measured as a diameter using ImageJ software, n > 200. UV-Vis spectroscopy analysis was performed using a NanoDrop 2000c Spectrophotometer, absorption range: 190 - 840 nm (Thermo Scientific). 1 µL of a diluted suspension of PBNPs was pipetted onto a measurement pedestal and Nanodrop software was used to analyse the data. For Fourier transform-infrared spectroscopy (FT-IR) analysis, samples in crystal and powder form were analysed, using either Bruker Alpha-I FT-IR spectrometer (caPBNPs; analysis done by Anca Frinculescu, TICTAC Communications Ltd., St. George's University of London using Bruker Optics Ltd.) or Frontier IR/NIR systems (Perkin Elmer). Spectra were generated at RT in the mid-IR region (4,000 - 400 cm^{-1}). Elemental analysis (EA) of caPBNPs as the freeze-dried powder (with and without thallium loading) was done by Medac Ltd. Carbon, hydrogen and nitrogen % mass (wt %) was determined by the quantitative dynamic flash combustion method using the FlashEA® 1112 Elemental Analyzer. The instrument was calibrated with the analysis of standard compounds using the linear regression method incorporated in the EAGER300™ software. For the thallium and iron analysis, inductively coupled plasma - optical emission spectroscopy analysis (ICP-OES, Varian Vista MPX ICP-OES system) was performed. The sample was digested with nitric acid and sulfuric acid on a hotplate. A calibration curve was prepared using serial dilutions of the standard solution. The concentration of metal in the sample solution was calculated by running the sample solution against the calibration curve. The X-ray diffraction analysis (XRD) and small-angle X-ray scattering (SAXS) analysis were done by Dr Steven Huband at the X-ray Diffraction Research Technology Platform (University of Warwick). Thermogravimetric analysis (TGA) was carried out by Dr Daniel Lester at the Polymer Characterisation Research Technology Platform, University of Warwick. XRD measurements were made on a 3rd generation Malvern Panalytical Empyrean equipped with multicore (iCore/dCore) optics, a Co kα source and a Pixcel3D detector operating in 1D receiving slit mode. Grazing incidence measurements with an incidence angle of 0.5° were made in the range 15–90° (2θ) with a step size of 0.04°. The caPBNPs samples were measured in reflection, while chPBNPs samples needed to be held between Kapton windows and measured in transmission. The TGA data was recorded on a Mettler Toledo TGA/DSC 1, running in a nitrogen atmosphere with a flow rate of

50 mL/min. The samples were prepared in 70 µL pans and subjected to a temperature profile of 40 - 1000°C at a ramp rate of 70°C min^{-1}. SAXS analysis was performed using a Xenocs Xeuss 2.0 equipped with a micro-focus Cu Kα source collimated with Scatterless slits. The scattering was measured using a Pilatus 300k detector. The associated modelling worked on an assumption that the nanoparticle core consists of Prussian blue and the shell consists of 50% H_2O and 50% citric acid or chitosan. The nanoparticles were modelled as spheres.

3.3.4 Radiolabelling with ^{201}Tl: [^{201}Tl]TlCl (30-1000 kBq) was added to 250 µL of the aqueous suspension of caPBNPs or chPBNPs (1 mg/mL and 0.5 mg/mL, respectively), mixed and incubated at RT for various amount of time (5 - 180 min). ChPBNP were also subjected to radiolabelling at increased temperature (37 - 70°C) for varying durations in order to accelerate and increase the efficacy of the radiolabelling process. Radiolabelling efficiency (RE) was determined by thin layer chromatography (TLC); if RE was under 90%, the ^{201}Tl-PBNPs mixture was purified by centrifugation at 12,000 RPM for 5 min using Amicon® filter tubes (0.5 mL, 10,000 MWCO) and resuspended with MilliQ water. This process was repeated three more times. For the TLC method, 1-3 µL of [^{201}Tl]TlCl (control) and ^{201}Tl-caPBNPs or ^{201}Tl-chPBNPs was spotted on 10 cm long cellulose paper strips (Whatman), dried at RT and developed in 10 mM EDTA salt solution (ethylenediaminetetraacetic acid disodium salt, dihydrate). TLC papers were visualised by PhosphorImager (Amersham Typhoon) and analysed with Amersham Typhoon Software (Fig. 3.12). R_f values were 1 for ^{201}Tl and 0 for ^{201}Tl-PBNPs.

3.3.5 Radiolabelling stability: 50 µL of aqueous suspensions of purified ^{201}Tl-caPBNPs or ^{201}Tl-chPBNPs (concentration: 0.5 mg/mL and 0.25 mg/mL, respectively) were added to 50 µL of either human serum (H4522), RPMI-1640 medium or MilliQ water and kept at RT and 37°C for 24 h, 72 h and 7 days. After each time point, radiolabelling efficiency was assessed by TLC. To assess the stability in 0.9% NaCl and 5-150 mM KCl solutions, 50 µL of ^{201}Tl-caPBNPs or ^{201}Tl-chPBNPs aqueous solution (concentration: 0.5 mg/mL and 0.25 mg/mL, respectively) was centrifuged at 12,000 rpm for 5 min using Amicon® filter tubes (0.5 mL, 10,000 MWCO), resuspended with 50 µL of 0.9 % NaCl or 5-150 mM KCl solutions and kept at RT for 24 h, 72 h and 7 days, followed by RE (%) assessment by the TLC method.

3.3.6 Cell culture: Human breast adenocarcinoma cells MDA-MB-231 (ATCC® HTB-26™) were cultured in Dulbecco's Modified Eagle Medium (DMEM, low glucose 1000 mg/L). Human prostate cancer cells DU145 (ATCC® HTB-81™), human lung cancer cells A549 (ATCC® CCL-185™) and human ovarian cancer cells SKOV3 (ATCC® HTB-77™) were cultured in RPMI-1640 medium. Both media were supplemented with 10% fetal bovine serum, 5% L-glutamine, penicillin (100 units) and 100 µg/mL streptomycin. Cultured cells were trypsinised and seeded at 250,000 cells per well in 24-well plates 16 hours before each experiment and grown at 37°C in a humidified 5% CO_2 atmosphere. 625 mM KCl solutions,

prepared by dissolving KCl (BDH Laboratory) in 0.9% NaCl, were added to medium to inhibit unbound ^{201}Tl uptake (final KCl concentration: 25 mM; described elsewhere [140]). All cell lines were tested for the presence of mycoplasma at least monthly (PCR test, Eurofins).

3.3.7 Cellular uptake and efflux: Cells were prepared in multi-well plates as described above. Fifteen minutes before each experiment the medium in each well was replaced by 200 µL fresh medium. To some wells, 10 µL of 625 mM KCl solution was added (to a total of 200 µL volume). To measure ^{201}Tl uptake, stock [^{201}Tl]TlCl solution or ^{201}Tl-caPBNPs/^{201}Tl-chPBNPs were diluted with water to the required concentration (0.6 – 20 kBq/µL) and 50 µL was added to each well. Plates were incubated at 37°C for a specified period. Then, the radioactive incubation solution was collected, adherent cells were briefly washed thrice with PBS and lysed with 1 M NaOH for 15 min at RT. Unbound radioactivity (incubation medium and PBS washings) and cell-bound radioactivity (lysate) were measured with a CompuGamma CS1282 gamma counter (counts per minute, CPM, energy window: 81-110). Empty plates were checked for any excessive activity attached to the plastic at the end of each experiment using a Berthold monitor.

To measure the rate of efflux of ^{201}Tl or ^{201}Tl-caPBNPs/^{201}Tl-chPBNPs, cells were first incubated at 37°C for 3 h with 50 kBq ^{201}Tl or ^{201}Tl-PBNPs in 250 µL medium, which was then removed. Adherent cells were washed briefly with 250 µL PBS and 250 µL of fresh non-radioactive medium was added to each well. Cells were incubated for varying durations (from 15-180 min) at 37°C, after which medium was collected and cells washed, lysed and activity inside cells measured as described above. To compare ^{201}Tl uptake and efflux in cancer cells with and without PBNPs, 50 µL of caPBNPs (0.5 mg/mL) or chPBNPs (0.25 mg/mL) was added to A549 cells in 200 µL medium and incubated for 16 h, then washed thrice with PBS. 200 µL fresh medium and 50 µL of stock [^{201}Tl]TlCl (50 kBq) were added and incubated at 37°C for 90 min. After this time, the protocols for uptake and efflux were followed. The continuous washout experiment involved repeated medium changes on the same cells. In brief, after incubation with 30 kBq ^{201}Tl, ^{201}Tl-caPBNPs or ^{201}Tl-chPBNPs as above, replacing radioactive medium with fresh medium and allowing a further 15 minutes of efflux, medium was again removed, cells were washed once with PBS and fresh medium added. This process was repeated 4 times at intervals from 15-60 min. After 180 min cells were lysed and ^{201}Tl activity measured as described above, converting CPM to activity by means of a calibration curve. The retained activity was expressed as a percentage of the activity found inside cells at each timepoint compared to the activity accumulated inside cells at the beginning of the experiment.

Figure 3.3 illustrates a schematic representation of the procedures for uptake and efflux assays conducted on cancer cells incubated with [^{201}Tl]TlCl and ^{201}Tl-PBNPs.

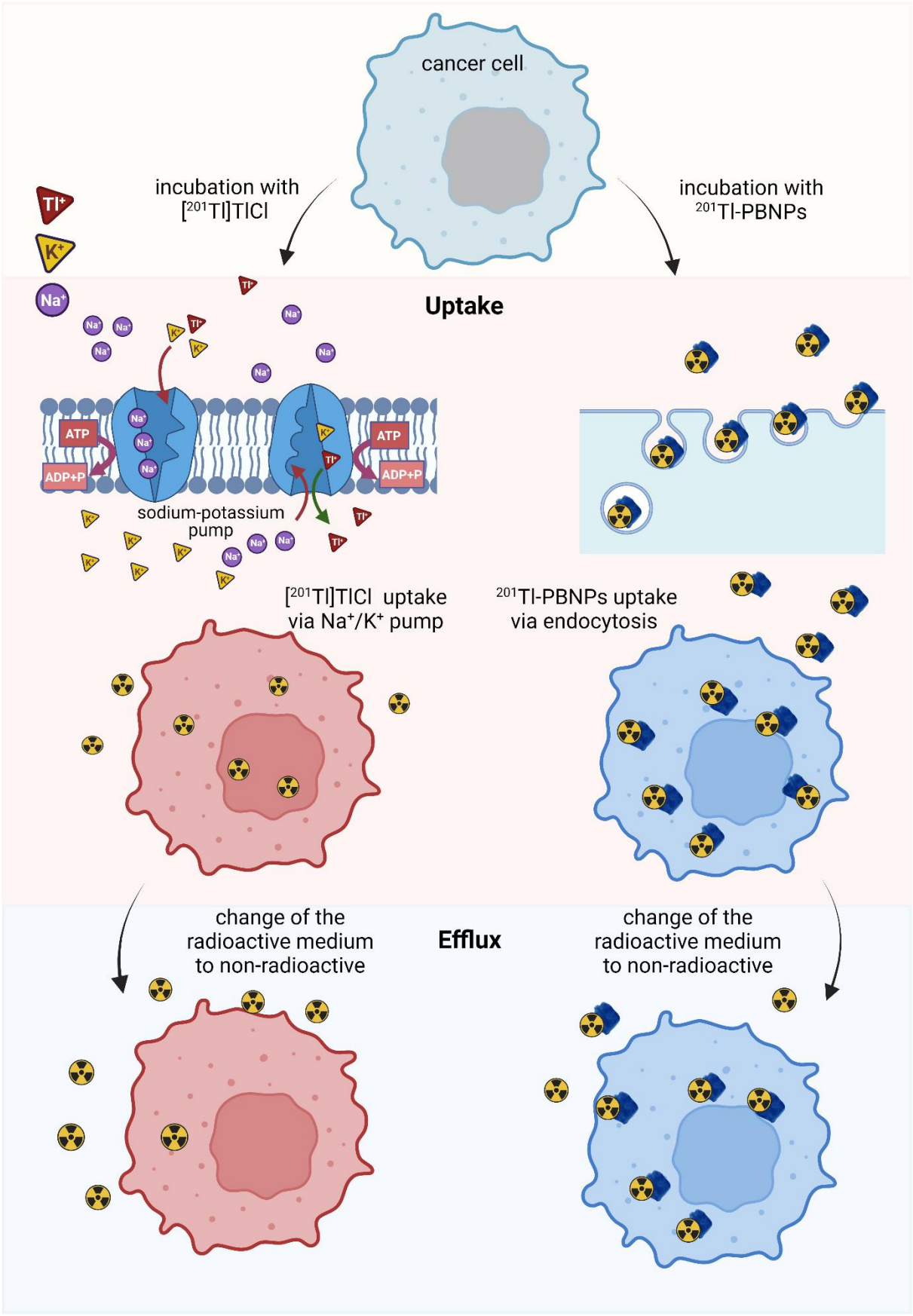

Figure 3.3 Schematic representation of the uptake and efflux assays comparing cancer cells incubated with [^{201}Tl]TlCl and ^{201}Tl-PBNPs.

3.3.8 Radiotoxicity: Clonogenic assays were carried out to assess the reproductive viability of cancer cells after exposure to ^{201}Tl, ^{201}Tl-caPBNPs and ^{201}Tl-chPBNPs, as well as different concentrations of non-radioactive caPBNPs and chPBNPs. 50 µL of 250-1,000 kBq [^{201}Tl]TlCl, ^{201}Tl-caPBNPs/^{201}Tl-chPBNPs or non-radioactive PBNPs, were added to A549 cells in 200 µL medium. To some wells, 10 µL of 625 mM KCl solution was added (to a total of 250 µL volume, final KCl concentration – 25 mM). After 3 h, the radioactive incubation solution was removed, cells were washed thrice with PBS, trypsinised, re-suspended in non-radioactive medium, seeded at 1,000 cells/well in a 6-well plate and cultured for 5-8 days, changing medium every 2-3 days. Colonies were fixed and stained with 0.05% crystal violet in 50% methanol and counted manually, defining colonies as containing >50 cells. Uptake experiments were done simultaneously to calculate activity per cell necessary to achieve 50 and 90% reduction in clonogenic survival. A linear quadratic survival model was used for calculations. A **γH2AX assay** was used to estimate the DNA damage due to ^{201}Tl radiation. A549 cells were seeded on coverslips coated with poly-L-lysine (50 µg/mL) placed in each well of a 24-well plate. Following a 3 h incubation with 50 µL of [^{201}Tl]TlCl or ^{201}Tl-caPBNPs/^{201}Tl-chPBNPs solutions (1000-4,000 kBq/mL), medium was removed and coverslips were washed with PBS, fixed with 3.7% formalin in PBS, treated for 15 min with 0.5% Triton X-100® and 0.5% IGEPAL CA-630® solution, incubated with 1% goat serum/2% bovine serum albumin (BSA) in PBS for 1 h, washed with PBS, incubated overnight at 4°C with mouse antiphospho-histone H2A.X monoclonal antibody (Merck, 1:1600 in 2% BSA), washed with 2% BSA in PBS and incubated with goat anti-mouse secondary fluorescent antibody Alexa Fluor®488 (Invitrogen, 1:500 in PBS) for 2 h at 4°C. Cells were stained and mounted with ProlongTM Gold Antifade Reagent with DAPI (Invitrogen). A TCS SP5 confocal microscope with Leica software was used to obtain fluorescent images and CellProfiler was used to quantify numbers of foci per nucleus.

3.3.9 In vivo study with chPBNPs: chitosan coated - PBNPs were synthesised as described earlier and radiolabelled with [^{201}Tl]TlCl at 70°C for 1 h (final chPBNPs concentration: 0.25 mg/mL, activity concentration: 43 MBq/mL). [^{201}Tl]TlCl for the control group injected with unbound thallium was obtained by diluting the stock solution with 0.9% NaCl to the required activity concentration. Cell culture and tumour inoculation: human lung cancer cells (A549) were cultured and harvested as described earlier. The cell suspension in PBS was prepared at a concentration of 20 x 10^6 cells/mL. All animal experiments were performed in accordance with the UK Home Office Animals (Scientific Procedures) Act 1986. Ten female BALB/C nu/nu mice (8 weeks old) were purchased form Charles River Laboratories (UK). After one week of acclimatisation at the Biological Service Unit (St. Thomas' Hospital), the animals were subcutaneously injected with 2x10^6 A549 cells (100 µL) in the left flank below the shoulder (under brief anaesthesia: 2.0% isoflurane, O_2 flow rate of 1.0 L/min) and monitored for the health status, weight and tumour size. Tumours were measured twice weekly using an

electronic calliper until they reach the size appropriate for an intratumoral injection (tumour volume larger than 50 µL). The tumour volumes were calculated using the formula $V=(w^2xl)/2$ (where 'w' is the tumour width and 'l' is the length, measured by a calliper) [141]. After 5 weeks, 9 out of 10 mice developed tumours with an average volume of 252.7 ± 104.9 µL, while in one mouse the tumour became reabsorbed after 2 weeks. SPECT/CT imaging: mice were randomised across 2 groups: the control group, where 4 mice were injected with ^{201}Tl as [^{201}Tl]TlCl, and ^{201}Tl-PBNPs group, with 5 mice injected with ^{201}Tl-chPBNPs. SPECT/CT imaging was done for 3 mice at each group, whereas the remaining mice were used only for the biodistribution study. Mice were anaesthetised with 2.0% isoflurane (VetTech Solutions, Ltd) at a O_2 flow rate of 1.0 L/min, and 0.4-0.5 MBq of ^{201}Tl or ^{201}Tl-PBNPs in 10 µl volume was slowly injected into the tumours. After 1 h under anaesthesia, 3 mice from the group were imaged with the SPECT/CT scanner (NanoScan SPECT/CT 80W, Mediso Ltd., Budapest, Hungary) using the standard mouse whole body collimator (APT63) with 64 pinholes and acquisition software Nucline™ version 3.04.025. The scanner was calibrated for ^{201}Tl before the experiment (activity calibration factor 1.61062). Three mice were scanned simultaneously using a 3-mouse hotel and counts were acquired using a dual energy window: 72.30 keV ± 10% and 167.40 keV ± 10%. SPECT image reconstruction was performed in Tera-TomoTM 3D SPECT reconstruction software using Regularised OSEM reconstruction with the following settings: TT3D high dynamic range, regularisation = medium, matrix size: 128x128, iterations: 48, subsets: 3, Monte Carlo quality: medium, attenuation and scatter correction and 0.5 mm isotropic voxel size. Subsequently, a helical CT acquisition was performed with 360 projections, pitch 1.0, 50 kVp, 980 mA, exposure time 170 ms, binning 1:4. The data were reconstructed in Nucline™ version 3.04.025 using Filtered Back Projection (filter type: cosine) with isotropic voxel size of 0.25 mm. Decay correction was applied to time of injection. Mediso automated bed removal was applied using FusionTM software version 3.09.008 (Mediso). After SPECT/CT scanning, mice were allowed to recover from anaesthesia. All mice were re-anaesthetised and re-scanned by SPECT/CT at 24 h and 48 h post injection. When the 48 h scanning procedure was completed, mice were culled by humane killing method under Schedule 1 of the Animals (Scientific Procedures) Act 1986 (by dislocation of the neck and permanent cessation of circulation as a confirmation method). Dissection of organs was performed immediately for the quantification of ex vivo biodistribution of ^{201}Tl, followed by the autoradiography and ex vivo histology. VivoQuant v3.5-patch2 software (inviCRO, Massachusetts, USA) was used to view and quantify all reconstructed images. SPECT/CT biodistribution: the regions of interest (ROIs) were manually contoured for tumours and kidneys using CT to mark their boundaries. SPECT/CT images were shown as maximum intensity projection (MIPs) or in transverse sections with the same intensity scale bar for all the groups. Data are expressed as standardised uptake values (SUV) and decay corrected. Ex vivo biodistribution: the

following organs from each mouse were dissected and weighed: tail, skin, heart, blood, lungs, liver, kidneys, stomach, small intestine, large intestine, muscle, bone, bladder, urine, brain, pancreas, spleen, tumours and inguinal lymphatic nodes. Radioactivity in each organ was measured with the CompuGamma CS1282 gamma counter (over 60 sec, energy window: 81-110). Calibration line for converting results from the gamma counter (counts per minute) to Bq was prepared by measuring different [^{201}Tl]TlCl activities in dose calibrator (Capintec) and the gamma counter, and is shown in chapter 2 (Fig. S2.1). Biodistribution data are expressed as percentage of injected activity (decay corrected) %IA or percentage of injected activity (decay corrected) per gram (%IA/g). The in vivo experiment was performed in collaboration with Dr Juan Pellico. Figure 3.4 illustrates the in vivo protocol that was followed.

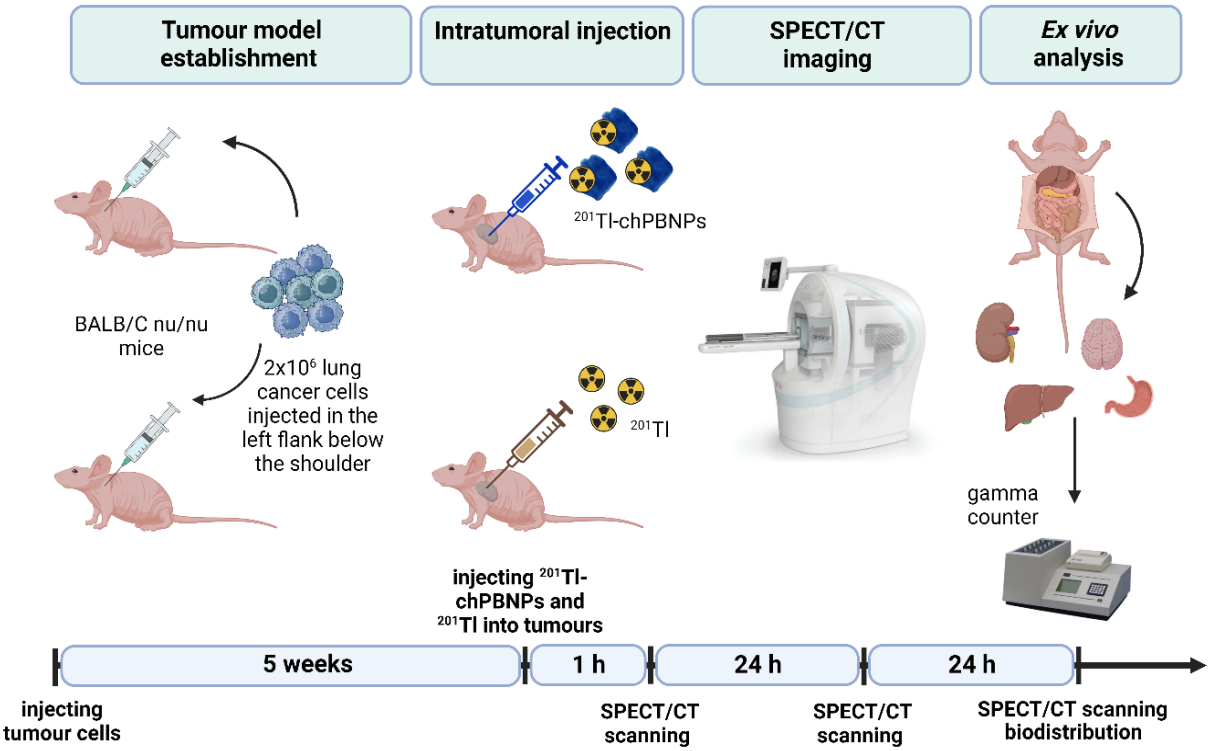

Figure 3.4 The in vivo experimental protocol.

Autoradiography: half of the resected tumour from each mouse was used for the autoradiography study to confirm the presence of radioactivity after 48 h. Tumour tissue was embedded in O.C.T. compound (Optimal Cutting Temperature compound, #361603E, VWR) and snap-frozen in isopentane cooled with liquid nitrogen. Sections of 20 µm were cut using a Cryostat SLEE MNT, exposed to phosphor imaging plates for 21 days and imaged with AmershamTM Typhoon™ (GE healthcare). Ex vivo histology of tissues: the second half of the resected tumour and one kidney from each mouse were preserved with 4% (v/v) paraformaldehyde in PBS (Severn Biotech), over 16 h at 4°C. After a brief PBS wash, the tissue was transferred to 80% ethanol, left for 3 weeks to decay and taken to the

Institute of Neurology, University College London (IQPath, London, UK) for the histology analysis. The tissue was embedded in paraffin and sectioned. Haematoxylin and eosin (H&E) staining was performed for all the samples to assess morphological changes within tissue. Additionally, immunohistochemical staining was carried out for the tumour samples to estimate tumour proliferation (Ki-67). All sections were scanned with a Hamamatsu Nanozoomer S630 digital slide scanner.

3.3.10 Statistical analysis: Data were analysed in Excel Microsoft 2016 and GraphPad Prism 9.1.0/10.0.2, and expressed as mean ± SD. To compare two sets of measurements and assess the significance, two statistical tests were chosen: parametric t-test and non-parametric Mann-Whitney test. Shapiro-Wilk test was used to check the measurements for normal distribution. A value of $P < 0.05$ was considered statistically significant. Figures were created with GraphPad Prism 10 and BioRender.com.

3.4 Results

3.4.1 Prussian blue nanoparticles characterisation

PBNPs were synthesised following a straightforward method involving mixing either $FeCl_3$ with $K_4Fe(CN)]_6$ or $FeCl_2$ with $K_3Fe(CN)]_6$ in the presence of citric acid or chitosan, used as stabilisers to ensure homogenous dispersion of nanoparticles. The obtained nanoparticles, when dispersed in water, displayed a dark blue colour and no visible aggregation was observed for a long period of time when stored at RT or 4°C.

The size distribution and zeta potential of caPBNPs and chPBNPs were determined using Dynamic light scattering (DLS). The average hydrodynamic diameter of caPBNPs measured by this method was found to be 78.4 ± 9.0 nm (n=10, polydispersity index - PDI: 0.100 ± 0.036). Citric acid coated nanoparticles displayed a negative zeta potential of average -41.7 ± 14.2 mV (n=10) due the presence of the carboxylic acid in the nanoparticles' coating. The TEM images (Fig. 3.5) further revealed that caPBNPs form regular cubic shape crystals with an average diameter of 47.1 ± 11.5 nm (n=506, PDI not calculated).

The hydrodynamic diameter of chPBNPs, measured using the DLS method, was on average 307.7 ± 113.7 nm (n = 5, PDI: 0.181 ± 0.017) and they displayed a positive zeta potential of +41.8 ± 3.0 mV (n = 6). However, the size of these nanoparticles based on the TEM images was comparable to that of the caPBNPs, measuring on average 57.6 ± 27.3 nm (n = 276, PDI not calculated). Electron microscopy photos also revealed the irregular spherical shape of chPBNPs (Fig. 3.6).

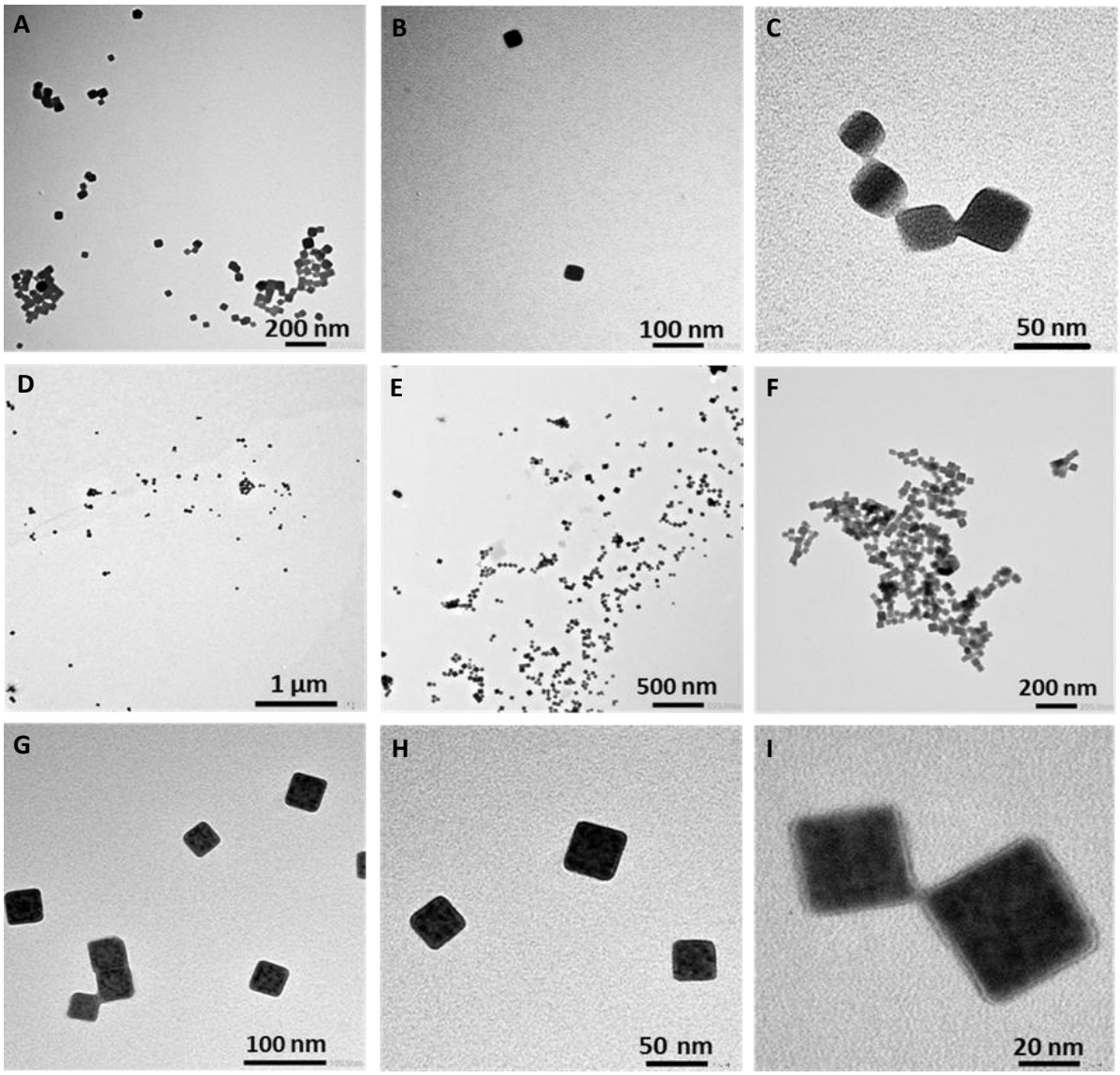

Figure 3.5 TEM images of caPBNPs. **A)**, **B)** and **C)** show images of caPBNPs without adsorbed Tl. **D)**, **E)**, **F)**, **G)**, **H)** and **I)** represent images of caPBNPs after 3 h incubation with TlCl. TEM images displayed the characteristic cubic shape of caPBNPs with an average diameter of 47.1 ± 11.5 nm (without Tl) and 46.1 ± 11.2 nm (with incorporated Tl). There was no substantial difference observed in TEM appearance between native nanoparticles and nanoparticles doped with Tl. Scale bar: 20 – 1000 nm.

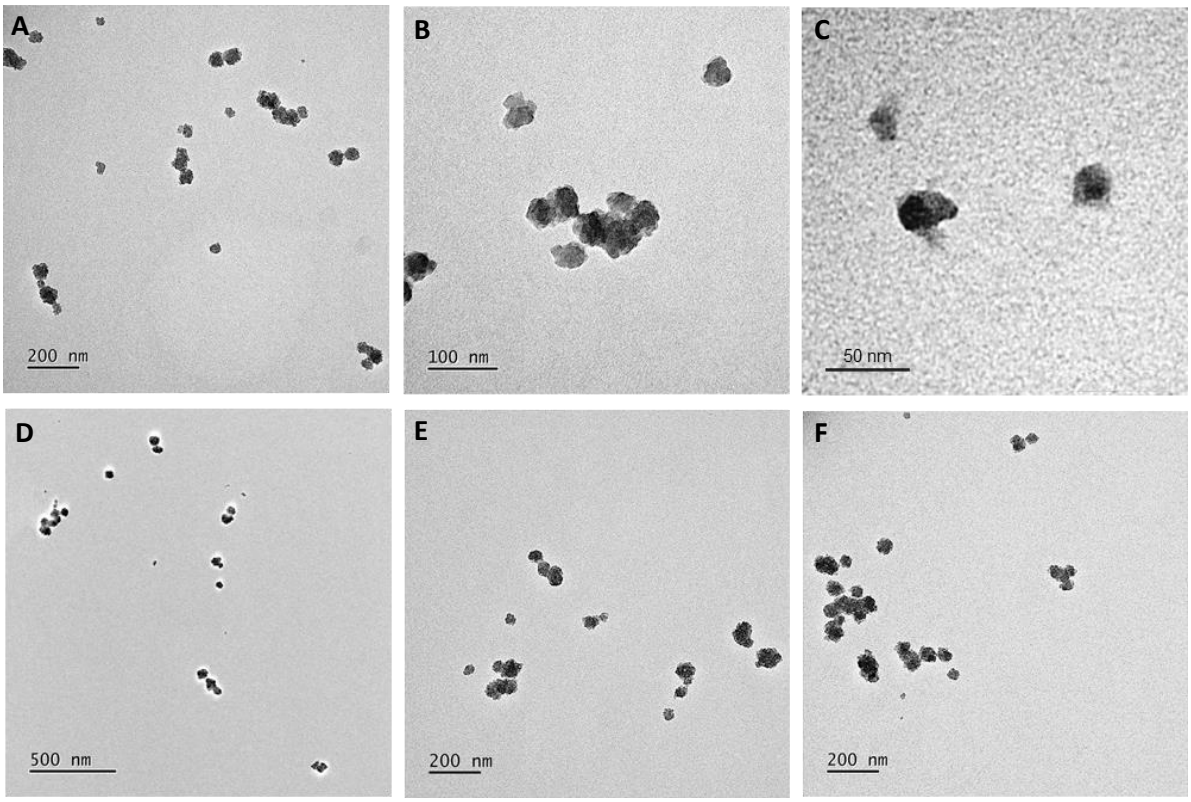

Figure 3.6 TEM images of chPBNPs. A), B) and **C)** represent images of chPBNPs without adsorbed Tl. **D), E)** and **F)** represent images of chPBNPs after 3 h incubation with TlCl. TEM images showed irregular granular shape of chPBNPs with an average diameter of 57.6 ± 27.3 nm (without Tl) and 59.4 ± 21.2 nm (with incorporated Tl). There was no substantial difference observed in TEM appearance between native nanoparticles and nanoparticles doped with Tl. Scale bar: 50 – 500 nm.

By employing the small-angle X-ray scattering (SAXS) method, it was possible to distinguish between the nanoparticle core and the surrounding shell and estimate their dimensions. The mean core radius and mean shell thickness of caPBNPs and chPBNPs measured with and without Tl are listed in Table 3.1.

Sample	Core radius (nm)	Shell thickness (nm)
caPBNPs	48.1 ± 13.5	2.7 ± 1.8
Tl-caPBNPs	34.7 ± 15.8	3.2 ± 3.0
chPBNPs	38.9 ± 14.5	3.8 ± 2.3
Tl-chPBNPs	32.1 ± 13.9	4.0 ± 2.4

Table 3.1 Small-angle X-ray scattering analysis results presenting an average core radius and shell thickness for caPBNPs and chPBNPs. The SAXS analysis and modelling was done by Dr Steven Huband at the X-ray Diffraction Research Technology Platform (University of Warwick).

The results indicate that the average core radius of both types of nanoparticles was between 32.1 and 48.1 nm, with a shell thickness ranging between 2.7 and 4.0 nm. For both citric acid- and chitosan-coated nanoparticles, the nanoparticle core showed a size reduction in the presence of Tl-doping. This difference in size however was not statistically significant. Additionally, the size estimation of thallium containing PBNPs using TEM images (46.1 ± 11.2 nm for Tl-caPBNs and 59.4 ± 21.2 nm for Tl-chPBNPs) indicated no size changes following thallium doping.

The UV-visible absorption spectra (Fig. 3.7 A and B) for both types of nanoparticles showed a broad absorption band from 600 to 850 nm with a maximum around 700 nm. This is consistent with UV analysis of PBNPs published already in the literature [142].

The Fourier-transform infrared spectroscopy (FT-IR) spectrum of powdered caPBNPs (Fig. 3.7 C) exhibits a strong characteristic C≡N stretching vibration around 2062 cm^{-1} for the Fe^{2+}–CN–Fe^{3+} group present in the crystal lattice. Fe^{2+}–CN vibrations were also identified at 604 cm^{-1} and 498 cm^{-1}. In addition, the asymmetric and symmetric carboxyl stretching bands were visible at 1605 and 1396 cm^{-1}, which confirmed the presence of citric acid. The obtained spectrum matched the Prussian blue spectrum obtained from the TICTAC spectral library.

Similarly, chPBNPs exhibited a distinct C≡N vibration at 2073 cm^{-1} (Fig. 3.7 D). Additionally, a strong band spanning from 3188 to 3324 cm^{-1} was identified, indicating N-H and O-H stretching, as well as the intramolecular hydrogen bonds. The absorption bands at around 2924 and 2883 cm^{-1} were attributed to C-H symmetric and asymmetric stretching, and are typical for polysaccharides [143]. The presence of N-acetyl groups was confirmed by the bands at approximately 1621 cm^{-1} (C=O stretching of amide I) and 1377 cm^{-1} (C-N stretching of amide III), respectively. A band at approximately 1550 cm^{-1} characteristic for N-H bending of amide II was not found, potentially due to overlapping with other bands within this region. Bands at around 1412 and 1378 cm^{-1} validated the CH_2 bending and CH_3 symmetrical deformations and at 1516 cm^{-1} corresponded to N-H bending of the primary amine, while bands at 1060 and 1025 cm^{-1} were indicative of C-O stretching.

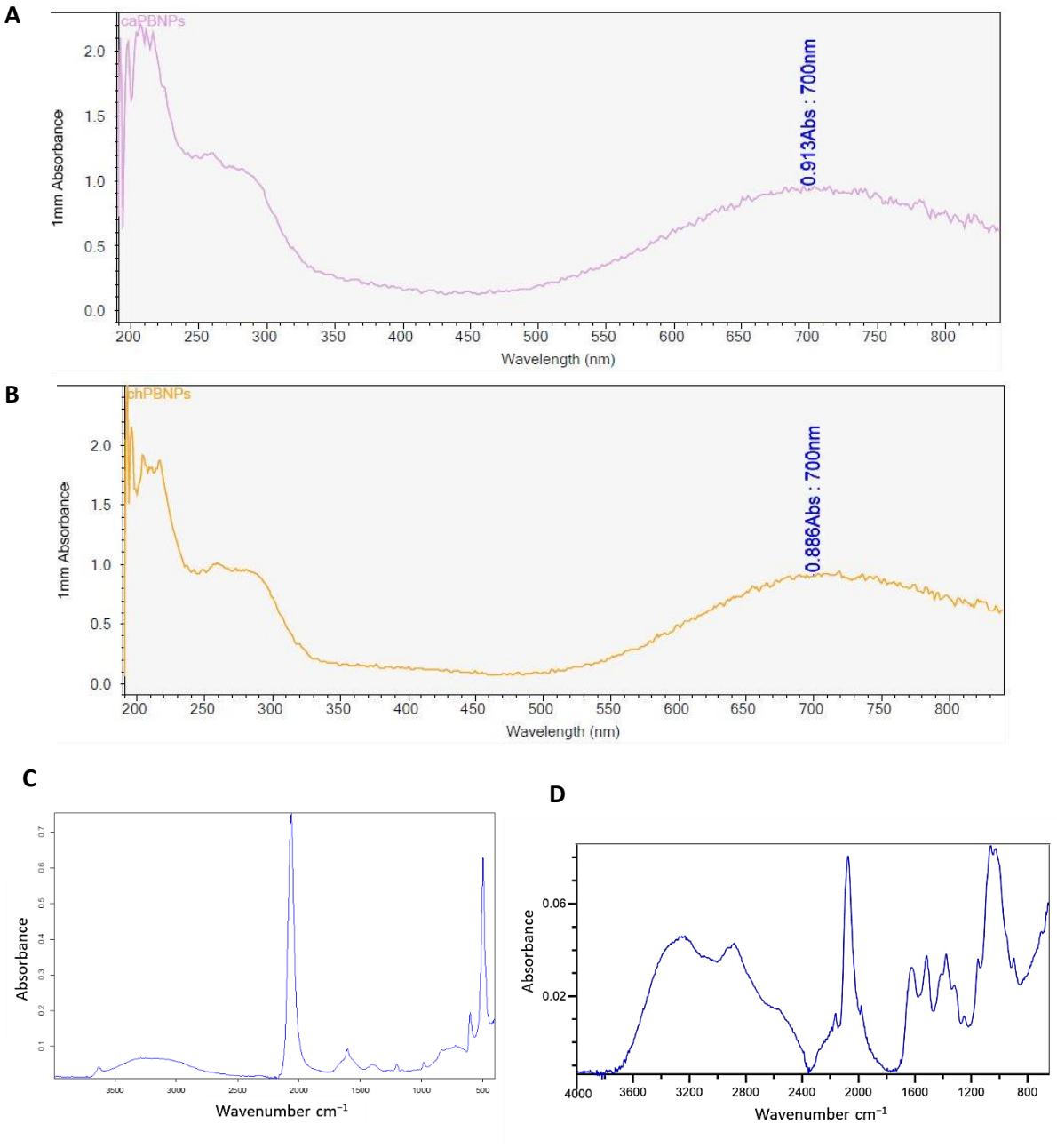

Figure 3.7 UV and FT-IR spectra of caPBNPs and chPBNPs. A) UV spectrum (absorbance vs wavelength - nm) of caPBNPs. **B)** UV spectrum (absorbance vs wavelength –nm) of chPBNPs. Both UV spectra have marked absorbance at 700 nm, characteristic for Prussian blue. **C)** FT-IR spectrum (absorbance vs wavenumber - cm^{-1}) for caPBNPs (extracted from Opus software) and **D)** chPBNPs (created with GraphPad Prism).

The binding capacity of caPBNPS for non-radioactive thallium (I) was measured by elemental analysis (Table 3.2). The results showed that after 3 h incubation with TlCl at room temperature (RT), caPBNPs contain around 14.8 ± 0.3 % of thallium (wt %) and calculated Fe:Tl molar ratio is approximately 5:1.

Element (wt %)	C	H	N	Fe	Tl
caPBNPs	22.9 ± 1.8	3.2 ± 0.04	18.4 ± 0.6	24 ± 1.2	0.03 ± 0.03
Tl-caPBNPs	17.1 ± 0.8	2.4 ± 0.05	17 ± 0.4	19 ± 5.8	14.8 ± 0.3

Table 3.2 Elemental analysis results for caPBNPs and Tl-caPBNPs. CaPBNPs at 1 mg/mL were incubation with TlCl aqueous solution (2000 mg/mL, v:v=1:1) over 3 h and then freeze-dried. Analysis was done by Medac Ltd.; n=3.

Thermogravimetric analysis (TGA) was used to analyse the amount of coating for both types of nanoparticles. TGA of caPBNPs and chPBNPs showed three major weight-loss events. The first occurred below 100°C and corresponds to the loss of adsorbed/coordinated water molecules (Fig. 3.8).

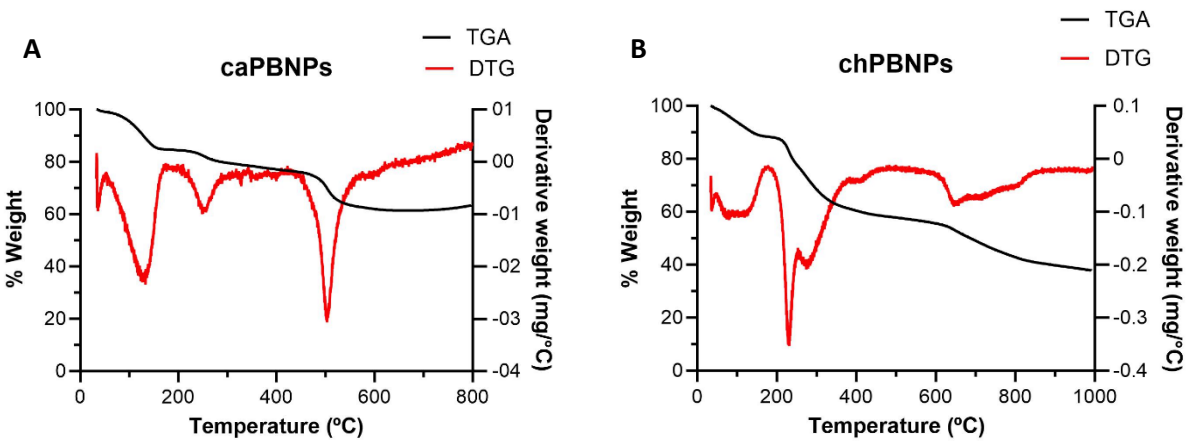

Figure 3.8 Thermogravimetric analysis and derivative thermogravimetric analysis results for **A)** caPBNPs and **B)** chPBNPs.

The release of citric acid from caPBNPs is visible from 100 to 300°C (Fig. 3.8 A), while the loss of chitosan from chPBNPs can be observed between 200°C and 400°C (Fig. 3.8 B). The third weight loss event happening after reaching temperature of 450°C can be attributed to the degradation of nanoparticles and decomposition to iron oxide [144]. The amount of citric acid and chitosan coating were calculated as 34.4% and 45.8% for caPBNPs and chPBNPs respectively (Table 3.3).

Sample	Coating (%w)	Molecules per nanoparticle
caPBNPs	34.4	8.1×10^4
chPBNPs	45.8	143.0

Table 3.3 Thermogravimetric analysis calculations for caPBNPs and chPBNPs. Based on TGA data and the weight of caPBNPs and chPBNPs before and after the measurements, the percentage of citric acid on caPBNPs was estimated as 34.4% (w/w) and the percentage of chitosan present on chPBNPs was estimated to be 45.8% (w/w).

X-ray diffraction analysis (XRD) data for caPBNPs and Tl-caPBNPs revealed characteristic peaks consistent with Fm-3m Prussian blue crystal structure. The addition of Tl has a large impact on the intensity of the diffraction pattern but does not change the positions of the peaks (Fig. 3.9).

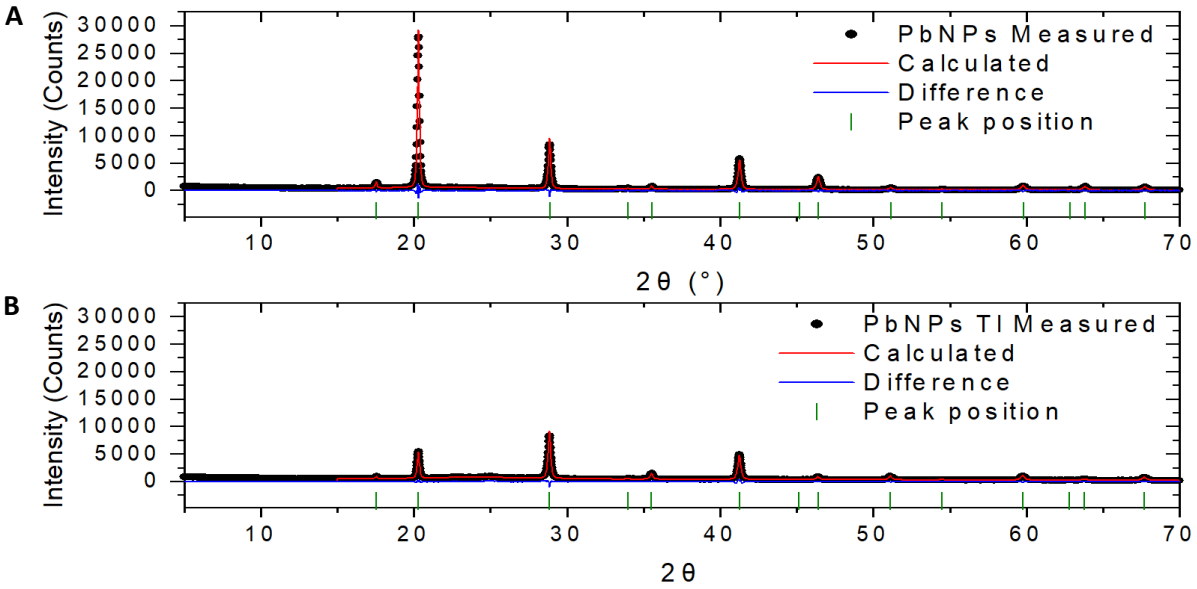

Figure 3.9 X-ray diffraction analysis of caPBNPs and Tl-caPBNPs. A) XRD analysis of caPBNPs and **B)** Tl-caPBNPs. The analysis was done by Dr Steven Huband at the X-ray Diffraction Research Technology Platform (University of Warwick).

3.4.2 Radiolabelling and stability

Prussian blue nanoparticles radiolabelling with $^{201}Tl^+$: A TLC method with EDTA (ethylenediaminetetraacetic acid) disodium salt as a mobile phase was applied to distinguish between unbound ^{201}Tl and nanoparticle bound ^{201}Tl (^{201}Tl-PBNPs), and to calculate the radiolabelling efficiency (RE). An example of a TLC plate and normalised signal intensity vs R_f for unbound ^{201}Tl and ^{201}Tl bound by PBNPs are shown in Figure 3.10.

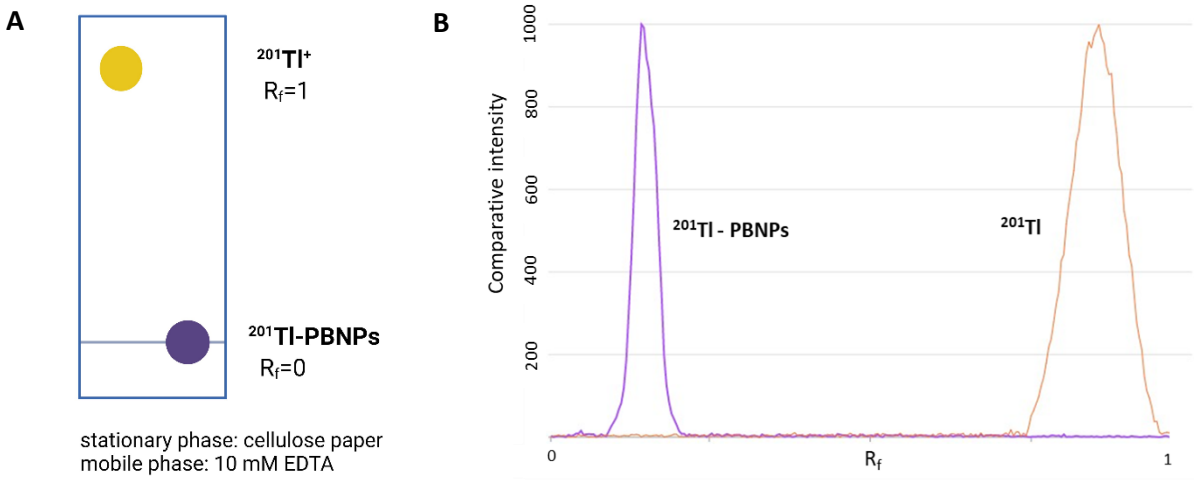

Figure 3.10 Thin layer chromatography of [^{201}Tl]TlCl and ^{201}Tl-PBNPs. A) Graphical description of a TLC plate. **B)** Signal intensity versus R_f for [^{201}Tl]TlCl (control) and ^{201}Tl-PBNPs. Radiolabelling efficiency was calculated as an area under the intensity signal and shown as % of the band area (Amersham Typhoon Software).

^{201}Tl radiolabelling efficiency assessed by the TLC method for caPBNPs was, on average, 89.9 ± 3.5% after 90 min incubation at RT whereas for chPBNPs it was around 89.4 ± 7.7% (180 min incubation, RT). RE increased with the time of incubation from 62.3 ± 2.3% after 5 min to 89.9 ± 3.5% after 90 min for caPBNPs, decreasing slightly after 120 min to 84.5 ± 4.0%. The radiolabelling efficiency of chPBNPs increased from 44.5 ± 4.2% after 5 min to 89.4 ± 7.7% after 180 min of incubation (Fig. 3.11).

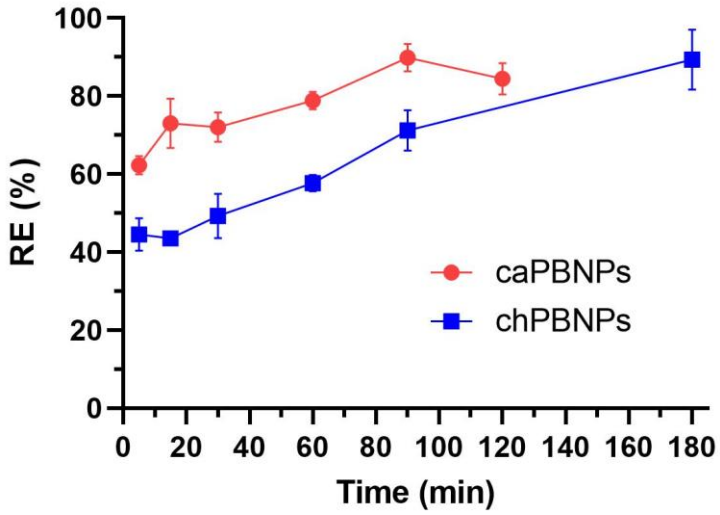

Figure 3.11 Radiolabelling efficiency of caPBNPs and chPBNPs vs incubation time. CaPBNPs and chPBNPs radiolabelling efficiency (RE %) over time (5 - 180 min) for caPBNPs at 0.5 mg/mL with 30 kBq of ^{201}Tl and chPBNPs at 0.25 mg/mL with 30 kBq of ^{201}Tl. All RE were calculated before the purification process, n=3.

Increasing the incubation temperature from 25°C to 70°C led to a higher RE for chPBNPs with average values of 97.0 ± 0.3% (n=3) after one hour of incubation. An example of ^{201}Tl radiolabelling by chPBNPs at 25°C before and after purification and at 70°C is shown in Figure 3.12.

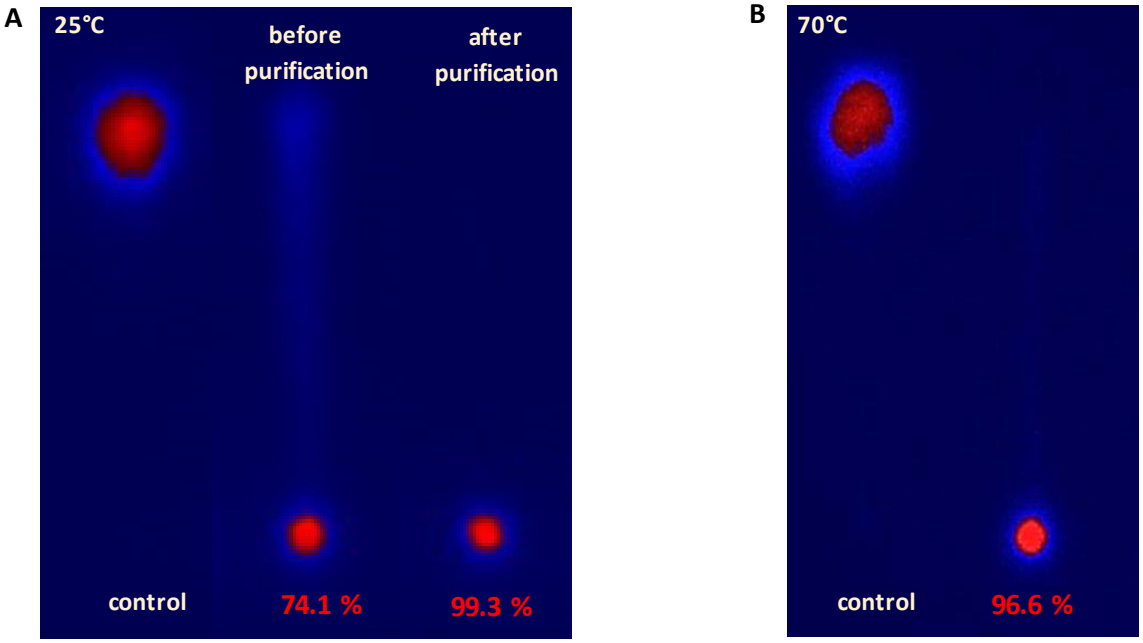

Figure 3.12 Radiolabelling efficiency of chPBNPs measured by the TLC method. A) Exemplar of TLC plate imaged with phosphor imager and calculated radiolabelling efficiency (RE%) at RT after 90 min incubation before and after the purification process. **B)** Exemplar of TLC plate imaged with phosphor imager and calculated RE (%) at 70°C after 60 min incubation. No purification was performed. chPBNPs concentration: 0.25 mg/mL, ^{201}Tl activity: 30 kBq.

Radiolabelling stability (RLS): Radiolabelled caPBNPs (^{201}Tl-caPBNPs) were stable in water, RPMI medium and human serum at RT and at 37°C for at least 7 days (RLS > 94%), while radiolabelled chPBNPs (^{201}Tl-chPBNPs) were less stable in medium with RLS decreasing to 72.3 ± 2.3% at RT after 7 days. At 37°C, the ^{201}Tl-chPBNPs RLS was not lower than 86.3 ± 5.4% after 7 days (Fig. 3.13 A and B).

The stability in 25 mM KCl solution was also measured for both types of nanoparticles (Fig. 3.14). Thallium, which is similar to potassium in respect of its ionic radius and charge, can potentially compete with Tl for the interstitial spaces within the Prussian blue crystal structure. KCl solution was added in uptake and toxicity experiments to inhibit unbound ^{201}Tl uptake and it might have influenced the stability of radiolabelled nanoparticles. While ^{201}Tl-caPBNPs were stable up to 7 days in 25 mM KCl at RT, ^{201}Tl-chPBNPs stability dropped to 52.5 ± 4.1% and 54.2 ± 4.4% after 72 h and 7 days, respectively. Further investigation of ^{201}Tl-caPBNPs radiostability in increasing concentrations of KCl (5-150 mM) revealed that their stability after 24 h deceases from 95.1 ± 1.3% in 5 mM KCl to 73.8 ± 4.2% when ^{201}Tl-caPBNPs were placed in 150 mM KCl (Fig. 3.14).

3.4.3 ^{201}Tl-caPBNPs and ^{201}Tl-chPBNPs uptake and efflux in cancer cells

In order to determine the amount of ^{201}Tl activity bound to PBNPs taken up by cancer cells and compare it to the unbound ^{201}Tl uptake, uptake assays were performed by incubating different cancer cell lines with the same amount of activity (30 kBq/well). KCl solution was used in some samples to inhibit the uptake of unbound ^{201}Tl (final KCl concentration: 25 mM). Cellular uptake of ^{201}Tl-caPBNPs (concentration: 0.5 mg/mL added per well) and ^{201}Tl-chPBNPs (concentration: 0.25 mg/mL added per well) was performed in DU145, MDA-MB-231, A549 and SKOV-3 cells over 3 h (Fig. 3.15 A and B).

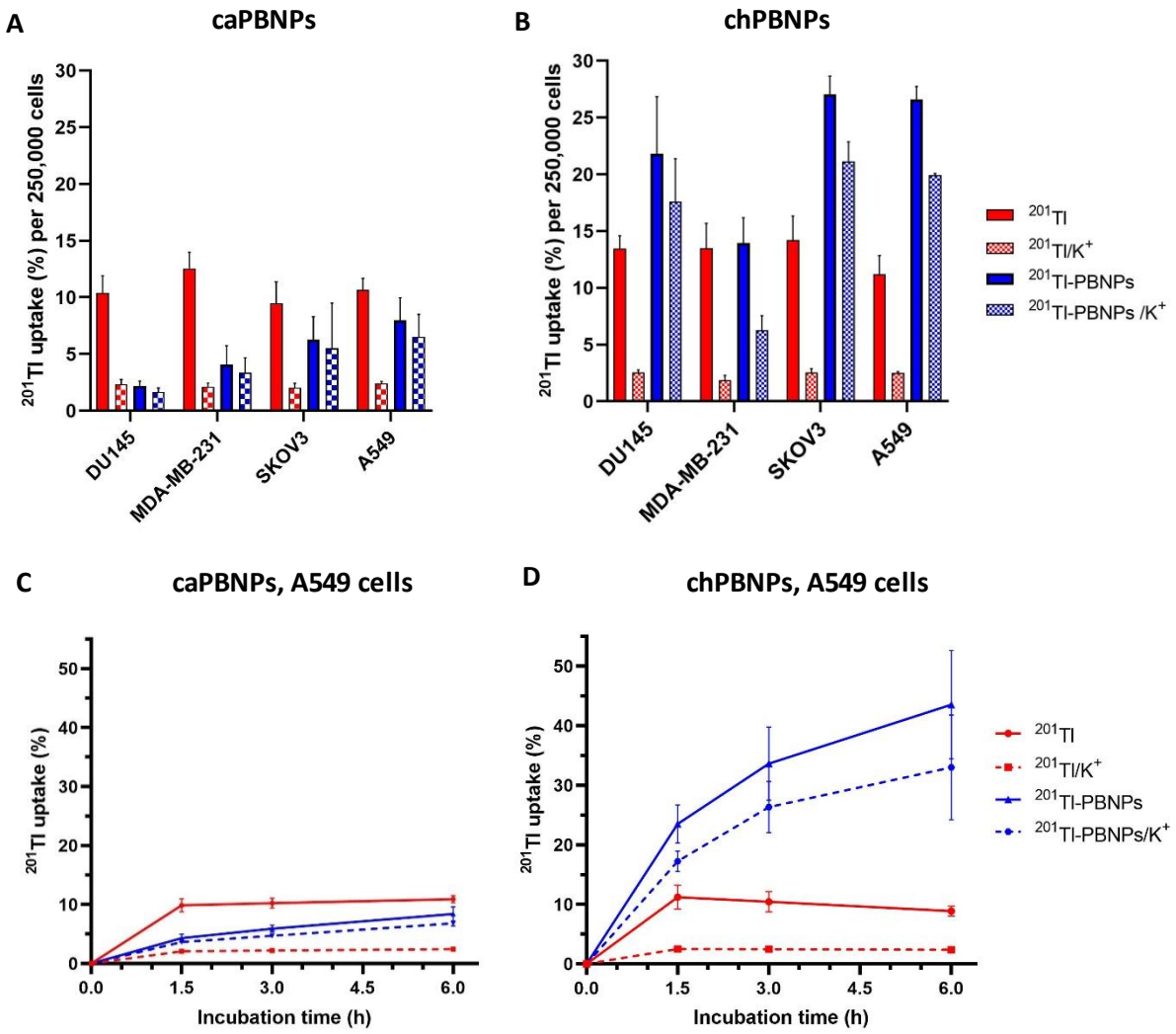

Figure 3.15 ^{201}Tl-PBNPs uptake in different cancer cell lines. Uptake of ^{201}Tl and **A)** ^{201}Tl-caPBNPs, and **B)** ^{201}Tl-chPBNPs in four different cell lines: prostate cancer (DU145), breast cancer (MDA-MB-231), ovarian cancer (SKOV3) and lung cancer (A549) cell lines after 3 h incubation. Uptake timeline in A549 cells (up to 6 h) of ^{201}Tl and **C)** ^{201}Tl-caPBNPs or **D)** ^{201}Tl-chPBNPs. Data are presented as mean ± SD, n=3, triplicates. 25 mM KCl was used to inhibit unbound ^{201}Tl uptake. CaPBNP concentration: 0.1 mg/mL, chPBNPs concentration: 0.05 mg/mL. ^{201}Tl activity used: 30 kBq/well, 250,000 cells were seeded for each experiment.

^{201}Tl-caPBNPs uptake in all cell lines ranged between 2.2 ± 0.4% and 8.0 ± 2.0% calculated per 250,000 cells, substantially lower than the uptake of unbound ^{201}Tl, which was between 9.5 ± 1.9% and 12.6 ± 1.4%. The ^{201}Tl-caPBNPs uptake measured with additional potassium ions was on average 18.1% lower compared to the ^{201}Tl-caPBNPs uptake conducted in medium only. This is much smaller value than the average difference in uptake of unbound ^{201}Tl with and without KCl solution, calculated as 79.0% (Fig. 3.15 A).

On the other hand, ^{201}Tl-chPBNPs uptake in all tested cell lines after 3 h was on average 1.7 times higher than the uptake of unbound ^{201}Tl, ranging between 13.9 ± 2.2 % and 27.1 ± 1.6 % (Fig. 3.15 B). The uptake values for ^{201}Tl-chPBNPs with KCl is on average 30.3% lower than the uptake values without KCl. For both types of PBNPs the average uptake was higher in SKOV3 and A549 cells, which are known for their phagocytotic properties. Lung cancer cells (A549) were chosen as a model cell line for caPBNPs and chPBNPs for further experiments due to the high uptake rates.

The uptake timeline for caPBNPs and chPBNPs in A549 cells was done to establish the optimal incubation time for further experiments and is presented in Figure 3.15 C and D. For both types of nanoparticles, it showed a steady increase of radioactivity taken up by cells over time up to 6 hours. The uptake timeline for unbound ^{201}Tl confirmed the pattern observed before, where the maximum activity uptake is reached around 90 minutes.

Efflux assays were conducted to evaluate the rate at which intracellular activity is eliminated from cells after the removal of the radioactive medium. After A549 cells were incubated with ^{201}Tl-caPBNPs for 3 h and the radioactive medium was replaced with a fresh one, the accumulated radioactivity was washed out from cancer cells significantly more slowly than when cells had been incubated with unbound ^{201}Tl, reaching plateau at around 50.8 % (95% confidence level (Cl): 43.8 – 57.3%) compared to 10.0% (95% Cl: 7.5-12.6%) calculated for unbound ^{201}Tl (Fig. 3.16 A). ^{201}Tl-chPBNPs showed even slower wash out rate, reaching a plateau at around 68.1% (95% Cl 62.7-73.3%) (Fig. 3.16 B).

To measure the continuous wash out of nanoparticles from cells, after the initial accumulation of ^{201}Tl or ^{201}Tl-PBNPs, the radioactive medium was replaced for a non-radioactive and cells were incubated for 15 min. After this time, the medium was collected, and the same cells were exposed to a repeated change of medium every 15 to 60 min. At the end, cells were lysed, and the remaining activity measured. In this experiment, 50% of the initial ^{201}Tl-caPBNPs activity was washed out after 0.34 h (95% Cl: 0.20 – 0.56) reaching a plateau at 23.4% (95% Cl 6.5 – 38.0 %) compared to 0.13 h (95% Cl: 0.13 - 0.14) for unbound ^{201}Tl, which was nearly completely washed out (plateau at 0.7 %, 95% Cl: 0-1.7 %) (Fig. 3.16 C). For ^{201}Tl-chPBNPs, it took nearly 1 h (0.94 h; Cl 95%: 0.17-1.33) to wash out 50% of the initial accumulated activity reaching the plateau at 39.3% (Cl 95%: 13.98-52.13%) (Fig. 3.16 D).

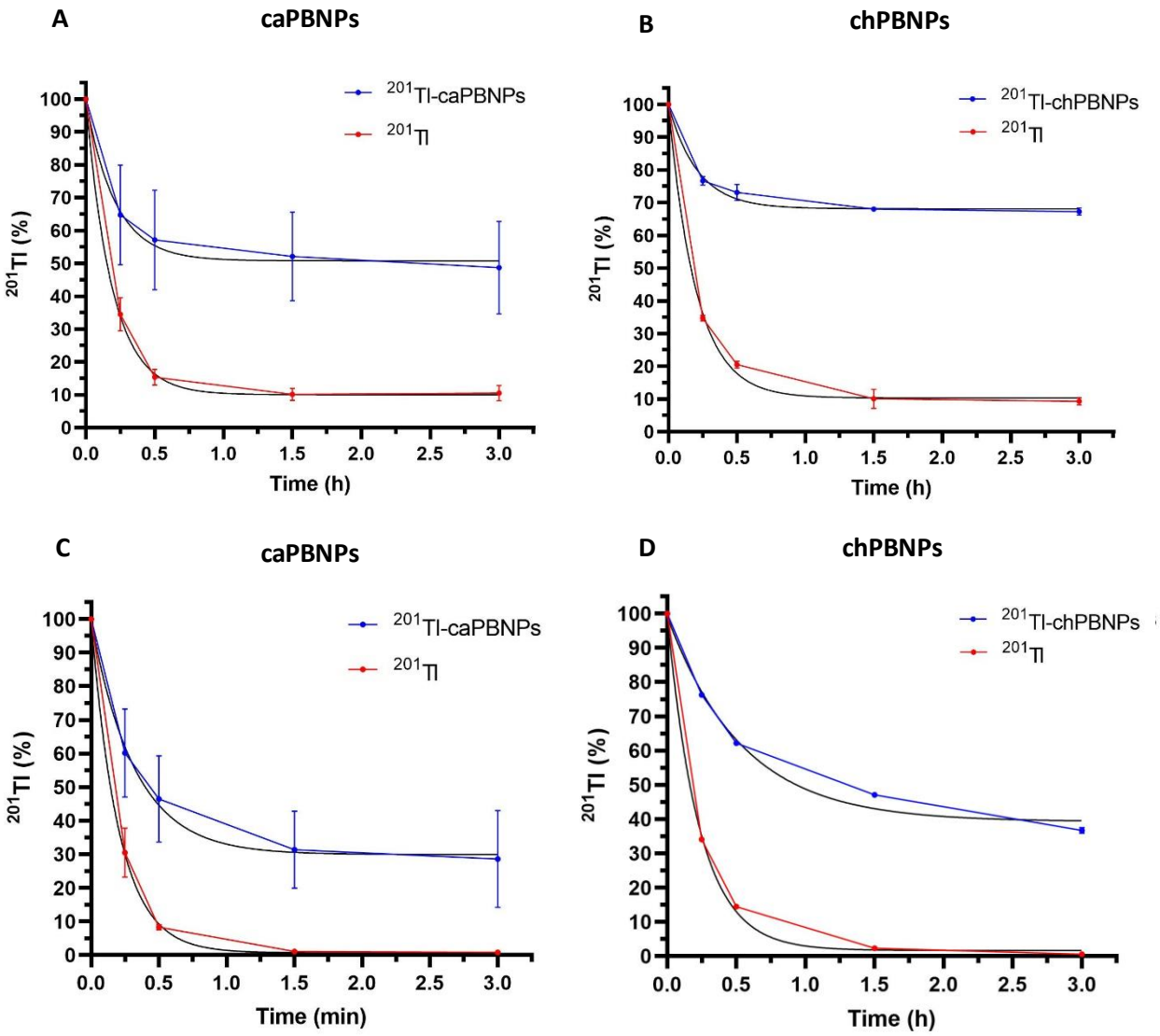

Figure 3.16 ^{201}Tl-PBNPs efflux in lung cancer cells. Efflux of ^{201}Tl and **A)** ^{201}Tl-caPBNPs and **B)** ^{201}Tl-chPBNPs in lung cancer cells (A549). The amount of activity from the preceding uptake assay is defined as 100% at time 0. Radioactive medium was replaced with non-radioactive and ^{201}Tl activity was measured over time. **C)** Continuous efflux of ^{201}Tl and ^{201}Tl-caPBNPs vs time. The time needed to wash out 50% of the initial accumulated activity calculated for ^{201}Tl: 0.13 h (CI 95%: 0.13-0.14), plateau at 0.7% (CI 95%: 0-1.70%); the time needed to wash out 50% of the initial accumulated activity calculated for ^{201}Tl-caPBNPs: 0.34 h (CI 95%: 0.20-0.56) plateau at 23.4%, (CI 95%: 6.50-38.0). **D)** Continuous efflux of ^{201}Tl and ^{201}Tl-chPBNPs vs time. The time needed to wash out 50% of the initial accumulated activity calculated for ^{201}Tl: 0.16 h (CI 95%: 0.14-0.19), plateau at 1.7% (CI 95%: 0-6.20); the time needed to wash out 50% of the initial accumulated activity calculated for ^{201}Tl-chPBNPs: 0.94 h (CI 95%: 0.17-1.33) plateau at 39.3% (CI 95%: 13.98-52.13%). Data was fitted with an exponential decay equation (Y = (Y0 - plateau) *exp(-K*X) + plateau, black line, GraphPad Prism). Data are presented as mean ± SD, triplicates, n=3 except D) where n=1. CaPBNP concentration: 0.1 mg/mL, chPBNPs: 0.05 mg/mL. ^{201}Tl activity used: 30 kBq/well, 250,000 cells were seeded for each experiment.

3.4.4 caPBNPs and chPBNPs ability to capture ^{201}Tl inside lung cancer cells

In order to assess the ability of caPBNPs and chPBNPs to capture radioactive thallium inside cancer cells, pre-incubation over 16 h with unlabelled caPBNPs or chPBNPs was performed, followed by 1.5 h incubation with [^{201}Tl]TlCl. In cells incubated with caPBNPs beforehand, [^{201}Tl]TlCl uptake was significantly higher compared to cells without prior incubation with nanoparticles, and increased with nanoparticles concentration (Fig. 3.17 A).

ChPBNPs were even more effective in capturing ^{201}Tl inside cells. ^{201}Tl uptake increased from 12.4 ± 0.2% to 66.4 ± 0.7% when cells were pre-incubated with chPBNPs (Fig. 3.17 B). Moreover, ^{201}Tl washout from cells containing caPBNPs or chPBNPs was significantly delayed compared to unbound ^{201}Tl, with a plateau of 45.2% (95% CI: 31.9 – 57.2%) and 66.8% (95% CI: 61.1 - 72.0%), respectively (Fig. 3.17 C and D).

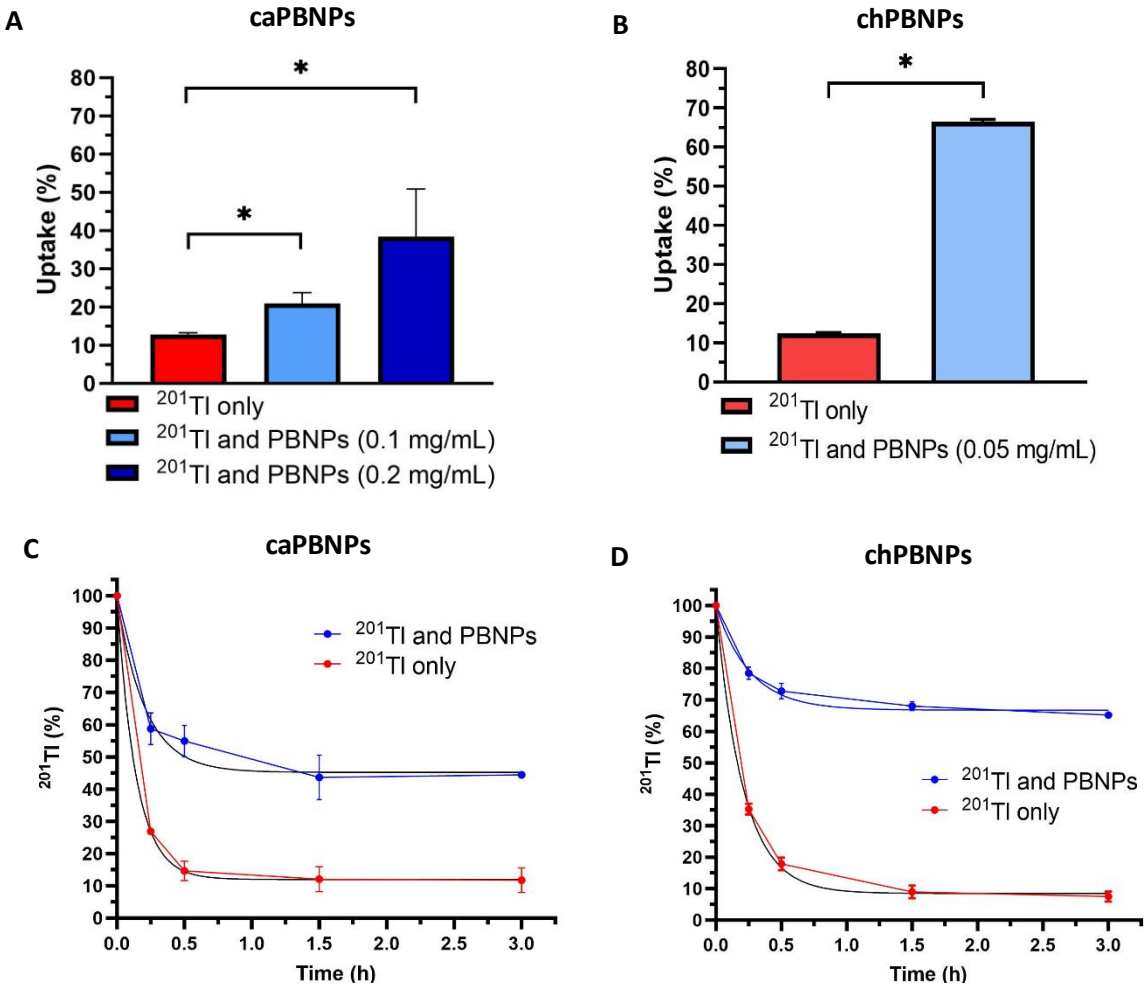

Figure 3.17 ^{201}Tl retention in cancer cells pre-incubated with unlabelled caPBNPs and chPBNPs. ^{201}Tl uptake in lung cancer cells (A549) after 90 min incubation with 30 kBq/well [^{201}Tl]TlCl with and without **A)** caPBNPs and **B)** chPBNPs prior incubation. caPBNPs concentration: 0.1 and 0.2 mg/mL.; chPBNPs concentration: 0.05 mg/mL. Efflux of ^{201}Tl from A549 cells pre-incubated with **C)** 0.1 mg/mL of caPBNPs and **D)** 0.05 mg/mL of chPBNPs. Nonlinear regression line was fitted (black line). Data are presented as mean ± SD, triplicates, n=3, * indicates significance with P<0.05, unpaired t-test.

3.4.5 ^{201}Tl-caPBNPs and ^{201}Tl-chPBNPs radiotoxicity

The radiotoxicity of radiolabelled caPBNPs and chPBNPs was first assessed with γH2AX assay to measure the amount of double strand breaks (DSB) in the nuclear DNA (also called foci) triggered by the radioactive nanoparticles and compared to unbound ^{201}Tl. Examples of γH2AX confocal fluorescence microscopy images for A549 cells treated with ^{201}Tl-caPBNPs, ^{201}Tl and the controls are presented in Figure 3.18 A showing a small increase in DNA DSB in cells incubated with ^{201}Tl-caPBNPs and KCl compared to cells incubated with the same activity of unbound ^{201}Tl.

Quantitative data from γH2AX study revealed that non-PB-bound ^{201}Tl caused, on average, 14-fold increase in DNA DSB when cells were incubated with ^{201}Tl activity of 1,000 kBq/well compared to the negative control (Fig. 3.18 B). ^{201}Tl-caPBNPs with and without KCl had non-significant effects on the amount of detected DNA damage (^{201}Tl-caPBNPs activity: 250-1,000 kBq/well). The uptake assays performed alongside the γH2AX experiments showed the average ^{201}Tl uptake of 0.07-0.34 Bq/cell for [^{201}Tl]TlCl, 0.03-0.19 Bq/cell for ^{201}Tl-caPBNPs and 0.02-0.17 Bq/cell for ^{201}Tl-caPBNPs/K^+.

On the other hand, lung cancer cells treated with 1,000 kBq/well of ^{201}Tl-chPBNPs with and without KCl had significantly higher average number of foci per nucleus (10.2 times) compared to cells incubated with unlabelled-chPBNPs (control, $P<0.05$, Mann-Whitney test), while unbound ^{201}Tl caused, on average, 11.3-fold increase in the nuclear DNA damage comparing to cells treated with saline only (Fig. 3.19 A and B). γH2AX confocal fluorescence microscopy images for A549 cells treated with ^{201}Tl-chPBNPs, ^{201}Tl and the controls are shown in Figure 3.19 A. The uptake assays done at the same time as the radiotoxicity experiments showed an average ^{201}Tl uptake of 0.08 - 0.26 Bq/cell for [^{201}Tl]TlCl, 0.25 - 1.15 Bq/cell for ^{201}Tl-chPBNPs and 0.23 - 1.11 Bq/cell for ^{201}Tl-chPBNPs/K^+.

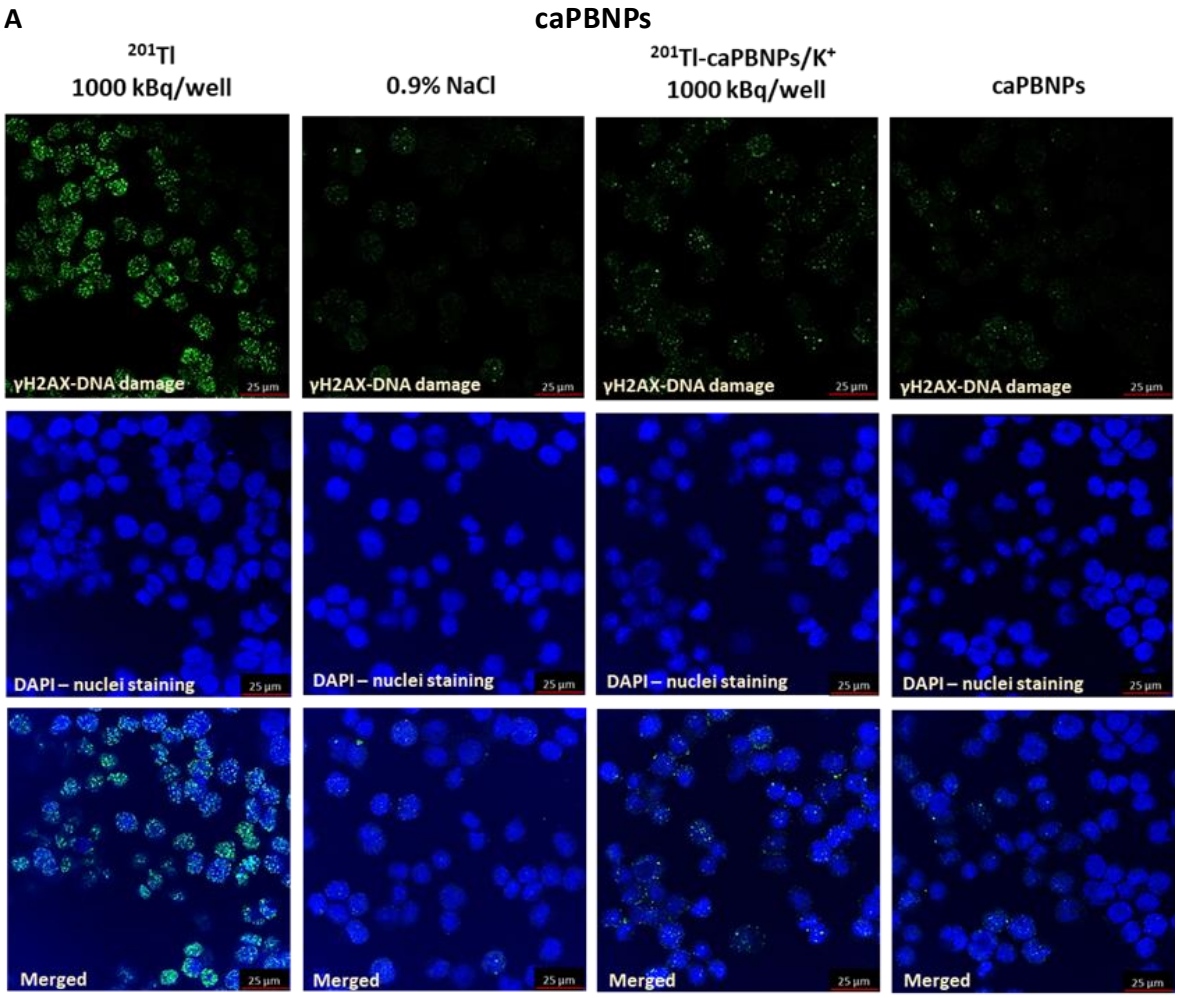

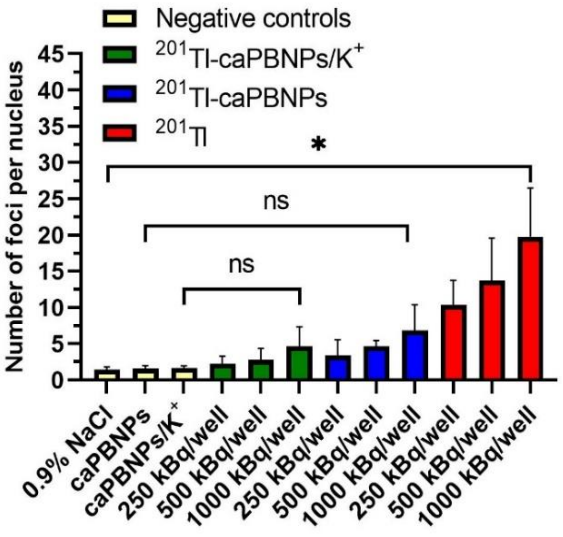

Figure 3.18 ^{201}Tl-caPBNPs nuclear DNA damage in lung cancer cells. A) Exemplar confocal fluorescence microscopy images (100x, scale bar - 25 µm) of lung cancer cells (A549) incubated for 3 h with [^{201}Tl]TlCl, 0.9% NaCl (negative control), ^{201}Tl-caPBNPs and caPBNPs (negative control), followed by immunofluorescence staining with green fluorescence for γH2AX (smart gain (SG) and smart offset (SO) were kept constant for all conditions in the experiment). Nuclear DNA is stained with DAPI (blue). **B)** Average number of foci per nucleus in A549 cells after 3 h incubation with [^{201}Tl]TlCl, ^{201}Tl-caPBNPs, ^{201}Tl-caPBNPs/K$^+$ or 0.9% NaCl, caPBNPs and caPBNPs/K$^+$ (negative controls). Activity added per well: 250 – 1000 kBq. A range of 24 to 57 nuclei per condition were analysed across all experiments; same settings were kept within the experiment. 3-9 pixel units were set as a typical diameter of foci. Bars represent mean ± SD, n=3, * indicates significance with $P < 0.05$, ns - not significant, Mann-Whitney test.

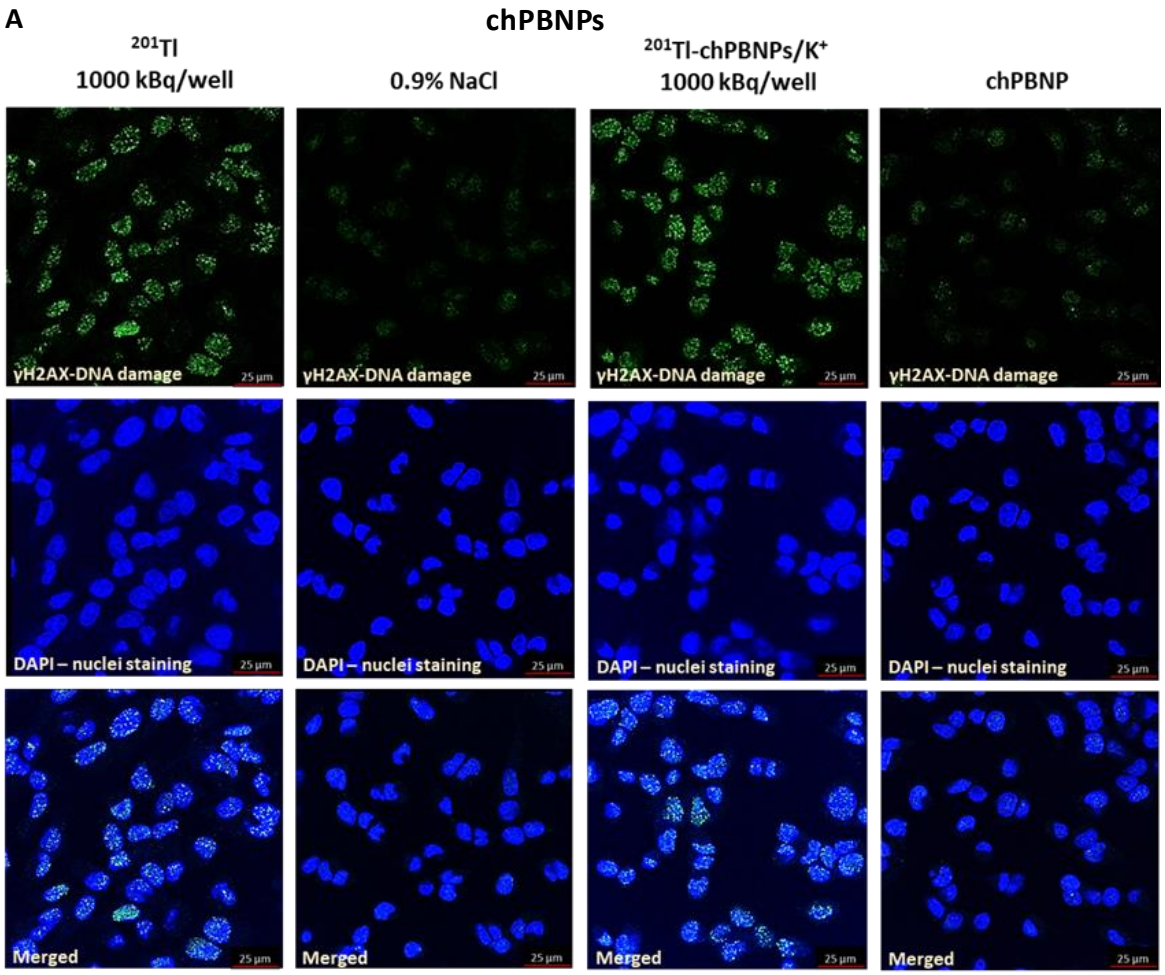

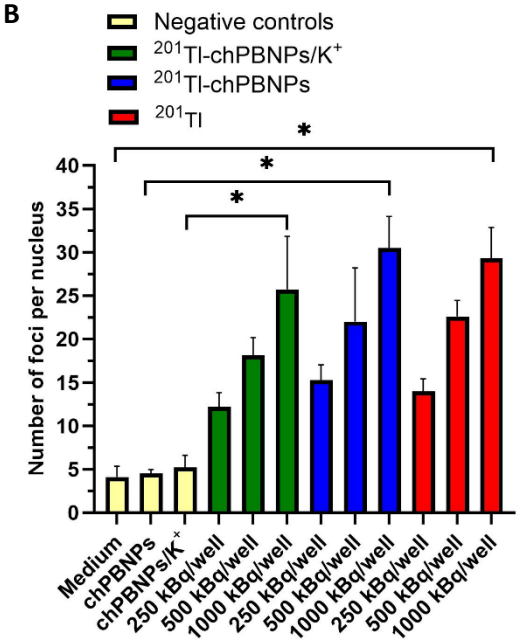

Figure 3.19 ^{201}Tl-chPBNPs nuclear DNA damage in lung cancer cells. A) Exemplar confocal microscopy images (100x, scale bar: 25 µm) of lung cancer cells (A549) incubated for 3 h with [^{201}Tl]TlCl, 0.9% NaCl (negative control), ^{201}Tl-chPBNPs/K$^+$ and chPBNPs/K$^+$ (negative control), followed by immunofluorescence staining with green fluorescence for γH2AX (smart gain (SG) and smart offset (SO) were kept constant for all conditions in the experiment). Nuclear DNA is stained with DAPI (blue). **B)** Average number of foci per nucleus in A549 cells after 3 h incubation with [^{201}Tl]TlCl, ^{201}Tl-chPBNPs, ^{201}Tl-chPBNPs/K$^+$ or 0.9% NaCl, chPBNPs and chPBNPs/K$^+$ (negative controls). Activity added per well: 250 – 1000 kBq. A range of 24 to 57 nuclei per condition were analysed across all experiments; same settings were kept within the experiment. 3–9-pixel units were set as a typical diameter of foci. Bars represent mean ± SD, n=3, * indicates $P < 0.05$, Mann-Whitney test.

In order to investigate the difference in the long-term radiotoxic effect of ^{201}Tl and ^{201}Tl bound by nanoparticles (^{201}Tl-caPBNPs and ^{201}Tl-chPBNPs), the clonogenic survival of A549 cells was performed (Fig. 3.20).

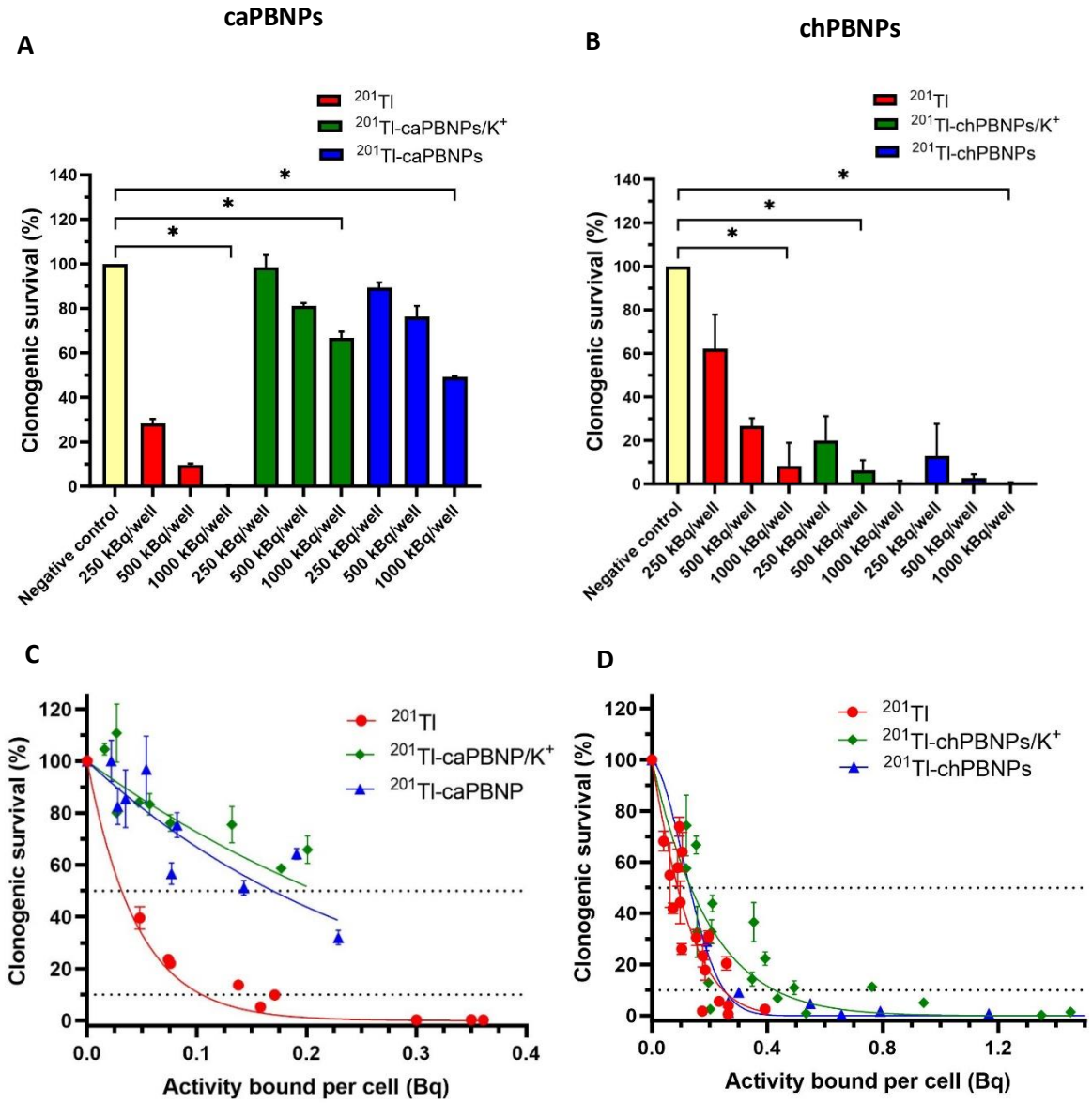

Figure 3.20 PBNPs clonogenic radiotoxicity in lung cancer cells. A) Clonogenic survival vs activity added per well in lung cancer cells (A549) treated with ^{201}Tl, ^{201}Tl-caPBNPs and ^{201}Tl-caPBNPs/K$^+$ and with **B)** ^{201}Tl, ^{201}Tl-chPBNPs and ^{201}Tl-caPBNPs/K$^+$. **C)** ^{201}Tl-caPBNPs clonogenic survivals (%) versus the activity bound per single cell after 3 h incubation with [^{201}Tl]TlCl, ^{201}Tl-caPBNPs or ^{201}Tl-caPBNPs/K$^+$ in A549 cells (n=3). **D)** ^{201}Tl-chPBNPs clonogenic survivals (%) versus the activity bound per single cell after 3 h incubation with [^{201}Tl]TlCl or ^{201}Tl-chPBNPs or ^{201}Tl-chPBNPs/K$^+$ in A549 cells (n=6). Linear quadratic survival model was fitted and calculated activity causing at least 50% and 90% reduction for ^{201}Tl-chPBNPs/K$^+$, ^{201}Tl-chPBNPs and [^{201}Tl]TlCl is visible in Table 3.4. Some error bars are smaller than the data points and not visible. Data are presented as mean ± SD, triplicates, n=3 or n=6 (chPBNPs). Bars represent mean ± SD, * indicates P < 0.05, Mann-Whitney test.

Incubation of A549 cells with 1,000 kBq/well of ^{201}Tl-caPBNPs for 3 h significantly decreased the clonogenic survival to 66.7 ± 2.8% in the presence of KCl and to 49.1 ± 0.4% in its absence (Fig. 3.20 A). This level of radiotoxicity however is much smaller than the radiotoxicity observed for 1,000 kBq/well of unbound ^{201}Tl, which reduced the clonogenic survival to 0.3 ± 0.1% (without KCl).

When 1,000 kBq/well of ^{201}Tl-chPBNPs were incubated with A549 cells for 3 hours, the clonogenic survival significantly dropped to 0.8 ± 0.6% in the presence of KCl and further to 0.5 ± 0.3% in its absence (Fig. 3.20 B). ^{201}Tl-chPBNPs activity of 0.13-0.14 kBq/cell was needed to reduce the clonogenic survival by at least 50% (A_{50}) compared to untreated cells, around 1.4 times higher than for ^{201}Tl (0.09 Bq/cell, without K^+). However, when the activity per cell required to achieve 90% cell killing efficiency (A_{10}) is compared, the activities for ^{201}Tl-chPBNPs and ^{201}Tl are the same (0.25 Bq/cell), and half the activity of ^{201}Tl-chPBNPs needed when additional potassium ions are added (Fig. 3.20 D, Table 3.4). It was not possible to calculate the A_{50} or A_{10} for ^{201}Tl-caPBNPs with confidence due to the data points being concentrated above 50% of the clonogenic survival (Fig. 3.20 C).

A_{50} (Bq/cell)			**A_{10} (Bq/cell)**		
^{201}Tl	^{201}Tl-chPBNPs	^{201}Tl-chPBNPs/K^+	^{201}Tl	^{201}Tl-chPBNPs	^{201}Tl-chPBNPs/K^+
0.09	0.13	0.14	0.25	0.25	0.43
[0.07-0.11]	[0.06-0.16]	[0.09-0.18]	[0.19-0.30]	[0.22-0.29]	[0.30-0.70]

Table 3.4 Clonogenic radiotoxicity calculations for ^{201}Tl-chPBNPs showing the activity needed to reduce the clonogenic survival by at least 50% (A_{50}) and activity needed to reduce the clonogenic survival by at least 90% (A_{10}) for ^{201}Tl-chPBNPs in the presence and absence of KCl. Data are presented as mean ± SD. Confidence level of 95% (CI 95%) is shown in brackets.

In order to eliminate any potential cytotoxic effects on the clonogenic survival caused either by Prussian blue or the coatings used for PBNPs, clonogenic assays with different concentrations (0.06 – 2 mg/mL) of unlabelled, non-radioactive nanoparticles were done. CaPBNPs did not cause any cytotoxicity in concentrations up to 0.4 mg/mL (2 mg/mL added per well) (Fig. 3.21). On the other hand, chPBNPs showed cytotoxicity in concentrations above 0.05 mg/mL (0.25 mg/mL added per well) (Fig. 3.21). Concentrations higher than 0.05 mg/mL of chPBNPs significantly reduced (paired t-test) the clonogenic survival to 43.7 ± 6.0 %, therefore were not used in any of the in vitro or in vivo experiments.

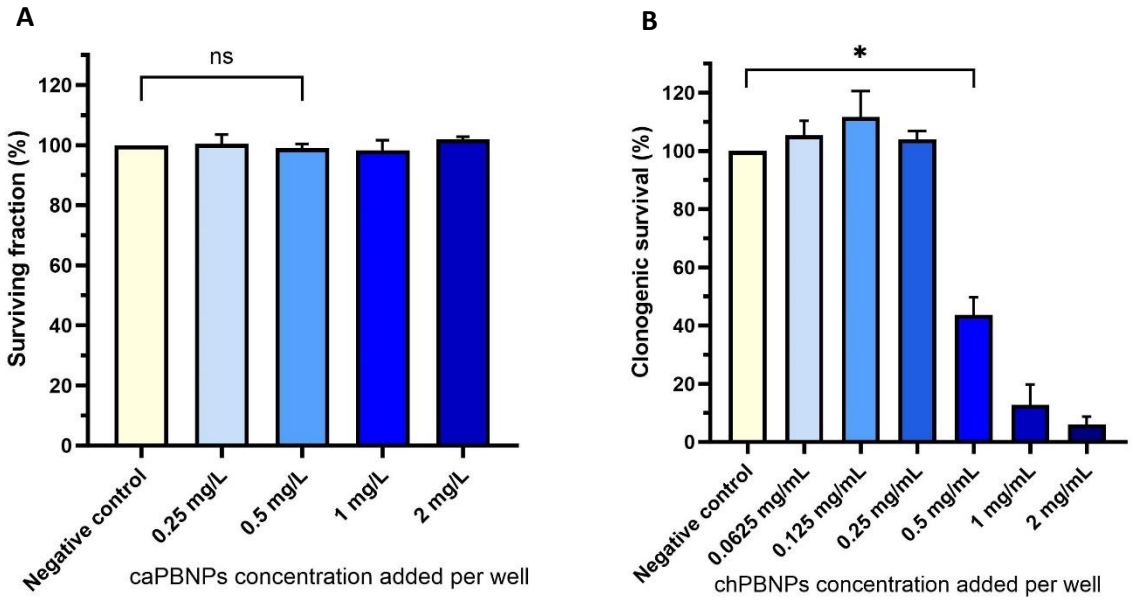

Figure 3.21 Cytotoxicity of non-radioactive caPBNPs and chPBNPs. A) caPBNPs cytotoxicity in lung cancer cells (A549) measured as clonogenic survivals (%) versus concentration added per well (0.25– 2.0 mg/mL) as 50 µL into 200 µL of medium. **B)** chPBNPs cytotoxicity in A549 cells measured as clonogenic survivals (%) versus concentration added per well (0.0625– 2.0 mg/mL) as 50 µL into 200 µL medium. Concentrations higher than 0.25 mg/mL were not used in any of the in vitro or in vivo experiments. Data are presented as mean ± SD, triplicates, n=3.

3.4.6 In vivo study

Maximum intensity projections (MIPs) of SPECT/CT images acquired at 1 h post administration (p.a.) for both the ^{201}Tl group (control group) and the ^{201}Tl-chPBNPs group revealed that most of the activity was contained within the tumours (Fig. 3.22 A). Additionally, a very small amount of activity was detected in kidneys (Fig. 3.22 B). This presence of ^{201}Tl in kidneys 1 h after the injection suggests that the diffusion process from the tumour tissue commences shortly after the intratumoral injections. For ^{201}Tl-chPBNPs group, this process however looks to have a slower progress. After 24 and 48 h p.a., the activity distribution in the control group was predominantly in kidneys with a small amount visible in other organs such as small and large intestine (Fig 3.22 B).

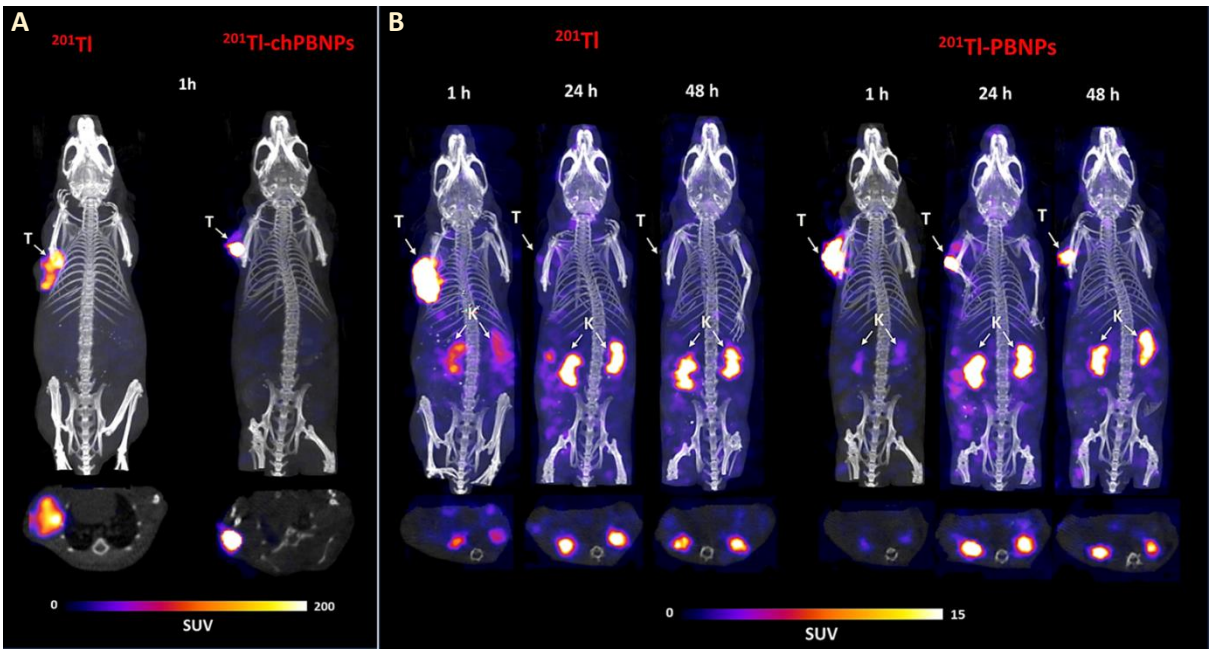

Figure 3.22 Activity distribution in tumours and kidneys after 1 h, 24 h and 48 h. A) MIPs images taken after 1 h after injecting mice with [^{201}Tl]TlCl (left) and ^{201}Tl-chPBNPs (right) and associated transverse images showing the activity distribution within the tumour (SUV scale: 0-200). **B)** MIPs images taken after 1 h, 24 h and 48 h after injecting mice with [^{201}Tl]TlCl (three to the left) and ^{201}Tl-chPBNPs (three to the right). The associated transverse images (SUV scale: 0-15) are presenting the activity accumulated in kidneys. CT images are overlayed with SPECT images and used as anatomical reference (grayscale). Arrows are pointing tumours (T) and kidneys (K).

The signal from ^{201}Tl within the tumour tissue 24 h and 48 h p.a. was minimal in the control group (Fig. 3.23 A). In ^{201}Tl-chPBNPs group, the activity was mostly spread between the tumour and the kidneys, and also observed in small and large intestines, although in much smaller amounts. ^{201}Tl retention in tumours in mice injected with ^{201}Tl-chPBNPs was visibly higher after 24 h and 48 h compared to the control group as shown in the transverse images in Figure 3.23 B. The quantitative SPECT/CT technique was employed to assess the in vivo biodistribution of ^{201}Tl within both the ^{201}Tl-PBNPs group and the control group over a 48-hour period. The tumour and kidney uptake were determined by quantifying the SPECT images after 1 h, 24 h and 48 h p.a. With the aim to compare the biodistribution of ^{201}Tl in both groups, the quantification of activity within manually marked regions of interest (ROIs) of the tumours and kidneys was performed with decay correction to time of administration.

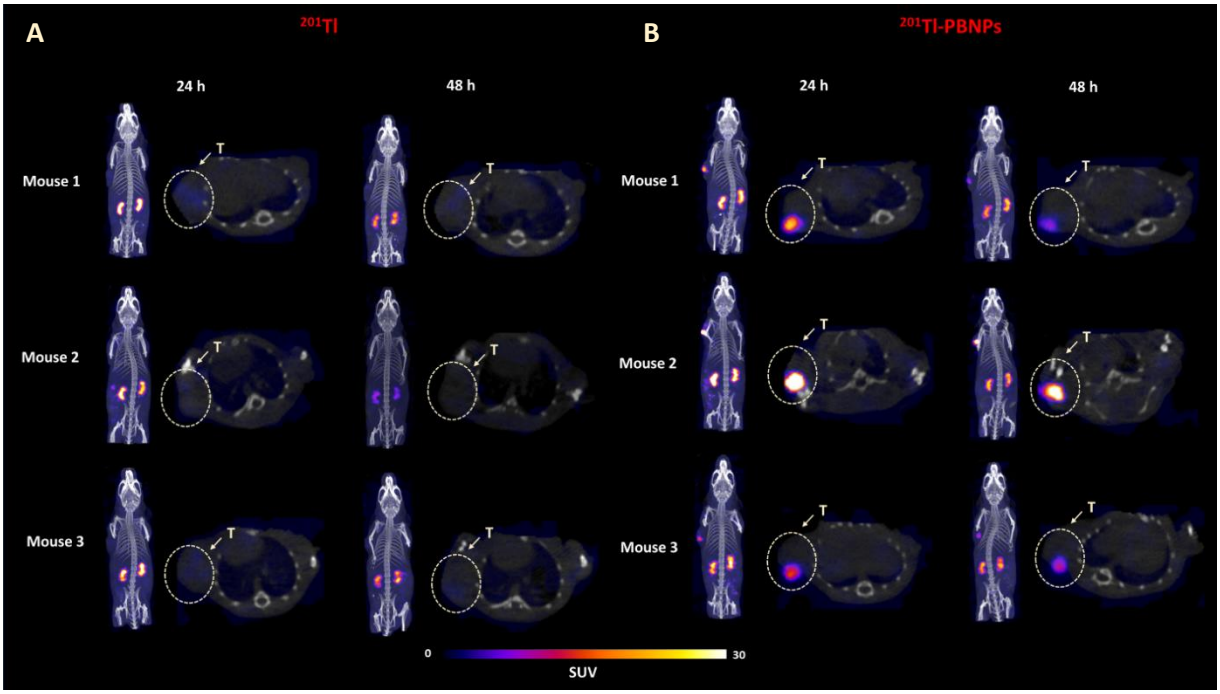

Figure 3.23 Activity distribution in tumours after 24 h and 48 h. MIPs and transverse images of SPECT/CT of mice injected with **A)** [^{201}Tl]TlCl (control group) and **B)** ^{201}Tl-chPBNPs after 24 h and 48 h p.a. The transverse images show the activity distribution within the tumour (white circle) with visibly higher activity present in mice injected with ^{201}Tl-chPBNPs compared to the control group. CT images are overlayed with SPECT images and used as anatomical reference (grayscale). SUV scale: 0-30. Arrows are pointing tumours (T).

The biodistribution of ^{201}Tl activity in tumours and kidneys based on SPECT/CT images is presented in Figure 3.24 A and B and expressed as % IA.

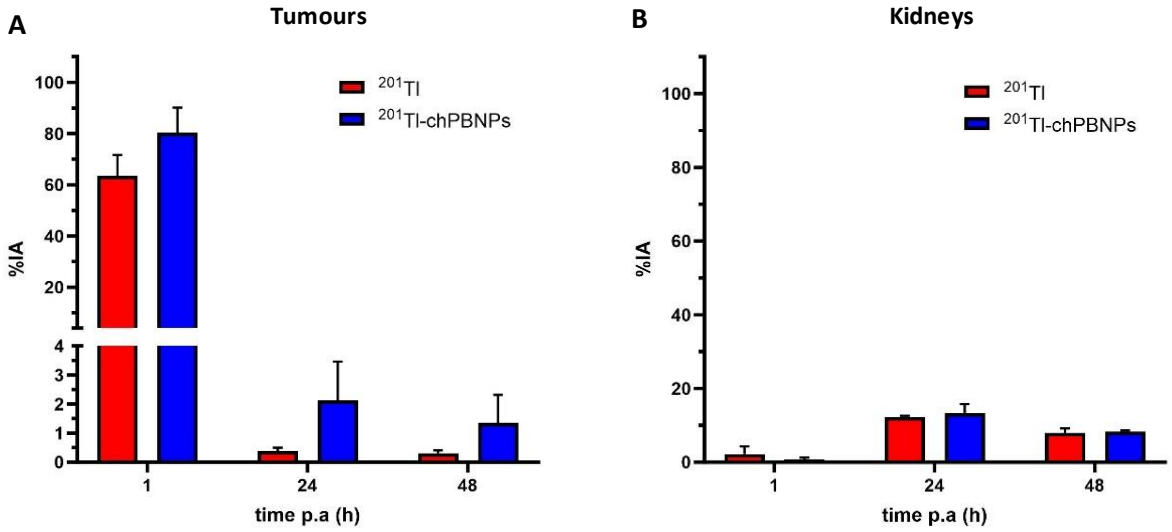

Figure 3.24 Quantitative analysis of SPECT/CT images after 1 h, 24 h and 48 h in mice injected with [^{201}Tl]TlCl and ^{201}Tl-chPBNPs in **A)** tumours and **B)** kidneys. Data is shown as average ± SD and expressed as % IA. n=3 mice per group. Data was tested for normal distribution using Shapiro-Wilk test; statistical significance was performed using unpaired t-test (non-significant).

After 1 h p.a., on average 80.4 ± 9.8% IA of activity inside tumours in ^{201}Tl-chPBNPs group compared to 63.6 ± 8.1% IA in the control group was observed. At the same time, the activity accumulated in kidneys after 1 h p.a. was on average three times lower versus the control group.

Ater 24 and 48 h, the difference in ^{201}Tl retention between these two groups was clearly visible, with approximately 5.5 times more activity present in tumours after 24 h and 4.4 times higher activity after 48 h in ^{201}Tl-chPBNPs group than in mice injected with [^{201}Tl]TlCl. The renal clearance is similar in both groups at 24 and 48 h p.a.

At the end of the experiment, mice were culled, dissected and organs of interest (tail, skin, heart, blood, lungs, liver, kidneys, stomach, small intestine, large intestine, muscle, bone, bladder, urine, brain, pancreas, spleen, tumours and inguinal lymphatic nodes) were removed for assessing the ex vivo biodistribution. The results presented in Figure 3.25 A revealed that ^{201}Tl activity is mostly present in kidneys, on average 21.5 ± 2.6% IA/g in ^{201}Tl group and 20.9 ± 4.1% IA/g in the ^{201}Tl-chPBNPs group, with no significant difference between both groups (Fig. 3.25 B). Activity was also present in urine, indicating predominantly renal excretion in both groups.

The average activity remaining in tumours after 48 h was significantly different, around 3.6 times higher in ^{201}Tl-chPBNPs group comparing to the control group (calculated as 7.6 ± 7.0% IA/g and 2.1 ± 0.3% IA/g, respectively, Mann-Whitney test, $P < 0.05$) (Fig. 3.25 C).

The rest of the activity was taken up by multiple organs, on similar levels in ^{201}Tl group and ^{201}Tl-chPBNPs, including small intestine (3.2 ± 0.5% IA/g and 3.7 ± 0.5% IA/g, respectively), large intestines (3.0 ± 0.4% IA/g; 4.2 ± 1.9% IA/g, respectively) and pancreas (4.2 ± 0.3% IA/g; 4.9 ± 0.6% IA/g, respectively).

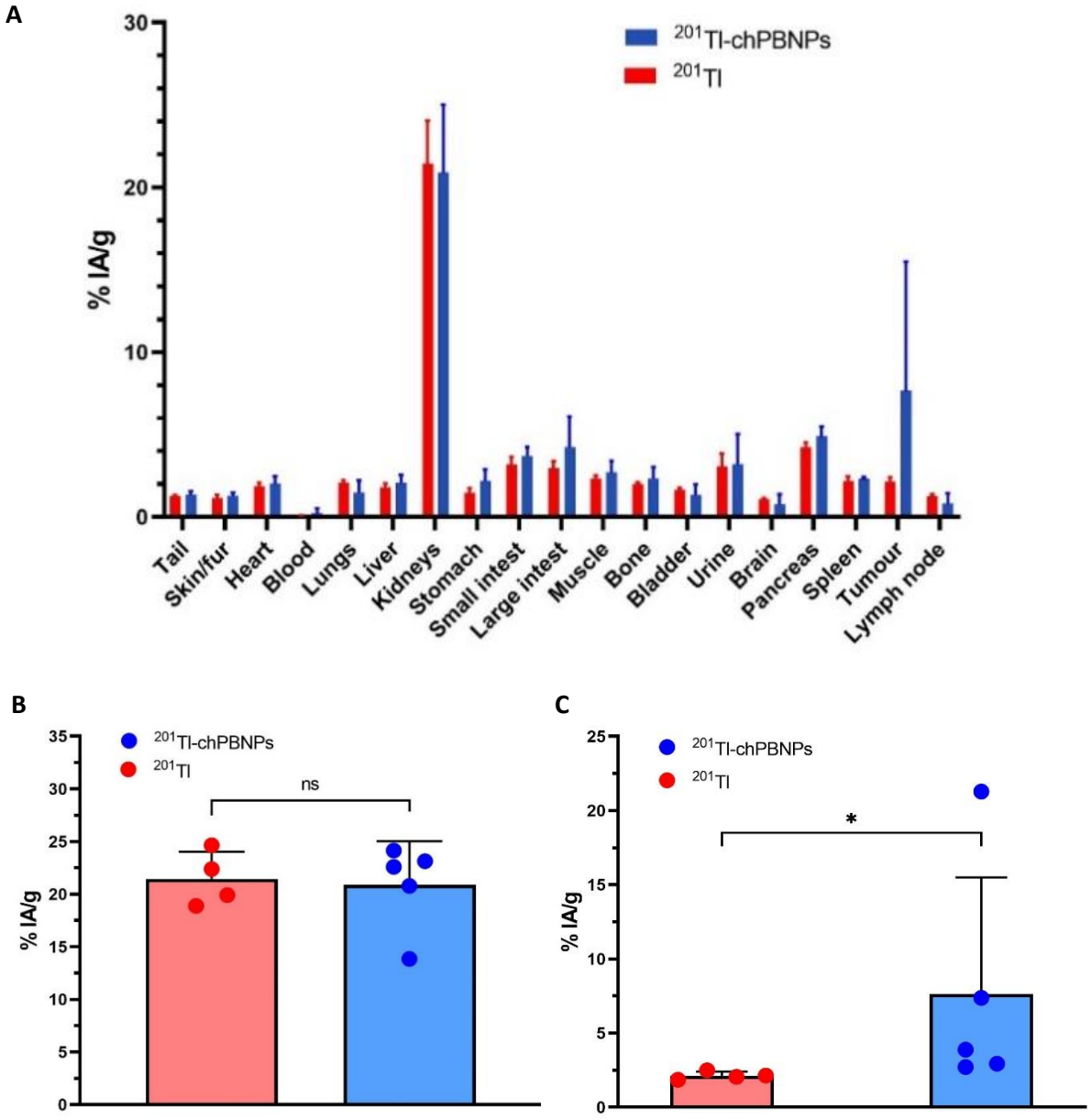

Figure 3.25 Ex vivo biodistribution at 48 h presented as % IA/g. A) Uptake in organs in mice injected with [^{201}Tl]TlCl (control group) and ^{201}Tl-chPBNPs presented as %IA/g. **B)** Uptake in kidneys (as %IA/g) after mice were injected with [^{201}Tl]TlCl and ^{201}Tl-chPBNPs. **C)** Uptake in tumours (as %IA/g) in mice injected with [^{201}Tl]TlCl and ^{201}Tl-chPBNPs. Mann-Whitney test and t-test were used to assess significance, with $P < 0.05$ regarded as statistically significant. Shapiro-Wilk test was used to check the data for normal distribution. Data is shown as average ± SD, (n=4/5 mice per group).

Figure 3.26 presents biodistribution in both groups as % IA and shows the higher level of ^{201}Tl accumulation in liver, kidneys, small intestine and large intestine. A notable observation is that once activity has left the tumour, the biodistribution after 48 h is remarkably similar whether unbound ^{201}Tl or ^{201}Tl-PBNPs were injected. Therefore, it could be assumed that free ^{201}Tl is released from the tumour, not PBNPs.

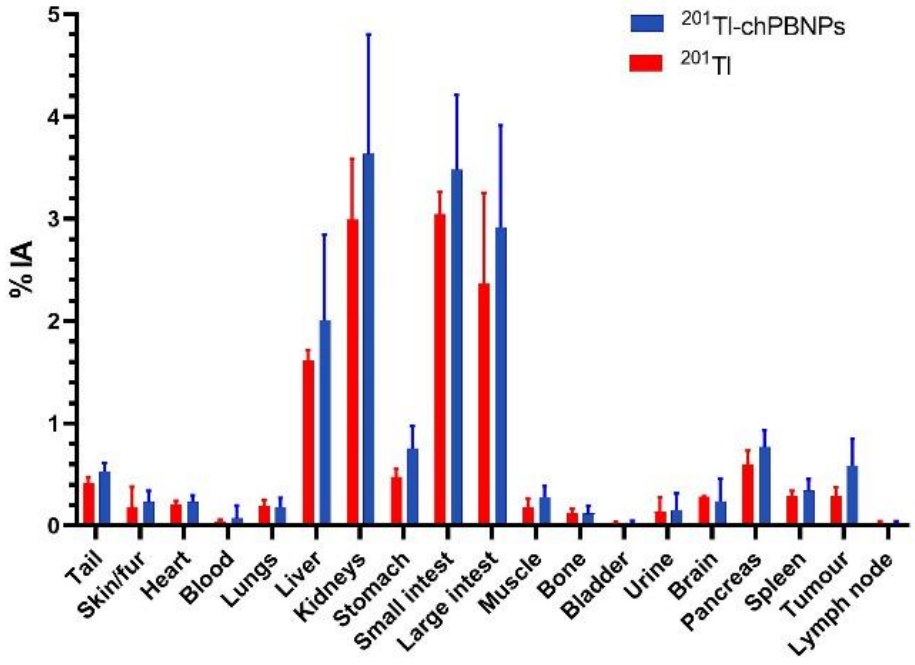

Figure 3.26 Ex vivo biodistribution at 48 h presented as %IA in mice injected with [^{201}Tl]TlCl (control group) and ^{201}Tl-chPBNPs). Data is shown as average ± SD, (n=4 - 5 mice/group).

Autoradiography of thin sections of resected tumours confirmed the presence of radioactivity in both groups. It also demonstrated the heterogeneous distribution of ^{201}Tl within the tumour tissue, that could be attributed to the intratumoral injection and uneven diffusion of ^{201}Tl within the tumour tissue (Fig. 3.27).

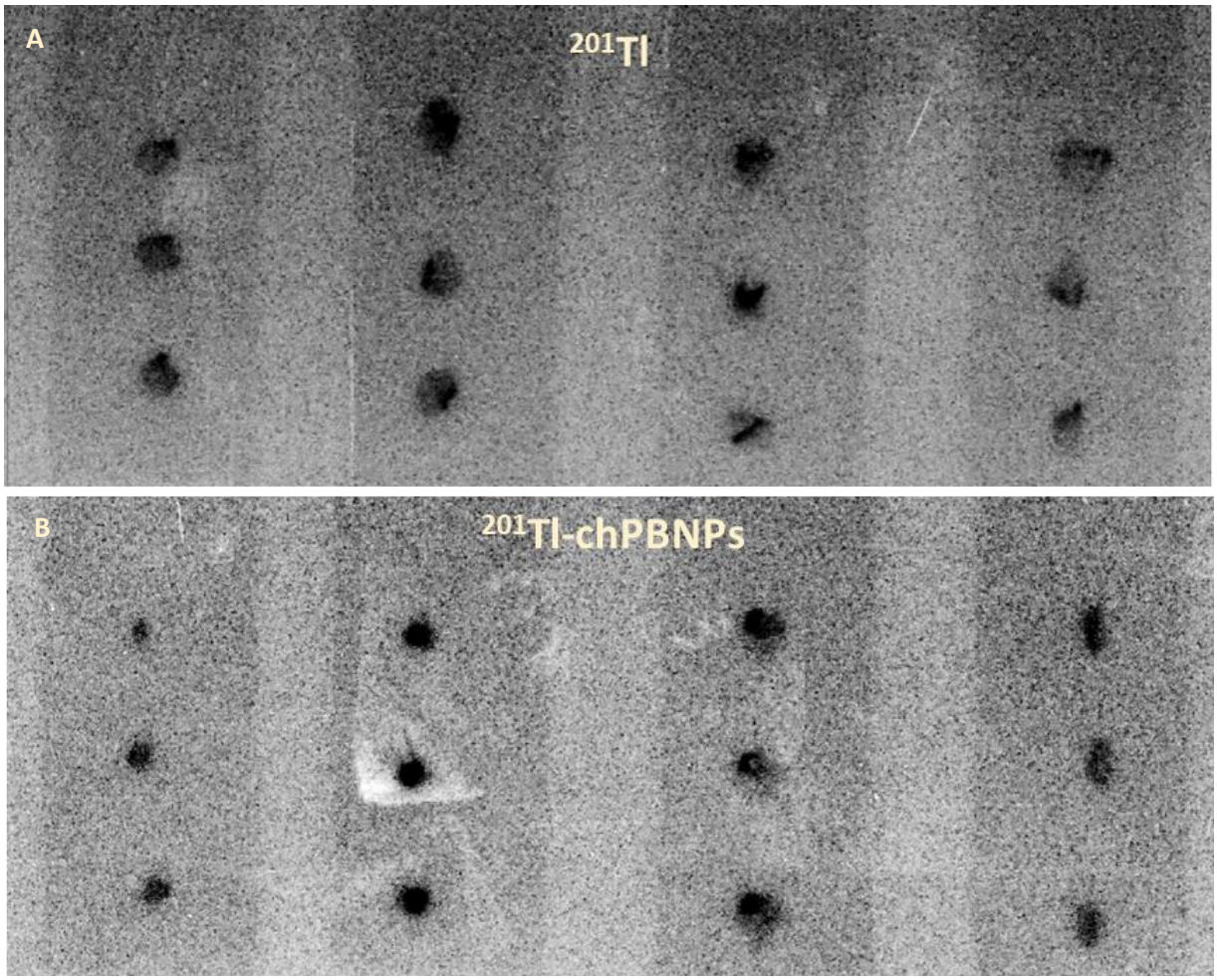

Figure 3.27 Tumour autoradiography. A) Autoradiography in tumours injected with unbound ^{201}Tl and resected 48 h p.a. **B)** Autoradiography in tumours injected with ^{201}Tl-PBNPs and resected 48 h p.a. Tumours were exposed to phosphor imaging plates for 3 weeks due to a low activity present in the tumours at the end of the *in vivo* experiment.

To evaluate potential radiotoxic effects associated with the presence of unbound ^{201}Tl and ^{201}Tl bound to chPBNPs in tumour tissue, H&E staining and Ki-67 immunohistochemistry assays were performed on the excised tumour tissue. Ki-67 is recognised as a reliable marker for assessing cell proliferation, while H&E staining reveals the morphological alterations. Although some morphological changes were observed in the tumour tissue (Fig. 3.28), both groups displayed larger areas of proliferating cells (marked brown). Large variations were observed among the sections taken from different regions within the same tumour and between tumours, owing to the heterogeneous nature of the tumour tissue.

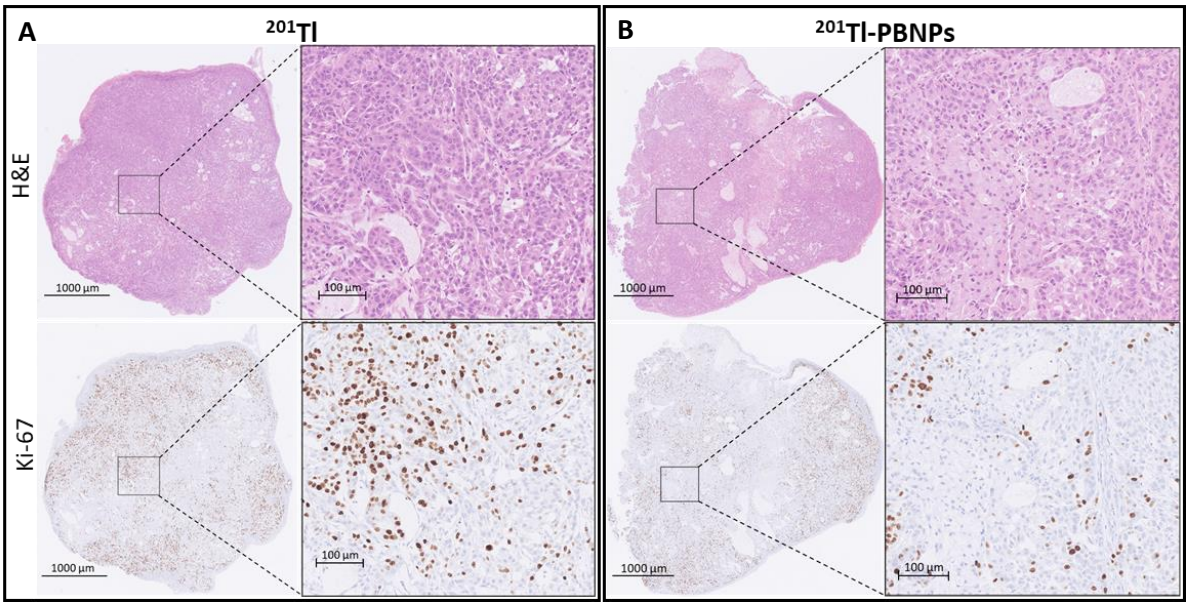

Figure 3.28 Tumours histology. Haematoxylin and eosin (H&E) staining and Ki-67 staining in thin tumours section collected 48 h p.a. after injecting mice with **A)** [^{201}Tl]TlCl and **B)** ^{201}Tl-chPBNPs intratumorally. Scale bars are 1000 µm and 100 µm.

3.5 Discussion

Two types of nanoparticles featuring a Prussian blue core were synthesised using a co-precipitation method: the first type was coated with citric acid (caPBNPs) while the second type featured a chitosan coating (chPBNPs). The highly negative surface charge observed for caPBNPs and the positive surface charge for chPBNPs, which confirmed the successful surface modifications, led to electrostatic repulsions between nanoparticles which accounted for the stability of the nanoparticles' dispersion in water for several weeks. To assess the size and morphology of synthesised nanoparticles, three complementary techniques were applied: transmission electron microscopy (TEM), dynamic light scattering (DLS) and small angle X-ray scattering (SAXS). TEM is a high-resolution imaging technique that uses a focused electron beam transmitted through a thin sample, to provide detailed images of the core of the nanoparticles. The morphology and size observed by TEM revealed homogenous, cubic-shaped caPBNPs, very similar to those already published in literature [131] with the average diameter of 47.1 ± 11.5 nm, around 10 nm smaller than the irregularly shaped chPBNPs. There was no substantial difference in TEM appearance between native nanoparticles and nanoparticles doped with Tl, indicating that thallium (I) ions incorporation does not impact their opacity, size or shape. This is in line with data already published for Prussian blue nanoparticles with a different type of coating [136]. While TEM is well-suited for studying individual nanoparticles at high resolution, it captures only a small portion of the overall sample. DLS is another valuable tool for estimating the size distribution of

nanoparticles in solutions; it measures the fluctuations in scattered light intensity caused by the Brownian motion of particles in a liquid medium. The average size estimated by DLS was larger than the TEM estimation for both types of nanoparticles. This is widely recognised [131,145,146] given that the DLS technique provides information about the hydrodynamic diameter, which takes into account not only the core but also the coating of the particles and any adherent water molecules. DLS average size estimation for chPBNPs was more than 5 times higher than the average size measured by TEM (307.7 ± 113.7 nm compared to 57.6 ± 27.3 nm), which might be caused by the large molecular weight of chitosan and the interparticle interactions. The calculated percentage of chitosan attached to chPBNPs was around 45.8% (w/w), which might have had an impact on the DLS measurements. Due to the significant variation in chPBNPs size compared to the other techniques used, it was concluded that the DLS was not suitable for assessing this type of chPBNPs. A third method used to investigate the nanoparticle shape and dimensions was SAXS, which measures the scattering of X-rays by nanoscale structures and can be used to determine both the core and shell size of the nanoparticle. The average size of caPBNPs and chPBNPs was calculated as 98.9 nm and 81.6 nm, respectively, including the shell with thickness between 2.7 and 3.8 nm. The addition of thallium ions to caPBNPs and chPBNPs reduced the nanoparticle average size to 72.6 and 68.2 nm, respectively, measured by SAXS. In a similar manner to DLS, particles size distribution measured by SAXS involves much higher number of nanoparticles compared to the TEM method and tends to be more statistically reliable. However, the accuracy of the obtained results is largely based on applying the right mathematical model to fit the experimental scattering data. These models take into account factors such as particle shape, size distribution, and the nature of the core and shell materials. In this case the Monte Carlo method was used to retrieve form-free size distributions from the SAXS data. Furthermore, the nanoparticles were modelled on the assumption of their shape and the coating consisting of 50% water and citric acid or chitosan. While a strong agreement between the theoretical model and experimental data was achieved, any observed variations in size, including the difference in size between the native and thallium-dopped nanoparticles, could potentially be attributed to it. The SAXS technique has been performed and modelled thanks to a collaboration with at the X-ray Diffraction Research Technology Facility, University of Warwick.

CaPBNPs and chPBNPs structures were analysed by UV spectroscopy, thermogravimetric analysis, infrared spectroscopy and X-ray diffraction (XRD) technique, and compared with the data available in literature [139,144,145,147]. The crystal structure of Prussian blue was confirmed as cubic close-packed structure (Fm-3m), along with the presence of functional groups characteristic of citric acid and chitosan. As expected, thallium doping did not change the position of the main diffraction peaks in the XRD analysis but altered the signal intensity. This suggests that thallium ions are not integrated

into the crystal lattice but are rather located in the interstitial spaces [136]. Elemental analysis for caPBNPs before and after 3 h incubation with non-radioactive thallium revealed that around 14.8 ± 0.3% of the sample total weight can be attributed to thallium. This is lower than thallium maximum adsorption capacity previously calculated as 26.6% for Prussian blue nanoparticles coated with PEG-NH_2 stabiliser [136].

The initial assumption was that the different coatings applied to the synthesised nanoparticles would not affect the inherent capacity of the Prussian blue core to capture thallium but might influence its loading rate. It was also anticipated that these coatings could potentially influence the nanoparticles' biological behaviour and their subcellular localisation. Radiolabelling with ^{201}Tl was performed over different time intervals using the TLC method to assess the efficacy of caPBNPs and chPBNPs in capturing radioactive thallium. The experiment revealed the difference in the rate of thallium capture between caPBNPs and chPBNP. The process for chPBNPs was considerably slower; achieving an equivalent radiolabelling efficiency of approximately 89% at room temperature (RT) required a longer incubation time of 3 h, contrasting with the 1.5-hour duration for caPBNPs. The slower radiolabelling process might be related to the electrostatic repulsion between thallium cations and positively charge chPBNPs shell. Raising the incubation temperature accelerated the radiolabelling process significantly, reducing the time required to achieve the average radiolabelling yield of 97.0 ± 0.3% to just 1 hour. Radiolabelling stability of ^{201}Tl-caPBNPs and ^{201}Tl-chPBNPs was tested in water, cell culture medium, and human serum at RT and 37°C. Interestingly, the radiolabelling stability of ^{201}Tl-chPBNPs in medium seems to be lower compared to their stability in water at RT, particularly after 72 h. A decrease in stability was also observed when ^{201}Tl-chPBNPs were subjected to incubation with KCl. This experiment illustrates that radioactive thallium could be gradually released from nanoparticles as time progresses and different ions present in the medium may have an impact on the rate of thallium release. This process might involve substitution of radioactive thallium by other cations, such as potassium, sodium or ammonium, in the interstitial gaps of the crystal lattice structure. The precise process behind thallium release from the nanoparticle crystal structure remains unknown, and it is important to highlight that these experiments were not specifically designed to explore this aspect.

Adding KCl solution to the culture medium during in vitro cell experiments with PBNPs was intended to show that the activity taken up by cancer cells is associated with ^{201}Tl bound to nanoparticles as K^+ can substantially decrease unbound ^{201}Tl uptake. The reduced uptake observed for both PBNPs types in the presence of K^+ suggests the possibility of a higher concentration of unbound ^{201}Tl in the sample due to the decreased stability of ^{201}Tl-PBNPs in KCl-supplemented medium. Another reason for the lower uptake values in the presence of KCl could be reduced ^{201}Tl-PBNPs stability inside cancer cells

and accelerated wash-out of ^{201}Tl, potentially caused by an imbalance in extracellular-to-intracellular K^+ ratio.

The in vitro evaluation of the cellular behaviour of radiolabelled caPBNPs and chPBNPs consisted of uptake assays, efflux (wash out) assays and two different radiotoxicity assays aiming to compare the radiotoxic potential of ^{201}Tl bound by nanoparticles with unbound ^{201}Tl. While caPBNPs were taken up by cancer cells only in small amounts, lower than unbound ^{201}Tl, we observed significantly higher uptake of chPBNPs in all tested cell lines compared to the average uptake values of unbound ^{201}Tl. This is explained by the different surface charge of these nanoparticles. Positively charged nanoparticles often exhibit enhanced interactions with negatively charged cellular membrane due to electrostatic attraction, potentially facilitating endocytosis and leading to increased cellular uptake [148]. It is worth noting however, that the relationship between nanoparticle charge and endocytosis is complex and depends on various factors, including nanoparticle size, shape, surface chemistry, and the specific type of cell being targeted [149].

Higher concentrations of chPBNPs led to an increased cellular uptake and subsequently might have induced cell toxicity, as observed when cells were exposed to chPBNPs concentrations exceeding 0.05 mg/mL. However, this trend was not visible for caPBNPs, possible due to a smaller uptake and toxic threshold not being reached. The increased cytotoxicity for positively charged nanoparticles is well described in literature [150]. Additionally, the presence of primary amine groups might also have an impact on the reduced survival of cells exposed to chPBNPs [151].

The uptake timeline in lung cancer cells was performed for caPBNPs and chPBNPs. The amount of radioactivity bound to nanoparticles taken by A549 cells steadily increased with time for both types of nanoparticles, indicating that the maximum nanoparticles uptake is regulated by a different thermodynamic equilibrium than the one seen for unbound thallium ions, where maximum uptake was observed after around 1.5 h. Uptake studies for other types of nanoparticles, such as gold nanoparticles or silica-coated nanoparticles showed that nanoparticle uptake kinetics depends on their size and shape as well as the type of cells and the precise uptake mechanism [152,153]. For example, the mechanism of entry of gold nanoparticles in HeLa cells is predominantly via receptor-mediated endocytosis, where the receptor availability determines the uptake rate and saturation [152].

PBNPs ability to capture thallium inside cells was also tested by measuring the difference between ^{201}TlCl uptake in cells with and without preloading with PBNPs. In this experiment cells were incubated with non-radiolabelled nanoparticles first, followed by 90 min incubation with [^{201}Tl]TlCl. Unbound thallium uptake is regulated by a concentration gradient between the intracellular to extracellular

space reaching its peak in A549 cells after around 90 min at 32:1 concentration ratio (very similar to literature estimates for K^+ ratios ranging from 30:1 to 50:1 [110]). However, when Prussian blue nanoparticles are accumulated within cells, ^{201}Tl intracellular to extracellular concentration ratio increases significantly to 104:1 (for caPBNPs, 1 mg/mL added) and 261:1 (chPBNPs, 0.25 mg/mL added). These findings suggest that PBNPs are able to bind thallium ions within their crystal structure inside cells, and effectively remove free thallium ions from cellular cytoplasm, which results in increased influx of thallium from the medium to reach the new thermodynamic equilibrium. This increased ^{201}Tl uptake in cells may lead to higher radiotoxicity and therefore should increase the efficiency of potential therapy using ^{201}Tl. This approach, known as pre-targeting, has been applied in targeted therapies where the targeting vehicle is separated from the radiotoxic agent and the two are administered separately in order to enhance the therapeutic effect while reducing possible side effects [19,23]. This approach has not yet been studied for radioactive thallium, nor the radiotoxicity of ^{201}Tl when cells are pre-incubated with PBNPs and requires further investigation. Conversely, it is also possible that the presence of PBNPs within cancer cells may have the potential to hinder the accumulation of ^{201}Tl in sensitive subcellular targets, such as the cell nucleus, potentially leading to a reduction in its toxicity compared with the same activity of unbound ^{201}Tl.

An important aspect of the in vitro analysis involved the assessment of ^{201}Tl release from cancer cells and the influence of PBNPs on the rate of ^{201}Tl release. Unbound ^{201}Tl washes out from A549 cells rapidly, with less than 10 min required to remove 50% of the initially accumulated activity. In a continuous change of surrounding medium, mimicking the physiological environment of tumour cells, nearly all of the unbound thallium is washed out. The washout rate, however, slows down in the presence of PBNPs. The time needed to wash out 50% of the initial radioactivity from cells rises to more than 20 min for caPBNPs and to nearly 1 h for chPBNPs. Furthermore, following the replacement of the medium five times with fresh, non-radioactive medium, approximately 23.4% (for caPBNPs) and 39.3% (for chPBNPs) of the activity remains within the cells whereas almost none remains when PBNPs are absent. These findings carry significance in terms of the potential application of ^{201}Tl in radionuclide therapy. Prolonging the retention of radioactive thallium within cancer cells could potentially influence the level of radiotoxicity. However, in this scenario, again we should also consider the differences in subcellular distribution between unbound ^{201}Tl and ^{201}Tl bound to PBNPs described in chapter 4 and its impact on the radiotoxicity.

The radiotoxic effect of ^{201}Tl bound to both types of nanoparticles in A549 cells was assessed by measuring clonogenic survival and the average number of DNA damage (foci) per nucleus. Exposing cells to 250-1000 kBq/well of ^{201}Tl bound to caPBNPs led to a substantial reduction in clonogenic survival compared to untreated cells. The radiotoxic impact was even more pronounced for chPBNPs

where the surviving fraction of cells was reduced nearly to 0 for the highest activities tested. The average amount of intracellular activity per cell required to achieve 90% reduction in clonogenicity over 3 h period bound to chPBNPs was comparable to unbound ^{201}Tl. Nuclear DNA damage measurable by the γH2AX assay showed a significant increase in the nuclear DNA DSBs caused by 1000 kBq/well of ^{201}Tl-chPBNPs compared to the negative control. CaPBNPs delivering the same amount of activity have only a marginal influence on the extent of DNA damage. The variation in radiotoxic potential observed between caPBNPs and chPBNPs may be associated with the higher cellular uptake and/or their more prolonged retention of chPBNPs within cancer cells, resulting in the delivery of a higher level of activity to individual cells. Another possible explanation could be related to differences in the subcellular distribution of these nanoparticles, with chPBNPs being potentially situated in closer proximity to the cell nucleus. This hypothesis will be further explored in the next chapter. The presence of chitosan primary amine groups can potentially facilitate endosomal escape via the proton sponge effect. Multiple amine groups situated on the surface of nanoparticles can effectively capture protons, resulting in acidification and increased osmotic pressure within the vesicle, ultimately leading to its rapture [154]. Altered subcellular localisation when ^{201}Tl is bound to PBNPs could explain why ^{201}Tl-chPBNPs cannot exceed the radiotoxicity of unbound ^{201}Tl, despite having a more favourable kinetic profile.

Seeing that the radiotoxic effect of chPBNPs, measured by the DNA damage assay and clonogenic survival, was similar to that of unbound thallium, these nanoparticles were subsequently studied in an in vivo mouse model to assess the retention of activity within the tumour tissue and the related radiotoxic effect in extracted tumours. The selection of an intratumoral delivery for this purpose was driven by two primary reasons. Firstly, it served to circumvent the absence of tumour targeting in the design of the particles, and secondly, it aimed to prevent the potential sequestration of nanoparticles by macrophages. No prior investigations on Prussian blue nanoparticles injected intratumorally had been reported before. Following the injection, the administered activity was clearly visible within the tumour tissue in both groups scanned after 1 h. The elimination of the injected activity via the kidneys, although slower in the ^{201}Tl-PBNPs group, exhibited a similar pattern to the control group, suggesting a compromised stability of ^{201}Tl-PBNPs and the subsequent release of thallium from the nanoparticulate system over 48 h, rather than release of the intact radiolabelled nanoparticles from the tumours. There are no previous in vivo studies investigating ^{201}Tl-PBNPs coated with chitosan after intratumoral injection in mice and only a few research articles could be found describing biodistribution of ^{201}Tl bound to PBNPs after intravenous injection in healthy mice, although different surface stabilisers were used. Injecting ^{201}Tl-PBNPs coated with dextran intravenously, which had an average diameter of 65.8 ± 8.2 nm, have shown that although the most of activity 48 h after the

injection can be found in kidneys, it also accumulated in lungs and liver between 1 and 24 h post administration (p.a.) [138]. Another study presenting ^{201}Tl-PBNPs coated with glucose-functionalised aminotriethyleneglycol ligands or amino polyethyleneglycol (average size 2.4 ± 0.6 nm) revealed that the majority of the injected radioactivity after 48 h p. a. was observed either in kidneys or kidneys and liver [136]. It is crucial to recognise however that both studies highlighted the significance of surface functionalisation on the biodistribution of PBNPs, which makes it very difficult to compare between different types of nanoparticles. The size of the nanoparticles and their morphology will also influence the biodistribution.

Despite the potential release of ^{201}Tl from chPBNPs once inside the tumour, mice treated with radiolabelled chPBNPs retained, on average, 3.6 times more activity within their tumours when measured after 48 h in extracted tumours (ex vivo biodistribution), compared to mice injected with [^{201}Tl]TlCl. This higher remaining activity within the tumour tissue in mice injected with ^{201}Tl-chPBNPs was also visible on the SPECT/CT images, with approximately 5.5 times more activity present in tumours after 24 h and 4.4 times higher activity after 48 h than in mice injected with [^{201}Tl]TlCl (in vivo biodistribution). The large standard deviation associated with the amount of ^{201}Tl retained in tumours after 24 and 48 h could be related to the intratumoral injecting technique and some of the activity being injected outside the tumour tissue. Histological analysis of the tumours revealed it heterogenous nature, with proliferating cells visible in samples taken from both groups.

As this was a preliminary study only, more information in needed to fully assess the kinetics of chPBNPs tumoral retention and chPBNPs toxicity. For example, shorter time intervals for SPECT/CT scanning, covering the period of 1 to 6 h after the injection, could provide a more detailed description of radiolabelled chPBNPs washout rate and biodistribution in other organs than kidneys. Nonetheless, ^{201}Tl-chPBNPs have proven to retain significantly higher amount of ^{201}Tl inside the tumour after 48 h.

3.6 Conclusions

Two different types of Prussian blue nanoparticles coated with citric acid or chitosan were successfully synthesised. These nanoparticles have different shapes and opposite surface charges while sharing similarities in terms of size, crystal structure, UV absorption and ability to bind thallium (I) ions. Radiolabelling of both nanoparticle types proved to be efficient, resulting in radiostable nanoparticles under diverse conditions up to 72 h. Nevertheless, the different surface charges of these nanopartides prompted varying ^{201}Tl radiolabelling rates and release rates, as well different behaviours in the in vitro cellular uptake experiments. The positively charged chPBNPs were internalised by cells to a greater extent, reaching a threshold where they induced cytotoxicity even without radioactivity.

Compared to free ^{201}Tl, the wash out rate of accumulated radioactivity was much slower thanks to the presence of caPBNPs and chPBNPs. Both types of PBNPs demonstrated the ability to capture and retain unbound thallium within cells (pre-targeting). When assessing the radiotoxic impact on cells, chPBNPs exhibited radiotoxicity comparable to that of unbound ^{201}Tl, as indicated by yH2AX and clonogenic assays, whether measured against the activity added to the well and the calculated internalised activity per cell. Subsequently, these nanoparticles were tested in vivo, where they showcased significantly higher retention of ^{201}Tl in tumours compared to unbound ^{201}Tl after 48 h and predominantly renal clearance. This finding has confirmed the enhanced retention of ^{201}Tl bound to PBNPs observed in the in vitro experiments.

Chapter 4: The subcellular distribution of unbound ^{201}Tl and nanoparticle bound ^{201}Tl

4.1 Introduction

Thallium-201 (^{201}Tl), like other Auger electron-emitters, produces low energy (<25 keV) Auger electrons (AE) which travel short distances from the point of decay (<1 μm), leading to a relatively high linear energy transfer (4-26 keV/μm) [44,45]. Apart from the energy deposited by AE along their short tracks, the potential energy associated with the charged ions generated in the Auger cascade significantly contributes to the extensive ionisation and excitation of molecules in close proximity to the decay sites. In volumes smaller than 100 nm in diameter, the predominant factor influencing the local dose is believed to be the energy imparted by the charged atom [47]. Although the potential energy of the charged atom constitutes only a small fraction of the energy released by AE, the majority of the potential energy will be deposited into the target if the radionuclide is directly incorporated into it. As the target size decreases, the significance of ionisation potential becomes more pronounced [47]. The potential energy released per decay for ^{201}Hg (daughter of ^{201}Tl) was calculated as 1.5 keV [47]. This surpasses the energy calculated for ^{125}I (0.9 keV), which is recognised as an effective AE-emitter known for introducing direct DNA damage when incorporated directly into the DNA structure [50,51,155]. The release of potential energy around the site of decay and the highly localised energy deposition related to the AE emission within nanometres of decaying atoms can prove valuable in targeting small tumours or even individual cancer cells. Given that AE-emitters are most effective at short ranges, achieving their maximum potential may necessitate targeted delivery to a sensitive subcellular location, such as the nucleus, cell membrane, or mitochondria [52]. Understanding the subcellular localisation of radionuclides is not only beneficial but can also be critical in designing effective targeted radiotherapy for AE-emitters. Additionally, this knowledge plays a vital role in microdosimetry calculations essential for optimising treatment planning in radiation therapy. It also contributes to understanding the radiobiological effects and factors that influence cellular response to radiation exposure.

Until recently, the primary focus of radionuclide studies involving AE-emitters has been the nuclear DNA, regarded as the central target for radiation therapy. Particulate radiation can directly hit DNA causing various types of damage, such as single- and double-stand DNA breaks (SSBs and DSBs), DNA base damage and DNA crosslinks, which, if left unrepaired, can result in cellular death. A similar effect can be achieved indirectly by highly reactive hydroxyl radicals ($^{\cdot}$OH), which are generated during the radiation-induced radiolysis of water [34]. It has been proposed that the dose rate imparted by AE-emitters to the nucleus is closely related to their distribution within the cell [156]. Theoretical dosimetry calculations have also shown that a significant portion of the AE' energy is deposited within

a sphere of approximately 2 nm in diameter, which coincides with the size of the DNA helix [157]. This suggests that the distance between the radionuclide and DNA helix plays a crucial role. A study using a model of a double-stranded plasmid DNA and the gel electrophoresis technique has demonstrated that ^{99m}Tc and ^{125}I can directly impact the DNA only when they are in very close proximity, shorter than that referred to as the 'critical distance', as predicted by microdosimetry calculations [158,159]. Furthermore, when the radionuclide is positioned a bit further than the 'critical distance', the indirect damage to the DNA can be observed. Other experiments comparing radiotoxicity of ^{125}I localised in different subcellular compartments suggest that a significantly greater toxic effect is achieved when the radionuclide is located in the nucleus as opposed to the cytoplasm or the cell membrane [160,161].

Various methods have been established to facilitate the delivery of AE-emitters to the nucleus, with one of the most common approaches involving the direct binding of the radionuclide to DNA sequences. An example of this strategy is 5-[^{125}I]-Iodo-2'-deoxyuridine (^{125}IUdR), which is a thymidine analogue. During the synthesis phase of the cell cycle, ^{125}IUdR can be incorporated into the DNA, and this approach has demonstrated promising results both in vitro [161] and in vivo [162]. Another strategy, involving incorporation of ^{125}I into oligonucleotides that can bind to specific DNA sequences, forming a triple helix (known as triplex-forming oligonucleotides), demonstrated a significant radiotoxicity by increasing DNA DSBs [163]. Alternatively, targeting nuclear proteins presents another way to deliver AE-emitters to the nucleus. For example, poly-ADP ribose polymerase (PARP) is a nuclear repair enzyme involved in the repair of SSBs and is often overexpressed in various tumour cells. It can be successfully targeted with AE-emitter labelled PARP inhibitors, such as ^{123}I-MAPi, which has shown a significant potential in the therapy of brain tumours [164].

Numerous cell surface receptors, such as the human epidermal growth factor (EGF) receptors (EGFR), can undergo nuclear translocation upon ligand binding and receptor-mediated internalisation. The migration of the EGF/EGFR complex towards the nucleus is facilitated by an endogenous nuclear localisation sequence (NLS) that is recognised by nuclear pore receptors. When using ^{111}In-labelled human EGF in breast cancer cells that overexpress EGFR, approximately 10% of the radiolabelled construct was found within the nucleus [165]. As ^{111}In-EGF uses the EGFR as a nuclear transport carrier, it was possible to further increase the nuclear translocation of the EGF/EGFR complexes by combining them with a selective tyrosine kinase inhibitor – gefitinib, causing enhanced radiotoxicity in breast cancer cells [166].

NLS-containing peptides can be also attached to antibodies, as seen in ^{111}In-trastuzumab [167], or nanoparticles, such as gold nanoparticles [168] to facilitate their transport into the nucleus. Among these NLS peptides, the TAT peptide has emerged as an effective way for guiding nanoparticles

towards the nucleus. This is achieved through specific interactions with import receptors, known as importin α and β, which subsequently enable entry into the nucleus through nuclear pore complexes [169]. The core sequence of TAT peptide, TAT_{47-57}, is derived from the transactivator of transcription (TAT) of human immunodeficiency virus type 1. It consists of 11 amino acids (Tyr-Gly-Arg-Lys-Lys-Arg-Arg-Gln-Arg-Arg-Arg) and includes a high concentration of positively charged lysine and arginine residues, which may potentially engage in further interactions with negatively charged DNA. The conjugation of the TAT peptide to mesoporous silica nanoparticles has enabled their active transport across the nuclear membrane [169]. When these nanoparticles were loaded with the anticancer drug doxorubicin, they exhibited significantly increased radiotoxicity in comparison to doxorubicin encapsulated within silica nanoparticles that did not incorporate the TAT peptide. This effect was observed only when the size of the nanoparticles fell within the range of 25 to 50 nm as opposed to those with a larger diameter [169]. In another in vitro study, gold nanoparticles with an attached TAT peptide were observed to reach the cell nucleus [170]. Interestingly, not only the presence of the nuclear localisation sequence (NLS) but also the size of the nanoparticles played a crucial role in their ability to pass through the nuclear envelope, which consists of nuclear pore complexes with a diameter ranging from 20 to 70 nm [169].

While the primary emphasis still lies in directing AE-emitters to the nucleus, there is a growing body of research highlighting the significance of extranuclear targets. Some studies proposed that elevated oxidative stress, mostly induced indirectly by free radicals, in mitochondria [171] or a cell membrane phospholipid structure [172] can lead to cellular death. It has been indicated that ionising radiation can alert mitochondrial functions, change mitochondrial gene expression and induce apoptosis [36]. Incubating cancer cells with ^{99m}Tc-pertechnetate and various ^{99m}Tc-labelled compounds exhibiting differential mitochondrial accumulation revealed varying degrees of radiotoxicity, leading to a conclusion that the subcellular distribution of radionuclides significantly contributes to the observed radiotoxic effect [173]. Targeting the cellular membrane could also be considered as an effective strategy for radionuclide therapy. For example, when a non-internalising ^{125}I-labelled monoclonal antibody was bound to the cell surface, the generated free radicals caused the re-organisation of lipid rafts and the activation of multiple receptor-mediated signalling pathways, which resulted in increased cell toxicity [35]. In summary, increasing evidence underscores the significance of precise subcellular targeting to various cellular compartments, making it a key factor in improving the effectiveness of radionuclide therapy employing AE-emitters.

The subcellular distribution of thallium in cells treated with thallium (I) chloride remains so far unknown. However, some clues about where unbound thallium might be localised within a cell can be inferred from the physicochemical properties and the toxicity profile of non-radioactive thallium.

Thallium strongly resembles potassium, having a very similar ionic radius (Tl^+ - 164 pm vs K^+ - 152 pm) and the same charge and hydration sphere. It can be transported inside cells via membrane potassium channels such as the Na^+/K^+ pump as supported by the evidence presented in chapter 2. Once inside a cell, thallium disrupts numerous vital physiological and metabolic processes. It replaces potassium in many potassium-dependent enzyme systems, often with a higher affinity for these enzymes than potassium itself [174]. The most investigated thallium toxicity mechanism, linked to its capacity to mimic potassium, is its interference with mitochondrial processes and energy production. Thallium affects the activity of essential enzymes in the respiratory chain, including pyruvate kinase, succinic dehydrogenase, and fructose-1,6-bisphosphatase, leading to dysfunctions in energy production within mitochondria [175]. Histopathological evidence confirms the swelling and vacuolisation of mitochondria after thallium exposure in neurons and liver cells [176,177]. Increased levels of reactive oxygen species (ROS) and a change in transmembrane mitochondrial potential could also play a role in the toxicity observed towards mitochondria [177]. Additionally, it has been suggested that by replacing potassium, thallium may block 60S subunit biogenesis, inhibit the synthesis of proteins and therefore inactivate ribosomal functions [175]. Several studies have also established a connection between thallium and nuclear damage as well as genetic alterations within cells [178–180]. As an alternative mechanism to potassium substitution, some authors suggest that Tl affinity to amino-sulfhydryl groups could be responsible for blocking enzymes' active centres containing thiol amino acids residues [86]. Impairment in the oxidative stress response in cells following the exposure to thallium is linked to a decreasing concentrations of glutathione, an antioxidant with an active cysteine sulfhydryl group, whose main function is to maintain redox homeostasis and protect cells against damage done by ROS [181]. It is worth noting however that the efflux of thallium from cells appears to be comparable to that of potassium. Therefore, the notion that thallium exerts toxicity through binding to sulfhydryl groups seems less likely.

In light of the intricate toxicity profile of non-radioactive thallium, it is evident that it can potentially localise within various cellular compartments, such as mitochondria, ribosomes, or the cell nucleus, and disrupts numerous cellular processes and functions, most likely by interfering with potassium pathways. Very little is known about the subcellular distribution of potassium in cancer cells. Given that non-radioactive thallium is found within cells at much higher concentrations than ^{201}Tl, the distribution of thallium based on its toxicity mechanism may not accurately mirror the distribution of radioactive thallium. Nonetheless, it has the potential to offer valuable insights into the possible subcellular localisation of radioactive thallium when present in trace concentrations.

There are several methods available to locate radionuclides or stable isotopes on the subcellular level, including subcellular fractionation, fluorescent imaging, microautoradiography, laser ablation-

inductively coupled plasma–mass spectrometry (LA-ICP-MS), ion beam analysis (IBA) and synchrotron-based X-ray fluorescence (XRF). These techniques have been covered in detail in a recently published review paper, along with their respective applications, strengths and limitations [182]. Another powerful technique not listed in the review is the transmission electron microscopy (TEM) combined with energy dispersive X-ray spectroscopy (EDS), applied in materials science and nanotechnology to obtain both structural and chemical information of a sample at the nanometre scale. In EDS, an X-ray detector is used to measure the energy of X-rays emitted from the sample when it is bombarded with high-energy electrons. As each element has characteristic X-ray emission energies, by analysing the energy spectrum of the emitted X-rays, it is possible to identify the elements present in the sample and quantify their concentrations. TEM provides detailed structural information, including information about the size and morphology of the sample at very high spatial resolution.

All the techniques mentioned above are potentially very useful when investigating the subcellular distribution of chelated or nanoparticle-bound radionuclides. On the other hand, the localisation of unchelated radionuclides, such as $[^{201}Tl]Tl^+$, $[^{99m}Tc]TcO_4^-$, $[^{123}I]I^-$ and $[^{18}F]BF_4^-$ presents a considerably greater challenge because these radionuclides cannot be 'trapped' within the cell by fixation and instead diffuse freely in accordance with their concentration gradients [12,140]. In such cases, it is crucial not only to find the most appropriate analytical technique, but also the right method of sample preparation and results interpretation. Another challenge posed by thallium (I) ions is the absence of a chemical approach for creating a conjugate [99] with an antibody or a fluorescent label. This limitation makes certain available techniques unsuitable for the purpose of defining subcellular localisation of unbound thallium (I).

In chapter 2, radioactive thallium (I) chloride ($[^{201}Tl]TlCl$) demonstrated significant radiotoxic potential, outperforming other AE-emitters, such as ^{67}Ga or ^{111}In. However, in chapter 3, when $^{201}Tl^+$ is bound to Prussian blue nanoparticles coated with citric acid (^{201}Tl-caPBNPs), it showed only minimal radiotoxicity, even though it delivers an equivalent activity per cell. This observation has led to a hypothesis that $^{201}Tl^+$ bound to caPBNPs is prevented from reaching a specific subcellular compartment necessary to manifest its full radiotoxic potential.

4.2 Aims

The main objective of this research was to identify the specific subcellular localisation of unbound thallium (I), which demonstrated to have significant radiotoxicity in chapter 2. Various techniques, such as cell fractionation, LA-ICP-MS, IBA, SIMS and TEM/EDS were explored to achieve this goal due to the challenge posed by the ability of Tl^+ to diffuse during sample preparation and its distribution depending on the gradients of intracellular and extracellular concentrations.

In addition, this chapter investigates the subcellular localisation of Prussian blue nanoparticles (PBNPs) coated with citric acid and chitosan by TEM, TEM/EDS, IBA and fluorescent microscopy. The aim was to establish a connection between the subcellular distribution and the observed comparative radiotoxic effects of ^{201}Tl when unbound or bound to PBNPs. Furthermore, this chapter explores whether modifying the nanoparticle shell to target a particular subcellular compartment, namely the nucleus, has any influence on its final localisation.

4.3 Materials and methods

Cell culture consumables and chemicals, unless specified, were purchased from Sigma-Aldrich, UK. Various cell types were employed in the experiments based on their availability and suitability for a specific method used.

4.3.1 Cell culture: Human prostate carcer cells DU145 (ATCC® HTB-81™), human lung cancer cells A549 (ATCC® CCL-185™) and human ovarian cancer cells SKOV3 (ATCC® HTB-77™) were cultured in RPMI-1640 medium, supplemented with 10% fetal bovine serum, 5% L-glutamine, penicillin (100 units) and 100 µg/mL streptomycin. Cultured cells were trypsinised and seeded 16 hours before each experiment and grown at 37°C in a humidified 5% CO_2 atmosphere. Bromodeoxyuridine (5-bromo-2'-deoxyuridine, BrdU) in aqueous solution 5 mg/500 µL (Biolegend) was diluted 30-fold with medium and 100 µL of the solution was added to 10 mL of medium (10 µM final concentration). SKOV cells and DU145 cells were incubated with the medium supplemented with BrdU for the total of 3 days, with medium changed every 12 h [183]. All cell lines were tested for the presence of Mycoplasma at least monthly (PCR test, Eurofins).

4.3.2 Cell viability and clonogenic survival assessment after incubation with TlCl: 50 µL of 400 - 2000 mg/L of TlCl was added to A549 cells in 200 µL medium. For the viability assessment, the incubation solution was removed after 1.5 h, cells were washed twice with PBS, trypsinised, stained with Trypan blue and viable and non-viable cells were counted manually using a haemacytometer. Cell viability was determined by calculating the percentage of viable cells in relation to the total number of cells. For the clonogenic survival experiment, the incubation solution was removed after 1.5 h, cells were washed thrice with PBS, trypsinised, re-suspended in fresh medium, seeded at 1,000 cells/well in a 6-well plate and cultured for 7-8 days, changing medium every 2-3 days. Colonies were fixed and stained with 0.05% crystal violet in 50% methanol and counted manually, defining colonies as containing more than 50 cells.

4.3.3 Subcellular fractionation: A549 cells were seeded at 100,000 cells per well in 24-well plates 16 h before the experiment. The fractionation method described previously [184] was used with some modifications (Fig. 4.1). In brief, fifteen minutes before the experiment, medium in each well was replaced by 200 µL fresh medium. [^{201}Tl]TlCl was diluted with PBS to the activity concentration of 1 MBq/mL and 50 µL was added to each well. After 16 h of incubation at 37°C in a humidified 5% CO_2 atmosphere, the 24-well plates were put on ice, the radioactive medium was collected, and the adherent cells were briefly washed three times with 250 µL of cold PBS. The activity present in all PBS washes and the medium was measured by a gamma counter ('medium' fraction). Then, 250 µL of cold 200 mM sodium acetate solution and 500 mM sodium chloride (pH = 2.5) were added to each well, incubated with cells on ice for 10 min and then removed, combined with a subsequent wash of 250 µL of cold PBS, and measured as a fraction by the gamma counter ('membrane' fraction). Next, the cells were lysed with 250 µL of cold Nuclei EZ Lysis buffer on ice. After 2 h incubation, cells were transferred to eppendorf tubes, centrifuged for 5 min at 1,000 rpm and the supernatant was collected. The remaining pellet was resuspended in 250 µL of cold PBS, centrifuged, and again the supernatant was collected. This process was repeated, and the supernatants were combined.

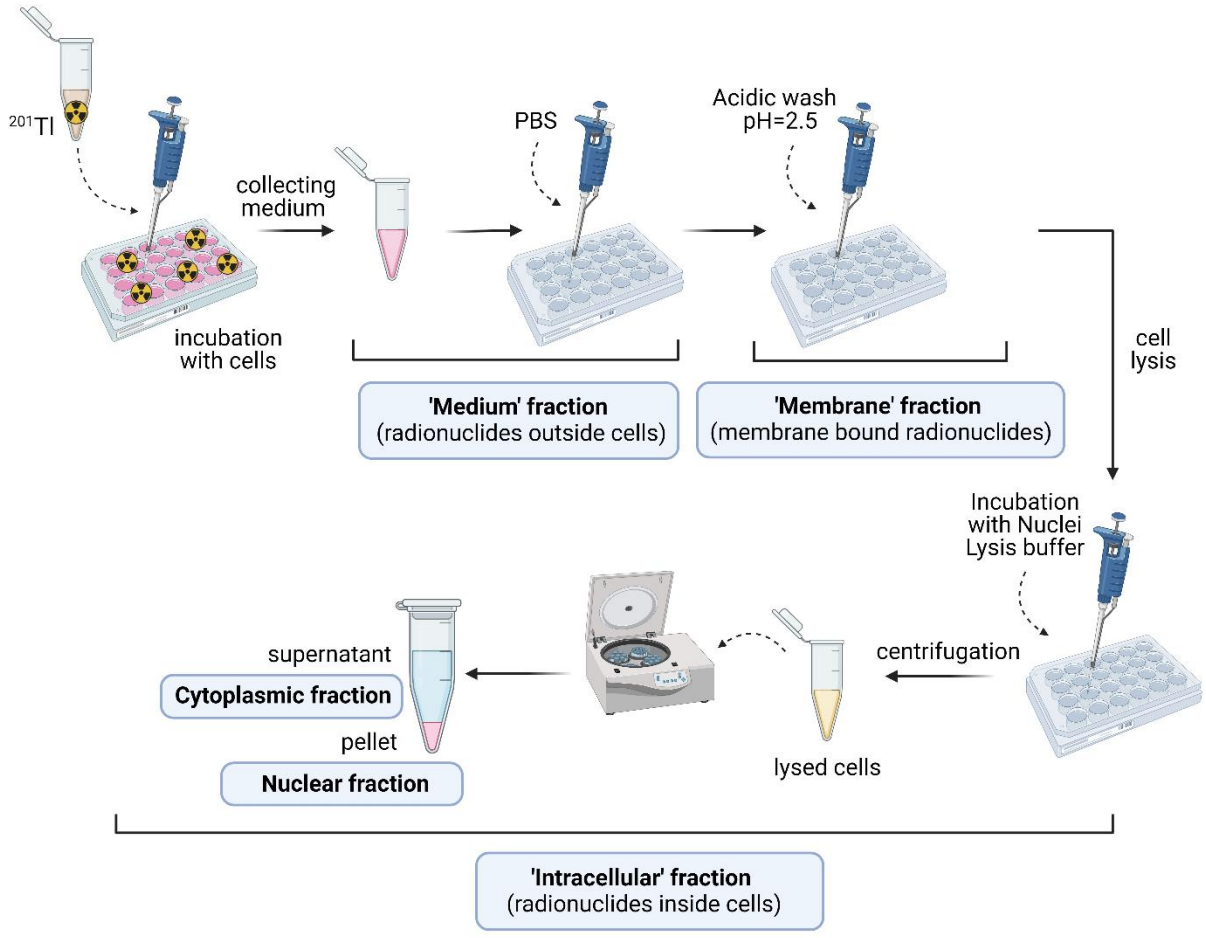

Figure 4.1 Subcellular fractionation workflow.

The activity present in the combined supernatant fractions (cytoplasmic fraction) and the activity present in the pellet (nuclear fraction) were quantified by a gamma counter (as counts per minute, CPM).

4.3.4 Laser ablation – inductively coupled plasma – mass spectrometry (LA-ICP-MS) was performed in collaboration with Charlie Beales, Dr Maral Amrahli, Dr Alexander Griffiths and Dr Theodora Stewart at the London Metallomics Facility, KCL. Whole cells sample preparation: 75,000 prostate cancer cells (DU145) were seeded 16 h before the experiment on cover glasses placed at the bottom of each well of a 24-well plate. Cells were incubated for 90 min with 50 µL of 1.5, 3.0 and 6.0 µmol/L solutions of non-radioactive TlCl in 0.9% NaCl and 200 µL of RPMI medium. In the negative control, cells were incubated with 50 µL of MilliQ water and 200 µL RPMI of medium. Then, the medium was removed, adhered cells were briefly washed once with 250 µL PBS and fixed with 99.9% methanol over 30 sec. The cover glasses with cells were transferred from the 24-well plate to microscope slides. Laser ablation and ICP-MS analysis was performed with a Teledyne Analyte Excite Laser with Thermo iCapTQ with 3 µm spatial resolution (6 different areas ablated per concentration, a field of minimum 5 cells) PerkinElmer NexION 350D Inductively Coupled Plasma-Mass Spectrometer. ImageJ was used to quantify ^{205}Tl signal in obtained images, which was measured as the average intensity of Tl signal assessed within the region of interests marked as single cells. The Tl signal threshold was set manually and was constant for all assessed areas within the same concentration. Preparation of cell sections: DU145 cells and DU145 cells pre-incubated with bromodeoxyuridine as described earlier were trypsinised, centrifuged and quantified using a haemacytometer. Then 3,000,000 cells in 200 µL PBS solution were incubated with 50 µL of 1.0, 5.0 and 10.0 µmol/L TlCl aqueous solution or MilliQ water (negative control) for 90 min. During this time, intermittent resuspension of cells by pipetting was carried out. Following the incubation, cells were resuspended in 400 µL of warm 18% gelatine solution (1.8 g of gelatine dissolved in 10 mL of PBS at 37°C), placed in a plastic mould and allowed to solidify at 4°C. No PBS washes were done after TlCl incubation to avoid thallium redistribution. A small piece of the gelatine was cut out, embedded in O.C.T. compound (Optimal Cutting Temperature compound, #361603E, VWR) and snap-frozen in cold isopentane cooled down with liquid nitrogen. 10 µm thick sections were cut using a cryostat (Cryostat SLEE MNT), placed on a microscope slide and stored at 4°C. Cell sections were stained with ProlongTM Gold Antifade Reagent with DAPI (Invitrogen) and imaged with a TCS SP5 confocal microscope with Leica software. LA-ICP-MS analysis was done by Teledyne Analyte Excite Laser with Thermo iCapTQ with 3 µm spatial resolution and PerkinElmer NexION 350D Inductively Coupled Plasma-Mass Spectrometer (optimised experiment settings: fluence 1.5 J/cm^2, dosage of 5, rep rate of 167 Hz). The workflow of the LA-ICP-MS method is presented in Figure 4.2.

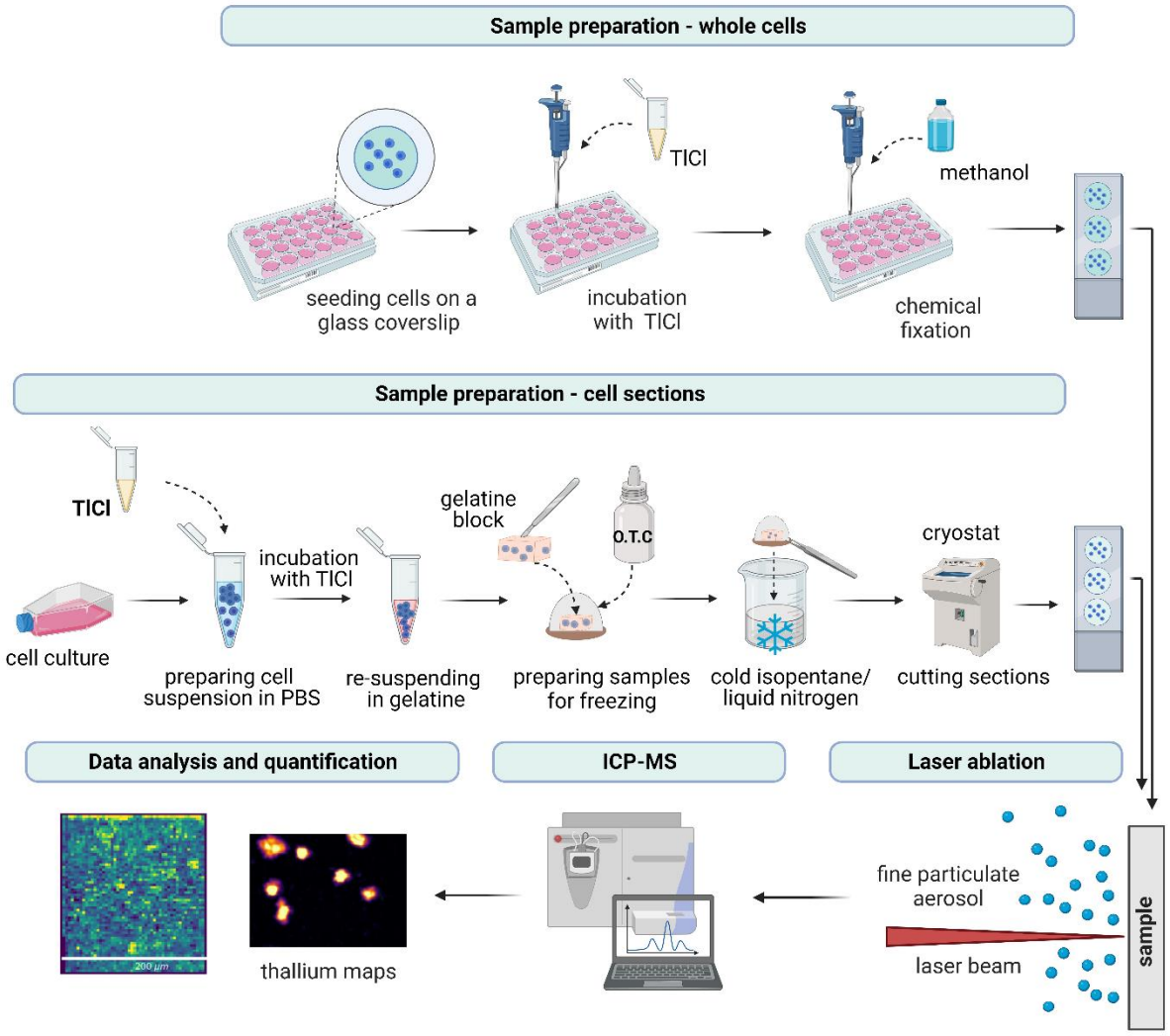

Figure 4.2 LA-ICP-MS method workflow.

4.3.5 Ion beam analysis (IBA) was performed at the UK National Ion Beam Centre, Guildford, in collaboration with Dr Catia Costa and Prof Melanie Bailey. Leica frame slides (11505190, Leica microsystems) were incubated with poly-L-lysine (50 µg/mL) for 1 h to improve the cells' adherence on the PET membrane. DU145 or SKOV3 cells were seeded at 200,000 cells per slide 16 hours before each experiment and grown at 37°C in a humidified 5% CO_2 atmosphere. CaPBNPs were synthesised and incubated with non-radioactive TlCl as described in chapter 3 and incubated with SKOV3 cells only. Shortly before the experiment, old medium was removed. 120 µL of TlCl aqueous solution (2000 mg/L, 8.3 mM) or Tl-caPBNPs (0.5 mg/mL) was added to 480 µL of medium, mixed, and added to cells grown on the PET membrane. For negative controls, 120 µL of MilliQ water was added instead of TlCl solution. After 90 min (or 180 min for incubation with Tl-caPBNPs), cells were placed at 4°C for 10 min, then incubation medium was removed, medium residue was dried with Whatman filter paper. Each Leica

slide was submerged in isopentane cooled with liquid nitrogen (-120°C) for 10 sec then immediately freeze-dried for 16 h (-40°C, <1 mPa). Slides were stored at 4°C until the analysis, when they were inserted in a vacuum chamber pumped to 10−6 mBar and irradiated using 2.5 MeV proton beam (current: 300-600 pA; terminal voltage: 1250 kV) produced by a 2 MV Tandem accelerator (High Voltage Engineering, Netherlands) at normal incidence with a spot size of approximately 1.5 x 1.5 µm. Elastically backscattered protons were detected using a PIPS charged particle detector with an active area of 150 mm^2 mounted at 25° exit angle (β). A silicon drifted detector (SDD) with an active area of 80 mm^2 was positioned at a central angle of 135° relative to the beam direction. The X-ray detector was fitted with a 130 µm beryllium foil. Both detectors were fitted with a sampling cone to stop backscattered and X-ray signals from the chamber from entering the detectors. To help locate cells in the beam chamber, before irradiation with the proton beam, cells were imaged with a light microscope (Nikon AZ100) and a copper finder grid (Agar Scientific, G2483) was secured with a kapton tape to the back of the Leica slide. Elemental PIXE maps and EBS maps were collected simultaneously for cells incubated with thallium and negative controls, alongside line scans and point measurements. Calibration was done using a BCR-126A lead glass standard. Data were acquired and analysed using OMDAQ-3 software (Oxford Microbeams, Ltd. UK). PIXE signal was normalised to EBS signal to eliminate the impact of cell thickness. Quantitative analysis was performed using ImageJ and Microsoft Excel 2016 software based on the obtained PIXE maps of single cells and line scans. Regions of interest (ROIs) corresponding to the cell cytoplasm and nucleus were delineated based on the light microscope images and PIXE maps. Subsequently, the area under thallium signal within these ROIs was calculated to quantify the relative concentration of thallium present in the cytoplasmic and nuclear areas. Thallium signal corresponding to the cytoplasm and nucleus was normalised by dividing it by the 'length' of the respective ROI. A total of 20 prostate cancer single cells (DU145) and 20 ovarian cancer single cells (SKOV3) were subjected to this quantification process. The workflow of the IBA method is presented in Figure 4.3.

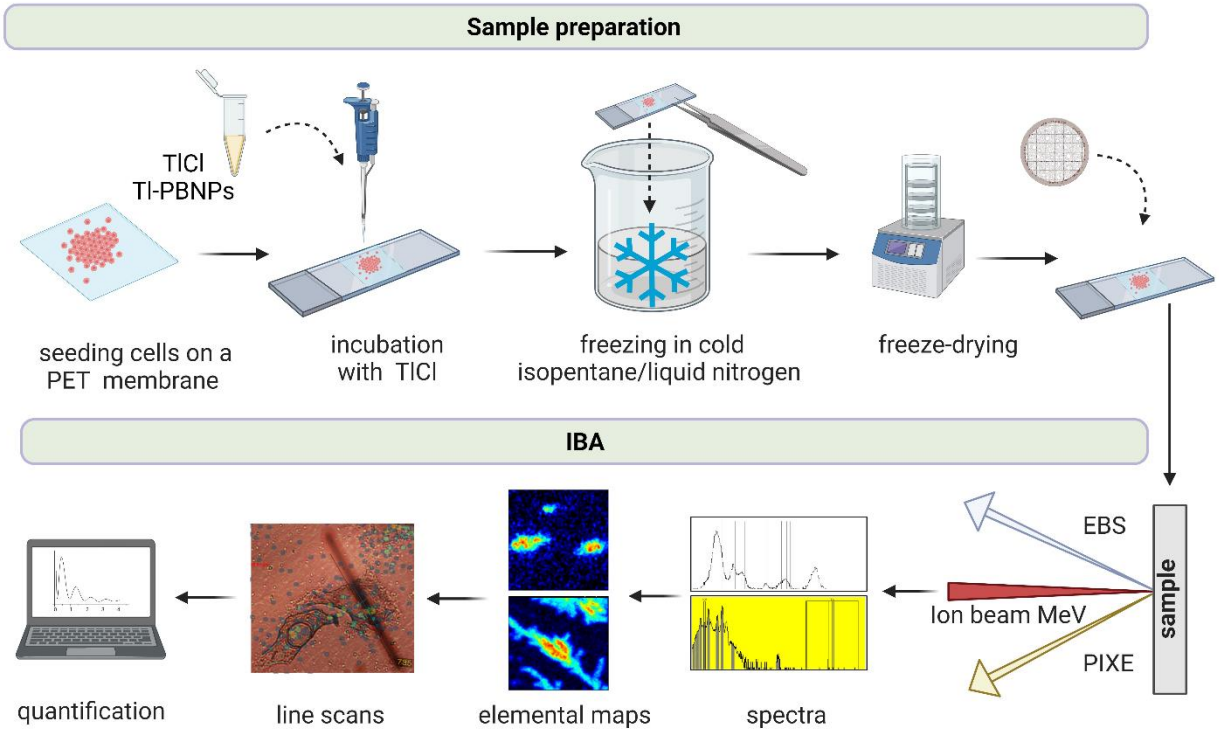

Figure 4.3 IBA method workflow.

4.3.6 Time-of-flight secondary ion mass spectrometry (ToF-SIMS) analysis was performed by Dr Catia Costa at the UK National Ion Beam Centre, Guildford, using a sample already imaged with the PIXE/EBS technique in order to investigate the suitability of the method for detecting unbound thallium (I) on the surface of cancer cells and secondly, to assess the compatibility of those two methods used one after another. Ion mass spectrometry analysis was carried out using an ION-TOF GmbH (Munster, Germany) TOF.SIMS.5 instrument. A 25 keV Bi^{3+} primary ion beam was operated delivering 1.0 µA of current with the high current bunched mode. The MacroRaster mode was employed, where the stage moves under the beam to provide a mosaic of the total area analysed. Images were acquired with 1 scan, 10 shot/pixel, 128 x 128 pixel resolution frames/patch, a maximum patch side length of 0.25 mm and a pixel density of 100 pixel/mm. Homogenates were imaged in triplicate s over 250 x 250 µm areas for peak intensity comparison and over a single large area (3 x 3 mm) for image comparison. All data were acquired in positive mode and with a 100 µs TOF cycle. All spectra and ion images were generated using SurfaceLab 6.5.

4.3.7 Transmission electron microscopy (TEM) analysis for caPBNPs and chPBNPs was done at the Advanced Bioimaging Facility in collaboration with Dr Saskia Bakker, University of Warwick via Seedcorn access. 250,000 cells per well in 24-well plates were seeded 16 h before the experiment. 15 min before the experiment, the medium in each well was replaced by 200 µL fresh medium and 50 µL of MilliQ water, caPBNPs, Tl-caPBNPs (concentration: 0.5 mg/mL), chPBNPs or Tl-chPBNPs (concentration: 0.25 mg/mL) was added into each well. After 3 h, the incubation medium was removed, then cells were washed twice with cold PBS, trypsinised, and moved to eppendorf tubes and centrifuged at 0.5 g for 5 min. Supernatant was removed and 800 µL of 2.5% EM grade glutaraldehyde solution (G015, TAAB) in PBS was added. After 1 h at RT, cells were centrifuged at 0.5 g for 5 min, re-suspended in 500 µL PBS and centrifuged again. This process was repeated twice. After stepwise dehydration in 25%, 50%, 75% and 100% acetone, cells were infiltrated with 50% resin for 1 h followed by 100% resin (Agar Scientific Low Viscosity Epoxy Resin) for 24 h. The resin was left at 60°C overnight and then ultrathin sections on an RMC ultramicrotome were cut and stained with 2% uranyl acetate. The samples were imaged in a JEOL JEM 2100 Plus with Gatan OneView CMOS camera.

4.3.8 Energy dispersive X-ray spectroscopy (EDS) combined with transmission electron microscopy (TEM) was performed at the Centre for Ultrastructural Imaging (CUI), KCL, in collaboration with Dr Pedro Machado and Alejandra Carbajal. Sample preparation: a carbon coated sapphire disc (Leica ACE 600, Leica Microsystems) was placed in each well of a 24-well plate and incubated with poly-L-lysine (50 µg/mL) for 30 min. 75,000 lung cancer cells (A549) were seeded 16 h before the experiment. 15 min before the experiment, the medium in each well was replaced by 200 µL fresh medium. For imaging unbound thallium (I), 50 µL of aqueous TlCl solution (2000 mg/L) was added to each well. In the negative control, 50 µL of MilliQ water was added to 200 µL of medium. For imaging thallium (I) bound to PBNPs, 50 µL of either caPBNPs, Tl-caPBNPs (concentration: 0.5 mg/mL), chPBNPs or Tl-chPBNPs (concentration: 0.25 mg/mL) was added into each well. Synthesis of caPBNPs and chPBNPs, and their incubation with non-radioactive thallium (I) chloride, are described in detail in the Methods section in chapter 3. After 3 h incubation time, medium was removed, the sapphires were high-pressure frozen using a Leica EM ICE and subsequently freeze substituted (Leica AFS 2, Leica Microsystems) with 0.2% uranyl acetate in dry acetone, and finally embedded into Lowicryl HM20. Thin sections were cut using an ultramicrotome (UC7, Leica Microsystems) and collected on carbon support film GS 2x1 copper grids (TAAB Laboratories Equipment Ltd., UK). All experiments were performed on a JEOL JEM F200 operated at 200 kV, using a standard TEM holder. The holder was tilted 19° towards the Ultim Max EDS detector (Oxford Instruments). The EDS datasets were analysed using AZtec version 6.1. For determining the concentration of elements present in the samples, QuantMaps

were generated for the quantitative analysis. Comparative spectra were collected at selected regions for analysing the differences between regions with and without nanoparticles. The amount of thallium within PBNPs was expressed as the percentage of total weight (wt%) and the average was calculated based on the data obtained from 10 energy spectra of the regions containing Tl-PBNPs and cytoplasmic regions without visible nanoparticles in various cells and distant locations. EDS maps and TEM overlays were generated to visualise the elemental distribution across different imaging sites. The workflow of the EDS/TEM method is presented in Figure 4.4.

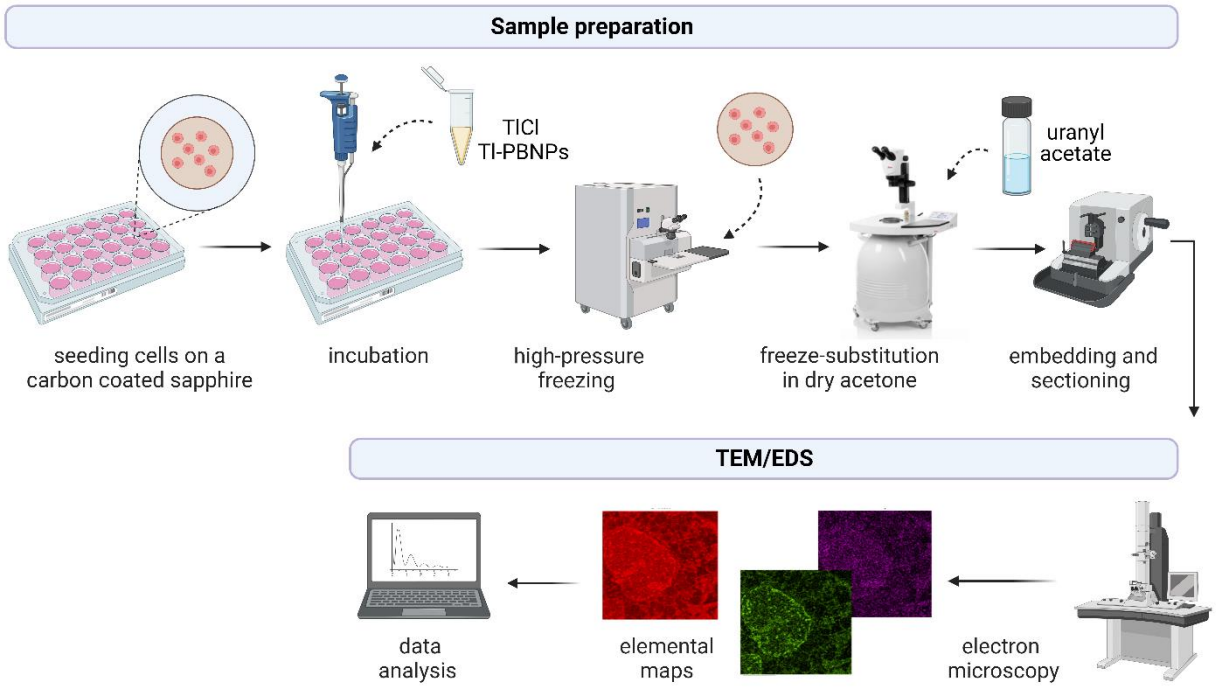

Figure 4.4 EDS/TEM method workflow.

4.3.9 Targeting Prussian blue nanoparticles to the nucleus

Changing the size of citric acid coated Prussian blue nanoparticles (caPBNPs): the synthesis of caPBNPs is described in chapter 3. Modifications to the synthetic method were made by varying the amount of citric acid added to $FeCl_3$ aqueous solution or $K_4[Fe(CN)_6]$ aqueous solution, increasing the molar concentration of $FeCl_3$ solution or increasing the molar concentration of $K_4[Fe(CN)_6]$ solution (Table 4.1). The size of synthesised caPBNPs was assessed by dynamic light scattering (DLS) as described in chapter 3. To synthesise caPBNPs-TAT, 0.01 mmol of EDC (1-(3-dimethylaminopropyl)-3-ethylcarbodiimide hydrochloride) and 0.015 mmol of sulfo-NHS (N-hydroxysulfosuccinimide) were dissolved in 200 µL of MilliQ water, added to 3 mL of 0.5 mg/mL caPBNPs suspension in water, and the mixture was stirred for 30 min at RT. After the reaction, the mixture was moved to Amicon® ultra

centrifugal filters (30,000 MWCO) and centrifuged at 5,000 rpm for 3 min. The nanoparticles were resuspended in 3 mL of HEPES buffer solution (pH = 8.2). Then, 0.001 mmol of TAT peptide (HIV-1 TAT (47-57), AnaSpec) dissolved in 200 µL of MilliQ water was added and the mixture was stirred for 3 h at RT. The product was purified by ultrafiltration using Amicon® ultra centrifugal filters (30,000 MWCO) at 4,000 rpm for 5 min and washed 3 times with MilliQ water. Synthesis of modified chitosan coated Prussian blue nanoparticles with carboxyfluorescein (chPBNPs-CF), chitosan coated Prussian blue nanoparticles with TAT peptide attached (chPBNPs-TAT) and chitosan coated Prussian blue nanoparticles with TAT peptide linked to 5-carboxyfluorescein (chPBNPs-TATFAM) was performed in collaboration with Dr Juan Pellico, KCL. ChPBNPs were synthesised and purified as described in the previous chapter. To synthesise chPBNPs-CF, 0.06 mmol of EDC and 0.065 mmol of sulfo-NHS were dissolved in 200 µL of MilliQ water. Then, 0.05 mmol of 6-carboxyfluorescein (Merck) dissolved in 100 µL of MilliQ water was added and the mixture was stirred at RT for 20 min. Afterwards, 500 µL of chPBNPs (2.5 mg/mL) were added into the reaction and the solution stirred for 16 h at RT. Finally, chPBNPs-CF were purified by ultrafiltration using Amicon® ultra centrifugal filters (30,000 MWCO) at 13,000 rpm for 3 min and washed 5 times with MilliQ water. To synthesise chPBNPs-TAT, 0.01 mmol of EDC and 0.015 mmol of sulfo-NHS were dissolved in 200 µL of MilliQ water. Then, 0.001 mmol of TAT peptide (HIV-1 TAT (47-57), AnaSpec) dissolved in 200 µL of MilliQ water was added and the mixture was stirred for 20 min at RT. Afterwards, 500 µL of chPBNPs (1 mg/mL) were added into the reaction and the solution stirred for 16 h at RT. Finally, chPBNPs-TAT were purified by ultrafiltration using Amicon® ultra centrifugal filters (30,000 MWCO) at 13000 rpm for 3 min and washed 5 times with MilliQ water. To synthesise chPBNPs-TATFAM**,** 0.01 mmol of EDC and 0.015 mmol of sulfo-NHS were dissolved in 200 µL of MilliQ water. Then, 0.001 mmol of [5-FAM]-TAT peptide (TAT (47-57) labelled with [5-FAM]-5-carboxyfluorescein (Insight Biotechnology Ltd) dissolved in 200 µL of MilliQ water was added and the mixture stirred for 20 min at RT. Afterwards, 500 µL of chPBNPs (1 mg/mL) were added into the reaction and the solution stirred for 16 h at RT. Finally, chPBNPs-TATFAM were purified by ultrafiltration using Amicon® ultra centrifugal filters (30,000 MWCO) at 13000 RPM for 3 min and washed 5 times with MilliQ water. The amount of TAT peptide and fluorescent tags (carboxyfluorescein and TAT peptide conjugated with carboxyfluorescein) incorporated was determined by thermogravimetric analysis (the method is described in detail in chapter 3). The zeta-potential and particle size of caPBNP-TAT were assessed with the DLS method described in chapter 3.

4.3.10 Assessing subcellular distribution of chPBNP-CF and chPBNPs-TATFAM by fluorescent microscopy: A549 cells were seeded on coverslips coated with poly-L-lysine (50 µg/mL) placed in a 24-well plate. Following a 3 h incubation with 50 µL of chPBNP-CF, chPBNPs-TATFAM and fluorescent controls (non-conjugated [5-FAM]-TAT peptide and 6-carboxyfluorescein), medium was removed, coverslips were washed twice with PBS, fixed with 3.7% paraformaldehyde in PBS, treated for 5 min with 0.5% Triton X-100®/ 0.5% IGEPAL CA-630® solution and washed again with PBS. Cells were stained and mounted with ProlongTM Gold Antifade Reagent with DAPI (Invitrogen). A TCS SP5 confocal microscope with Leica software was used to obtain fluorescent and bright field images. Serial z-stack images (z-step: 1.0 µm, number of steps: 10) were taken for each field of view, with a minimum of 15 cells per image. Quantification of the fluorescent signal was based on a previously published method [185]. CellProfiler was used to quantify the total fluorescent signal per cell and the fluorescent signal in the nucleus per cell using the maximum intensity projection of z-stacks of both nucleus and carboxyfluorescein channels obtained using ImageJ. The workflow for the fluorescent microscopy method is presented in Figure 4.5.

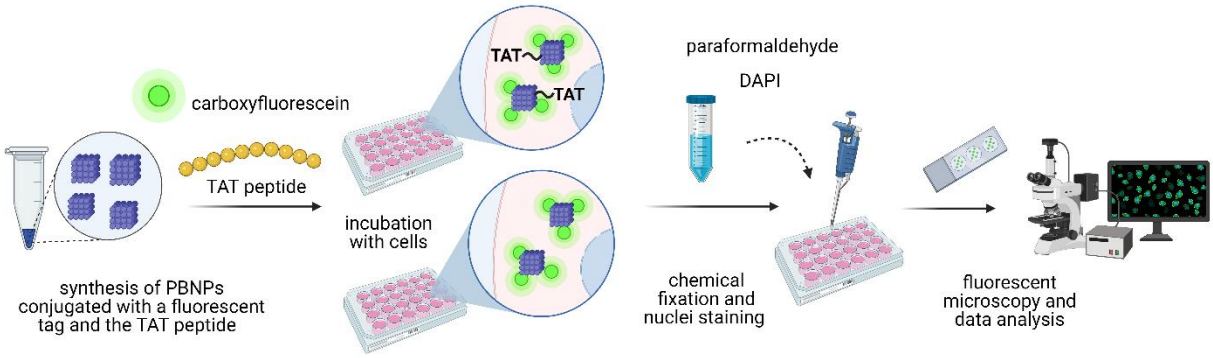

Figure 4.5 Fluorescent microscopy workflow.

4.3.11 Data analysis: Data were analysed in Excel Microsoft 2016 and GraphPad Prism 9.1.0/10.0.2, and expressed as mean ± SD. Graphs and figures were created with GraphPad Prism 10 and BioRender.com.

4.4 Results

Assessing the subcellular distribution of unbound Tl^+

4.4.1 Subcellular fractionation of unbound $^{201}Tl^+$

Subcellular fractionation is one of the most common laboratory techniques used to separate different cellular organelles and structures based on their size, density, and other physical properties. In general, a radionuclide that does not enter cells or is not attached to the cell membrane is typically found in the 'medium' fraction. Radionuclides that bind to the cell membrane make up the 'membrane' fraction. When radionuclides are located within the cell, they form the 'intracellular' fraction, which can be further divided into the 'nuclear' and 'cytoplasmic' fractions. This method was first performed on lung cancer cells (A549) incubated with $^{201}Tl^+$ in parallel to cells incubated with nanotexaphyrins (described in chapter 5); this experiment served as a control measure for assessing subcellular distribution of nanoparticles. The subcellular localisation of ^{201}Tl is presented in Figure 4.6.

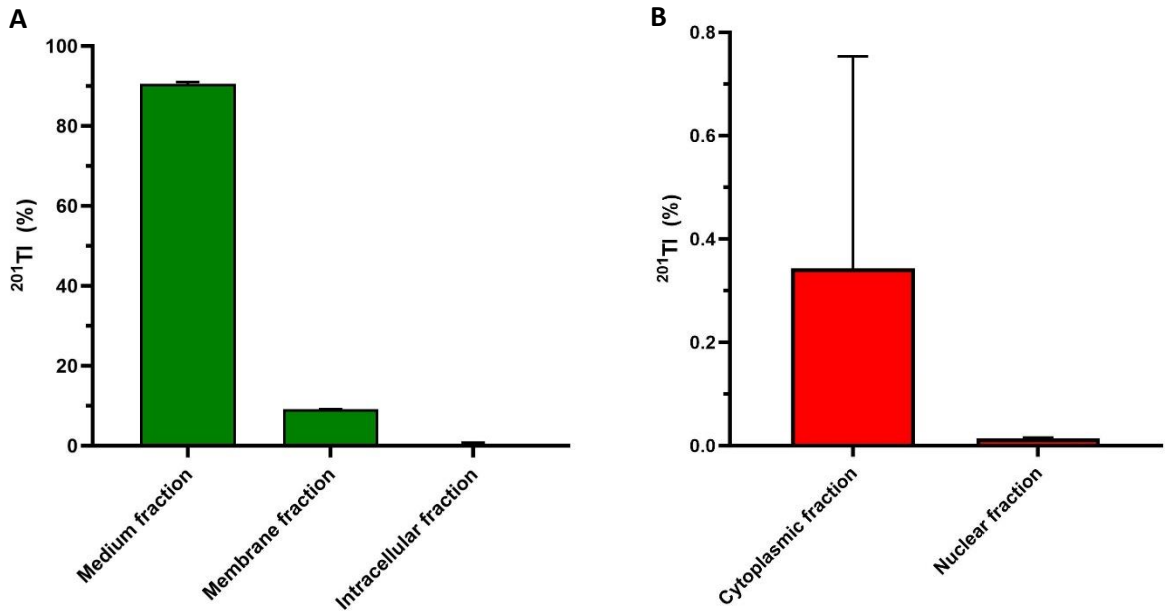

Figure 4.6 Results of $^{201}Tl^+$ subcellular fractionation. A) Distribution of $^{201}Tl^+$ (expressed as percentage of total activity) in 'medium' fraction (^{201}Tl outside the cell), 'membrane' fraction (^{201}Tl is bound to the cell membrane) and 'intracellular' fraction (^{201}Tl inside the cell). **B)** Distribution of ^{201}Tl in the 'cytoplasmic' and 'nuclear' fractions. Cells were initially incubated with [^{201}Tl]TlCl for 16 h, average uptake of $^{201}Tl^+$ after 16 h was 9.46 ± 0.33%, 100,000 cells seeded per well, 50 kBq per well, A549 cells, n=3.

Most of the activity was found in the 'medium' fraction (90.5 ± 0.4%), which consisted of 84.7 ± 2.1% activity found in the collected medium and 5.8 ± 1.7% found in three subsequent PBS washes. 9.1 ± 0.2% of the total activity was present in the 'membrane' fraction. Lastly, a minimal amount of activity was found in the intracellular fraction (0.36 ± 0.41%), which includes 0.014 ± 0.002% activity present

in the nucleus and 0.343 ± 0.410% present in the cytoplasm. In contrast, [^{201}Tl]TlCl cellular uptake performed in parallel to the fractionation experiment measured as described in chapter 2, was on average 9.46 ± 0.33%. These results demonstrated that thallium rapidly diffuses out of cells during each change of incubating solution. Furthermore, it becomes evident that the longer cells are kept in a fresh solution during the procedure or the more they are washed, the lower the thallium content remaining inside the cells.

4.4.2 Laser ablation - inductively coupled plasma - mass spectrometry (LA-ICP-MS) of unbound Tl^+

LA-ICP-MS enables spatial elemental mapping and quantification in biological samples with a very high sensitivity. This technique was employed to establish thallium (I) subcellular distribution in fixed single prostate cancer cells (DU145) growing in various areas of the well (6 to 7 different areas per concentration) after 90 min incubation with three different concentrations of aqueous TlCl solution (1.5, 3.0 and 6.0 µmol/L) added to the medium. Examples of light microscopy images of DU145 cells incubated with TlCl, ^{205}Tl maps and ^{205}Tl maps co-localised with the light microscopy image are shown in Figure 4.7.

Presented images show thallium signal (as ^{205}Tl) located inside cancer cells and co-localised with ^{31}P signal (Fig. 4.7 C). While it was evident that thallium was present inside cells and not in the media/background, drawing conclusions about the subcellular distribution of thallium proved challenging, primarily due to the limited spatial resolution of the technique and uncertainties regarding the precise location of the nucleus.

Thallium signal associated with individual cells was used to assess the distribution of thallium (I) among cells in various cell populations. Quantification of ^{205}Tl signal in DU145 cells relied on the signal intensity, measured as the average intensity of the signal per cell detected within the cell boundries. The analysis involved evaluating the corrected total signal by substracting the background signal, which was then used for comparing signal intensity between individual cells and cells populations.

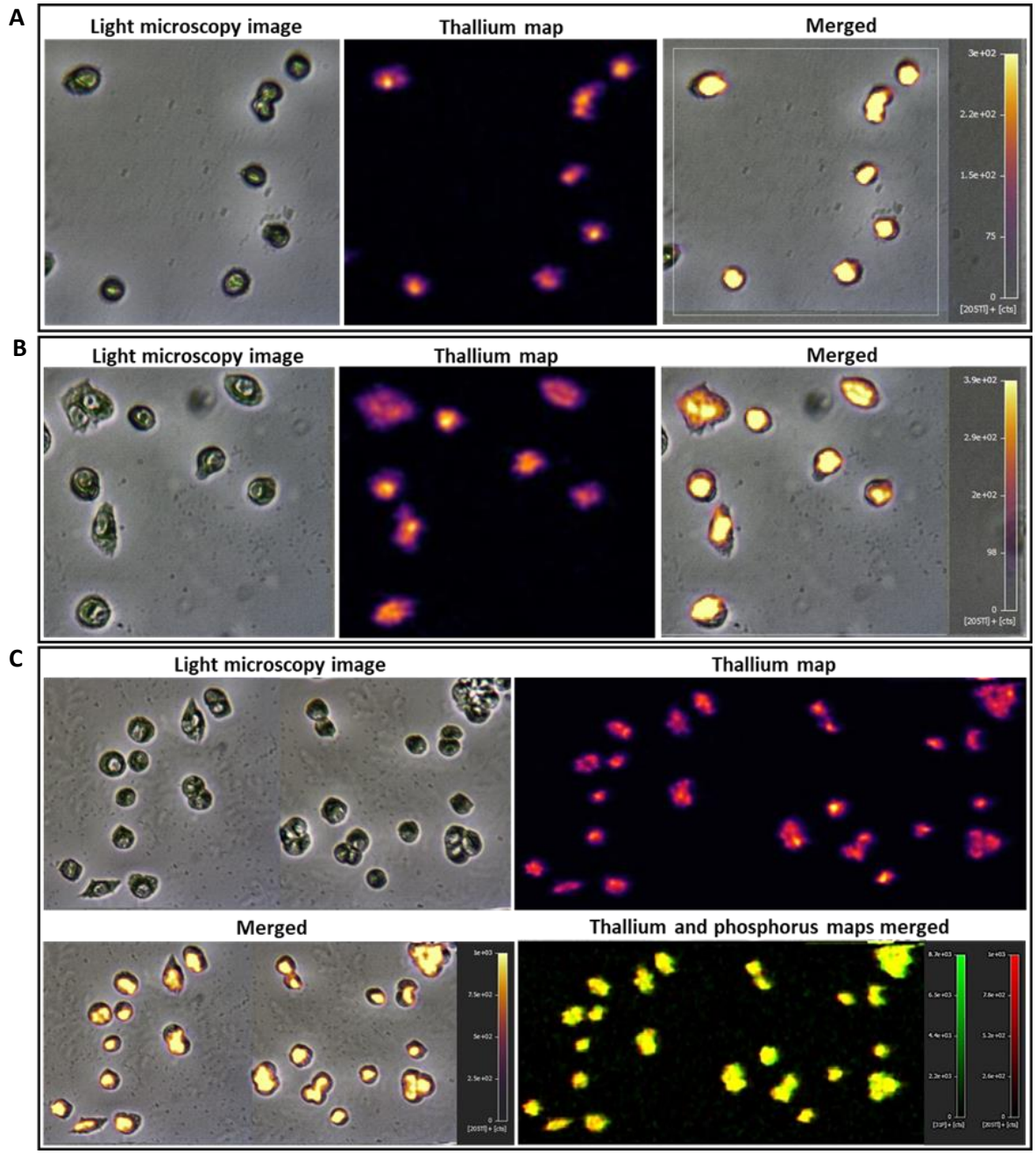

Figure 4.7 LA-ICP-MS analysis of unbound Tl^+ in whole cells. LA-ICP-MS analysis in three different samples (A, B and C) presenting a light microscopy image, thallium map, a merged image of the microscope picture with the thallium signal and a merge image of thallium (red) and phosphorus (green) signal in the third sample. Experiments were performed on prostate cancer cells (DU145) incubated for 90 min in media with **A)** 1.5 µmol/L, **B)** 3.0 µmol/L and **C)** 6.0 µmol/L of TlCl added. On thallium maps and merged images 95th percentile threshold has been applied.

An increase in thallium signal intensity was observed among cells exposed to rising concentrations of TlCl from the average of 383 ± 62 when cells were exposed to 1.5 µmol/L TlCl to 1238 ± 208 for cells incubated with 6.0 µmol/L TlCl (Fig. 4.8 A). Variations were also detected in cells growing in different

regions within the incubation well but exposed to the same concentration of TlCl; however, the range between the minimum and maximum values did not exceed a threefold difference (Fig. 4.8 B). The highest variance in thallium distribution among individual cells was noted in cells growing in the same area and incubated with 6.0 µmol/L TlCl.

A

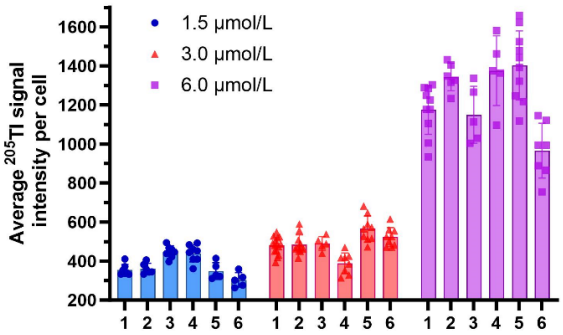

B

Average ^{205}Tl signal intensity per cell	Concentration of TlCl added to medium		
	1.5 µmol/L	3.0 µmol/L	6.0 µmol/L
Mean ± SD	383 ± 62	489 ± 70	1238 ± 208
Min value	263	315	754
Max value	494	682	1660

Figure 4.8 LA-ICP-MS quantification. A) ^{205}Tl signal expressed as the average intensity of ^{205}Tl signal per cell, based on ImageJ quantification of ^{205}Tl signal intensity in DU145 cells after 90 min incubation with 1.5 µM, 3.0 µM and 6.0 µM of TlCl in RPMI medium. Six different areas were ablated per concentration (1-6) and each area contained between 5 and 15 cells. Bars symbolise the average Tl intensity per area. Data are presented as mean ± SD, with single points representing results for individual cells. **B)** A table summarising the average (± SD) intensity of Tl signal per cell with minimum and maximum values of ^{205}Tl signal in DU145 cells incubated with 1.5 µM, 3.0 µM and 6.0 µM of TlCl in RPMI medium.

With the aim to gain a deeper insight into the distribution of thallium within individual cells, the sample preparation method was modified to ablate thin cell sections (10 µm) instead of ablating whole cells. In this modified approach, following a 90 min incubation with thallium (I) chloride, cells were resuspended in gelatine without removing the thallium chloride solution. This step was designed to avoid thallium displacement from its original location. Subsequently, the cell sections were obtained and initially stained with DAPI solution to mark the nucleus location. The quality of prepared samples was assessed using a fluorescent confocal microscope (Fig. 4.9).

The majority of the 10 µm cell sections displayed a nucleus that was stained blue and visible under the confocal microscope; however, there were instances where certain cells did not exhibit this staining. This observation proved that the presence of a nucleus cannot be assumed in every cell section. Furthermore, sections lacking a nucleus could be employed to assess the quantity of thallium in the cell cytoplasm without the potential interference from the nucleus.

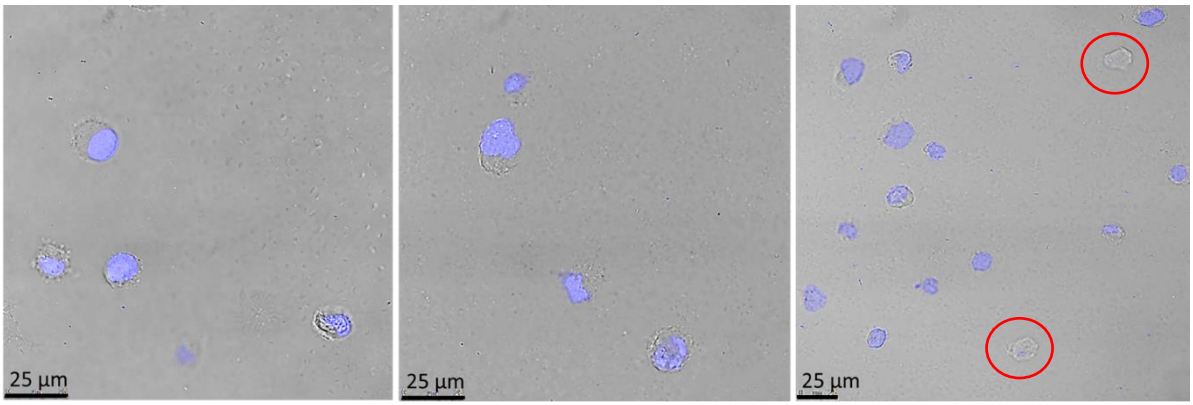

Figure 4.9 Light microscope images of cell sections stained with DAPI. Examples of DU145 cell 10 µm sections stained with DAPI and imaged with a fluorescent confocal microscope. DAPI stain was used to define the location of a cell nucleus. Cells without stained nucleus (i.e. where the section did not include nucleus) are marked in red. Scale bar – 25 µm.

LA-ICP-MS analysis was performed on various cell samples, including cells incubated with three different concentrations of TlCl, cells pre-incubated with bromodeoxyuridine (BrdU) followed by TlCl incubation, and negative control samples. Unfortunately, the bromine signal arising from BrdU interfered with the accurate measurement of the thallium signal, leading to the exclusion of cells incubated with BrdU from the assessment. Moreover, only cells incubated with 1 µmol/L TlCl solution added to the medium are presented, because higher concentrations in other samples resulted in signal saturation. Examples of these cells and negative controls are shown in Figure 4.10.

The LA-ICP-MS images revealed uneven distribution of the $^{205}Tl^{+}$ signal within the gelatine matrix. In some instances, concentration of the thallium signal was observable within the cell sections. However, some cell sections did not show a detectable thallium signal. Due to the inability to accurately localise the cell nucleus within the ablated cell sections or to identify those lacking a nucleus, combined with the presence of elevated thallium concentrations in the gelatine matrix, this experiment did not yield conclusive results.

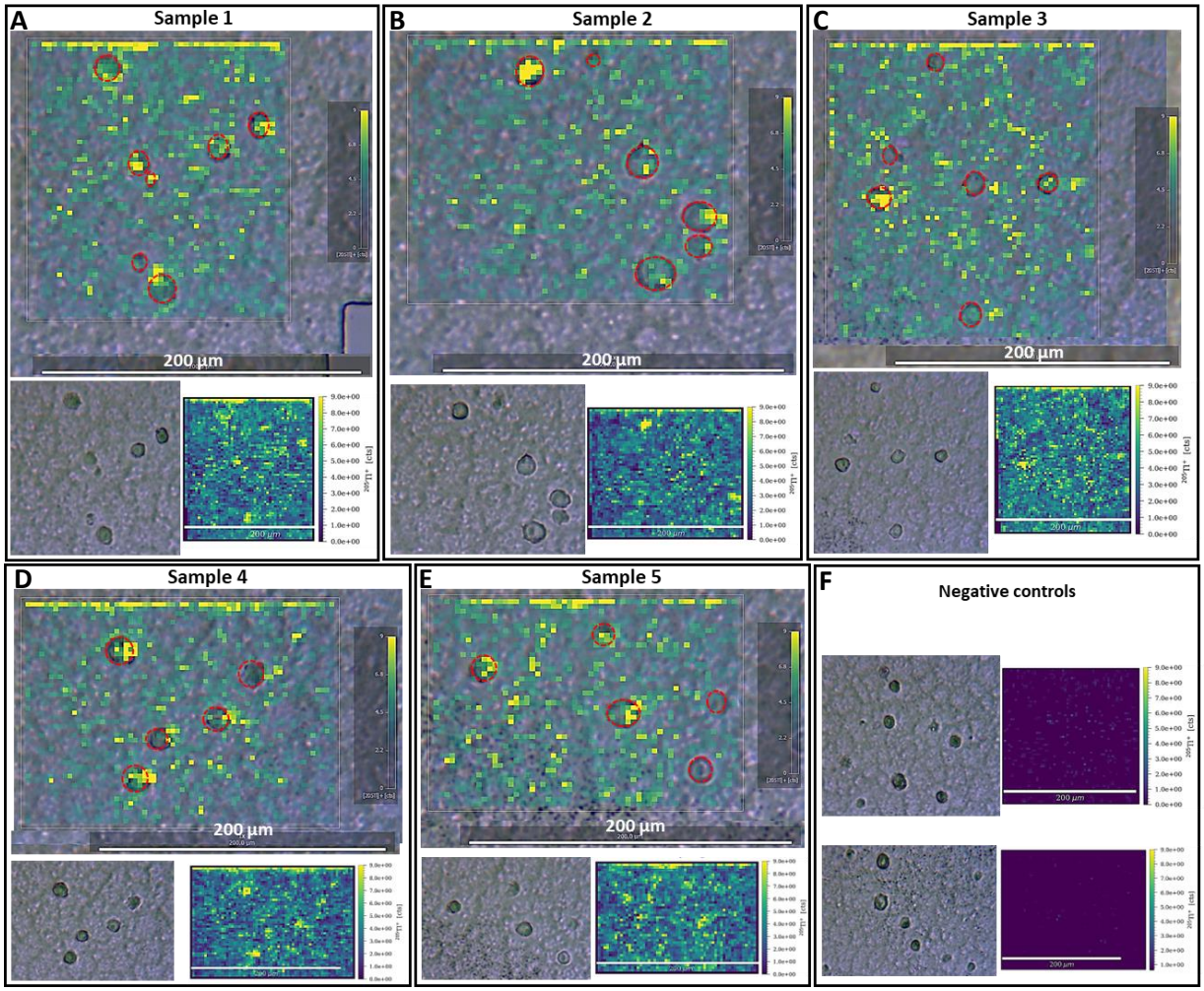

Figure 4.10 LA-ICP-MS analysis in cell sections. A), B), C), D), E) Samples 1 to 5 include a light microscope image, ^{205}Tl signal map and an overlay of a light microscope image with ^{205}Tl map. Thallium signal was measured in 10 µm sections of DU145 cells incubated with 1 µM of TlCl. Negative controls include a light microscope image and a ^{205}Tl map measured in 10 µm sections of DU145 cells incubated MilliQ water. Scale bar – 200 µm.

4.4.3 Energy dispersive X-ray spectroscopy (EDS) combined with transmission electron microscopy (TEM) of unbound Tl^+

EDS is an elemental spectroscopy technique, which is usually combined with electron microscopy. It captures and analyses the characteristic X-rays generated from the sample material and can precisely determine its elemental composition within a specific area of the cell captured with a high resolution. In the sample preparation method, cells were rapidly frozen in liquid nitrogen in order to allow instantaneous fixation of the cell and prevent any potential diffusion of thallium from its original location. The cells were also freeze-substituted with uranyl acetate in dry acetone to further preserve the sample and enhance contrast between different cellular components. Examples of EDS/TEM analysis of lung cancer cell (A549) sections are presented in Figure 4.11.

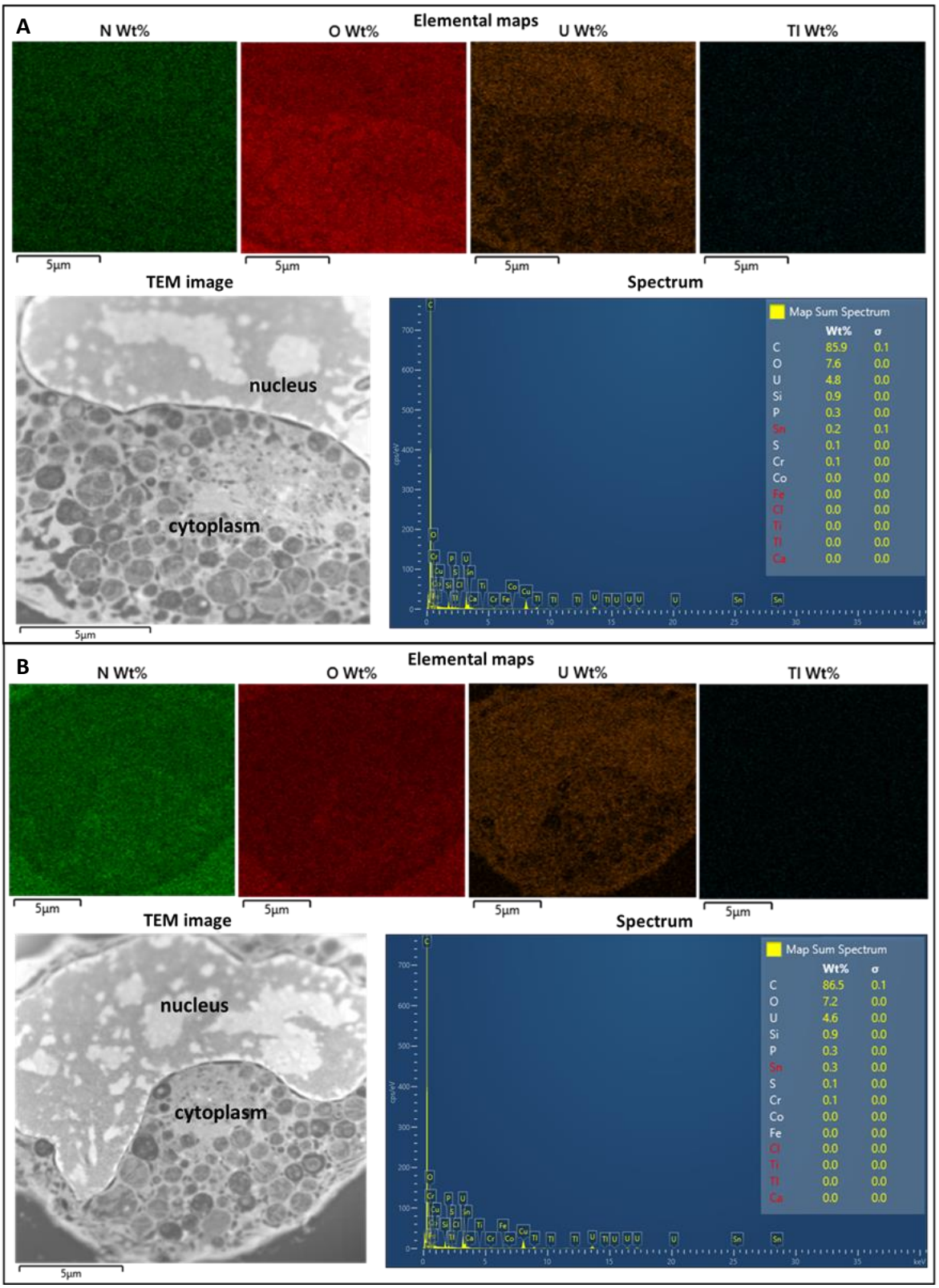

Figure 4.11 TEM/EDS analysis of Tl^+ in cell sections. Two examples of TEM/EDS analysis **A)** and **B)** showing elemental maps (from left to right) of nitrogen, oxygen, uranium and thallium (as weight percentage, wt%), a TEM image of a cell 10 µm section, and a spectrum map (cps/eV vs keV). EDS datasets were analysed using Aztec (Oxford Instruments). For determining the concentration of elements present in the samples, QuantMaps were generated for the quantitative analysis. Scale bar – 5 µm. Lung cancer cells (A549) were used in this experiment. Uranium present in the sample comes from the uranyl acetate solution used in the sample preparation.

Thallium signal was not detected in any cells in the samples analysed (n=11) and the amount of thallium quantified in the cell fragments did not exceed 0. Uranium present in the sample comes from the uranyl acetate solution. This experiment illustrated the inability to detect thallium inside cancer cells using EDS with the parameters applied, even when employing a high concentration of TlCl (400 mg/L).

4.4.4 Ion beam analysis (IBA) of unbound Tl^+

Ion beam analysis is a group of techniques that involves the detection of radiation emitted when a sample material is bombarded by an ion beam. Particle-induced X-ray emission (PIXE) and elastic backscattering spectrometry (EBS) were selected for examining the intracellular distribution of thallium in prostate and ovarian cancer cells. Over 80 individual cells were imaged with PIXE and EBS, including negative control samples (cells incubated in media with water added instead of TlCl), and approximately 50 line scans were conducted across these cells. Examples of the elemental distribution of phosphorus, sulfur, chlorine, potassium, bromine (when cells were pre-incubated with BrdU) and thallium, together with the overlay image of thallium signal and a microscope picture of the cells, are presented in Figure 4.12 and 4.13.

Light microscope pictures were used to identify the morphology of the cell and its nucleus. Across all the cells subjected to PIXE and EBS imaging, it was consistently observed that thallium signal was distributed across the cancer cells, visible in both the cytoplasm and the nucleus. A notable apparent tendency for thallium ions to accumulate within the nucleus was identified in the majority of cells. Additionally, co-localisation of thallium and sulfur was detected. Bromine signal was visible in cells pre-incubated with BrdU and localised within the cell nucleus but too weak to use it as a marker for the nucleus.

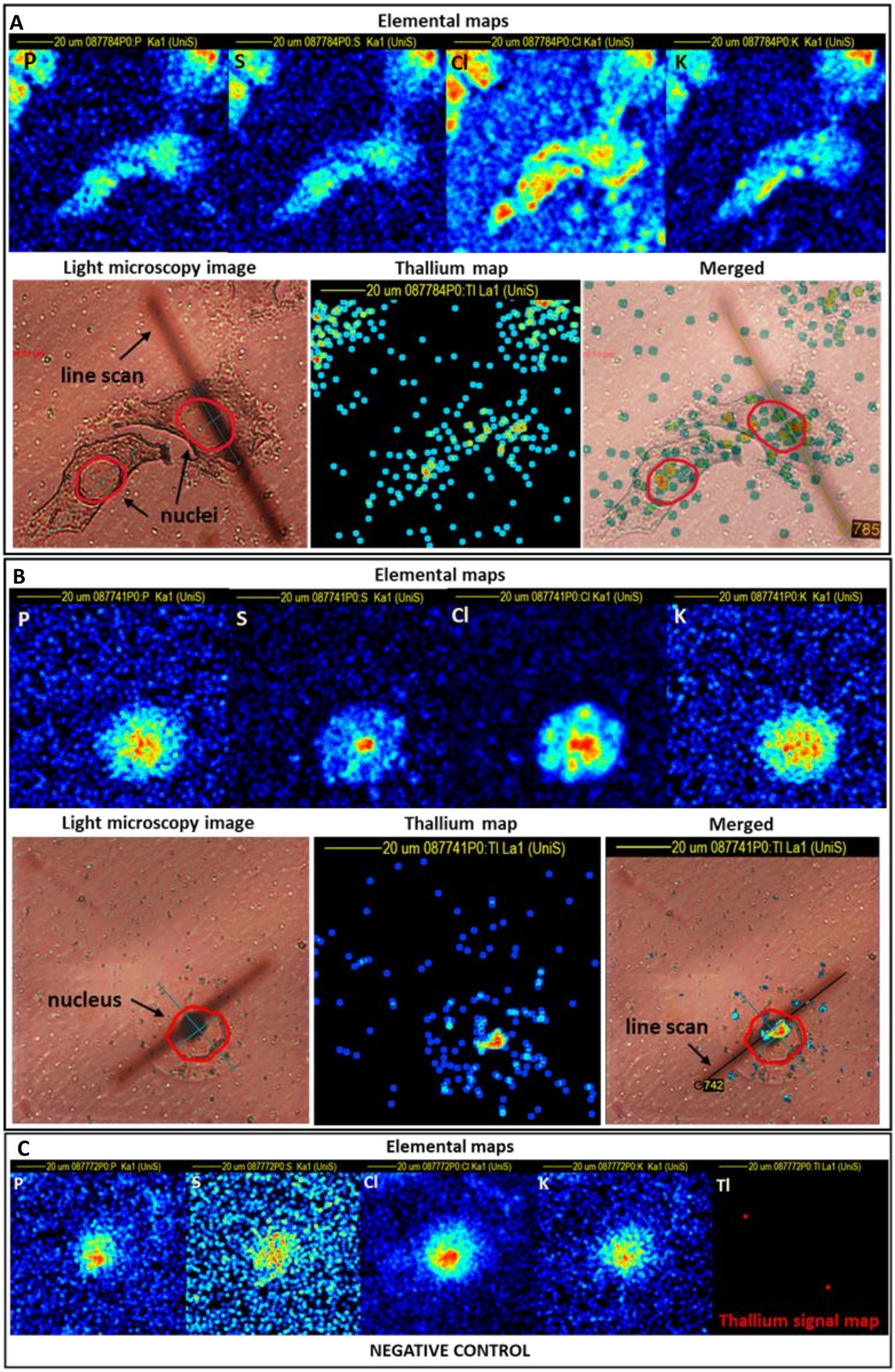

Figure 4.12 PIXE analysis of Tl^+ in prostate cancer cells. Two examples **A)** and **B)** of PIXE analysis in DU145 cells showing elemental maps of phosphorus, sulfur, chlorine and potassium (from left to right), a light microscope image, thallium signal map and an overlay of the microscope image with PIXE thallium signal. Cell nucleus is marked red. The line scan is visible on the microscope picture. **C)** PIXE analysis in DU145 cells without thallium (a negative control) showing elemental maps of phosphorus, sulfur, chlorine, potassium and thallium.

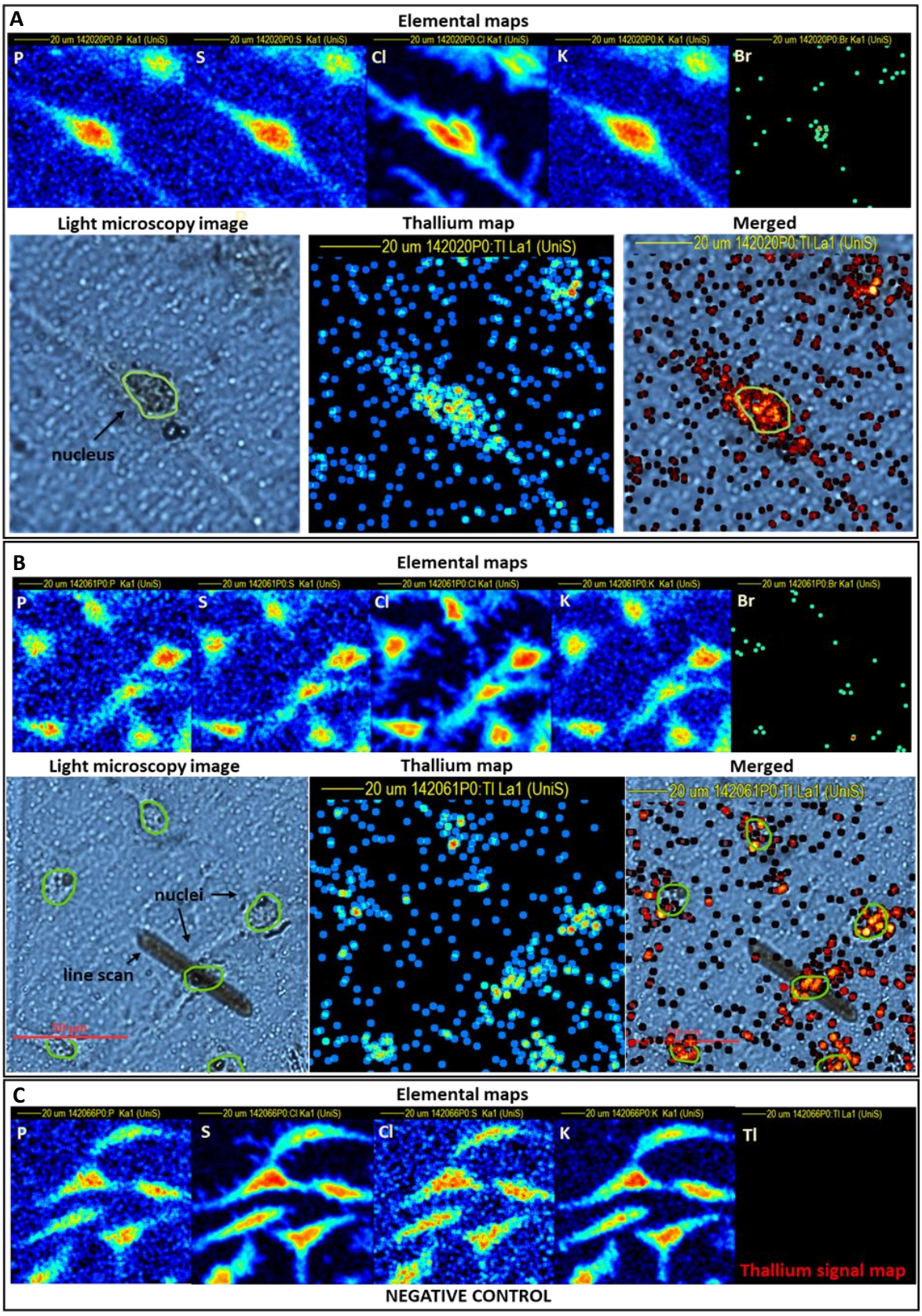

Figure 4.13 PIXE analysis of Tl^+ in ovarian cancer cells. Two examples **A)** and **B)** of PIXE analysis in SKOV3 cells showing elemental maps of phosphorus, sulfur, chlorine and potassium (from left to right), a light microscope image, thallium signal map and an overlay of the microscope image with PIXE thallium signal. Cell nucleus is marked in green. The line scan is visible on the microscope picture. **C)** PIXE analysis in DU145 cells without thallium (negative control) showing elemental maps of phosphorus, sulfur, chlorine, potassium and thallium (from left to right).

Quantification of the thallium signal was based on PIXE line scans going through individual cells, including the cytoplasmic and nuclear regions (Fig. 4.14). For DU145 cells, 20 line scans were performed, and a corresponding 20 line scans were done for SKOV3 cells, all of which were subjected to quantification. EBS technique is sensitive to changes in sample thickness, therefore, to eliminate the influence of cell thickness on the accumulation of elements, the thallium signal was standardised against the total EBS signal.

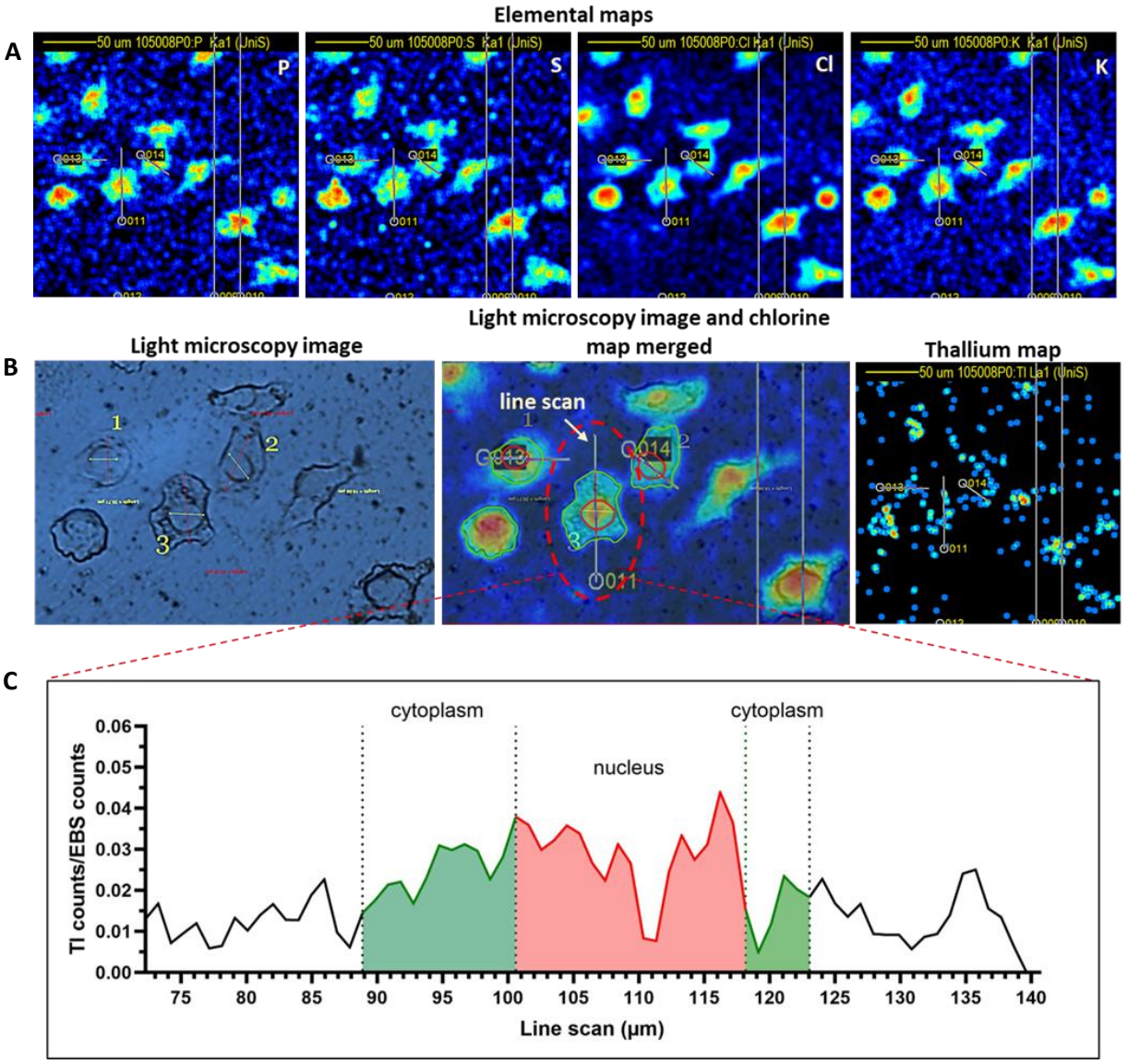

Figure 4.14 IBA quantification. A) Exemplar PIXE elemental maps showing phosphorus, sulfur, chlorine and potassium (from left to right) distribution in prostate cancer cells with marked line scans. **B)** A light microscope image, an overlay image of microscope picture and chlorine PIXE map with marked cell (green) and nucleus (red), and thallium distribution map (from left to right). **C)** Exemplar thallium PIXE signal line scan (normalised to EBS signal) with marked cytoplasmic and nuclear regions. Area under the curve was calculated for the related region (marked green for cytoplasm and red for the nucleus), divided by the length of the line scan and a ratio for the amount of thallium in the nucleus vs the amount of thallium in the cytoplasm calculated.

Calculated ratio of the amount of thallium present in the nucleus to the amount of thallium present in the cytoplasm was on average 1.81 ± 1.50 for DU145 cells and 1.82 ± 1.03 for SKOV3 cells. This confirmed the visual observation of thallium preferential accumulation in the cell nucleus in both types of cells.

The results demonstrated that IBA is effective in detecting unbound thallium at the subcellular level in individual cancer cells. This method also facilitates quantification, leading to conclusions regarding the ratio of thallium present in the cytoplasm and the nucleus.

4.4.5 Secondary ion mass spectrometry (SIMS) of unbound Tl^+

Time-of-flight secondary ion mass spectrometry (ToF-SIMS) is a powerful analytical technique for evaluating the elemental and molecular composition of solid surfaces and thin films. The sample is bombarded with a pulsed primary ion beam and the ejected secondary ions are analysed by a mass spectrometer to determine the elemental, isotopic, or molecular composition of the surface. The distribution of the ions from the surface of the sample is represented by two-dimensional maps based on the particles that reach the detector. A freeze-dried sample containing individual prostate cancer cells (DU145) that had been incubated with TlCl for 90 min was initially scannd with PIXE/EDS to image the distribution of thallium, followed by the SIMS analysis. Results obtained from analysisng the cells with both methods combined are presented in Figure 4.15 A and B**.** While the subcellular distribution of potassium and chlorine could be visible using both techniques, thallium signal inside cells was only detected by PIXE/EDS. Neither of the stable isotopes of thallium - ^{203}Tl and ^{205}Tl - were detected on the cell surface in itensities above the background by the mass spectrometry. This result showed that, without further modifications, SIMS is not suitable for localising thallium on a subcellular level.

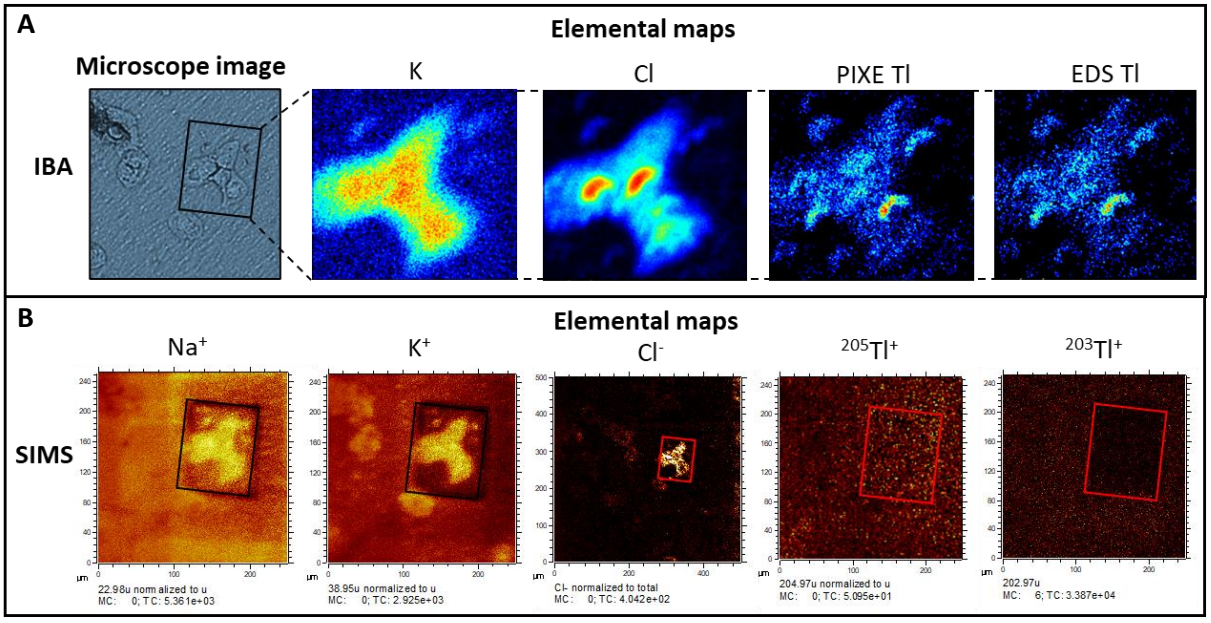

Figure 4.15 IBA and SIMS analysis of Tl^+ in the same sample. A) IBA analysis of a cluster of prostate cancer cells (DU145) showing light microscopy image, PIXE elemental maps of potassium, chlorine and thallium, and EDS elemental map of thallium (from left to right). **B)** SIMS analysis of the same cluster of lung cancer cells showing elemental maps of sodium, potassium, chlorine and ions with mass/charge ratio 204.97 ($^{205}Tl^+$) and 202.97($^{203}Tl^+$); from left to right. Thallium signal was not detected while analysing the surface of the sample. Black or red frame illustrates the IBA scanned area.

4.4.6 Cytotoxicity of non-radioactive TlCl in prostate cancer cells

The toxicity of a non-radioactive TlCl solution in RPMI medium, ranging from 80 to 400 mg/L as the final concentration, was evaluated in prostate cancer cells (DU145). This assessment involved a viability assay, a clonogenic survival assay, and the observation of cell morphology under a light microscope.

After incubating cells with various TlCl concentrations for 90 min, there were no apparent signs of toxicity observed. The majority of the cells remained adhered to the bottom of the incubation well, and there were no noticeable changes in their morphology. Cell viability was over 95% across all TlCl concentrations (Fig. 4.16 A). However, the clonogenic survival assay revealed a reduction in clonogenic survival when raising the concentration of TlCl in medium, decreasing to 67.7 ± 1.2% when cells were exposed to a 400 mg/L TlCl solution (Fig. 4.16 B).

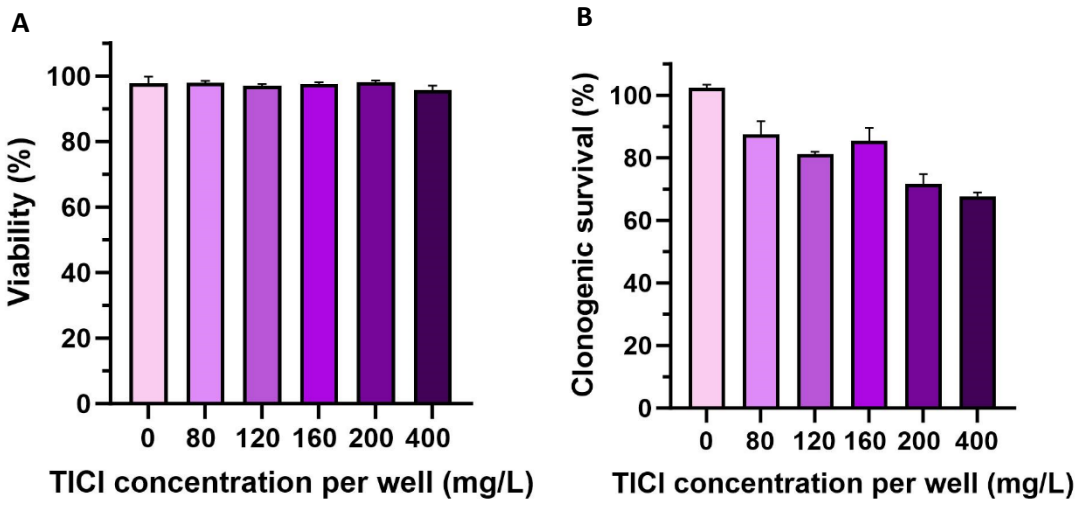

Figure 4.16 Cytotoxicity of thallium (I) chloride in prostate cancer cells. A) Cell viability in DU145 cells incubated for 90 min in medium containing 80-400 mg/L of TlCl aqueous solution. **B)** Clonogenic survival in DU145 cells incubated for 90 min in medium containing 80-400 mg/L of TlCl aqueous solution. Bars represent mean ± SD, triplicates, n=1.

Assessing the subcellular distribution of caPBNPs, chPBNPs, Tl-caPBNPs and Tl-chPBNPs.

4.4.7 Transmission electron microscopy (TEM) of Prussian blue nanoparticles

TEM is a widely employed technique for visualising the internalisation and subcellular distribution of nanoparticles and nanoparticle aggregates. This technique was used to assess the subcellular localisation of Prussian blue nanoparticles coated with citric acid (caPBNPs) and chitosan (chPBNPs). It required preparation of thin cell sections, which were stained with uranyl acetate to enhance the image contrast. Sample preparation for TEM imaging of PBNPs without Tl did not involve snap freezing and cells were chemically fixed with glutaraldehyde as there was no risk of altering their localisation by additional washings. Multiple cell sections were prepared from cells incubated with both types of PBNPs and as well as cells without PBNPs and analysed with TEM. Selected examples shown in Figure 4.17 and 4.18.

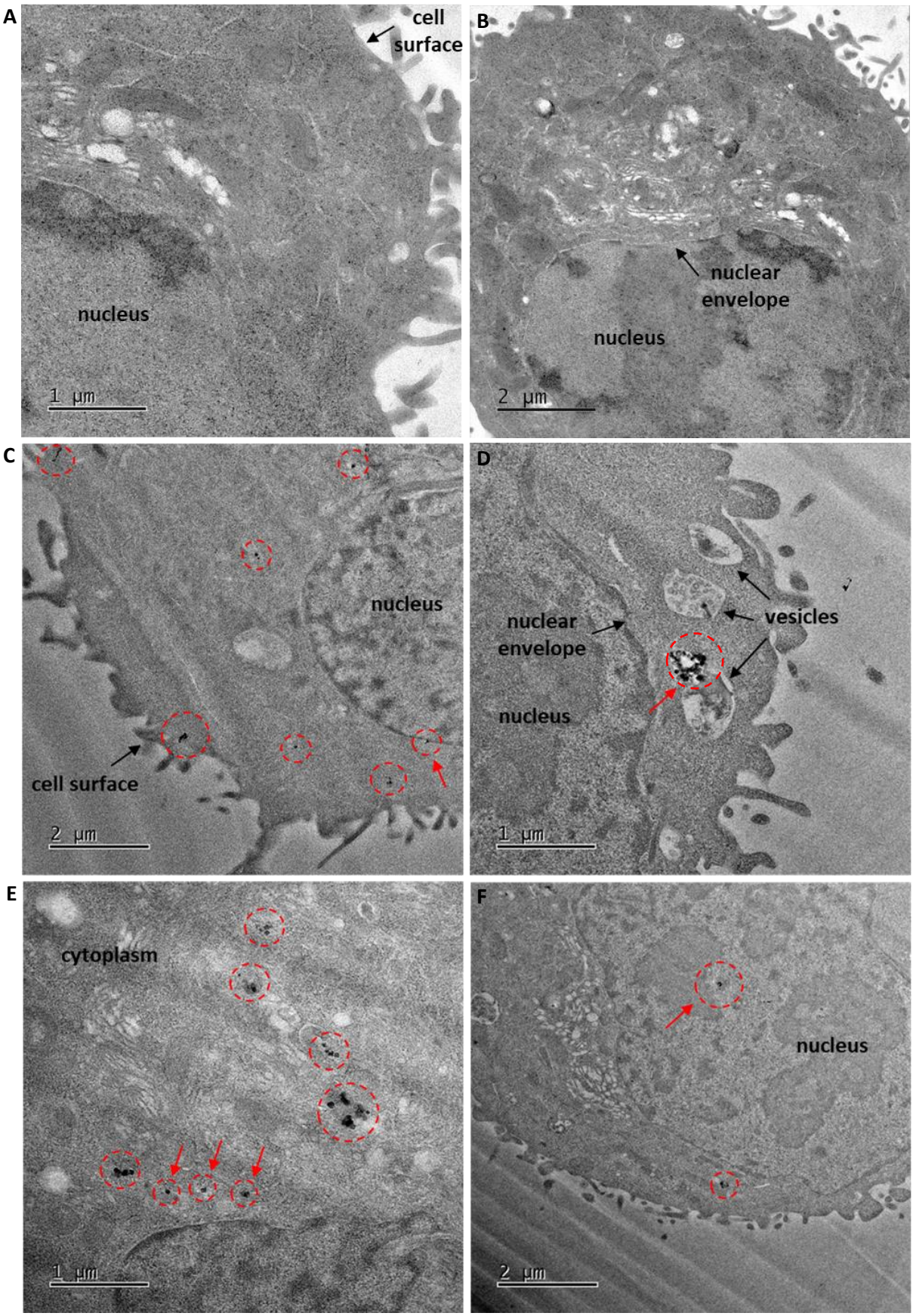

Figure 4.17 TEM images of caPBNPs in lung cancer cells. A) and B) TEM images of cell sections of lung cancer cells (A549) without PBNPs. **C), D), E)** and **F)** TEM images of cell sections of lung cancer cells (A549) incubated for 3 h with 50 µL of 0.5 mg/mL caPBNPs solution added to 200 µL RPMI medium. Cell nucleus, nuclear envelope, cytoplasm and cell surface are marked with black arrows. Nanoparticles visible are enclosed in red circles. Red arrows indicate caPBNPs interacting with the nuclear envelope (C), within a vesicle (D), individual caPBNPs (E) and caPBNPs in the cell nucleus (F).

CaPBNPs (Fig. 4.17) were observed mostly in the cell cytoplasm as regular, cubic shaped individual nanoparticles as well as in clusters encapsulated in vesicles. Although the majority of nanoparticles were spotted in the cytoplasmic region of the cell, some individual nanoparticles were detected in the close proximity to the cell nucleus or in the cell nucleus (Fig. 4.17 A and D). ChPBNPs were present inside lung cancer cell sections in a much higher quantity than caPBNPs. Some images showed the cellular membrane wrapping around the nanoparticles and forming vesicles (Fig. 4.18 A).

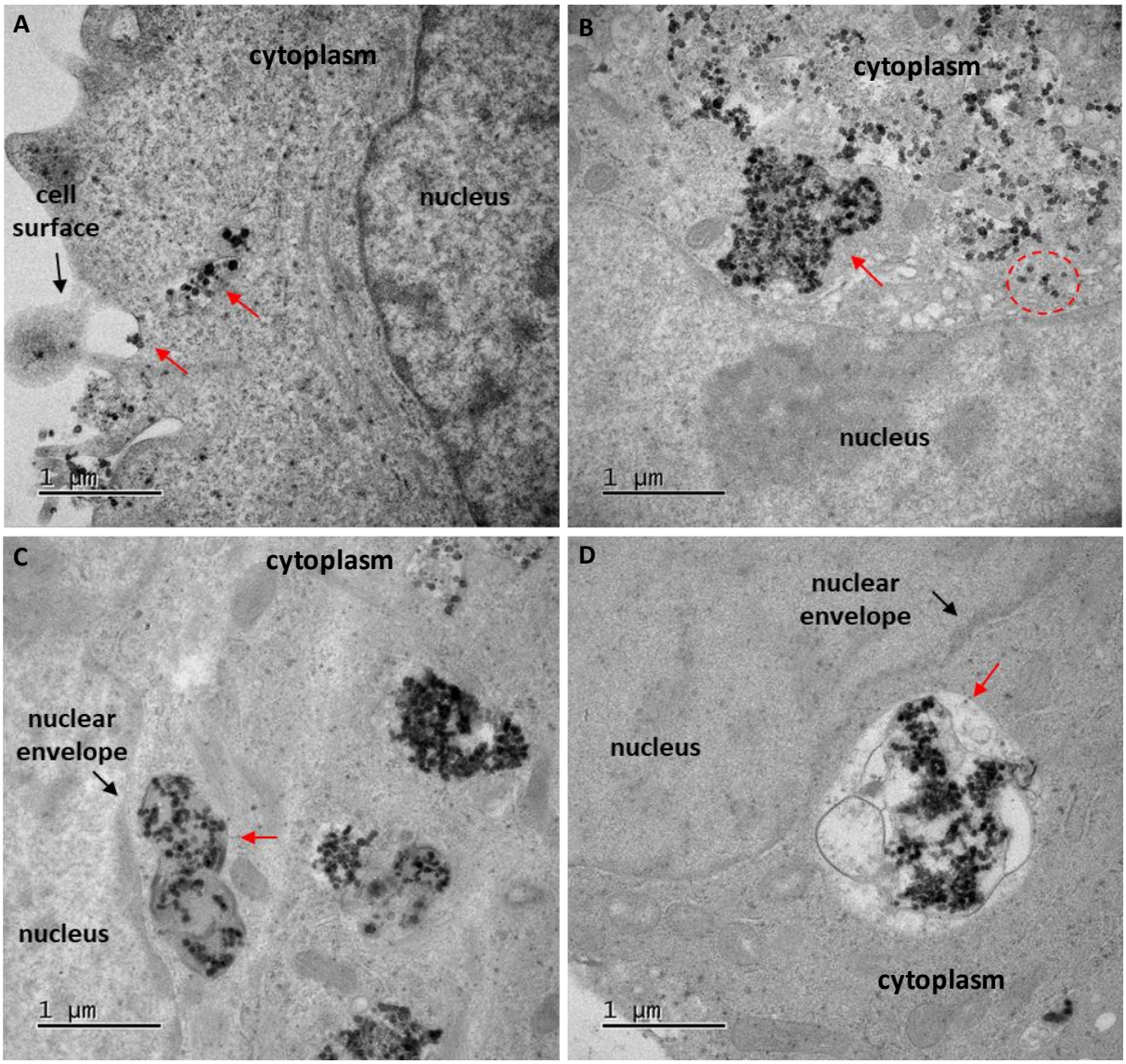

Figure 4.18 TEM images of chPBNPs in lung cancer cells. A), B), C) and D) TEM images of cell sections of lung cancer cells (A549) incubated for 3 h with 50 µL of 0.25 mg/mL chPBNPs solution added to 200 µL RPMI medium. Cell nucleus, nuclear envelope and cell surface are marked with black arrows. Individual nanoparticles are highlighted with a red circle (B). Red arrows indicate chPBNPs enclosed with the cell membrane (A) and chPBNPs within a vesicle close to the cell nucleus (B), (C) and (D).

The majority of chPBNPs were spotted clustered in vesicles very close to the cell nucleus. chPBNPs were also present as single nanoparticles in the cytoplasm (Fig. 4.18 B). There was no difference in appearance or localisation between native nanoparticles and thallium doped nanoparticles for both types of PBNPs.

4.4.8 Energy dispersive X-ray spectroscopy (EDS) combined with transmission electron microscopy (TEM) of PBNPs and Tl-PBNPs

Energy dispersive X-ray spectroscopy (EDS) combined with electron microscopy has emerged as a powerful analytical tool in nanotechnology as it offers a non-destructive way to investigate the elemental composition and distribution of nanoparticles with remarkable spatial resolution. This technique was conducted on thin sections of lung cancer cells incubated with caPBNPs and chPBNPs both with and without thallium doping. Results are shown in Figure 4.19 for caPBNPs and Figure 4.20 for chPBNPs.

Both types of nanoparticles can be spotted in the cytoplasmic region of the cell as white dots, mostly clustered in vesicular compartments. ChPBNPs accumulated in lung cancer cells to a greater extent compared to caPBNPs despite the lower concentration used for sample preparation.

The EDS analysis revealed a co-localisation of iron signals with nanoparticles imaged with TEM. Thallium-doped nanoparticles exhibited a co-localised thallium signal, while nanoparticles which had not been incubated with Tl exhibited no thallium signal. The subcellular localisation of PBNPs of both types could be linked to vesicular compartments, where thallium was observed. However, individual nanoparticles within the cytoplasm were also spotted.

Furthermore, the elemental analysis conducted via EDS indicated distinct elemental distributions in regions where thallium accumulated within the nanoparticles, as depicted in EDS spectra (Fig. 4.19 B and Fig. 4.20 B). The average total weight percentage (wt%) of thallium in the regions of the cytoplasm containing Tl doped caPBNPs was estimated as 3.98 ± 1.55% compared to 0.03 ± 0.05 % in nanoparticle-free area (n=10). Even higher increase in wt% was noted for Tl doped chPBNPs, from 0.04 ± 0.1 % in the cytoplasmic regions without visible PBNPs to around 6.47 ± 5.2 % where Tl-chPBNPs were accumulating (n=10).

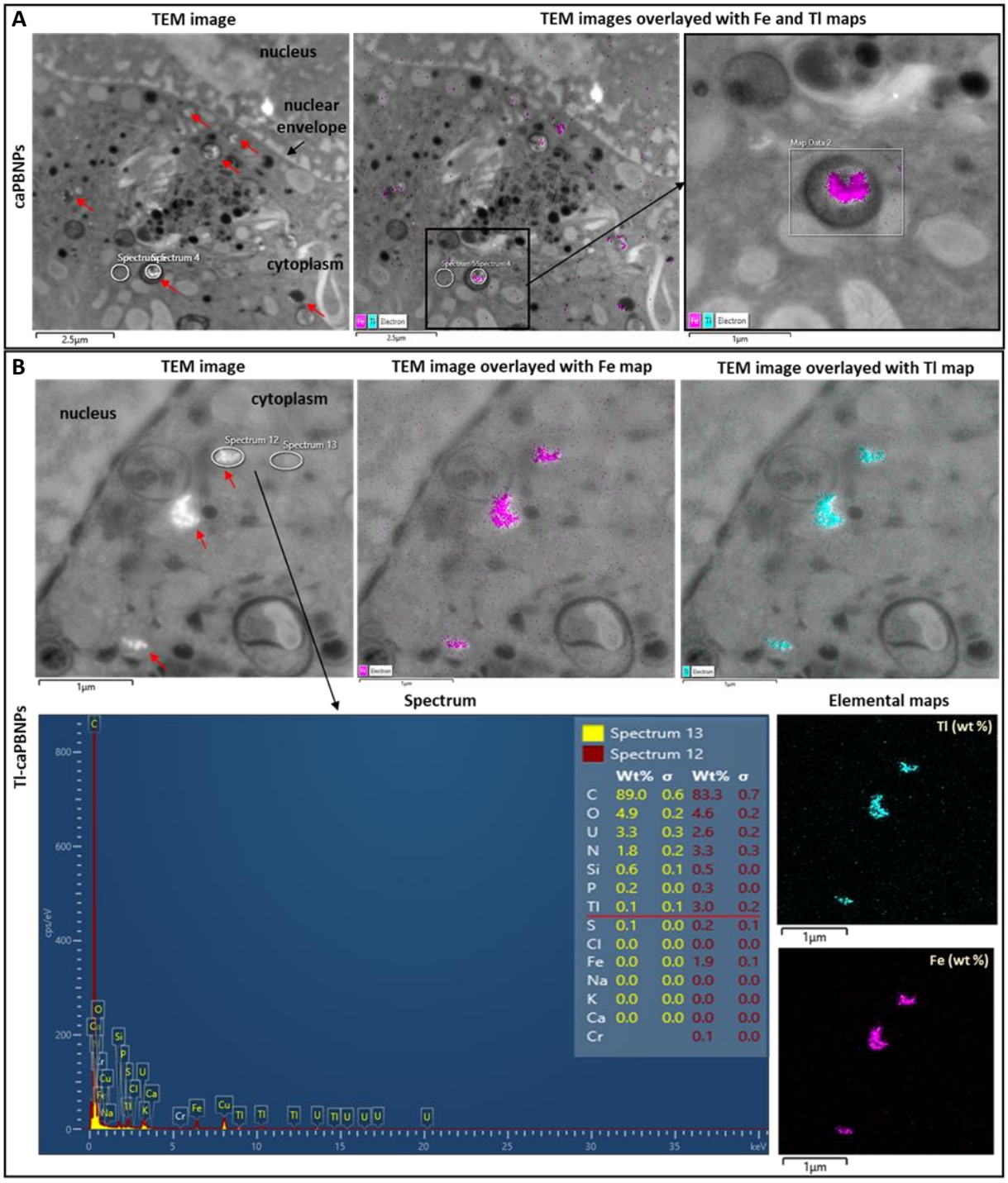

Figure 4.19 TEM/EDS analysis of caPBNPs and Tl-caPBNPs in lung cancer cells. A) TEM image and overlays with iron and thallium EDS signal of a thin cell section showing native caPBNPs. **B)** TEM image of thin cell sections showing Tl-caPBNPs, overlays with iron and thallium EDS signal, energy spectrum comparing elemental composition in nanoparticle region (spectrum 12) and nanoparticle-free region (spectrum 13) and elemental maps of thallium and iron (expressed as % of total weight). Red arrows indicate caPBNPs.

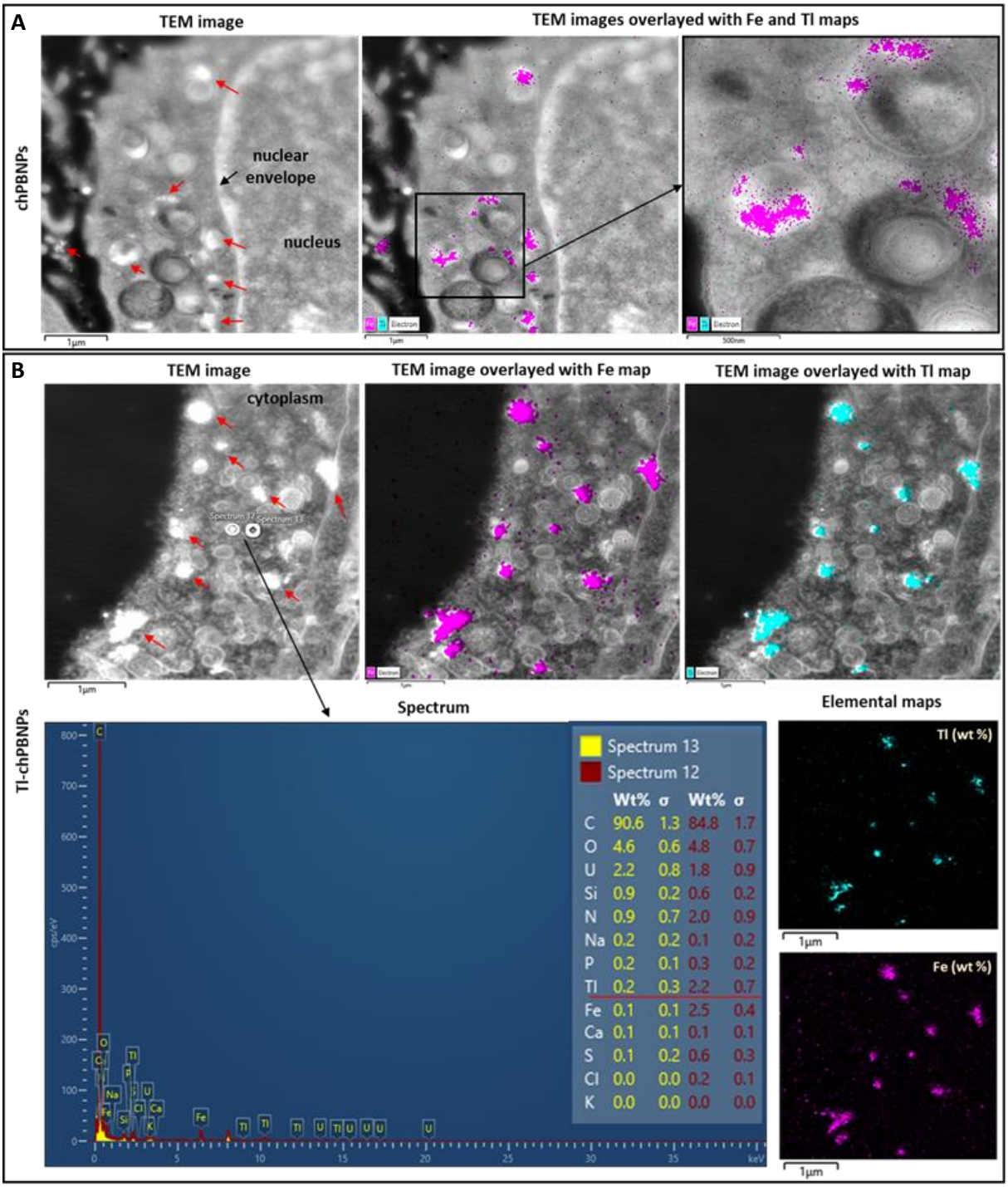

Figure 4.20 TEM/EDS analysis of chPBNPs and Tl-chPBNPs in lung cancer cells. A) TEM image and overlays with iron and thallium EDS signal of a thin cell section showing native chPBNPs. **B)** TEM image of a thin cell section showing Tl-chPBNPs, overlays with iron and thallium EDS signal, energy spectrum comparing elemental composition in nanoparticle region (spectrum 12) and nanoparticle-free region (spectrum 13) and elemental maps of thallium and iron (expressed as % of total weight). Red arrows indicate chPBNPs.

4.4.9 Ion beam analysis of Tl-caPBNPs

To assess the subcellular distribution of thallium in cells exposed to citric acid coated Tl-PBNPs and to evaluate the feasibility of the method for tracking nanoparticle distribution, PIXE analysis was conducted on ovarian cancer cells following a 3 h incubation period with Tl-caPBNPs. The resulting elemental maps revealed the concentration of phosphorus, sulfur, chlorine, and potassium predominantly in the central area of the cell, coinciding with the nucleus location (Fig. 4.21). However, the signals for thallium and iron appeared outside of the nucleus, within the cytoplasmic region of the cell.

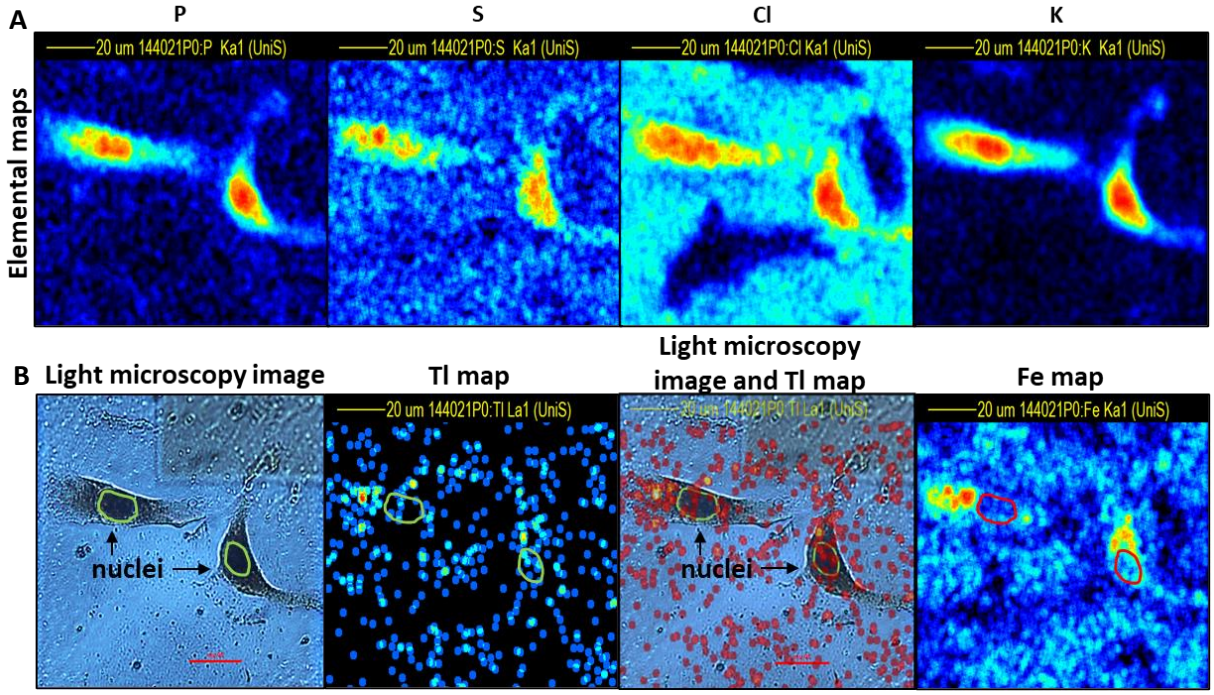

Figure 4.21 PIXE analysis of ovarian cancer cells incubated with Tl-caPBNPs. An example of PIXE analysis in SKOV3 cells incubated with Tl-caPBNPs for 3 h showing **A)** elemental maps of phosphorus, sulfur, chlorine and potassium (from left to right) and **B)** a light microscope image of SKOV3 cells, thallium signal map, an overlay of the light microscope image with PIXE thallium signal and iron signal map (from left to right). Cell nuclei are marked green and red (Fe map).

4.4.10 Targeting Prussian blue nanoparticles to the cell nucleus

The results from radiotoxicity assessments of PBNPs coated with citric acid (caPBNPs) and chitosan (chPBNPs) shown in chapter 3, alongside the differences in subcellular localisation between PBNPs and unbound thallium described earlier in this chapter, suggest that targeting ^{201}Tl radiolabelled PBNPs specifically to the cell nucleus may greatly increase their radiotoxic potential. Different approaches were taken to increase the presence of PBNPS in the cell nucleus (Fig. 4.22).

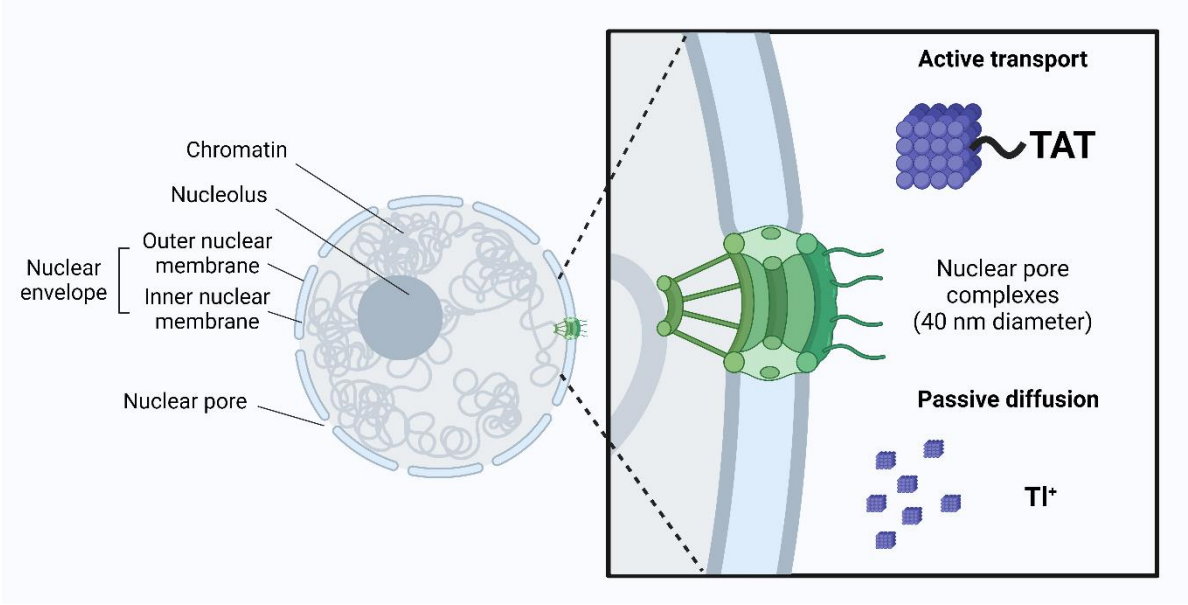

Figure 4.22 Schematic representation of the suggested transport routes of Tl^+ and PBNPs to the cell nucleus.

First attempted was the idea to reduce the size of caPBNPs to allow them to passively diffuse through the 20-70 nm diameter pores in the nuclear envelope [169]. Gold nanoparticles with a diameter below 10 nm have been shown to reach the nucleus [186]. As the rate of nucleation and therefore the size of nanoparticles greatly depend on the synthetic method and the specific conditions applied [124,187], various amounts of citric acid were added to the reaction mixture, as well as different molar concentrations of starting solutions were tested. Table 4.1 summarises the conditions of the synthesis and the resulting average nanoparticle size together with their polydispersity, measured by dynamic light scattering (DLS) method.

The smallest caPBNPs obtained by increasing threefold the molar concentration of $K_4Fe(CN)_6$ aqueous solution had the average diameter of 43.0 ± 0.6 nm (polydispersity index PDI: 0.103 ± 0.022). Further increase in the molar concentration of $K_4Fe(CN)_6$ was not linked to a greater size reduction of caPBNPs [48,49]. Additionally, raising the citric acid/Fe^{3+} molar ratio to 5:1 to increase nucleation did not, in our hands, reduce the size of citric acid coated PBNPs to 10 nm as has previously been reported [190]. Consequently, the nanoparticles produced in these reactions did not possess the necessary dimensions for passive transport to the cell nucleus. Reducing the size of chitosan-coated PBNPs was not attempted due to the lack of easily accessible methods for size assessment. DLS was considered not appropriate for determining the size of chPBNPs, which was explained in the previous chapter.

Reagents					Before purification				After purification			
Sample	$FeCl_3$ aq. (mM)	$K_4Fe(CN)_6$ aq. (mM)	Citric acid (mmol) added to $FeCl_3$	Citric acid (mmol) added to $K_4Fe(CN)_6$	Average size (nm)	SD	Polydispersity index (PDI)	SD	Average size (nm)	SD	Polydispersity index (PDI)	SD
1	1	1	0.5	0.5	68.6	8.7	0.116	0.049	78.4	9.0	0.100	0.036
2	1	1	0.02	0.02	93.3	1.4	0.067	0.020	-	-	-	-
3	1	1	0.1	0.1	118.0	2.3	0.020	0.011	-	-	-	-
4	1	1	0.25	0.25	64.9	0.7	0.069	0.012	-	-	-	-
5	1	1	1	1	66.1	1.0	0.037	0.008	-	-	-	-
6	1	1	5	0.5	86.9	0.8	0.049	0.013	-	-	-	-
7	1	1	5	5	71.8	1.4	0.097	0.017	-	-	-	-
8	1	2	0.5	0.5	54.4	0.6	0.077	0.024	-	-	-	-
9	1	3	0.5	0.5	43.0	0.6	0.103	0.022	48.1	0.5	0.099	0.008
10	1	3	0.5	1.5	47.6	0.7	0.135	0.003	-	-	-	-
11	1	4	0.5	0.5	46.2	0.2	0.095	0.012	-	-	-	-
12	1	5	0.5	0.5	47.5	0.4	0.134	0.027	-	-	-	-
13	1	10	0.5	0.5	58.6	1.2	0.099	0.011	-	-	-	-
14	2	1	0.5	0.5	70.5	1.0	0.237	0.007	-	-	-	-
15	4	1	0.5	0.5	523.5	10.4	0.284	0.018	-	-	-	-

Table 4.1 Reducing the size of caPBNPs. This table presents different molecular ratios of the reagents and their impact on the average size of the synthesised nanoparticles. The full description of caPBNPs synthetic method can be found in chapter 3, Methods section. Conditions shown in sample 1 were the standard conditions used to prepare caPBNPs for biological experiments and their physicochemical assessments (n=10), whereas samples 2 - 15 represent different testing conditions (n=1 for each sample). caPBNPs in sample 9 had the smallest diameter and underwent a further purification process using Amicon filter tubes as described in the Methods section, chapter 3. Nanoparticles obtained in reactions 2-9 and 10-15 were not purified.

An alternative strategy to size reduction involved altering the surface of the nanoparticles using a TAT peptide, with the aim of actively transporting these nanoparticles, which exceed the size of nuclear pores, into the nucleus. The amine groups of the TAT peptide were non-specifically conjugated to the carboxylic groups of the citric acid coating using a common coupling agent (EDC/sulfo-NHS). TAT conjugated caPBNPs (caPBNP-TAT) obtained in this reaction had an increased zeta-potential of 5.3 ± 0.3 mV (n=1) compared to caPBNPs without TAT peptide attached (-41.7 ± 14.2 mV, n=10), suggesting a successful coupling reaction. However, caPBNP-TAT dispersed in water were not homogenous, forming visible clumps and aggregates, with an average nanoparticle size measured by DLS of 2230.0 ± 155.6 nm (PDI: 0.293 ± 0.005).

In the next step, the TAT peptide was attached to chitosan coated PBNPs. Initially, the carboxylic group of the TAT peptide was activated using the EDC/sulfo-NHS coupling agent before being linked to the primary amine groups present in chitosan. Obtained nanoparticles (referred to as chPBNP-TAT) were stable in water, forming a homogenous, blue coloured suspension without any visible aggregations.

To evaluate the efficacy of the TAT peptide conjugation in directing chitosan-coated PBNPs to the nuclear compartment, fluorescence microscopy was employed. This analysis required additional adjustments to the surface of the nanoparticles. Carboxyfluorescein was used as a fluorescent marker and was linked to chPBNPs to create chPBNP-CF. Additionally, chPBNPs were conjugated with both TAT peptide and carboxyfluorescein, resulting in chPBNP-TATFAM. ChPBNPs, chPBNP-TAT and their corresponding fluorescent counterparts were subjected to the thermogravimetric analysis (TGA) to evaluate the efficiency of the conjugation. TGA results and the derivative thermogravimetric (DTG) curves are presented in Figure 4.23.

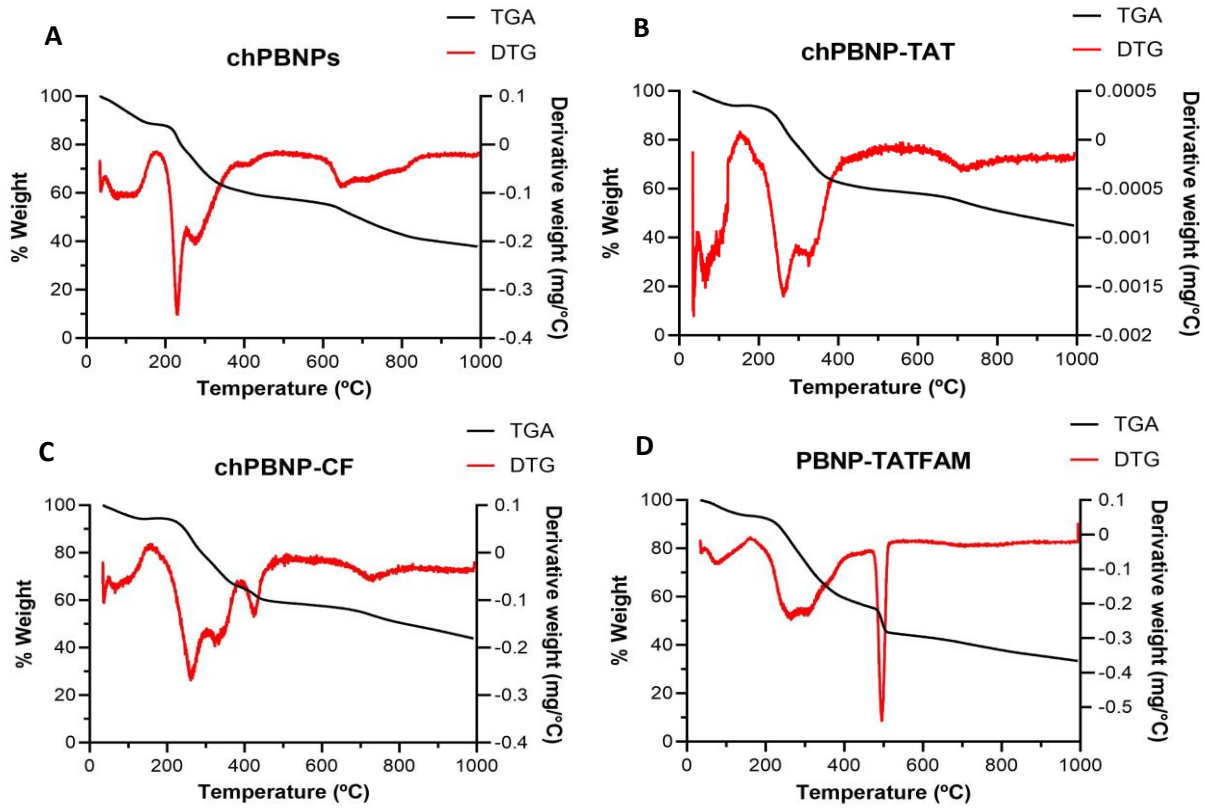

Figure 4.23 TGA and DTG analysis. TGA and DTG results for **A)** chPBNPs, **B)** chPBNP-TAT, **C)** chPBNP-CF and **D)** chPBNP-TATFAM presented as % weight and derivative weight (mass/temperature, mg/°C) versus temperature (°C).

For covalently conjugated TAT peptide, carboxyfluorescein and carboxyfluorescein-TAT with PBNPs, a weight loss occurring in the temperature range of 450 - 600°C was expected. This weight loss was noticeable for chPBNP-CF and chPBNP-TATFAM (Fig. 4.23 C and D) but was not evident for chPBNP-TAT (Fig. 4.23 B) indicating that the TAT peptide was not efficiently conjugated to these nanoparticles.

The calculated conjugation yields for chPBNP-CF and chPBNP-TATFAM were 5.4% and 9.8%, respectively (Table 4.2).

Sample	Coating (%)	Conjugation yield (%)	Molecules per nanoparticle
chPBNPs	45.8		143.0
chPBNP-CF		5.4	4.6
chPBNP-TATFAM		9.8	3.8

Table 4.2 TGA calculations. The calculated % of chitosan coating and the number of molecules per nanoparticle for chPBNPs, and the conjugation yield (%) and the number of molecules per nanoparticle calculated for chPBNPs-CF and chPBNP-TATFAM based on the TGA.

Fluorescent microscopy was performed to visualise the cellular uptake and the subcellular localisation of chPBNP-CF and chPBNP-TATFAM. In the experimental procedure, lung cancer cells (A549) cells were incubated with chPBNP-CF, chPBNP-TATFAM, as well as carboxyfluorescein and the carboxyfluorescein-TAT peptide conjugate ([5-FAM]-TAT). Cells incubated only with [5-FAM]-TAT or carboxyfluorescein did not show any fluorescence. Confocal microscopy images of cells incubated with chPBNP-CF and chPBNP-TATFAM were taken as serial z-stack images, which examples are presented in Figure 4.24 A and B.

The fluorescent signal in cells incubated with chPBNP-CF and chPBNP-TATFAM was observed in the cytoplasmic region and the cell nucleus. The quantification was based on the maximum intensity projections of z-stacks of both DAPI and carboxyfluorescein channels. A total of 172 cells (chPBNPs-CF) and 210 cells (chPBNP-TATFAM) were analysed. The fluorescent signal present in the nucleus counted per cell was expressed as a percentage of the total fluorescent signal recorded per cell. The analysis demonstrated that approximately 22.0 ± 8.7% of chPBNP-CF and 36.8 ± 12.0% of chPBNP-TATFAM fluorescence signal was localised in the cell nucleus (Fig. 4.25). Consequently, the attachment of the TAT peptide to the nanoparticles resulted in a statistically significant increase of 14.8% in nuclear localisation (unpaired t-test).

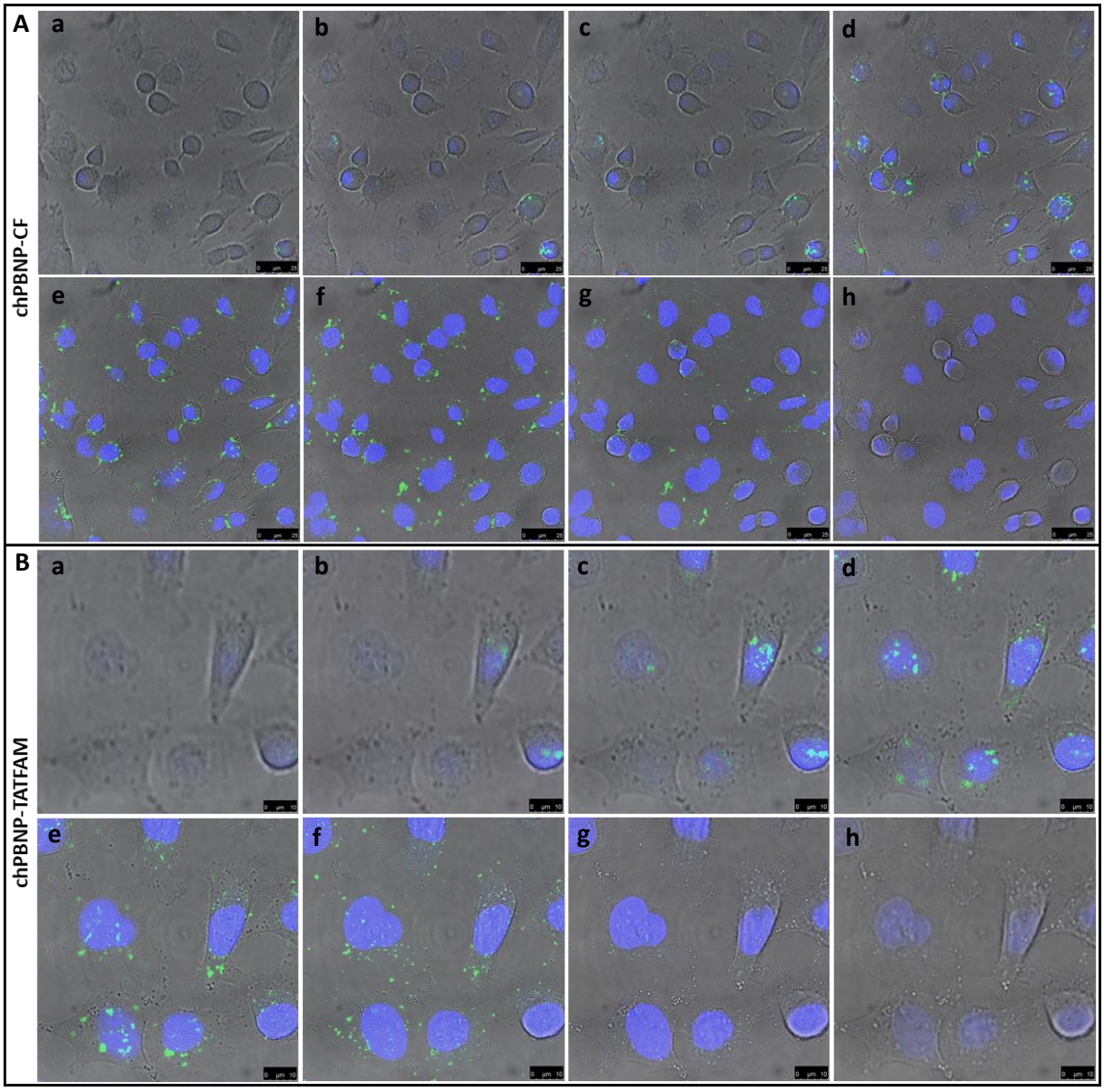

Figure 4.24 Fluorescent microscopy of chPBNP-CF and chPBNP-TATFAM. Exemplar confocal microscopy images of lung cancer cells (A549) cells incubated for 3 h with **A)** chPBNPs-CF and **B)** chPBNP-TATFAM. The images are an overlay of fluorescent signals (blue nuclei stain - DAPI, green stain - carboxyfluorescein) and bright-field images. Images were taken as z-stacks, 1 µm apart, 10 stacks per image, in triplicates, n=3 per condition. Exemplar 8 stacks are shown in this figure (a-h). Settings were consistent throughout the experiment; scale bar: 25 µm (A) and 10 µm (B). Cells incubated only with [5-FAM]-TAT or carboxyfluorescein did not show any fluorescence.

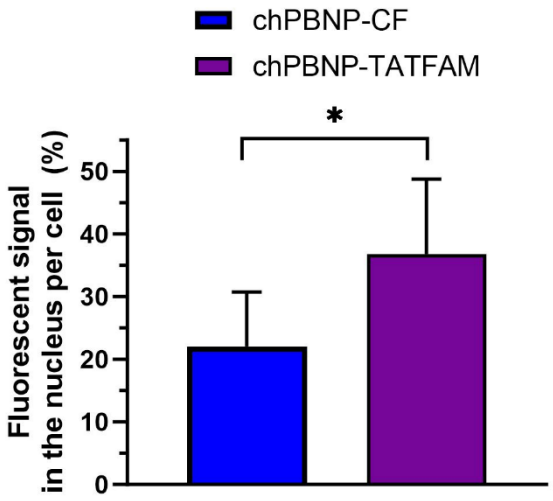

Figure 4.25 Quantification of the chPBNP-CF and chPBNP-TATFAM fluorescent signal. Percentage of the fluorescent signal per cell found in the nucleus expressed as a percentage of the total fluorescent signal per cell recorded, evaluated in lung cancer cells incubated with chPBNPs-CF and chPBNP-TAT FAM for 3 h. Images were taken as z-stacks, 1 µm apart, number of steps: 10. The same settings were kept throughout the experiment. A total of 172 cells (chPBNPs-CF) and 210 cells (chPBNP-TATFAM) were analysed, a minimum of 15 cells per image. Bars represent mean ± SD, triplicates, n=3, * means statistically significant as $P < 0.05$ (t-unpaired test).

4.5 Discussion

In this chapter, various analytical techniques were employed to examine the subcellular distribution of unbound thallium (I) and Prussian blue nanoparticles (PBNPs) carrying radioactive thallium (I) into cancer cells. Localising unbound thallium on a subcellular scale poses a specific challenge due to its nature as a freely diffusible ion and its potassium mimicking behaviour. Thallium does not appear to be trapped inside the cell or bound to intracellular proteins, especially given its rapid efflux from cells, requiring only 15 minutes for 50% of thallium to be removed from cells when the external solution is changed, and the potential for redistribution within cells as described in chapter 2.

4.5.1 The validity of the presented methods

For freely diffusible ions, providing an accurate evaluation of their subcellular localisation demands careful attention to sample preparation and pre-treatment procedures. The technique of chemical fixation and paraffin embedding is a commonly employed approach in the preparation of tissues and cells samples. This method typically involves several sequential steps, which include incubation with formalin or glutaraldehyde, a series of organic washes to dehydrate the sample, and ultimately embedding it in paraffin and cutting thin sections suitable for imaging. These steps provide ample opportunity for thallium ions to diffuse and relocate, or even diffuse out of cells completely. An alternative method involves rapid freezing of the sample in liquid nitrogen, followed by taking thin sections using a cryotome. This technique is believed to be superior in preserving the actual state of

elemental distribution in cells. Indeed, when comparing the distribution of elements with LA-ICP-MS in animal tissue sections fixed with the both previously mentioned sample preparation techniques, it has been demonstrated that the distribution and concentration of alkali metals such as potassium and sodium varied, indicating that the process of chemical fixation and the multiple washing steps employed might alter the true elemental distribution and quantification [191]. Similar conclusions were drawn when comparing these two preservation methods in tissue samples analysed by EDS [192]. In the experimental work described in this chapter, we aimed to either reduce the number of steps and washes during chemical fixation, for example in sample preparation for LA-ICP-MS analysis in whole cells, or use the snap-freezing method to avoid thallium efflux and redistribution.

Besides ensuring proper sample preparation, the selection of a suitable analytical technique was crucial. A diverse range of analytical techniques with varying capabilities and characteristics, such as resolution and sensitivity parameters, were employed to investigate the distribution of both unbound thallium and thallium bound to nanoparticles, using either radioactive or stable thallium. Many of the techniques outlined in this chapter rely on stable isotopes. For those techniques with lower sensitivity, higher concentrations of thallium were necessary to reach the detection limits. Two critical factors had to be considered here: the limited solubility of thallium (I) chloride in water and the toxicity associated with higher concentrations. Cytotoxicity studies involving TlCl in prostate cancer cells revealed that a concentration of 400 mg/L (1.67 mmol/L) of TlCl in the incubation medium could lead to long-term cytotoxic effects, as observed in the clonogenic survival experiment. Nevertheless, cells incubated with 400 mg/L of TlCl did not exhibit any immediate alterations in morphology or viability, and it was therefore assumed that they remained suitable for analytical methods requiring high concentrations of thallium for detection. Analytical techniques employing radioactive thallium are the optimal choice in this context. This is due to the fact that the average concentration of thallium in the radioactive sample, as calculated in chapter 2, falls within the nanomolar range, which is approximately 2000 times lower than the concentration of non-radioactive TlCl used in some of the analytical techniques. As demonstrated in chapter 2, cancer cells do not exhibit any adverse effects when exposed to nanomolar concentrations of non-radioactive thallium. While the choice of methods was constrained in the case of unbound thallium due to the reasons explained earlier, Prussian blue nanoparticles (PBNPs) offered a much broader range, primarily because they are less prone to rapid diffusion and their surface can be chemically modified.

One of the methods commonly used for a range of radionuclides chelated to compounds targeting specific receptors overexpressed inside the cell or on the cell membrane, is the subcellular fractionation method. This method entails chemical and physical isolation of subcellular compartments followed by the measurement of radioactivity within these compartments and yields

cumulative results averaged over an entire population of cells. It is important to note that subcellular fractionation is highly disruptive to cells and requires multiple washes with reagents. Consequently, it is reasonable to anticipate that the majority of diffusible radionuclides would be found in the initial washes, the quantity depending on the duration of incubation with the specific reagent. This method was selected primarily as a proof of this flaw and demonstrated that only a very small fraction, specifically 0.36% of $^{201}Tl^{+}$ could be localised within cells. Clearly, uncritically interpreting this result is deeply misleading and the method is fatally flawed in this case. Similarly to these findings, the nuclear accumulation of $[^{99m}Tc]TcO_4^-$ was significantly underestimated when employing this method [12]. While subcellular fractionation may not be ideal for thallium or technetium, it is commonly and more acceptably employed in research as a cost-effective technique for chelated radionuclides [184].

Laser ablation ICP-MS (LA-ICP-MS) is an analytical technique that allows precise mapping and quantification of elements in biological samples with an exceptional sensitivity down to ppq. Typically used for mapping elemental distribution in tissue samples, its spatial resolution, usually falling within a range of one to a few µm, could be a limiting factor when applied to subcellular imaging of individual cells [193]. While the thallium signal was clearly visible within fixed prostate cancer cells using low micromolar concentrations of TlCl for the cell incubation, assessing its subcellular distribution was hindered by the limitations in spatial resolution and the inability to identify the nucleus boundaries. Instead, LA-ICP-MS analysis served a different purpose by addressing a question related to evaluating variations in thallium distribution across cell populations. Another challenge in examining individual cells with LA-ICP-MS is the depth resolution. Since the laser beam traverses the entire cell volume, and the resulting signal is presented as a two-dimensional image, it is difficult to distinguish the specific cell compartment from which the signal originates. To overcome this limitation, thin cell sections were taken through the cells incubated with thallium, embedded in gelatine and imaged with LA-ICP-MS. This modification, however, did not help to localise the subcellular thallium signal, mainly due to the high level of thallium present in the surrounding gelatine. In this experiment cells were not washed after thallium incubation to prevent thallium displacement. Furthermore, accurately localising the cell nucleus also posed some difficulties. Previous attempts in similar analyses involved staining cells with Ir-DNA-intercalator [194] or incubating them with bromodeoxyuridine [183], a compound that binds to nuclear DNA. Bromodeoxyuridine is a commonly utilised chemical marker in molecular and cell biology research for labelling newly synthesised DNA and was introduced in LA-ICP-MS and IBA experiments to aid visualising the nucleus. In IBA, the bromine signal was detectable but relatively weak, while in LA-ICP-MS, it significantly interfered with the thallium signal, making it unsuitable for the intended purpose. In addition, LA-ICP-MS often suffers from matrix effects, which arise from the alterations of ionisation efficiency of target analytes in the presence of co-eluting compounds in the

same matrix, resulting in significant changes in signal intensity spanning multiple orders of magnitude [195]. To mitigate this effect, researchers commonly employ calibration standards, reference materials and correction techniques. Recent years have witnessed numerous advancements in LA-ICP-MS, particularly in terms of lateral resolution and quantification. Therefore, improving the spatial resolution to sub-micron scale [196], exploring additional three-dimensional image reconstructions [197] or super-resolution reconstructions [198] could be attempted in the future to enhance the method's suitability for imaging elements at the subcellular level.

Ion beam analysis is a collective term related to a range of methods where sample is exposed to highly energetic ion beams composed of protons, α-particles or other cations. Among these techniques, non-destructive particle-induced X-ray emission (PIXE) and elastic backscattering spectrometry (EBS) are frequently employed for the analysis of biological samples with detection limits typically within the range of ppm. To illustrate the utility of IBA in single-cell analysis, in earlier work PIXE was used to examine the distribution of platinum following exposure to cisplatin and carboplatin in both sensitive and resistant ovarian cancer cells [199]. A similar approach was adopted to visualise and quantify a novel platinum-based treatment for lung cancer at the subcellular level [183]. In this study, the authors successfully co-localised the platinum signal with the bromine signal, which accumulated in the cell nucleus following BrdU pre-incubation. Following a sample preparation procedure that involved snap-freezing and freeze-drying to enable analysis under vacuum and at ambient temperature, over 80 individual prostate cancer and ovarian cancer cells of various shape and sizes were subjected to IBA. The analysis involved the detection of emitted X-ray resulting from collisions of the incident ions with the inner shell electrons (PIXE) and back-scattered incident ions (EBS), achieving spatial resolution between 1 to 2 µm. While PIXE detected the bromine signal in ovarian cancer cells that were pre-incubated with BrdU, the signal was too faint to confidently localise the nucleus. As a result, the identification of regions of interest relied on the combination of PIXE/EBS elemental maps with light microscopic images of cells. During the analysis, a consistent pattern emerged, with a higher thallium signal detected in the regions corresponding to the cell nuclei. The quantified results re vealed that an estimated 64% of unbound thallium accumulates in this region. The question at hand was whether the observed thallium signal enhancement in the nuclear region of the cell was a genuine effect or an artifact of the technique employed. The quantification of thallium in the marked regions of the cell (nucleus and cytoplasm) was conducted by performing multiple line scans in both cell types and calculating the thallium signal within these regions. To account for the enhanced signal detected within the nucleus, which may be attributed to the fact that cell is usually thicker in that region, the thallium signal was adjusted by normalising it against the EBS signal - a parameter sensitive to variations in cell thickness. In imaging, it is a well-known effect that the signal found at the centre of

the area of interest is the strongest as both primary and scattered signals are being detected and accumulate in the middle, which can potentially lead to challenges in accurately assessing and interpreting the data. In this case, the position of the nucleus was not consistently at the centre of the cell. Furthermore, PIXE elemental maps of thallium and iron signals in cells exposed to Tl-caPBNPs demonstrated that thallium in this form, which does not seem to accumulate in the nucleus, is observed in higher concentrations in the periphery of the cell instead of the central region. This observation indicates that the thallium signal detected in the central part of the cell in its unbound form is not merely a result of signal scattering accumulation but accurately reflects the actual thallium localisation.

Despite the challenges mentioned earlier, IBA proved to be the most suitable method for detecting and quantifying unbound thallium in single cancer cells. Additionally, an important advantage of quantifying thallium signals using IBA, as opposed to ICP-MS and SIMS, is its recognition as a 'matrix effect'-free method that provides absolute values. IBA is frequently utilised as a reference technique and can provide certified standards to mitigate this effect when using other methods. To further improve the effectiveness of this method for subcellular mapping of diffusible elements, it would be advantageous to find an appropriate nuclear marker that does not affect their distribution and can be readily detected by IBA. Additionally, increasing the spatial resolution to the nanometre scale would significantly improve the quantification and imaging of individual cells using IBA.

Secondary ion mass spectrometry (SIMS) is a very sensitive analytical method capable of detecting concentrations in the range of ppm to ppb. It can be employed for the analysis of biological samples, offering elemental and molecular insights into the surface of the sample. In our comprehensive approach, SIMS was combined with IBA, and the same sample was subjected to analysis using both techniques. While PIXE and EBS successfully detected thallium, no signal for thallium was observed during the SIMS analysis. Since the primary ion beam in SIMS affects the top few nanometres of the sample surface [200], the absence of the thallium signal in SIMS analysis may suggest that thallium is not present on or near the surface of the cells that were incubated with TlCl. However, it is essential to consider that the detection sensitivity of elements dependents significantly on various factors, including the composition of the sample matrix, types of elements or molecules being tested, and the type of primary beam used. Consequently, the elemental maps obtained with SIMS represent the ions that reached the detector, rather than reflecting the ions present on the sample surface. Moreover, despite IBA being classified as a non-destructive method, it is important to acknowledge the potential adverse effects of the ion beam on the sample surface [201]. To further improve the suitability of this technique for subcellular imaging, the option of imaging cells at different depths and conducting 3D

reconstructions of entire cells or specific regions is available but necessitates acquiring slices of cells at varying depths and selecting regions of interest can present a challenge on its own [202].

An alternative method used for tracking the distribution of free thallium within cancer cells was energy-dispersive X-ray spectroscopy (EDS). When EDS is coupled with electron microscopy, it provides exceptionally high spatial resolution at the nanometre range. However, it is important to note that its detection limit remains relatively high (higher ppm range) [203]. Despite using a high molar concentration of TlCl (400 mg/L, 1.67 mmol/L) during the cell incubation process, the X-ray energy associate with thallium was not detected in prepared cell sections. Preparing samples for this method was labour-intensive, required a specific protocol to preserve thallium in its original location and specialised equipment. Nonetheless, although the protocol initially developed was not effective for analysing free thallium, it proved to be effective in assessing localisation of thallium bound to PBNPs. By combining EDS signals with TEM images, it became possible to precisely allocate thallium and iron signals to the nanoparticles with exceptional resolution, while at the same time revealing intricate details of the cell's interior. The acquired energy spectra further validated the increased thallium concentration within the regions containing the nanoparticles, in contrast to nanoparticle-free areas. TEM was employed to pinpoint the location of nanoparticles within the cells. For sample preparation, a method involving chemical fixation and paraffin embedding was selected, resulting in the production of high-contrast images.

Another method suitable for detecting PBNPs inside cancer cells was fluorescence microscopy. It is a very sensitive technique with a resolution similar to that of bright-field microscopy and has been widely used in studies on nanoparticle biodistribution [204]. Human embryonic kidney cells treated with caPBNPs conjugated to 5-(aminoacetamido) fluorescein exhibited a strong fluorescent signal in both the cytoplasm and endosomal compartments [145]. One of the limitations of evaluating NPs distribution with this method is the fact that fluorescent modifications of NPs surface may impact their size, molecular weight and structure and hence change their bioreactivity and transport inside cells.

Within the large range of analytical methods accessible for evaluating subcellular biodistribution of elements, there are techniques that have not been explored in this chapter for thallium subcellular localisation but are worth considering. Microautoradiography stands out for its ability to achieve a high level of sensitivity, which is possible thanks to extending the duration of exposure, as autoradiographic methods can record the radioactive decay of radiolabelled compounds on cellular and subcellular level [205]. Just like the cell fractionation method, microautoradiography employs radionuclides instead of stable isotopes. This approach provides more accurate representation of radionuclide distribution within cells without the need to overload cells with non-radioactive

equivalent to achieve specific detection limits. Microautoradiography, however, is technically very challenging, prone to artefacts and presents the same sample preparation issues as discussed earlier. Additionally, resolution of this technique could be a limiting factor for biodistribution on subcellular level. For this purpose, autoradiography has to be adjusted for electron microscopy imaging by selecting photosensitive emulsions with a right grain diameter, sensitivity and tracking properties [204,206]. Despite the advantages mentioned, this method is rarely employed today to assess radionuclides biodistribution within cells, and there have been few significant advances in its application since its discovery nearly a century ago.

Another method worth mentioning here is the synchrotron-based X-ray fluorescent microscopy for its high sensitivity (concentrations in ppb) and remarkable resolution in nm scale, which is possible thanks to the synchrotron radiation [207]. X-ray fluorescence (XRF) is a technique that involves the emission of characteristic X-rays from a material when it is exposed to high-energy X-radiation providing details on the sample elemental composition in a form of two-dimensional elemental maps. However, similarly to the IBA, XRF on its own does not provide information on the cellular structure and needs to be combined with other techniques such as soft X-ray tomography or hard X-ray ptychography [182] to relate the XRF elemental maps with cellular compartments.

In summary, each of the analytical methods outlined in this discussion possess its own merits and can provide answers to a stated question from its own unique perspective. It is also important to note that these techniques often come with their limitations, which can restrict their applicability in subcellular imaging. Nevertheless, when employed in tandem or in parallel, these methods can collectively provide the most precise and comprehensive insights into elemental composition or nanoparticle distribution. The integrated approach offers a more accurate assessment and can address a wider range of research questions.

4.5.2 The main findings and their biological significance

The most suitable method for detecting and quantifying unbound thallium in single cancer cells on the subcellular level proved to be the IBA. In the course of the analysis, a higher thallium signal was detected in the area corresponding to the cell nucleus (estimated as around 64%), suggesting that unbound thallium might concentrate within the nucleus. This observation might offer an explanation for the greater radiotoxic potential of free ^{201}Tl in comparison to ^{201}Tl bound by PBNPs described in the previous chapter. As of now, the potassium ions gradient across the nuclear membrane remains unknown in the intact cells [208], so it is unclear whether thallium ions mimic potassium ions in this respect. While several potassium channels have been previously identified within the nuclear

envelope [65], their precise role in cancer cells remains poorly understood. Among these channels, voltage-gated potassium channels, known as $K_v1.3$, have been discovered in the nuclear membrane of various human cancer cells and normal brain tissue, and demonstrated the ability to regulate the nuclear membrane potential and activate specific transcription factors [209]. Another type of voltage-gated potassium channels, called $K_v10.1$, have been found in the inner nuclear membrane in both human and rat models. It was postulated that $K_v10.1$ may be involved in maintaining potassium homeostasis in the nucleus and potentially indirectly interacting with heterochromatin influencing gene expression and genome stability [210]. The behaviour of potassium in the nucleus may offer insights into why thallium concentrates there, assuming it mimics the behaviour of potassium. This is further supported by reports linking thallium toxicity with nuclear damage and mutagenic effects within cells [178–180].

In case of thallium bound to PBNPs, EDS coupled with TEM was very effective in assessing thallium subcellular distribution, able to detect increased thallium concentration within the regions of a cell containing the nanoparticles, in contrast to nanoparticle-free areas. Although there was a notable increase in Tl-chPBNPs presence within the cell cytoplasm imaged with EDS/TEM compared to Tl-caPBNPs, consistent with their higher than caPBNPs cellular uptake, no visible difference in the subcellular distribution was observed between chPBNPs and caPBNPs. Both types of PBNPs were predominantly observed in clusters in the cytoplasmic region of the cell. TEM alone provided the capability to localised PBNPs in lung cancer cells and revealed in detail the journey of these nanoparticles once inside the cell. The process began with nanoparticle interactions with the cell membrane, subsequent engulfment by the membrane to form endosomal vesicles, and their release into the cytoplasm. This route is consistent with the endocytic mechanism of entry, which is very common among nanoparticles [211]. These findings also support previous observations of caPBNPs being contained within vesicles within the cytoplasm in breast cancer cells exposed to a concentration of 0.25 mg/mL of caPBNPs [131]. Moreover, the presence of some PBNPs in the cytoplasm without encapsulation in organelles was also demonstrated in our TEM images, where individual nanopartides were observed, with a few even visible in the cell nucleus. Nevertheless, it is possible that due to the nanometre size of individual nanoparticles, they could easily escape detection. Another important observation derived from the comparison of unbound Tl and Tl bound to PBNPs is that, when using the same EDS method settings, thallium was detectable in cell sections only when it was concentrated in a very small area. Therefore, it can be concluded, that when free thallium is taken up by cells, it doesn't accumulate in one specific location but is, instead, dispersed across a larger volume, making it more challenging to detect. Quantifying the amount of thallium located within PBNPs using EDS

allowed to estimate that around 130 to 160 times more thallium is present in the regions of PB nanoparticles compared to nanoparticle-free regions.

Nanoparticles can enter the nucleus through either passive diffusion across nuclear envelope pores or active transport facilitated by nuclear pore complexes (NPCs). The mode of transport mostly depends on the size of the nanoparticles and is dictated by the dimensions of the pores in the nuclear envelope [186]. Given that the sizes of both caPBNPs and chPBNPs are approximately 50 nm, they would not be expected to enter the nucleus passively, without attached nuclear localisation signal (NLS) recognised by the NPCs. However, chPBNPs possess a highly positive surface charge, which could potentially attract the NPs toward the negatively charged nuclear envelope. Indeed, TEM images revealed that numerous chPBNPs were in close proximity to the nuclear envelope, though they were not found inside the nucleus itself. This close proximity to the nucleus may explain the higher radiotoxic effect of Tl-chPBNPs on lung cancer cells shown in chapter 3, when compared to Tl-caPBNPs.

In an alternative approach, the surface of chPBNPs was modified by incorporating the NLS, intended to enable active translocation through nuclear pore complexes (NPCs) and chPBNPs with an attached TAT peptide were synthesised. Fluorescence confocal microscopy of both chPBNPs and PBNP-TAT, each conjugated with carboxyfluorescein, showed that 22.0 ± 8.7% and 36.8 ± 12.0%, respectively, of the fluorescent signal originated from the nuclear region of the cell. Consequently, the attachment of the TAT peptide resulted in a 14.8% increase in chPBNPs nuclear localisation, demonstrating that it is possible to enhance nuclear targeting through nanoparticle surface modifications. It cannot be ruled out that this moderate increase is linked to the presence of carboxyfluorescein, which might hinder the recognition of TAT by the nuclear pore complexes (NPCs). Therefore, once chPBNPs-TAT are successfully synthesised, they may reveal additional improvements in nuclear localisation.

Discovering the preference of thallium ions for the cell nucleus holds potentially great significance when it comes to the design of radiopharmaceuticals containing ^{201}Tl. It is essential to recognise that the majority of radiolabelled conjugates, whether composed of peptides or antibodies, are typically distributed on the cell surface or within the cell cytoplasm. Therefore, in addition to targeting the radiopharmaceutical specifically to the cancer cell, there may be a need for subcellular targeting to the nuclear compartment. Alternatively, a controlled release of ^{201}Tl from the radiolabelled compound, in the proximity of the nucleus, could also prove effective, provided that free thallium does not immediately exit the cell after release via the efflux. This mechanism was suggested for ^{201}Tl-chPBNPs in chapter 3, where we observed a slower washout of ^{201}Tl from tumours in mice injected with ^{201}Tl-chPBNPs compared to mice injected with unbound ^{201}Tl. The same mechanism could underlie the radiotoxic effect of ^{201}Tl bound by nanotexaphyrins, described in chapter 5.

Given that the methods detailed in this chapter did not allow for a precise localisation of unbound Tl in the cytoplasm, we cannot rule out the possibility that thallium may also favour other subcellular compartments such as mitochondria. The inner mitochondrial membrane is equipped with several potassium channels, and it is anticipated that potassium ion fluxes play an important role in oxidative phosphorylation [208]. It is then plausible that unbound thallium, by substituting for potassium, gains access to mitochondria. Targeting therapeutics to mitochondria is becoming increasingly feasible and has recently gained greater attention within the research community [212,213]. Hence, more effort in needed to develop a method or a combination of methods, which will allow determination of the subcellular localisation of thallium at the nanometre scale and with exceptional sensitivity, capable of detecting even trace levels of thallium.

4.6 Conclusions

Various analytical methods were employed to examine the subcellular distribution of both unbound thallium and thallium bound to PBNPs. These methods had different detection limits and resolution, utilising both radioactive and stable thallium isotopes. Two sample preparation techniques were employed for this purpose, chemical fixation/paraffin embedding and rapid freezing, depending on the specific needs of the analytical method used. For assessing the subcellular distribution of unbound thallium, IBA proved to be the best method, allowing quantification of the thallium signal. The calculated ratio of the amount of thallium present in the nucleus to the amount of thallium present in the cytoplasm was, on average, 1.81 ± 1.50 for DU145 cells and 1.82 ± 1.03 for SKOV3 cells. For estimating the localisation of PBNPs-bound thallium, EDS combined with TEM was the most suitable method, revealing that most of thallium was present in the cytoplasmic region of the cell. A few individual nanoparticles were also identified within the cell nucleus. There was no discernible difference detected in the subcellular localisation between caPBNPs and chPBNPs. Fluorescence microscopy indicated that approximately 22.0 ± 8.7% of fluorescent chPBNPs and 36.8 ± 12.0% of fluorescent chPBNPs modified with a TAT peptide were directed to the cell nucleus. More research is needed into subcellular localistaion of thallium in order to design an efficient radiopharmaceutical and explore other cytoplasmic targets, such as mitochondria.

Chapter 5: Assembling and investigating ^{201}Tl radiolabelled texaphyrin nanoparticles

The study presented in this chapter was funded jointly by the UK-Canada Globalink Exchange Doctoral Scheme (UKRI) and Mitacs and conducted over 12 weeks in close collaboration with Professor Raymond Reilly and Professor Gang Zheng at Leslie Dan Faculty of Pharmacy, University of Toronto, Canada.

5.1 Introduction

Prussian blue nanoparticles described in chapter 3 exhibit excellent ability to bind Tl^+ ions, without the need for oxidation to Tl^{3+}. The high standard redox potential for the Tl^+/Tl^{3+} pair ($E^\circ = +1.25$ V) indicates that thallium is mostly available as Tl^+ form in aqueous solutions and strong oxidation conditions are needed to generate Tl^{3+} [214]. However, Tl^{3+} has a much smaller ionic radius in comparison to Tl^+ (103 pm vs 164 pm)[89] and chemically resembles gallium and indium [215]. ^{67}Ga and ^{111}In, which have been previously studied for Auger electron (AE) radiotherapy, can be chelated by (*inter alia*) 1,4,7,10-tetraazacyclododecanetetraacetic acid (DOTA) [216] and diethylenetriaminepentaacetic acid (DTPA) [217,218]. These chelators, however, are known to be inadequate for Tl^{3+} [98] and the development of kinetically stable chelates of thallium is still underway. Considering the electrophilic character of Tl^{3+}, formation of complexes with electron-rich species, such as oxygen- and nitrogen-containing neutral molecules or anions, is preferable and might help to stabilise the tripositive oxidation state. Only a few chelators for Tl^{3+} have been assessed in the past, for example DOTA [89], DTPA [214], ethylenediaminetetraacetic acid (EDTA)[98], H_4pypa [99] and porphyrin derivatives [219], but all proved to have low stability when tested either in vitro or in vivo due to the Tl^{3+} reduction to 1+ oxidation state, and subsequent or simultaneous metal dissociation from the metal-complex. Bis-thallium (I) complexes of porphyrin derivatives have been synthesised using octaethylporphyrin (OEP) and tetraphenylporphyrin (TPP) with two Tl^+ ions bound per porphyrin ligand ('sandwich type' complexes), but these complexes were prone to the loss of metal in solution [220]. As mentioned before, Tl^{3+} ions, with a smaller ionic radius and higher oxidation state compared to Tl^+, should form more stable metal-complexes. Yet, the crystal structure of thallium (III) - Cl-OEP (2,3,7,8,12,13,17,18 octaethylporphyrinchlorothallium (III)) revealed a 5-coordinate complex with central Tl^{3+} ion displaced above the plane of the porphyrin ring [95] causing a distortion in the porphyrin macrocycle [96]. Furthermore, 5,10,15,20-tetrakis(pentafluorophenyl)porphyrin (PFPP)-Tl (III) complex, when tested in vivo in healthy rats, showed poor chelation stability as evidenced by free thallium ions accumulating

in myocardium [221]. While porphyrin derivatives have the capability to form complexes with Tl^{3+} and to some extend with Tl^{+}, the chelated thallium ion placed in the central cavity appeared to be too large to be accommodated inside the central porphyrin macrocycle with radius between 193 pm and 209 pm causing a distortion in the macrocycle geometry and the instability of the metal complex [95].

Texaphyrins are a synthetic subclass of porphyrins, also called 'expanded porphyrins' with a pentadentate cavity that binds metals through five donor nitrogen atoms, compared to a tetradentate cavity with four donor nitrogen atoms seen in porphyrins (Fig. 5.1) [222]. The inner coordination core of texaphyrins is around 20% larger in radius than the core present in porphyrin structures. Additionally, texaphyrins have a larger degree of aromatic delocalization within the macrocycle compared to porphyrins. The texaphyrins form stable, 1:1 complexes with a variety of metals, including indium (In^{3+}), bismuth (Bi^{3+}), manganese (Mn^{2+}) and trivalent lanthanides [222] with large ionic radii.

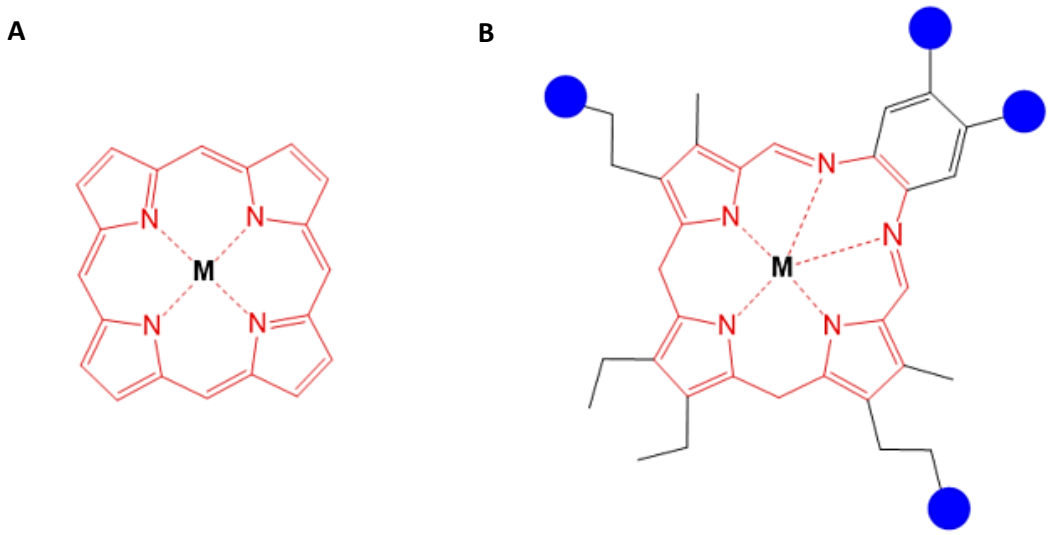

Figure 5.1 Comparison of porphyrin and texaphyrin macrocycles. A) The structure of porphyrin macrocycle with coordinated metal ion. **B)** The structure of texaphyrin with macrocycle marked in red and sites available for functionalisation (blue dots). M - coordinated metal.

The texaphyrin macrocycle contains multiple functionalisation sites (Fig. 5.1 B), enabling the attachment of a diverse array of moieties to the texaphyrin ring to achieve specific functionalities [223]. Examples of these modifications include conjugating polyethylene glycol (PEG) groups to increase texaphyrin bioavailability [224], attaching platinum-based compounds to overcome platinum resistance in cancer treatment [225], or incorporating a prostate cancer targeting ligand into the texaphyrin structure for a selective tumour delivery and enhanced cellular uptake [32]. Texaphyrins

can also be linked to phospholipids forming amphiphilic texaphyrin-phospholipid conjugates that have the capacity to self-assemble into liposome-like nanoparticles, known as nanotexaphyrins [223]. These nanostructures are capable of effectively binding radiometals without requiring an additional chelating agent. Depending on the coordinated metal (Gd, In, Mn, Lu), nanotexaphyrins can have versatile applications across a spectrum of diagnostic and therapeutic modalities, such as magnetic resonance imaging (MRI), single-photon emission computed tomography (SPECT), radiotherapy and photodynamic therapy (PDT) [32]. Successfully engineered dual mode ^{111}In-Mn-texaphyrin nanoparticles developed for SPECT and MRI diagnostics showed strong structural and metal chelation stability [226]. Furthermore, the biodistribution studies of ^{111}In-Mn-nanotexaphyrins in an orthotopic prostatic mouse model demonstrated non-targeted tumour uptake and retention at 22 h post-injection [226]. Texaphyrin-based nanoparticles with chelated metal ions have also great potential for multimodal theranostic applications, such as combining SPECT imaging with PDT by formulating hybrid ^{111}In/Lu nanotexaphyrins with prostate specific membrane antigen (PSMA) – targeting ligand. When tested in a murine tumour model, PSMA - ^{111}In/Lu nanotexaphyrins have shown increased specific tumour accumulation and demonstrated therapeutic potential by significantly delaying tumour growth [32].

Consequently, we surmise that texaphyrin compounds and texaphyrin nanoparticles might have potential as delivery systems for Tl^{+} and Tl^{3+} ions. Among other classes of chelators currently being explored by other members of the KCL team, this chapter describes an investigation of using texaphyrin-lipids and nanotexaphyrins as an innovative approach to solve the challenges in efficiently complexing ^{201}Tl and to selectively deliver ^{201}Tl into cancer cells for AE radiotherapy.

5.2 Aims

The aim of this study was to use the texaphyrin structure as a chelation platform to effectively bind Tl^{3+} ions for targeted delivery of ^{201}Tl to cancer cells for radionuclide therapy purposes (Fig. 5.2).

Since nanotexaphyrins effectively bind radiometals within their nanostructure, forming stable complexes without the need for additional chelators, they can potentially offer more protection against environmental factors such as reducing agents, and therefore stabilise thallium ions in 3+ oxidation state.

The main objectives for this preliminary project were to investigate the chelation conditions required to efficiently bind Tl^{3+} to texaphyrin-phospholipid (texaphyrin-lipid), assemble Tl-nanotexaphyrins,

characterise them and test their stability and uptake in lung cancer cell (A549) and ovarian cancer cells (SKOV3). These cell lines were chosen for the in vitro experiments due to their phagocytic properties, relatively high non-specific uptake of nanoparticles and availability.

This study involved work with non-radioactive Tl^{+} and Tl^{3+}, which were used for characterisation of Tl-texaphyrin-lipid complexes and testing their stability, as well as improving the nanoparticle assembling method and performing nanoparticle characterisation. ^{201}Tl was used to optimise the Tl^{+}/Tl^{3+} oxidation reaction and find the best radiolabelling conditions, assembling ^{201}Tl-nanotexaphyrins and testing their radiostability, cellular uptake and subcellular distribution.

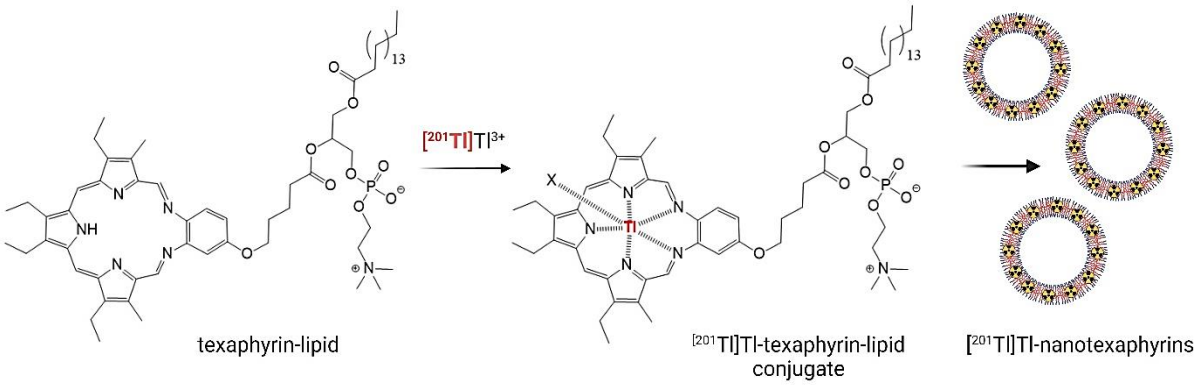

Figure 5.2 Schematic representation of $^{201}Tl^{3+}$ binding to the texaphyrin-lipid macrocycle, following by a formation of nanotexaphyrins.

5.3 Materials and methods

5.3.1 Materials: TlCl 10 mM solution was prepared by dissolving 2.4 mg of TlCl in 1000 µL of MilliQ water (18.2 MΩ.cm), sonicating and heating at 40°C for 1 h. 0.05 - 2.5 M HCl solution was prepared by diluting 37% HCl with MilliQ water. Texaphyrin-lipids were synthesised according to the method described previously by Prof G. Zheng's group [226] and the structure was confirmed by ultra-high performance liquid chromatography-mass spectrometry (UHPLC-MS). Texaphyrin-lipid 1 mM solution was obtained by dissolving 1 mg in 920 µL of 99.9% ethanol. 25 mM KCl solution was prepared by dissolving 75.5 mg KCl (EMD Millipore) in 50 mL of MilliQ water. Cell culture consumables and chemical compounds, unless specified, were purchased from Sigma-Aldrich, Canada. [^{201}Tl]TlCl in sterile, 0.9%

NaCl solution (213 - 236 MBq/2.8 mL) was obtained from Curium, USA (2.8 mCi/2.8 mL on the calibration date).

5.3.2 Cell culture: human lung cancer cells A549 (courtesy of Prof G. Zheng's group, Princess Margaret Cancer Research Centre, 101 College Street, Room 5-354, Toronto, M5G 1L7, Canada) and human ovarian cancer cells SKOV3 (Prof R. Reilly's group, Leslie Dan Faculty of Pharmacy, University of Toronto, 144 College St., Toronto, M5S 3M2, Canada) were cultured in RPMI-1640 medium (R8758). Both media were supplemented with 10% fetal bovine serum (Gibco, 12484-028), penicillin (100 units) and 100 µg/mL streptomycin. Cultured cells were trypsinised and seeded at 100,000 cells per well in 24-well plates 16 hours before each experiment and grown at 37°C in a humidified 5% CO_2 atmosphere. During experiments, cells were kept in fully supplemented medium. Cells were counted by the Bio Rad T20™ automated cell counter.

5.3.3 $^{201}Tl^{+}$/$^{201}Tl^{3+}$ and Tl^{+}/Tl^{3+} oxidation: the oxidation method described previously [98] was used with some modifications. Briefly, 100 µL of [^{201}Tl]TlCl or stable 10 mM TlCl aqueous solution was added to an oxidation bead (Pierce™ Iodination Beads, N-chloro-benzenesulfonamide sodium salt, ThermoFisher Scientific), then 10 µL of 2.5 M HCl (Fisher Chemicals) was added and the solution was shaken for 1 to 2 h. ^{201}Tl oxidation efficiency was assessed by the TLC method with acetone as a mobile phase [98] and TLC-SG chromatography paper (silica gel impregnated glass fibre, Pall Corporation) as solid phase. TLC plates were imaged with a Cyclone Plus Storage Phosphor System (Fig. 5.3 A).

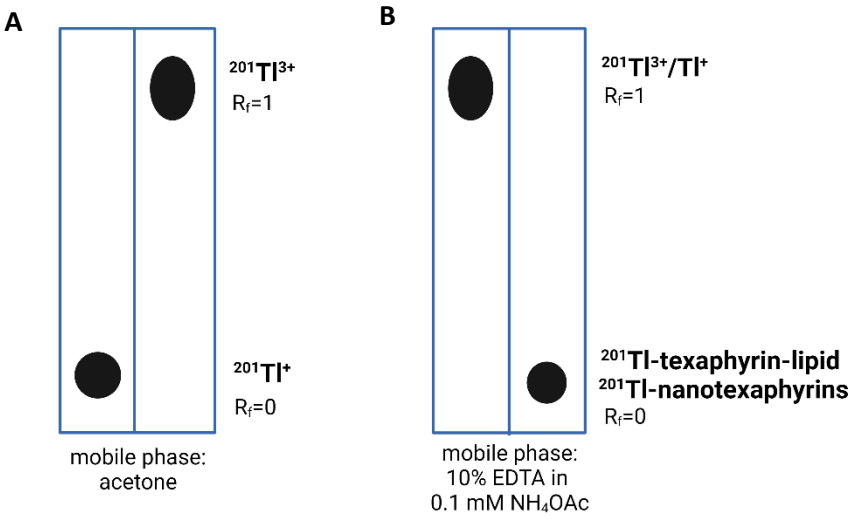

Figure 5.3 Schematic representation of the TLC method used in the study. TLC plate showing **A)** quantification of ^{201}Tl oxidation reaction and **B)** assessing ^{201}Tl-texaphyrin-lipid chelation yield and ^{201}Tl-nanotexaphyrins purity.

5.3.4 $^{201}Tl^{3+}/Tl^{3+}$ chelation with texaphyrin-lipids: 100 µL of oxidised [^{201}Tl]$TlCl_3$ or $TlCl_3$ was diluted five-fold with 0.1 M NH_4OAc buffer (pH = 7) or water and 1 mM texaphyrin-lipid ethanol solution was added. For ^{201}Tl, the molar ratio texaphyrin-lipid:Tl was calculated as 1:0.005 based on the concentration of non-radioactive ^{203}Tl in [^{201}Tl]TlCl measured previously (0.8 µmol/L ^{203}Tl, [140]). For non-radioactive thallium, texaphyrin-lipid:Tl ratio was set as 1:1 or 1:2. After adding [^{201}Tl]$TlCl_3$ or $TlCl_3$ to the texaphyrin-lipid solution, the mixture was left for 1 h at room temperature (RT); a change in colour was observed when forming non-radioactive Tl-texaphyrin-lipids from brown to green. A TLC method involving TLC-SG chromatography paper (silica gel impregnated glass fibre, Pall Corporation) and a mobile phase of 10% EDTA solution in 0.1 M NH_4OAc was used to assess chelation efficiency of ^{201}Tl-texaphyrin-lipids (Fig. 5.3 B). TLC plates were imaged with a Cyclone Plus Storage Phosphor System. UV-Vis spectra of non-radioactive Tl-texaphyrin-lipids were obtained with spectrophotometer (Biochrom Ultraspec 3100 Pro), after 6 to 7-fold dilution in 99.9% ethanol. UHPLC-MS was performed using a Waters Acquity UPLC Peptide BEH C18 column (130 A, 1.7 µm, 2.1 mm x 50 mm) with Waters 2695 controller, 2996 photodiode array detector and a Waters triple quadrupole mass detector (mobile phase: 0.1% TFA (A) and acetonitrile (B) in gradient (60% A + 40% B to 0% A+ 100% B in 3 min, kept at 100% B for 1 min, followed by a sharp change back to 60% A + 40% B), column temperature: 60°C, flow rate: 0.6 mL/min, positive ion mode ESI). Samples were diluted 10-fold in 99.9% ethanol. Mn and Cd complexes with texaphyrin-lipids were provided by Prof Gang Zheng's group [19,21].

5.3.5 Synthesis of ^{201}Tl-nanotexaphyrins and Tl-nanotexaphyrins: 150 µL of ethanol solution containing cholesterol (CHL, 40.6% total molar content), DSPE-PEG_{2000} (distearoylphosphatidylcholine polyethylene glycol 2000; 5.0% total molar content) and 1 mg DPPC (dipalmitoylphosphatidylcholine, 44.4-53.4% total molar content) (Avanti Polar Lipids, Inc) was added to 100 µL ^{201}Tl-texaphyrin-lipids or Tl-texaphyrin-lipids, mixed, and moved to a 1 mL syringe, then slowly co-injected with 750 µL of 0.1 M NH_4OAc buffer placed in a second 1 mL syringe via a microfluidic chip (Microfluidic Chip Shop) as illustrated in Figure 5.4.

Crude ^{201}Tl-nanotexaphyrin and Tl-nanotexaphyrin were purified with Amicon-Ultra 0.5 mL filter tubes (30,000 MWCO, Millipore) and centrifuged for 10 min at 12,000 rpm, then washed with 200 µL of phosphate buffered saline (PBS) 3-5 times. An TLC method (TLC-SG chromatography paper, mobile phase: 10% EDTA solution in 0.1 M NH_4OAc) was used to assess ^{201}Tl-nanotexaphyrin purity (Fig. 5.3 B). Activity of purified ^{201}Tl-nanotexaphyrins was measured with a dose calibrator (Capintec) and compared to the starting [^{201}Tl]TlCl activity for assessing the radiolabelling efficiency (RE).

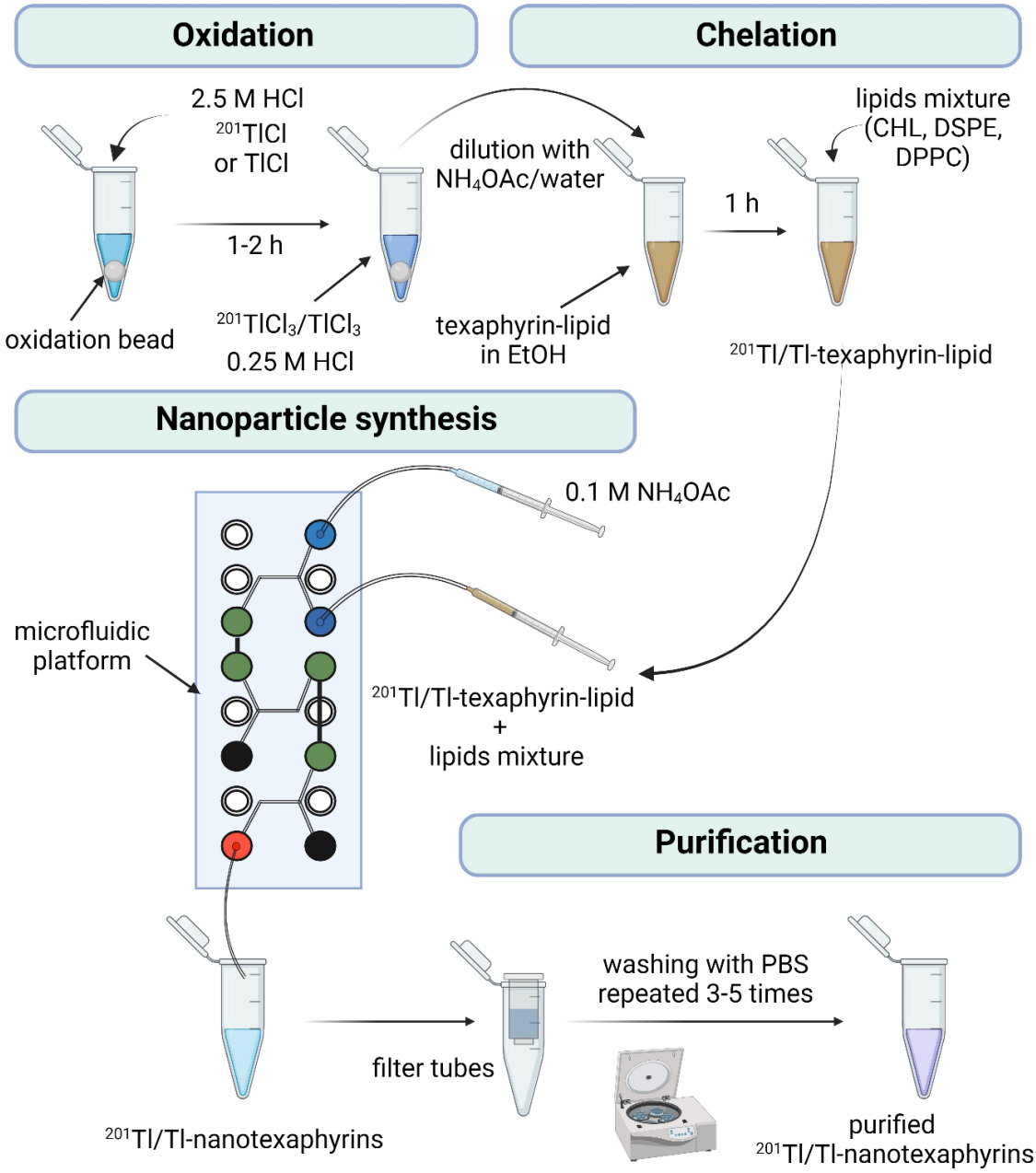

Figure 5.4 ^{201}Tl-nanotexaphyrins and Tl-nanotexaphyrins synthesis diagram including Tl^+/Tl^{3+} oxidation, dilution and chelation reaction with texaphyrin-lipids, synthesis of ^{201}Tl-nanotexaphyrins and Tl-nanotexaphyrins followed by their purification process.

5.3.6 Stability studies: Tl-texaphyrin-lipids were kept for up to 72 h either at RT or 37°C and analysed visually, by UV-Vis spectrometry and UHPLC-MS chromatography as described above. The size and dispersity of synthesised Tl-nanotexaphyrins were assessed in PBS by DLS measurements over a period of 72 h in a temperature range of 4-37°C. ^{201}Tl-nanotexaphyrins were kept in PBS at 4°C and 37°C for

up to 72 h and the radiostability was tested with a TLC method (mobile phase used: 10% EDTA in 0.1 M NH_4AcOH) (Fig. 5.3 B).

5.3.7 Characterisation of Tl-nanotexaphyrins: to determine the hydrodynamic diameter, polydispersity index (PDI) and surface charge of the nanoparticles, Tl-nanotexaphyrins were characterised using Malvern Zetasizer Nano-ZS 90 device. Tl-nanotexaphyrins suspension was diluted 10 times with PBS for the size measurements whereas no dilutions were made for the zeta potential measurements. Fluorescence spectra of intact Tl-nanotexaphyrins in PBS and disrupted Tl-nanotexaphyrins in methanol were measured using a Fluoromax fluorimeter (Horiba Jobin Yvon); the nanoparticles were excited at 465 nm, and emission spectra were collected from 700 to 850 nm. Transmission electron microscopy (TEM) images were obtained with FEI Tecnai 20 microscope (200 kV voltage) by Dr Miffy Cheng; Tl-nanotexaphyrin suspension was placed on a carbon-coated copper grids and negatively stained with 2% uranyl acetate.

5.3.8 Cellular uptake: fifteen minutes before the experiment, the culture medium in each well was replaced by 190 or 200 µL of fresh RPMI medium. To some wells, 10 µL of 25 mM KCl solution was added (to a total of 200 µL volume). Purified ^{201}Tl-nanotexaphyrins or Tl-nanotexaphyrins were diluted with PBS to the required concentration (1 MBq/mL or 20 µmol/L) and 50 µL was added to each well. Oxidised [^{201}Tl]TlCl or TlCl was diluted with PBS to the same concentration as ^{201}Tl/Tl-nanotexaphyrins and was added to each well as 50 µL. Plates were incubated at 37°C for 16 h, then the incubation solution was collected. Adherent cells were briefly washed thrice with PBS and lysed with 1 M NaOH for 15 min at RT. For the radioactive uptake: unbound radioactivity (incubation medium and PBS washings) and cell-bound radioactivity (lysate) were measured (counts per minute, CPM) with a gamma counter (Perkin Elmer Wallac Wizard 3 1480 Automatic Gamma counter). For the non-radioactive uptake: all samples were placed in a vacuum centrifuge and left overnight to evaporate water. Then, 100 µL of 70% (v/v) HNO_3 (environmental grade) was added to each Eppendorf tube and heated at 60°C for 2 h, and 1000 µL of 2% (v/v) HNO_3 was added to each sample, the contents vortexed and centrifuged for 5 min at 12,000 rpm. 800 µL of the supernatant was collected, added to 2 mL 2% (v/v) HNO_3, mixed and analysed by the PerkinElmer NexION 350 Inductively coupled plasma-mass spectrometer. A series of standards (10^{-2}-10^{-7} mg/L) were prepared diluting 1 g/L of TlCl solution in 2% (v/v) HNO_3 and calibration lines (as linear regression lines) were drawn for ^{203}Tl and ^{205}Tl. Quality of the ICP-MS measurements was ensured through repeat measurements of blanks and internal ^{193}Ir standards.

5.3.9 Cell fractionation: a fractionation method described in chapter 4 was used [184]. In brief, fifteen minutes before the experiment, medium in each well was replaced by 200 µL fresh medium. Purified ^{201}Tl-nanotexaphyrins were diluted with PBS to the required concentration (1 MBq/mL) and 50 µL was added to each well. Oxidised [^{201}Tl]$TlCl_3$ was diluted in the same manner. After 16 h of incubation at 37°C in a humidified 5% CO_2 atmosphere, the 24-well plates were put on ice, the radioactive incubation solution was collected, adherent cells were briefly washed three times with 250 µL of cold PBS. The activity present in all PBS washes and the medium was measured by a gamma counter ('medium' fraction). Then, 250 µL of cold 200 mM sodium acetate solution and 500 mM sodium chloride (pH = 2.5) were added to each well, incubated with cells on ice for 10 min and then removed, combined with a subsequent wash of 250 µL of cold PBS, and measured as a fraction by the gamma counter ('membrane' fraction). Next, the cells were lysed with 250 µL of cold Nuclei EZ Lysis buffer on ice. After 2 h incubation, cells were transferred to Eppendorf microcentrifuge tubes, centrifuged for 5 min at 1,000 rpm and the supernatant was collected. The remaining pellet was resuspended in 250 µL of cold PBS, centrifuged, and again the supernatant was collected. This process was repeated, and the supernatants were combined. The activity present in the combined supernatant fractions ('cytoplasmic' fraction) and the activity present in the pellet ('nuclear' fraction) were quantified by a gamma counter (as counts per minute, CPM).

5.3.10 Data analysis: results were analysed in Excel Microsoft 2016, GraphPad Prism 9 and ChemDraw 20.1, and expressed as mean ± SD. Figures were created with GraphPad Prism 9 and BioRender.com.

5.4 Results

5.4.1 $^{201}Tl^{+}$/$^{201}Tl^{3+}$ and Tl^{+}/Tl^{3+} oxidation reaction was conducted using an oxidising agent containing N-chloro-benzenesulfonamide (Iodobead) in 0.25 M HCl solution. Quantification was achieved through the TLC method (mobile phase: acetone), resulting in an average yield of 91.8 ± 3.1% (n=12). Upon removal of the oxidation bead from the reaction mixture, it was determined that oxidised $^{201}Tl^{3+}$ remained stable for a minimum of 72 h when stored at 4°C in 0.25 M HCl (Table 5.1).

Time (h)	$^{201}Tl^{3+}$ (%)
2	92.1 ± 3.3
24	91.5 ± 10.6
48	85.8 ± 3.4
72	86.8 ± 2.7

Table 5.1 $^{201}Tl^{3+}$ stability (expressed as % of total activity) in 0.25 M HCl after removal of the iodobead at 4 °C. The stability was assessed by the TLC method, solid phase: ITLC-SG, mobile phase: acetone, n=3.

Nevertheless, it was noted that 30-50% of the total ^{201}Tl activity used initially for the oxidation reaction adhered to the oxidation bead after its removal (oxidation bead was measured by a dose calibrator Capintec), and subsequent washes with 0.25 M HCl managed to recover only a small amount of the activity. The recovery method was deemed impractical due to the resultant sample dilution. The addition of the appropriate concentration of HCl was imperative for the oxidation reaction yield. Reducing the concentration of HCl from 0.25 M to 0.05 M led to a substantial decline in the conversion of $^{201}Tl^{+}$ to $^{201}Tl^{3+}$ as illustrated in Figure 5.5.

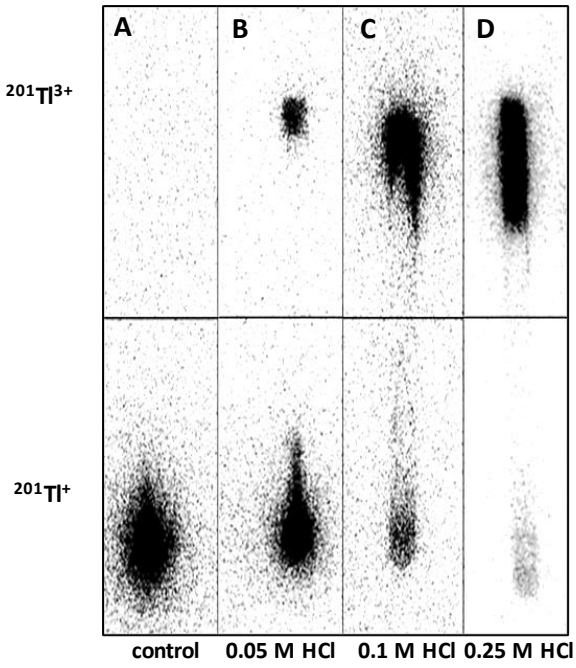

Figure 5.5 TLC analysis of $^{201}Tl^{+}/Tl^{3+}$ oxidation reaction performed with an oxidation bead (Iodobead) in various concentrations of HCl and imaged with a phosphor imager. **A)** TLC plate representing $^{201}Tl^{+}$ at the bottom of the plate when no oxidation agent was used (control). TLC plates representing $^{201}Tl^{+}$ at the bottom and $^{201}Tl^{3+}$ at the top of the plate after oxidation reaction was performed in **B)** in 0.05 M HCl solution, **C)** in 0.1 M HCl solution and **D)** 0.25 M HCl solution. Solid phase: ITLC-SG, mobile phase: acetone. $^{201}Tl^{3+}$ in these conditions migrate with the solvent front ($R_f = 1$) while $^{201}Tl^{+}$ remain at the baseline ($R_f = 0$).

Despite the absence of an analytical method to evaluate the conversion of non-radioactive Tl^{+} to Tl^{3+}, the conclusion was drawn that the oxidation reaction was occurring under the conditions tested, based on the following observation: when texaphyrin-lipids were incubated with TlCl solution in 0.25 M HCl, no change in colour was observed, and neither UV-Vis spectroscopy nor UHPLC-MS detected the presence of a Tl-texaphyrin-lipid complex. It was concluded that Tl^{+} cannot be chelated by texaphyrin-lipids under these conditions. However, when the texaphyrin-lipid solution was introduced to the same TlCl solution in 0.25 M HCl in the presence of the oxidising agent, a transformation occurred after approximately 0.5 h, resulting in a change of the mixture's colour to dark green, which

suggested the formation of Tl-texaphyrin-lipid complex. Furthermore, the existence of the texaphyrin-metal complex was confirmed through available analytical methods, described later in this chapter. The observations were similar when $TlCl_3$ in 0.25 M HCl was added to texaphyrin-lipid solution instead of TlCl (Fig. 5.6).

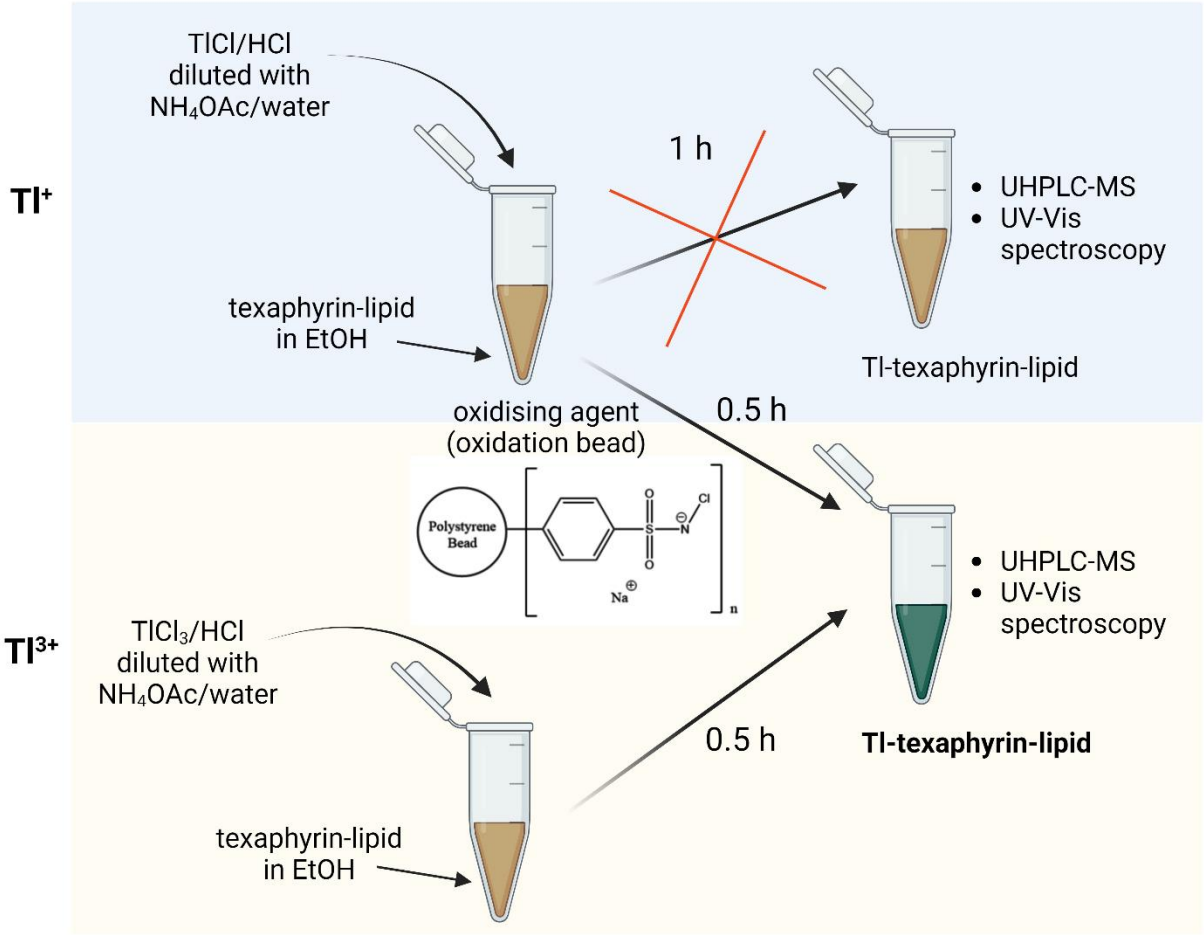

Figure 5.6 Schematic illustration of the oxidation reaction of Tl^{+} to Tl^{3+} and complex formation with texaphyrin-lipids. When TlCl is used as a substrate without the oxidation agent, the Tl-texaphyrin-lipid complex is not formed (no colour change). $TlCl_3$ and the addition of the oxidising agent to TlCl/HCl mixture enables the Tl-texaphyrin-lipid complex formation.

5.4.2 $^{201}Tl^{3+}/Tl^{3+}$ chelation with texaphyrin-lipids. In general, texaphyrin-lipid compounds are stable except under acidic conditions, in which the imine experiences rapid hydrolysis resulting in the degradation of the texaphyrin macrocycle [228]. It was observed that immediately after adding concentrated HCl, texaphyrin-lipid ethanol solution changed colour from dark brown to light green indicating hydrolysis. Furthermore, after 6-12 h the solution turned pink, a colour typical of one of the texaphyrin-lipid precursors, suggesting further destruction of the texaphyrin-lipid compound. In order to avoid the degradation of texaphyrin-lipid macrocycle, after adding oxidised thallium ($^{201}Tl^{3+}$

or Tl^{3+}) in 0.25 M HCl, diluting or neutralising acidic conditions was necessary and therefore different solutions and buffers were tested for this purpose. Calculated amounts of $^{201}Tl^{3+}$ (%) immediately after dilution and ^{201}Tl-texaphyrin-lipid chelation reaction efficiency (%) are presented in Table 5.2.

Added solution	pH	$^{201}Tl^{3+}$ (%)	^{201}Tl-texaphyrin-lipid (%)
1. water	1	75.3 ± 6.8	25.5 ± 4.5
2. ethanol	1	85.2 ± 2.1	9.8 ± 2.2
3. PBS	3	60.1 ± 5.7	17.6 ± 3.0
4. NH_4OAc	5	56.8 ± 5.4	23.3 ± 3.2

Table 5.2 Optimising conditions of $^{201}Tl^{3+}$ chelation to texaphyrin-lipid compounds. Different solutions (1-4) were added in order to neutralise acidic solution containing $^{201}Tl^{3+}$. pH was measured with a pH paper (pHydrion, Micro Essential Laboratory). The amount of $^{201}Tl^{3+}$ (%) was quantified by TLC method using acetone as a mobile phase ($^{201}Tl^{+}$: origin; $^{201}Tl^{3+}$: solvent front). The amount of ^{201}Tl-texaphyrin-lipid (%) was quantified by TLC using 10% EDTA solution in 0.1 M NH_4OAc as a mobile phase (^{201}Tl-texaphyrin-lipid: origin; $^{201}Tl^{+}/Tl^{3+}$: solvent front), n = 3.

A TLC method with acetone or 10% EDTA solution in 0.1 M NH_4OAc buffer as a mobile phase was used to assess the amount of retained $^{201}Tl^{3+}$ after dilution or unbound $^{201}Tl^{+}/^{201}Tl^{3+}$ after chelation reaction. Examples of TLC plates are presented in Figure 5.7.

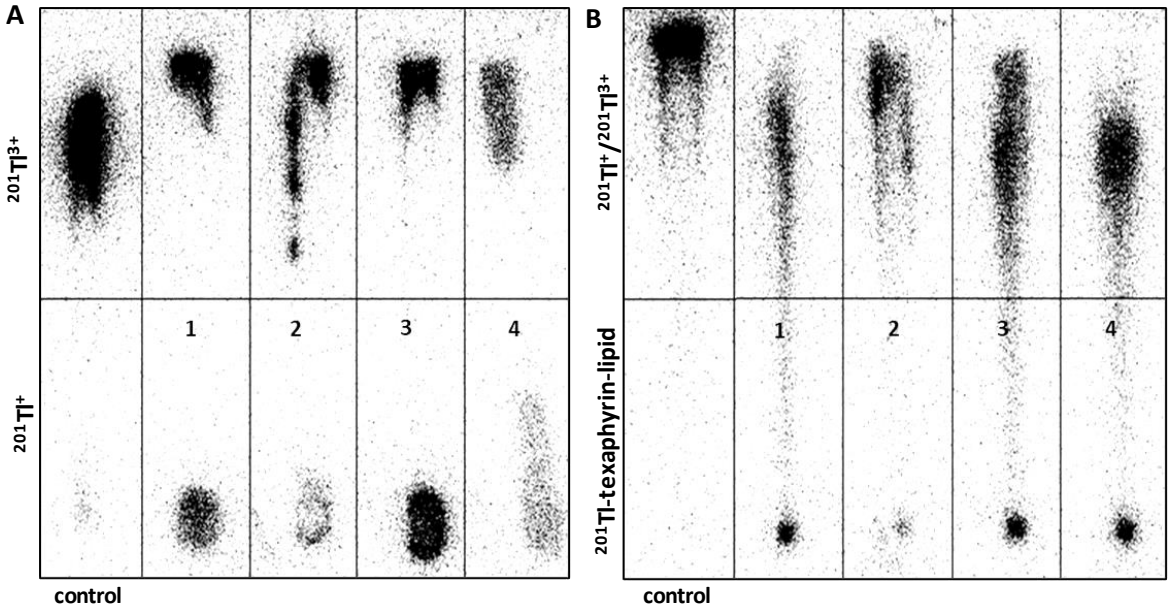

Figure 5.7 TLC images and quantification of free $^{201}Tl^{3+}$ and ^{201}Tl-texaphyrin-lipid imaged with a phosphor imager. **A)** TLC plates representing Tl^{+} at the bottom and Tl^{3+} at the top of the plate after diluting oxidised $^{201}Tl^{3+}$ in 0.25 M HCl 5 times with various solutions/buffers (1 to 4). Solid phase used: ITLC-SG, mobile phase: acetone. $^{201}Tl^{3+}$ in these conditions migrate with the solvent front (R_f = 1) while $^{201}Tl^{+}$ remain at the origin (R_f = 0). **B)** TLC plates representing ^{201}Tl-texaphyrin-lipid and free Tl^{3+}/Tl^{+}. Solid phase used: ITLC-SG, mobile phase: 10% EDTA in 0.1 M NH_4OAc. $^{201}Tl^{+}/^{201}Tl^{3+}$ in these conditions migrate with the solvent front (R_f = 1) while ^{201}Tl-texaphyrin-lipid remain at the origin (R_f = 0). Solvents/buffers used: 1) water, 2) 99.9% ethanol, 3) phosphate buffer saline, 4) ammonium acetate buffer, control: Tl^{3+} in 0.25 M HCl.

The highest chelation efficiency was observed when $^{201}Tl^{3+}$ was diluted with either water or 0.1 M NH_4OAc buffered solution (pH = 7) prior to the addition of the texaphyrin-lipids (with yields of 25.5 ± 4.5% and 23.3 ± 3.2%, respectively). These conditions were further validated during the optimisation process with stable TlCl, as Tl-texaphyrin-lipid samples remained stable for an extended duration when oxidised Tl^{3+} was diluted and neutralised with water or NH_4OAc, as opposed to PBS or ethanol.

Using these optimised conditions for the chelation of non-radioactive Tl^{3+} with texaphyrin-lipids (RT, diluted 5 times with water or NH_4OAc buffer), it was possible to obtain Tl-texaphyrin-lipid conjugates. This could be noted by a colour change from brown to dark green around 20 to 30 min after oxidised Tl^{3+} addition. The formation of the Tl-texaphyrin-lipid complex was confirmed by UV-Vis spectroscopy (Fig. 5.8) and UHPLC-MS (Fig. 5.9). Tl^{+} did not form complexes with texaphyrin-lipids under the above conditions where the oxidation agent was absent (Fig. 5.8 A and C). The absorption spectra of Tl-texaphyrin-lipid conjugates, following the oxidising of Tl^{+}, showed characteristic peaks at wavelengths of 340, 465 and 760 nm. Similar absorption spectra were also recorded for other metal chelated texaphyrin-lipids [226].

Absorption spectra of Tl-texaphyrin-lipid samples measured up to 72 h at RT remained unchanged and the green colour of the Tl-texaphyrin-lipid solution also persisted. The only exception was Tl-texaphyrin-lipid sample kept at 37°C for 24 h, where colour of the solution turned pink suggesting degradation of Tl-texaphyrin-lipid complex and the macrocycle structure (Fig. 5.8 D). This was confirmed by UV-Vis spectrometry, as no distinctive peaks indicative of Tl-texaphyrin-lipid complexes were detected.

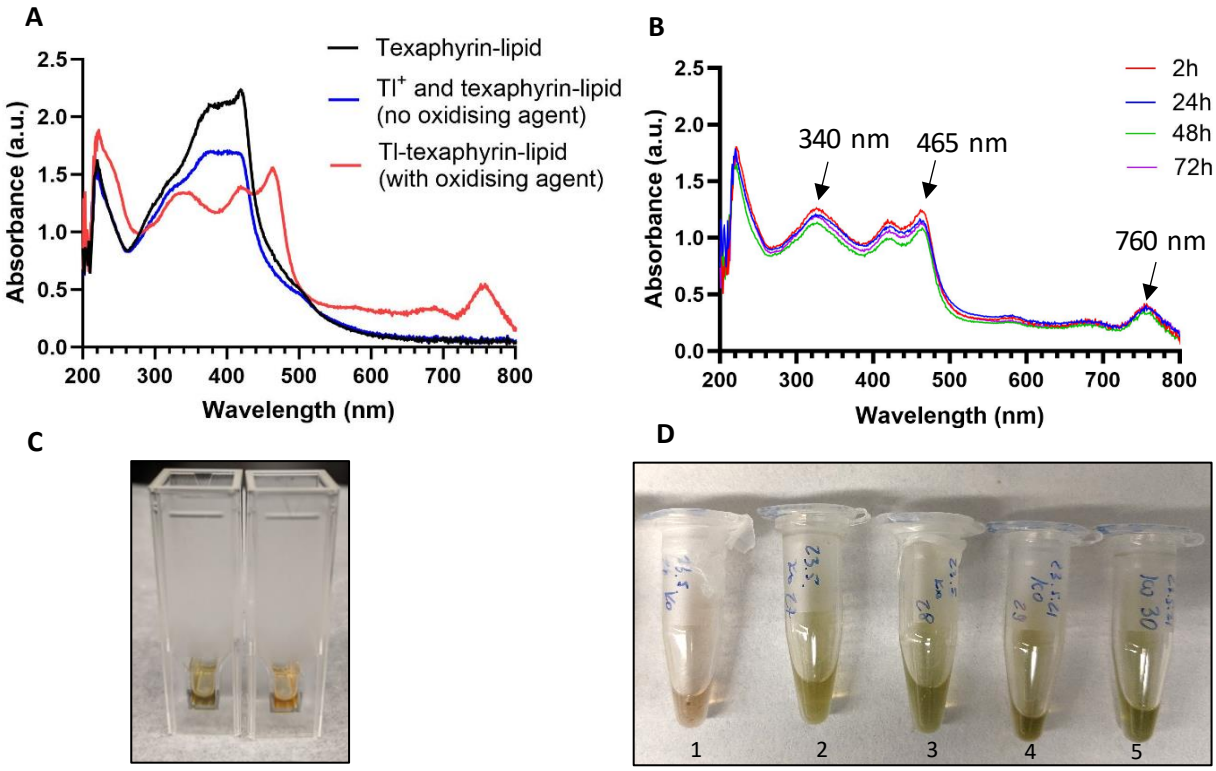

Figure 5.8 Forming complexes of Tl^{3+} with texaphyrin-lipids. A) UV-Vis spectra of texaphyrin-lipid (black line), Tl-texaphyrin-lipid after oxidation (red line) and Tl^{+} mixed with texaphyrin-lipid without the oxidising agent (blue line). **B)** UV-Vis spectra of Tl-texaphyrin-lipid (Tl^{+} oxidised with the oxidation bead) after 2-72 h at room temperature (RT). Arrows mark the absorption peaks characteristic for metalated texaphyrins. **C)** Cuvettes containing a green solution of Tl^{3+}-texaphyrin-lipid (left) and a light brown solution containing Tl^{+} with texaphyrin-lipids (right), where oxidising agent was not added. **D)** An image of Tl^{3+}-texaphyrin-lipid samples 24 h after adding Tl^{3+} to texaphyrin-lipid ethanol solution. All samples are green with the exception of sample 1, which was kept for 24 h at 37°C, whereas the rest of the samples (2-5) were kept at 25°C.

During the UHPLC-MS analysis, Tl-texaphyrin-lipid compounds displayed a retention time of 2.9 min (at wavelength of 465 nm), while the unchelated texaphyrin-lipid exhibited a retention time of approximately 3.6 min (Fig. 5.9 A and C). Previously, it was reported that a peak eluting at 3.6 min, using an identical methodology, corresponds to the unchelated texaphyrin-lipid [32]. The associated mass spectra showed the conjugate molecular weight of 1088.17 and the UV absorption spectra displayed a primary peak at 364 nm [32]. When Tl^{+} was added to texaphyrin-lipid solution in the absence of the oxidising agent (oxidation bead), there was no observed evidence of complex formation (Fig. 5.9 B). However, when Tl^{+} was oxidised, Tl-texaphyrin-lipid was formed, and peak of 2.8 min retention time was identified by a corresponding absorption spectrum and a mass spectrum (Fig. 5.9 C, D and E).

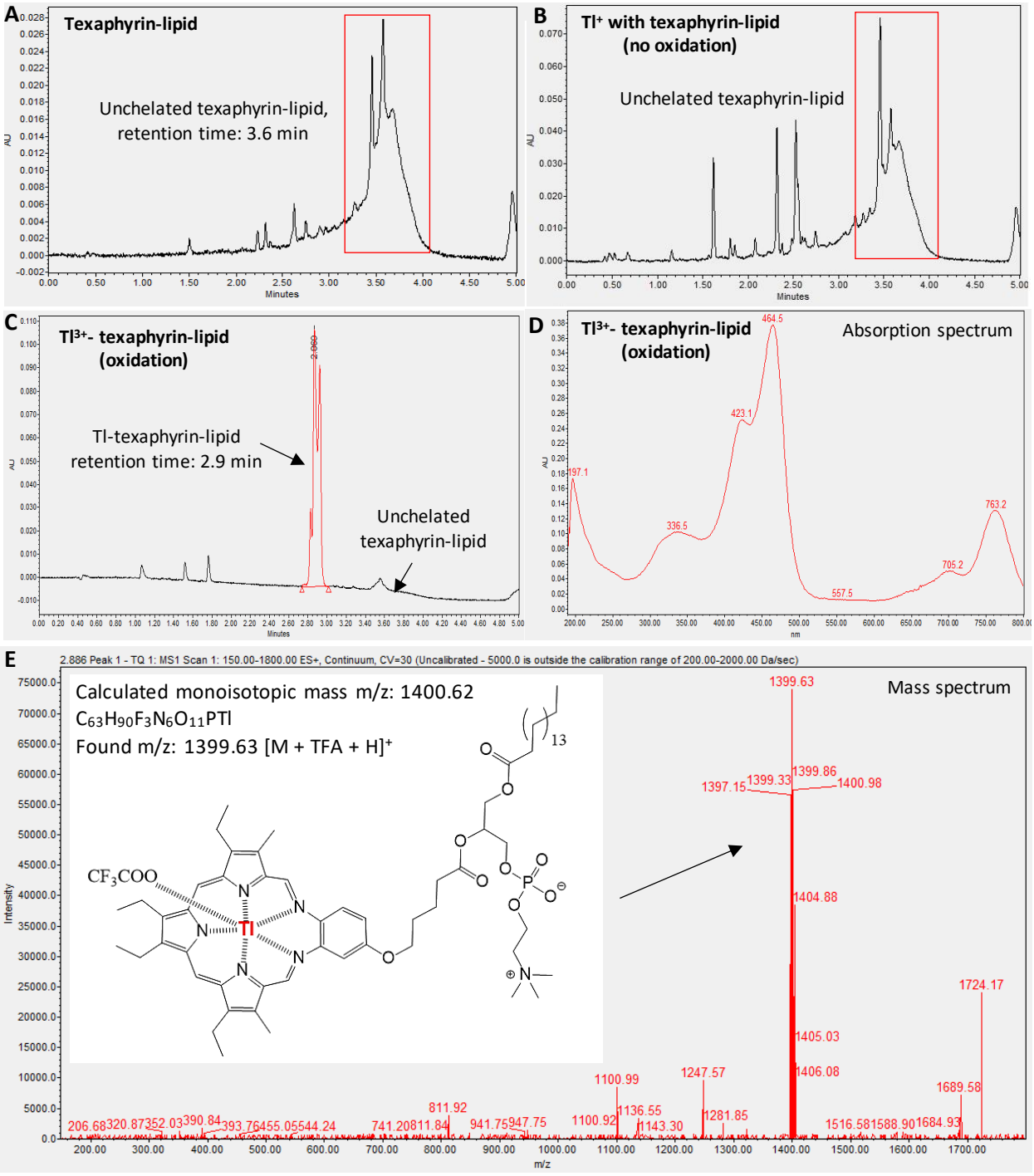

Figure 5.9 UHPLC-MS analysis of Tl-texaphyrin-lipid complexes. A) Chromatogram of unchelated texaphyrin-lipid showing the elution peak at approximately 3.6 min at 465 nm wavelength. **B)** Chromatogram of texaphyrin-lipid mixed with Tl^+ without the oxidising agent at 465 nm wavelength, showing no evidence of complex formation. **C)** Chromatogram of Tl-texaphyrin-lipid (oxidising agent used) with the elution peak at 2.9 min (465 nm wavelength) and corresponding **D)** absorption spectrum and **E)** mass spectrum of Tl-texaphyrin-lipid; m/z found: 1399.63 (main peak) matching formula of $C_{63}H_{91}F_3N_6O_{11}PTl$ (protonated Tl-texaphyrin-lipid associated with one trifluoroacetate ion); mobile phase: 0.1% TFA/acetonitrile. Exact mass: 1400.62, m/z 1400.62 (100%), 1401.62 (65.3%), 1398.62 (37.6%) (ChemDraw).

The stability of Tl-texaphyrin-lipid samples kept at RT for up to 72 h was also validated by the UHPLC-MS method. Retention peaks at around 2.9 min corresponding to Tl-texaphyrin-lipid were identified for all samples taken at different time points (6 - 72 h) and were confirmed by absorption spectra and mass spectra (Fig. 5.10 A, B, C and D). UHPLC-MS analysis demonstrated that most of Tl ions remained chelated after 72 h.

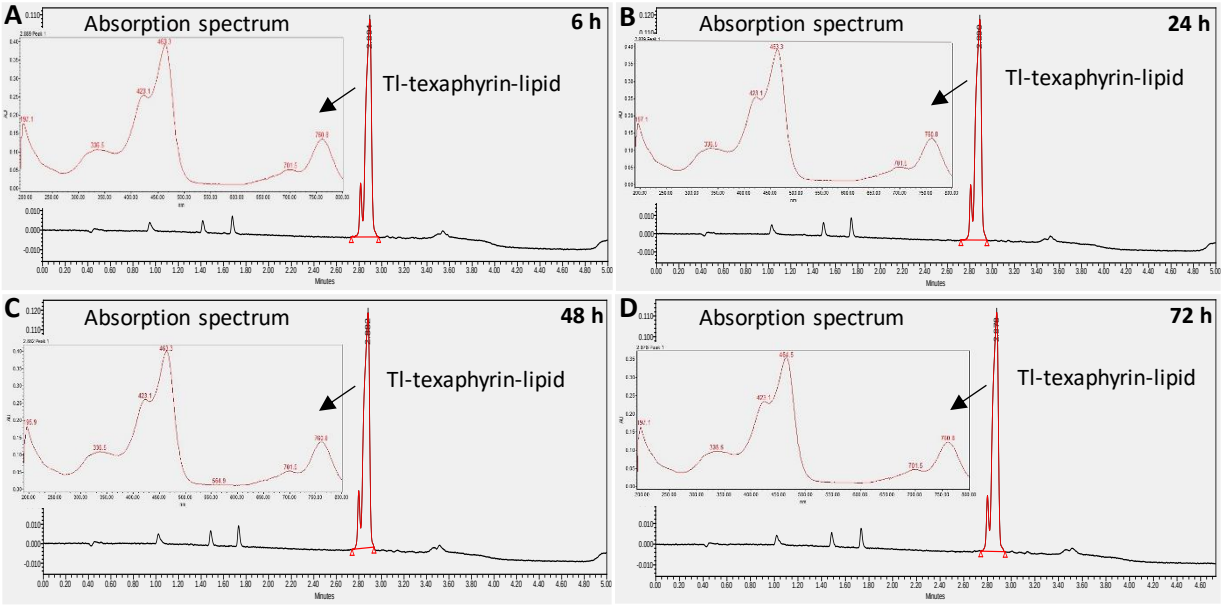

Figure 5.10 Examples of UHPLC-MS measurements of Tl-texaphyrin-lipid samples over a period of time. Chromatograms showing the peak eluting at around 2.9 min characteristic for Tl-texaphyrin-lipid and a corresponding absorption spectrum after **A)** 2 h, **B)** 24 h, **C)** 48 h and **D)** 72 h.

5.4.3 Nanotexaphyrin synthesis and characterisation. Non-radioactive Tl-nanotexaphyrins were synthesised as described in the methods section. Dynamic light scattering (DLS) measurement of Tl-nanotexaphyrins revealed that the nanoparticles are homogenous in size, measuring on average 147.4 ± 1.4 nm, with a polydispersity index (PDI) of 0.15 ± 0.03 (n = 3). The measured zeta potential was slightly negative: -1.5 ± 0.4 mV (n = 3). The size and dispersity of Tl-nanotexaphyrins were assessed in PBS over a period of 72 h and exhibited stability across a temperature range of 4-37°C, as indicated in Table 5.3.

Time	**0 h**		**24 h**		**48 h**		**72 h**	
T (°C)	Size (nm)	PDI	Size (nm)	PDI	Size (nm)	PDI	Size (nm)	PDI
4			143.2 ± 2.7	0.140	143.7 ± 1.1	0.154	144.2 ± 0.8	0.150
25	147.4 ± 1.4	0.150	143.8 ± 1.8	0.152	144.8 ± 2.0	0.159	144.1 ± 1.0	0.162
37			142.8 ± 1.2	0.151	146.0 ± 1.3	0.193	155.9 ± 3.6	0.230

Table 5.3 Tl-nanotexaphyrins stability over time at various temperatures. The size of non-radioactive Tl-nanotexaphyrins and the polydispersity index (PDI) were assessed by DLS from 0 to 72 h at 4, 25 and 37 °C, n=3.

Transmission electron microscopy (TEM) images showed homogenous and spherical vesicles sized 140-150 nm (Fig. 5.11) .

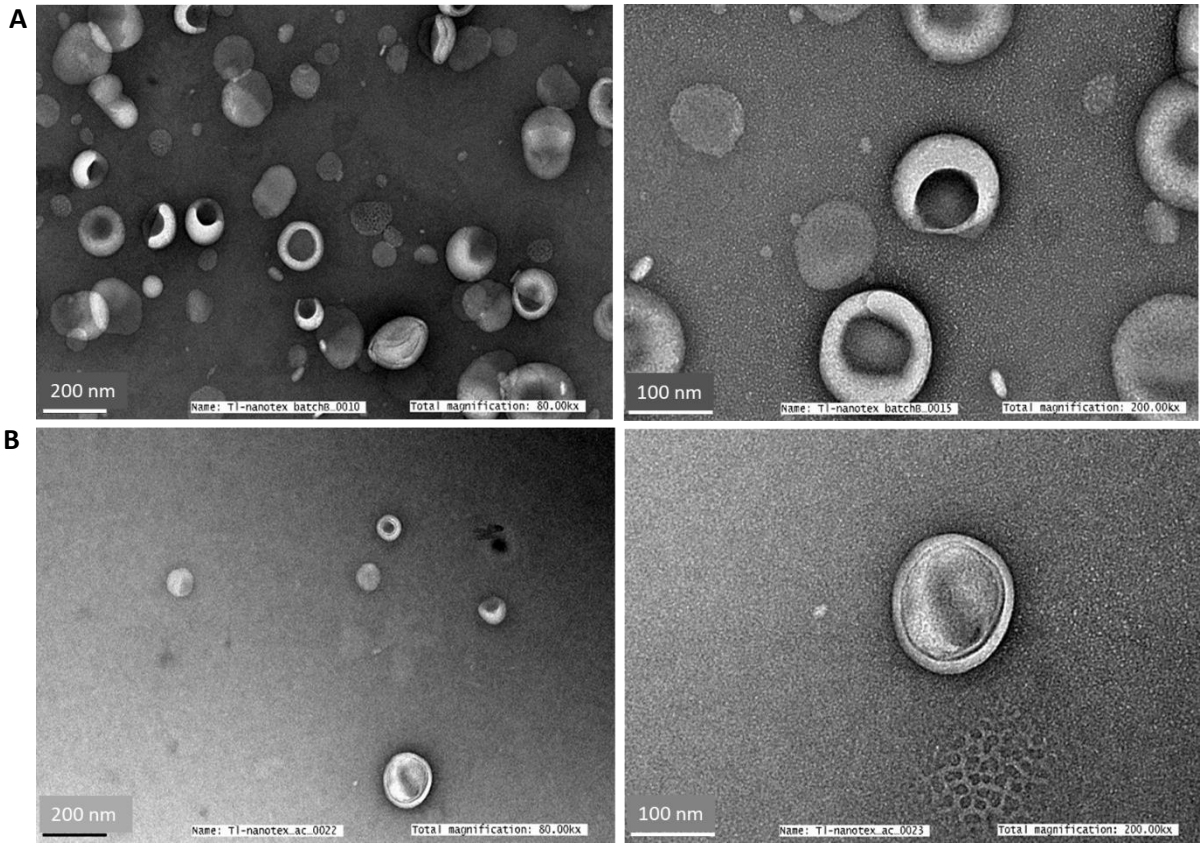

Figure 5.11 TEM images of Tl-nanotexaphyrins. Two different batched **A)** and **B)** of Tl-nanotexaphyrins in PBS were assessed at 80,000 magnification (scale bar: 200 nm) and 200,000 magnification (scale bar: 100 nm). Images taken by Dr Miffy Cheng, University of Toronto.

The fluorescence of non-radioactive Tl-nanotexaphyrins was also measured. Nanoparticles in PBS solution were excited at 465 nm wavelength and fluorescence emission spectrum was collected at 700-850 nm. As expected, no fluorescence peaks were observed in the region of 700-850 nm for the intact nanoparticles due to self-quenching. However, when Tl-nanotexaphyrin structure was disrupted by adding methanol, a distinct emission peak at 770 nm characteristic for Tl-texaphyrin-lipid component was noted (Fig. 5.12).

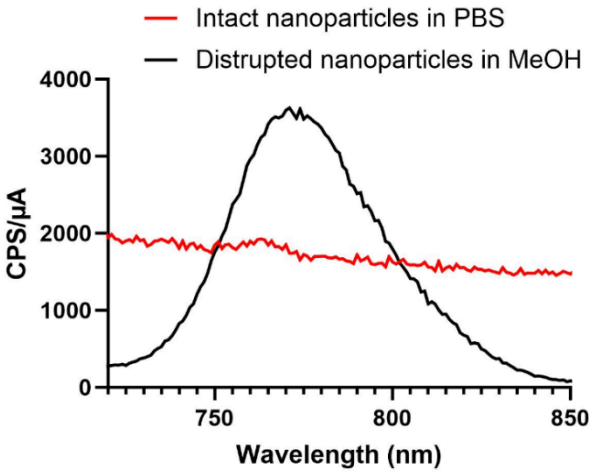

Figure 5.12. Fluorescence spectra of intact and disrupted Tl-nanotexaphyrins. Excitation wavelength: 465 nm, emission spectrum: 700-850 nm. Intact Tl-nanotexaphyrins were measured in PBS and MeOH was used to disrupt the Tl-nanotexaphyrin structure.

ICP-MS was performed to quantitively measure the cellular uptake of non-radioactive Tl-nanotexaphyrins incubated in lung cancer cells (A549) for 16 h. 25 mM KCl solution was used to inhibit unbound Tl uptake (Tl not chelated by nanotexaphyrins) as described in chapter 2. High concentrations of K^+ in medium can significantly suppress Tl^+ uptake in cells due to the competition for Na^+/K^+ pump binding sites. Tl uptake (%) is shown per 100,000 cells. Tl-nanotexaphyrins uptake in A549 cells was calculated as 2.8 ± 0.07%, 1.6 times higher than the uptake measured for the control with unbound Tl (1.7 ± 0.05%). However, when the unbound Tl uptake was inhibited by KCl solution, Tl-nanotexaphyrins uptake remained low at the level of 0.6 ± 0.01% (Fig. 5.13).

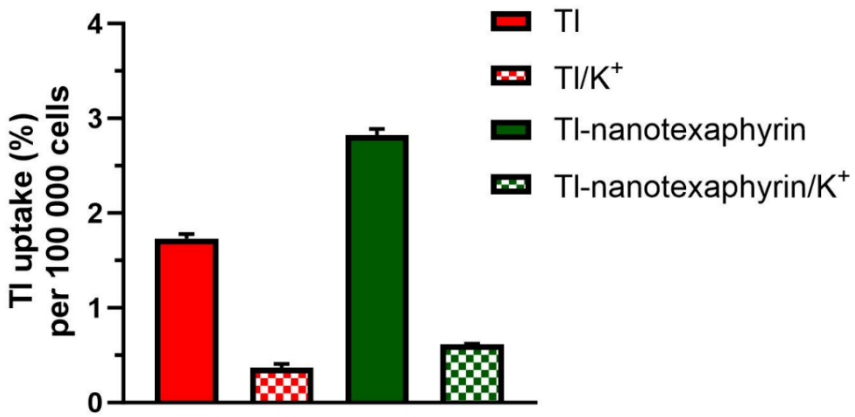

Figure 5.13 Uptake of Tl-nanotexaphyrins, measured by ICP-MS, in lung cancer cells (A549) incubated for 16 h with non-radioactive Tl-nanotexaphyrins. Oxidised TlCl in the same concentration was used as a control. 25 mM KCl solution was used to inhibit unbound Tl^+ uptake. 100,000 cells were seeded per well. Bars represent mean ± SD, done in triplicates, n=1.

Radioactive ^{201}Tl-nanotexaphyrins were synthesised as described in the methods section. Briefly, a mixture of lipids (CHL, DPPC and DSPE-PEG_{2000}) was added to ^{201}Tl-texaphyrin-lipids, mixed and slowly co-injected with 0.1 M NH_4OAc buffer using a microfluidic chip. A TLC method was used to assess Tl^{3+} oxidation rate and the purity of the synthesised nanoparticles (Fig. 5.3). Results from four independent experiment are gathered in Table 5.4. The radiolabelling yield of ^{201}Tl-nanotexaphyrins was low, with an average of 5.1 ± 4.4% and the average purity of the obtained nanoparticles was 77.4 ± 10.3% (n = 4).

Batch number	**1**	**2**	**3**	**4**
Dilution and purification	$^{201}TlCl_3$ diluted with NH_4OAc buffer; purification process repeated 3 times		$^{201}TlCl_3$ diluted with NH_4OAc buffer; purification process repeated 5 times	$^{201}TlCl_3$ diluted with water; purification process repeated 5 times
$^{201}Tl^+$/$^{201}Tl^{3+}$ oxidation yield	90.0 %	96.2 %	90.2 %	85.9 %
^{201}Tl-nanotexaphyrin purity pre-purification	16.7 %	20.2 %	29.9 %	24.4 %
^{201}Tl-nanotexaphyrin purity post-purification	71.6 %	82.9 %	66.1 %	88.8 %
Radiolabelling yield	7.8 %	9.8 %	2.4 %	0.5 %

Table 5.4 ^{201}Tl-nanotexaphyrin synthesis. Results from four independent experiments involving Tl^+/Tl^{3+} oxidation, dilution and chelation reaction with texaphyrin lipids, synthesis of ^{201}Tl-nanotexaphyrins and the purification process, as illustrated in Fig. 5.4. Radiolabelling yield was determined by comparing the activity of purified ^{201}Tl-nanotexaphyrins to the initial activity of [^{201}Tl]TlCl stock used for the experiment. $^{201}Tl^+$/ $^{201}Tl^{3+}$ oxidation yield was assessed by TLC using acetone as a mobile phase. ^{201}Tl-nanotexaphyrins purity before and after the purification process was assessed by TLC using 10% EDTA in 0.1 M NH_4OAc as a mobile phase. Data are presented as mean ± SD, n = 4.

The uptake of ^{201}Tl-nanotexaphyrins in lung cancer cells (A549) and ovarian cancer cells (SKOV3) after 16 h of incubation at 37°C was found to be 2.2 ± 0.11% and 2.7 ± 0.08%, respectively, with calculations based on 100,000 cells. These uptake values closely resemble the unbound ^{201}Tl uptake, which was measured at 2.5 ± 0.30% in A549 and 2.9 ± 0.06% in SKOV3 cells, as shown in Figure 5.14 A. This similarity suggests the release of ^{201}Tl, in the form of Tl^+, from the structure of ^{201}Tl-nanotexaphyrins under the conditions tested.

The percentage of ^{201}Tl activity measured in the 'medium' fraction, 'membrane' fraction, the 'cytoplasmic' fraction and the 'nuclear' fraction in both A549 cells and SKOV3 cells following incubation with ^{201}Tl-nanotexaphyrins or unbound ^{201}Tl is shown in Figure 5.14 B and C.

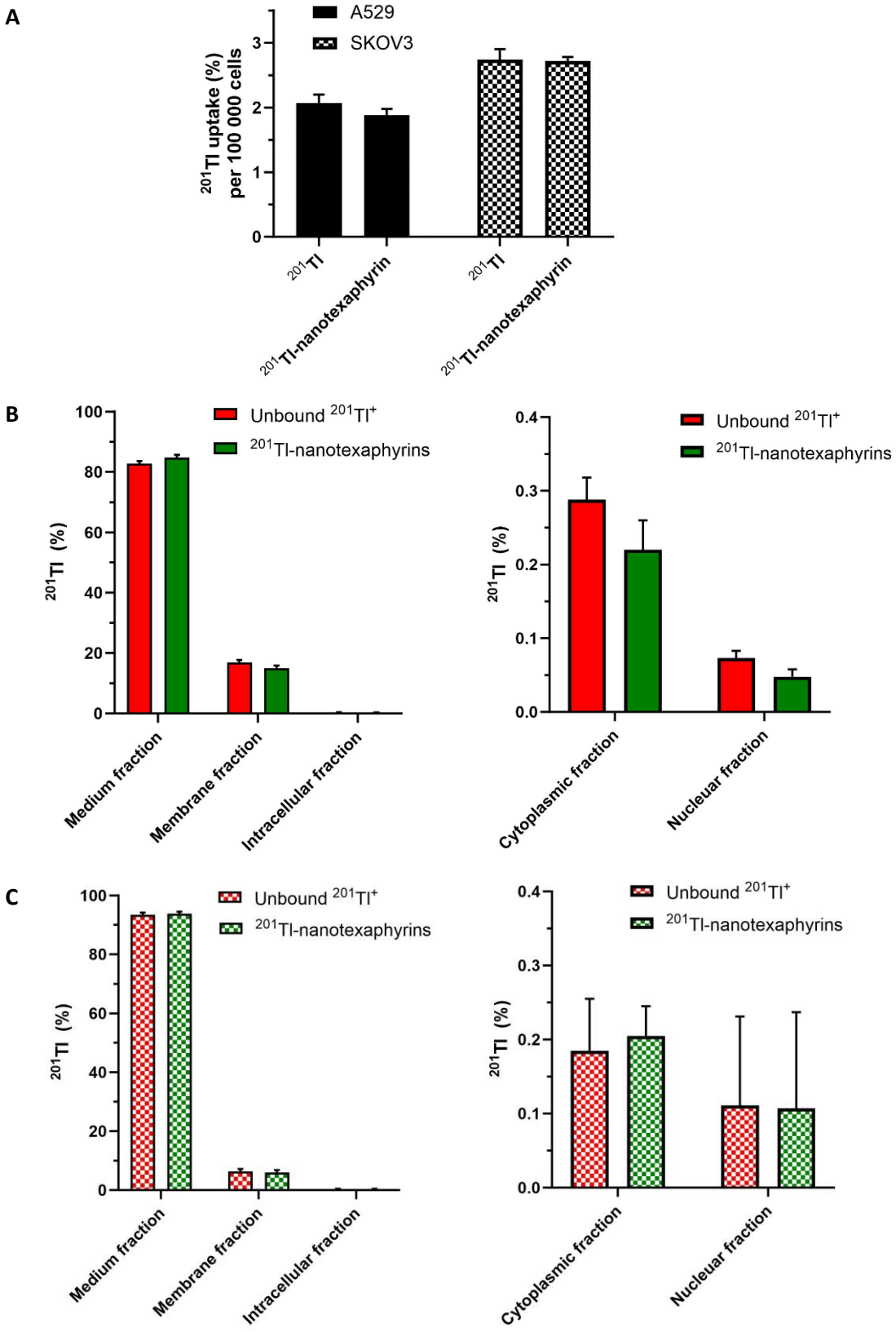

Figure 5.14 ^{201}Tl-nanotexaphyrin uptake in lung cancer cells and the subcellular distribution. A) ^{201}Tl-nanotexaphyrin and unbound ^{201}Tl uptake in lung cancer cells (A549) and ovarian cancer cells (SKOV3) calculated per 100,000 cells. **B)** Cell fractionation results in A549 cells per total number of cells counted (665,000) after 16 h incubation with ^{201}Tl-nanotexaphyrins and unbound ^{201}Tl. **C)** Cell fractionation results in SKOV3 cells per total number of cells counted (210,000) after 16 h incubation with ^{201}Tl-nanotexaphyrins and unbound ^{201}Tl. Bars represent mean ± SD, triplicates, n=2.

The amount of intracellular activity was significantly lower compared to the activity washed with the 'membrane' fraction. This could be attributed to a rapid efflux of unbound $^{201}Tl^{+}$ when cells are subsequently washed during the cell fractionation procedure [140]. ^{201}Tl activity distribution in cells incubated with ^{201}Tl-nanotexaphyrins remained on a comparable level to cells incubated with unbound ^{201}Tl in both cell lines.

The capability of ^{201}Tl-nanotexaphyrins to retain ^{201}Tl when stored in a PBS solution for different durations was assessed using the TLC method (mobile phase: 10% EDTA in 0.1 M NH_4OAc). ^{201}Tl-nanotexaphyrins were kept at 37°C for 2, 6 and 72 h as well as at 4°C for 72 h. Obtained results are presented in Table 5.5.

	Temperature	
Time	**4°C**	**37°C**
0 h	77.5 ± 16.0 %	77.5 ± 16.0 %
2 h	-	70.7 ± 9.7 %
6 h	-	59.5 ± 13.3 %
72 h	56.0 ± 1.4 %	29.1 ± 7.3 %

Table 5.5 ^{201}Tl-nanotexaphyrin radiostability in PBS solution. TLC method was used to assess the radiostability, mobile phase used: 10% EDTA in 0.1 M NH_4AcOH; $^{201}Tl^{+}$/$^{201}Tl^{3+}$ in these conditions migrate with the solvent front (R_f = 1) while ^{201}Tl-texaphyrin-lipids remain at the baseline (R_f = 0). Data are presented as mean ± SD, n = 2

In an attempt to increase the radiolabelling efficiency of ^{201}Tl-nanotexaphyrins, we combined stable Tl-texaphyrin-lipid (5% total molar lipid content, Tl:texaphyrin-lipid - 1:1 ratio) and ^{201}Tl-texaphyrin-lipid (5% total molar lipid content, ^{201}Tl:texaphyrin-lipid - 0.005:1 ratio) before adding additional lipid mixture (90% total molar lipid content) and forming nanoparticles via microfluidic system as described before. Obtained results are presented in Table 5.6.

$^{201}Tl^{+}$/$^{201}Tl^{3+}$ oxidation yield	91.8 %
^{201}Tl-texaphyrin-lipid yield	10.3 %
^{201}Tl-nanotexaphyrins purity before purification	11.9 %
^{201}Tl-nanotexaphyrins purity after purification	73.5 %
Radiolabelling yield	1.7 %

Table 5.6 ^{201}Tl-nanotexaphyrins 'doped' with stable Tl-texaphyrin-lipids radiolabelling yield. Final radiolabelling yield was determined by comparing the activity of purified ^{201}Tl-nanotexaphyrins to the initial activity of [^{201}Tl]TlCl stock used for the experiment measured by the Capintec dose calibrator. $^{201}Tl^{+}$/ $^{201}Tl^{3+}$ oxidation yield was assessed by TLC using acetone as a mobile phase. ^{201}Tl-nanotexaphyrins purity before and after the purification process was assessed by TLC using 10% EDTA in 0.1 M NH_4OAc as a mobile phase. Data are presented as mean ± SD, n = 1.

An alternative approach to enhance the efficiency of ^{201}Tl radiolabelling involved combining Cd-texaphyrin-lipid or Mn-texaphyrin-lipid ethanol solution (5% total molar lipid content each) with free base texaphyrin-lipid (5% total molar lipid content) and other lipids mixture (cholesterol (CHL): 40.6% total molar content, DSPE-PEG_{2000} (distearoylphosphatidylcholine polyethylene glycol: 5.0% total molar content, dipalmitoylphosphatidylcholine (DPPC): 44.4% total molar content) in ethanol. Oxidised $^{201}Tl^{3+}$ diluted 5 times with 0.1 M NH_4OAc buffer was added to the mixture and then the nanoparticle structure was formed by using the microfluidic system as shown in Figure 5.4. Obtained results are presented in Table 5.7.

$^{201}Tl^{+}$/$^{201}Tl^{3+}$ oxidation yield	91.8 %
^{201}Tl/Mn-nanotexaphyrins purity before purification	28.0 %
^{201}Tl/Cd-nanotexaphyrins purity before purification	9.4 %

Table 5.7 ^{201}Tl/Mn-nanotexaphyrin and ^{201}Tl/Cd-nanotexaphyrin radiolabelling yield before purification. Final radiolabelling yield was determined by comparing the activity of purified ^{201}Tl/Mn-nanotexaphyrins or ^{201}Tl/Cd-nanotexaphyrins to the initial activity of [^{201}Tl]TlCl stock used for the experiment measured by the Capintec dose calibrator. $^{201}Tl^{+}$ to $^{201}Tl^{3+}$ oxidation yield was assessed by TLC using acetone as a mobile phase. ^{201}Tl-nanotexaphyrins purity before the purification process was assessed by TLC using 10% EDTA in 0.1 M NH_4OAc as a mobile phase. Data are presented as mean ± SD, n = 1.

5.5 Discussion

Despite its high radiotoxic potential and world-wide availability, ^{201}Tl has not yet been fully evaluated for the targeted cancer therapy. This is largely because of the limited availability of suitable chelators and the hitherto relatively limited recognition of its significant Auger electron-emitting potential. In this study we explored the capacity of texaphyrin-lipid compounds to effectively bind $^{201}Tl^{3+}$ ions, aiming to facilitate the targeted delivery of this radionuclide to cancer cells for radiotherapeutic applications. Using non-radioactive thallium salts, we managed to synthesise and characterise Tl-texaphyrin-lipid compounds, which proved to be stable when kept at 25°C in ethanol solution for a minimum of 72 hours. Furthermore, the amphipathic nature of the texaphyrin phospholipids enable the Tl-texaphyrin-lipids to self-assemble into homogenous and spherical liposome-like structures of 140-150 nm in diameter, which were stable in aqueous conditions. During these experiments, however, we noticed that increased temperature (37°C or above) had a negative impact on formation and stability of Tl-texaphyrin-lipid compounds. Although an increased temperature did not influence

$^{201}Tl^{+}$ oxidation in acidic conditions, Tl^{3+} ions could have been released from the texaphyrin macrocycle due to the reverse Tl^{3+} reduction to 1+ oxidation state in neutralised aqueous conditions, following a mechanism that is not yet understood. Even though the five nitrogen atoms present in the expanded texaphyrin macrocycles efficiently bound Tl^{3+} ion, the complex thermodynamic stability could have been impaired by providing additional heat energy in the presence of water and unknown reducing agents. Modifying the texaphyrin-lipid structure by adding supplementary groups containing electron-rich atoms, such as carboxylic acid groups, might help to stabilise Tl^{3+} and prevent its reduction to 1+ oxidation state by providing additional axial ligands and therefore increase stability of the Tl-texaphyrin complexes at 37°C. It was observed that Tl^{+} binding by the texaphyrin-lipids does not occur in any tested conditions. This was expected considering the larger diameter of Tl^{+} ion and a lower stability with porphyrin-based chelators compared to Tl^{3+}.

Thermodynamic instability of ^{201}Tl-texaphyrin-lipids could also be observed in the nanoparticles, when radioactive Tl was released after 72 hours nearly two times faster at 37°C than at RT (Table 5.5). At the same time, no significant alterations in the size or dispersity of Tl-texaphyrin nanoparticles were detected by DLS (measured up to 72 h), even when Tl-nanotexaphyrins were kept at 37°C. This suggests that ^{201}Tl-nanotexaphyrin instability was not related to the liposomal-like structure of these nanoparticles, which remain intact at 37°C, but rather to the chelation stability of Tl-texaphyrins. In both non-radioactive and radioactive thallium cellular uptake experiments, the uptake of unbound Tl and Tl-nanotexaphyrins remains on a similar level, indicating that most likely Tl^{3+} ions are reduced to Tl^{+}, which could have been intensified by the presence of reducing agents released by cells. As the larger ionic radii of Tl^{+} cannot be easily bound by the texaphyrin macrocycle, it is released into the incubation medium and taken up by a Na^{+}/K^{+} pump in a similar manner to the unbound Tl ions. Adding KCl solution to inhibit unbound Tl uptake reduces Tl uptake from Tl-nanotexaphyrins significantly from 2.8 ± 0.07% to 0.6 ± 0.01%, indicating that mostly unbound Tl^{+} ions are present in the incubation medium. Furthermore, the ^{201}Tl subcellular distribution for unbound Tl and Tl-nanotexaphyrins remains similar, and even though this technique does not reveal the true intracellular Tl distribution due to a rapid efflux of Tl as discussed in chapter 4, it suggests that ^{201}Tl is washing out of cells at a comparable rate. This pattern of behaviour in the in vitro experiments has been previously observed for other types of chelators [99]. Tl-texaphyrin-lipids thermodynamic instability towards reduction is a potential problem for the future work and therefore more experiments are needed to fully investigate the impact of temperature on Tl-nanotexaphyrin stability.

It is worth noting that the slow release of $^{201}Tl^{+}$ from nanoparticles may prove beneficial, especially when ^{201}Tl conjugates are delivered in a close proximity to the tumour. Auger electrons

released during ^{201}Tl radioactive decay have a very short range (<1 µm) and it is likely they will have to be present in the close proximity of the radiosensitive cellular targets, such as the nucleus or the cell membrane [104,109]. It has been suggested in chapter 4 that the high radiotoxic potential of unbound thallium can be attributed to its affinity for the cell nucleus. By enabling a gradual release of $^{201}Tl^{+}$ ions from nanoparticles once inside the cell, we could avoid the need for the additional subcellular targeting of the engineered nanostructures in order to achieve maximum radiotoxic impact. Given the observed release of thallium from the texaphyrin structure, it seems unlikely that texaphyrins alone, without the nanoparticle structure, have a viable future for delivering radioactive thallium for therapeutic purposes.

Translating the optimised, non-radioactive method of synthesising Tl-nanotexaphyrins to bind radioactive ^{201}Tl proved difficult. Despite successful chelation and formulation of radioactive ^{201}Tl-nanotexaphyrins, with an average purity of 77.4 ± 10.3% after the purification process, the radiolabelling yield of ^{201}Tl-nanotexaphyrin was low, 5.1 ± 4.4%, and this has severely limited the scalability of the reaction and achieving enough activity for further experiments. All the attempts to further optimise the chelation reaction and nanoparticle synthesis to increase the radiolabelling yield, including 'doping' ^{201}Tl-nanotexaphyrins with non-radioactive Tl and combining ^{201}Tl with Cd-texaphyrin-lipid or Mn-texaphyrin-lipids using the postinsertion method [226], proved unsuccessful. The difference between the non-radioactive and radioactive Tl-texaphyrin-lipid chelation rate and stability could be linked to a concentration of Tl present in the reaction solution, which would be around 1000-2000 times lower in $[^{201}Tl]TlCl_3$ (^{201}Tl and ^{203}Tl combined) than $TlCl_3$ used in non-radioactive experiments. One of the main reasons for the texaphyrin-lipids' low radiolabelling rate with Tl^{3+} is the incompatibility of the oxidation conditions and stability of texaphyrin-lipid compounds. Tl^{3+} in a form that is readily available for complexation appears to be more stable in acidic conditions; in contrast, a concentrated acidic environment led to rapid degradation to texaphyrin-lipids [228]. By neutralising the acidic conditions to reduce the macrocycle degradation rate, we substantially reduce the amount of Tl^{3+} present in the sample due to an intensified Tl^{3+} to Tl^{+} reduction process. The low radiolabelling rate is also due to a retention of $^{201}Tl^{3+}$ on the oxidation bead surface during the oxidation process (30-50% of ^{201}Tl activity). Further improvements to the oxidation and chelation conditions are needed in order to increase ^{201}Tl radiolabelling efficiency.

5.6 Conclusions

The Tl^{+} to Tl^{3+} oxidation method used in this experiment is efficient but requires acidic conditions, which are not suitable for texaphyrin compounds, leading to the degradation of the macrocycle through hydrolysis. Using oxidised thallium, non-radioactive Tl-texaphyrin-lipid compounds were successfully synthesised and characterised by UV-Vis and UHPLC-MS. Obtained complexes were stable when kept at RT for at least 72 h. These compounds were successfully assembled into nanotexaphyrins and characterised by DLS, TEM and emitted fluorescence. Over a period of 72 h, no alterations in the size or polydispersity of the synthesised nanoparticles were observed. The uptake of Tl-nanotexaphyrins, quantified using ICP-MS, was comparable to that of unbound Tl. Moreover, the synthesis of ^{201}Tl-nanotexaphyrins was achieved with an average purity of 77.4 ± 10.3%, but the radiolabelling efficiency was low, with an average of 5.1 ± 4.4%. Measurement with a gamma counter indicated that the uptake of ^{201}Tl-nanotexaphyrins was similar to that of unbound $^{201}Tl^{+}$. The release of ^{201}Tl from ^{201}Tl-nanotexaphyrins in PBS solution exhibit a time-dependent pattern, with faster release observed at 37°C. Due to the low activity of the synthesised ^{201}Tl-nanotexaphyrins and the restricted project timeline, several planned biological investigations such as toxicity experiments could not be conducted. Further research is needed to fully evaluate the stability and radiotoxic potential of ^{201}Tl-nanotexaphyrins. Nonetheless, following the initial assessment, texaphyrins do not present significant advantages in terms of chelating thallium ions compared to other types of chelators under investigation.

Chapter 6: Summary and future considerations

The main focus of this doctoral thesis was the exploration of an Auger electron-emitter, ^{201}Tl, with the primary objective of evaluating its radiotoxicity and progressing towards radiopharmaceuticals for targeted treatment of small tumours, disseminated and metastatic cancer disease. Considering the scarcity of available literature on both ^{201}Tl radiobiology and radiochemistry, the initial phase of this project involved evaluating the radiotoxic potential of ^{201}Tl. Building on reports from previous studies that highlighted thallium's ability to accumulate in tumours during the diagnostic applications of [^{201}Tl]TlCl, this research further investigated the radiotoxic effects of $^{201}Tl^{+}$ in cancer cells, specifically exploring its native uptake mechanisms related to its mimicry of potassium. Throughout this study, several fundamental questions found their answers, including the mechanism of entry of thallium into cancer cells and the cytotoxic potency of the emitted electrons. It has been shown that $^{201}Tl^{+}$ can be effectively taken up by cancer cells by a mechanism that is inhibited by cardiac glycosides or potassium, i.e. likely via the sodium-potassium ATPase pump, leading to a substantial radiotoxic effect upon internalisation. The average cellular activity of $^{201}Tl^{+}$ needed for a 90% reduction in the clonogenic survival after 90-180 min incubation with [^{201}Tl]TlCl was found to be within a range of 0.1 – 0.3 Bq per cell, depending on the particular cell line used and conditions applied. It is worth noting that the incubation period used for these calculations is much shorter than the physical half-life of ^{201}Tl. Once incorporated into a targeted radiopharmaceutical, depending on the pharmacokinetics of the chosen targeting vector, ^{201}Tl has the potential to be significantly more radiotoxic than indicated by the above numbers. Nevertheless, as a result of this assessment, ^{201}Tl appeared to be more potent than other Auger electron-emitters like ^{111}In and ^{67}Ga, in line with the respective number and energy of Auger electrons emitted per decay. These findings played a critical role in laying the foundation for subsequent experiments, enabled further exploration of thallium's radiotoxic potential and justified developing thallium chelation chemistry in search for prospective clinical applications.

Encouraged by the initial results, numerous efforts by me and other team members have been undertaken to bind ^{201}Tl, either in the form of Tl^{+} or Tl^{3+}, in order to enable the targeted therapeutic approach and mitigate its rapid efflux from cancer cells. However, this proved to be a challenging task and will require some years of further research aimed at development of effective chelators.

In parallel with other team members efforts to develop thallium chelates, I have used the inherent ability of Prussian blue (PB) to incorporate Tl^{+} into its crystal structure. Two types of inorganic nanoparticles were synthesised, featuring a PB core and citric acid or chitosan coating. While the radiotoxic potential of $^{201}Tl^{+}$ bound to citric acid-coated PBNPs was substantially lower than unbound

thallium, ^{201}Tl bound to chitosan-coated PBNPs exhibited comparable radiotoxicity, requiring an average activity of 0.2-0.4 Bq/cell for a 90% reduction in clonogenicity over 180 minutes. When tested under in vivo conditions and injected directly into the tumour, chitosan-coated PBNPs exhibited significantly higher retention of ^{201}Tl in tumour tissue after 48 hours compared to unbound $^{201}Tl^{+}$. Nonetheless, when testing chitosan-coated PBNPs in pre-clinical settings, it was shown that the stability of the ^{201}Tl binding mechanism was compromised, leading to a more rapid washout of ^{201}Tl from the nanoparticulate form than initially anticipated based on in vitro studies.

In an alternative approach focused on binding ^{201}Tl in its 3+ oxidation state using organic texaphyrin-lipid-based nanoparticles, the instability of Tl^{3+} complexes became evident much earlier in the experimental procedures, specifically during the production process and initial stability testing. The challenge of ensuring both kinetic and thermodynamic stability of thallium-bound complexes, and the subsequent release of free thallium in the biological environment, has been encountered in prior studies [94,99]. Addressing this issue is crucial for two primary reasons: firstly, to allow sufficient time for ^{201}Tl in tumour cells to manifest its full radiotoxic potential, and secondly, to prevent adverse effects in healthy tissue.

Another set of questions in this study focused on the subcellular distribution of unbound Tl^{+}. Given that low-energy Auger electrons have limited travel distances from the decay site, coupled with the observed high radiotoxic potential of $^{201}Tl^{+}$, a hypothesis was developed suggesting that Tl^{+} might be distributed in close proximity to sensitive subcellular targets, such as the nucleus or mitochondria. Through the application of the ion beam analysis combined with light microscopy, it was revealed that Tl^{+} (as non-radioactive TlCl) is predominantly located in the cell nucleus, with the calculated average concentration ratio in the nucleus versus in the cytoplasm at approximately 1.8:1. This finding affirms the significance of thallium's subcellular localisation in the observed radiotoxicity. It also suggests that any therapeutic radiopharmaceutical design may require additional subcellular targeting or the implementation of a slow, sustained release of thallium within the cell, which facilitates its eventual delivery to the nucleus.

Although this PhD project has addressed certain questions, such as the radiotoxicity of unbound ^{201}Tl and its estimated subcellular distribution, some challenges persist. The ongoing quest for a method to effectively bind thallium and, more importantly, to sustain its stable binding in the biological environment for the required duration, remains an unanswered challenge that necessitates further research.

Among the extensive group of Auger electron-emitters, ^{201}Tl has been identified as one of the most promising radionuclides for targeted therapy, based on its overall dosimetry score and other

physicochemical properties [21]. Bolcaen et al. conducted a comprehensive comparison of various Auger electron-emitters, considering criteria such as the number of produced Auger electrons and other emissions, physical half-life, production and availability, radiochemistry, molar activity, vector availability, and dosimetry [21]. The primary objective of this study was to evaluate the suitability of Auger electron-emitters for future targeted radionuclide therapy while also highlighting the major hurdles encountered in the developmental stages. Indeed, ^{201}Tl stands out with one of the highest numbers of Auger electrons emitted per decay (36.9), and it lacks accompanying β-emission. It possesses a convenient half-life (73 h), a stable daughter (^{201}Hg), worldwide availability, and an established production method due to its previous extensive use in diagnostics. Additionally, it exhibits good molar activity and favourable cellular dosimetry. However, two significant obstacles were identified for ^{201}Tl: the lack of available chelators (as discussed previously in detail) and potential toxicity related to emitted gamma rays.

^{201}Tl emits X-rays with energies ranging from 67 to 82 keV (abundance 94%) and γ-ray photons at 135 and 167 keV (3% and 10% abundance, respectively) [60]. These emissions are valuable for imaging and dosimetry applications and have been widely employed in the past for myocardial imaging. However, when higher doses are administered for targeted cancer therapies, the emitted photons may have the potential to cause adverse effects. The extensive photon emission might lead to undesirable irradiation of healthy tissue, increasing the radiation dose received by patients, their families, caregivers, and medical personnel. As a result, the emission of γ-rays might constraint the maximum allowable radioactivity that can be administered to patients and limit the translation of Auger electron-emitting radiotherapeutics into clinical use.

Uusijärvi et al. extensively analysed the tumoral and cellular dosimetry of a wide range of radionuclides with various types of emission currently available for systemic tumour therapy, evaluating the impact of photon emission on the absorbed dose in both tumour and normal tissue [229]. One of the parameters used in the analysis was the photon-to-electron ratio, which was computed for various radionuclides (photon-to-electron ratio: p/e was calculated as the sum of the total photon energy emitted per decay divided by the sum of total electron energy emitted per decay). The estimated p/e ratio for ^{201}Tl was 2.15, a value notably lower compared to other Auger electron emitters such as ^{67}Ga, ^{111}In, which have p/e ratios of 4.46 and 11.8, respectively [229]. Moreover, the commonly used β-emitter ^{131}I, found in registered and frequently utilised therapeutic radiopharmaceuticals such as [^{131}I]I^-, [^{131}I]I-MIBG and ^{131}I-tositumomab (Bexxar), exhibits a similar p/e ratio of 2.0, with both the energy of photons (364 keV, abundance 81.2 % [230]) and electrons (192 keV as the energy of the most prominent electron [229]) much higher compared to ^{201}Tl (67-82 keV, 31 keV [229], respectively). The calculated average tumour-to-normal tissue absorbed dose ratio of

^{131}I is comparable to that of ^{201}Tl (8 vs 12) but only when the radionuclides are distributed uniformly within the tumour. For ^{201}Tl this ratio increases more than two times when it is localised within the cell nucleus whereas for ^{131}I it remains nearly unchanged. This implies that when ^{201}Tl is specifically targeted to the nucleus, it has the potential to outperform ^{131}I, which is clinically administered in high doses reaching 37 GBq [15], despite the associated high-energy gamma radiation. Therefore, the design of Auger electron-emitting radiopharmaceuticals with effective targeting to sensitive cellular compartments could significantly reduce the amount of activity needed for cancer therapy and thus reduce non-target dose due to photons.

Due to the limited range of emitted electrons, Auger electron-emitters are most effective in single cells, micrometastases or small tumours [21]. The tumour size with a radius of 620 μm (equivalent to 1 μL in volume, 1 mg in mass and approximately 700,000 cells) was considered the threshold size beyond which the tumour-to-normal tissue absorbed dose ratio reaches a plateau for low energy electrons like those of ^{201}Tl and the calculated absorbed dose ratio value did not show further increase [229]. Using this model and taking into account the calculated ^{201}Tl activity per cell necessary to achieve a 90% reduction in clonogenic survival (0.2 Bq/cell for MDA-MB-231 cells), the activity retained for at least 90 minutes, required for treating a single small tumour (1 μL volume), is approximately 0.07 MBq (based on the assumption that tumour cells consist of 50% of the total amount of cells).

Currently, given the absence of targeted approaches for delivering ^{201}Tl to cancer cells, assessing the potential therapeutic dose of a radiopharmaceutical containing ^{201}Tl, and consequently evaluating its dosimetric impact on healthy tissue, is difficult. Extrapolating ^{131}I maximum therapeutic activity of 37 GBq to ^{201}Tl, in order to achieve the activity of 0.07 MBq in a small tumour described earlier, the tumoral uptake should reach approximately 0.0002% of ^{201}Tl injected activity (% IA, equivalent to 0.2 % IA per g of tumour) and remain at this level for at least 90 minutes. Extending the tumour retention time of ^{201}Tl beyond the calculated 90 minutes is likely to enhance the therapeutic outcome and might facilitate the use of lower doses per cell, potentially allowing for a lower-than-calculated tumour uptake. In a clinical setting, the measurement of tumour uptake is usually derived from SPECT images and commonly expressed as a percentage of the administered dose per gram of tissue or standardised uptake value, which accounts for the size of the patient and allows meaningful comparison between individuals. Following the injection of patients with 120 MBq of [^{201}Tl]TlCl performed to evaluate the efficacy of treatment for malignant brain tumours, the average ^{201}Tl concentration measured within the tumour was at the level of 3.2 kBq/ml (corresponding to mean SUV_{max} value of 2) [231]. This accumulation, driven by thallium's inherent ability to concentrate in tumour tissue, is equivalent to approximately 0.003% IA per gram of tumour, assuming the tumour density is similar to that of water.

An additional example of tumoral uptake values in human studies is the uptake of ^{131}I combined with an anti-CD20 monoclonal antibody (also known as ^{131}I-tositumomab) in B-cell lymphoma. This uptake, estimated through a combination of gamma-camera imaging and tumour biopsies, averaged at 0.009% IA per gram of the tumour [232]. Both mentioned tumour uptake values are lower than the calculated necessary uptake of ^{201}Tl for therapeutic purposes. However, it is crucial to note that in clinical studies, tumour uptake values assessed using segmented SPECT images may introduce a higher margin of error influenced by the methodology employed. Several factors, including spatial resolution, sensitivity, image quality, and the quantification method used (such as manually marking the regions of interest and correcting for background activity), can significantly affect the reliability of tumour uptake quantification. When estimating the potential therapeutic effect of ^{201}Tl, it is important to highlight that, beyond the radiation dose delivered specifically to the cancer cell or a specific subcellular target, various other aspects can influence the therapeutic outcome. Therefore, the correlation between the dose delivered directly to the tumour cell and the observed therapeutic effect may not necessarily be linear. Certain factors, such as tumour microenvironment and radiosensitivity, heterogeneous expression of targeted markers, and radiobiological effects including bystander effect may all influence the treatment outcome [45]. The above calculations, although simplistic, give hope that once the appropriate binding mechanism is found and in combination with effective cellular and subcellular targeting, the γ-emission will not limit the use of ^{201}Tl in doses relevant to cancer therapy.

In conclusion, ^{201}Tl has demonstrated a high radiotoxic potential and once the suitable and stable binding mechanism is identified (such as via a not-yet-available effective chelator), an efficient radiopharmaceutical can be design with targeting to tumour cells and cellular compartments.

References

1. Ahmad AS, Ormiston-Smith N, Sasieni PD. Trends in the lifetime risk of developing cancer in Great Britain: Comparison of risk for those born from 1930 to 1960. British Journal of Cancer. 2015;112:943 – 7.

2. Debela DT, Muzazu SGY, Heraro KD, Ndalama MT, Mesele BW, Haile DC, et al. New approaches and procedures for cancer treatment: Current perspectives. SAGE Open Medicine. 2021;9:1–10.

3. Falzone L, Salomone S, Libra M. Evolution of cancer pharmacological treatments at the turn of the third millennium. Frontiers in Pharmacology. 2018;9:1300.

4. Allen C, Her S, Jaffray DA. Radiotherapy for Cancer: Present and Future. Advanced Drug Delivery Reviews. 2017;109:1–2.

5. Karger CP, Glowa C, Peschke P, Kraft-Weyrather W. The RBE in ion beam radiotherapy: In vivo studies and clinical application. Zeitschrift für Medizinische Physik. 2021;31:105–21.

6. Zijlstra A, Von Lersner A, Yu D, Borrello L, Oudin M, Kang Y, et al. The importance of developing therapies targeting the biological spectrum of metastatic disease. Clinical and Experimental Metastasis. 2019;36:305–9.

7. Li T, Ao ECI, Lambert B, Brans B, Vandenberghe S, Mok GSP. Quantitative imaging for targeted radionuclide therapy dosimetry - technical review. Theranostics. 2017;7:4551–65.

8. Bodei L, Herrmann K, Schöder H, Scott AM, Lewis JS. Radiotheranostics in oncology: current challenges and emerging opportunities. Nature Reviews Clinical Oncology. 2022;19:534–50.

9. Gudkov S, Shilyagina N, Vodeneev V, Zvyagin A. Targeted Radionuclide Therapy of Human Tumors. International Journal of Molecular Sciences. 2016;17.

10. Kitzberger C, Spellerberg R, Morath V, Schwenk N, Schmohl KA, Schug C, et al. The sodium iodide symporter (NIS) as theranostic gene: its emerging role in new imaging modalities and non-viral gene therapy. EJNMMI Research. 2022;12:1–14.

11. De la Vieja A, Riesco-Eizaguirre G. Radio-iodide treatment: from molecular aspects to the clinical view. Cancers. 2021;13:1–21.

12. Costa IM, Siksek N, Volpe A, Man F, Osytek KM, Verger E, et al. Relationship of in vitro toxicity of technetium-99m to subcellular localisation and absorbed dose. International Journal of Molecular Sciences. 2021;22:1–13.

13. Wilson JS, Gains JE, Moroz V, Wheatley K, Gaze MN. A systematic review of ^{131}I-meta iodobenzylguanidine molecular radiotherapy for neuroblastoma. European Journal of Cancer. 2014;50:801–15.

14. Kayano D, Kinuya S. Iodine-131 metaiodobenzylguanidine therapy for neuroblastoma: reports so far and future perspective. The Scientific World Journal. 2015;2015:189135.

15. Parisi MT, Eslamy H, Park JR, Shulkin BL, Yanik GA. ^{131}I-Metaiodobenzylguanidine Theranostics in Neuroblastoma: Historical Perspectives; Practical Applications. Seminars in Nuclear Medicine. 2016;46:184–202.

16. Gains JE, Aldridge MD, Mattoli MV, Bomanji JB, Biassoni L, Shankar A, et al. ^{68}Ga-DOTATATE and ^{123}I-mIBG as imaging biomarkers of disease localisation in metastatic neuroblastoma: Implications for molecular radiotherapy. Nuclear Medicine Communications. 2020;41:1169–77.

17. Jimenez C, Erwin W, Chasen B. Targeted radionuclide therapy for patients with metastatic pheochromocytoma and paraganglioma: From low-specific-activity to high-specific-activity iodine-131 metaiodobenzylguanidine. Cancers. 2019;11:1018.

18. Sgouros G, Bodei L, McDevitt MR, Nedrow JR. Radiopharmaceutical therapy in cancer: clinical advances and challenges. Nature Reviews Drug Discovery. 2020;19:589–608.

19. Knight JC, Cornelissen B. Bioorthogonal chemistry: implications for pretargeted nuclear (PET/SPECT) imaging and therapy. American journal of nuclear medicine and molecular imaging. 2014;4:96–113.

20. Liu S. The role of coordination chemistry in the development of target-specific radiopharmaceuticals. Chemical Society Reviews. 2004;33:445–61.

21. Bolcaen J, Gizawy MA, Terry SYA, Paulo A, Cornelissen B, Korde A, et al. Marshalling the Potential of Auger Electron Radiopharmaceutical Therapy. Journal of Nuclear Medicine. 2023;64:1344–51.

22. Salih S, Alkatheeri A, Alomaim W, Elliyanti A. Radiopharmaceutical Treatments for Cancer Therapy, Radionuclides Characteristics, Applications, and Challenges. Molecules. 2022;27:1–16.

23. Verhoeven M, Seimbille Y, Dalm SU. Therapeutic applications of pretargeting. Pharmaceutics. 2019;11:434.

24. Houghton JL, Membreno R, Abdel-Atti D, Cunanan KM, Carlin S, Scholz WW, et al. Establishment of the in vivo efficacy of pretargeted radioimmunotherapy utilizing inverse electron demand diels-alder click chemistry. Molecular Cancer Therapeutics. 2017;16:124–33.

25. Zhao J, Zhou M, Li C. Synthetic nanoparticles for delivery of radioisotopes and radiosensitizers in cancer therapy. Cancer Nanotechnology. 2016;7:9.

26. Pellico J, Gawne PJ, T. M. De Rosales R. Radiolabelling of nanomaterials for medical imaging and therapy. Chemical Society Reviews. 2021;50:3355–423.

27. Alavi M, Hamidi M. Passive and active targeting in cancer therapy by liposomes and lipid nanoparticles. Drug Metabolism and Personalized Therapy. 2019;34:1–8.

28. Llop J, Lammers T. Nanoparticles for Cancer Diagnosis, Radionuclide Therapy and Theranostics. ACS Nano. 2021;15:16974–81.

29. Varani M, Bentivoglio V, Lauri C, Ranieri D, Signore A. Methods for Radiolabelling Nanoparticles: SPECT Use (Part 1). Biomolecules. 2022;12:1–19.

30. Cai Z, Yook S, Lu Y, Bergstrom D, Winnik MA, Pignol JP, et al. Local Radiation Treatment of HER2-Positive Breast Cancer Using Trastuzumab-Modified Gold Nanoparticles Labeled with 177Lu. Pharmaceutical Research. 2017;34:579–90.

31. Cędrowska E, Pruszynski M, Majkowska-Pilip A, Męczyńska-Wielgosz S, Bruchertseifer F, Morgenstern A, et al. Functionalized TiO_2 nanoparticles labelled with ^{225}Ac for targeted alpha radionuclide therapy. Journal of Nanoparticle Research. 2018;20:83.

32. Cheng MHY, Overchuk M, Rajora MA, Lou JWH, Chen Y, Pomper MG, et al. Targeted theranostic 111In/Lu-nanotexaphyrin for SPECT imaging and photodynamic therapy. Molecular Pharmaceutics. 2022;19:1803–13.

33. Pouget JP, Mather SJ. General aspects of the cellular response to low- and high-LET radiation. European Journal of Nuclear Medicine. 2001;28:541–61.

34. Pouget J-P, Lozza C, Deshayes E, Boudousq V, Navarro-Teulon I. Introduction to Radiobiology of Targeted Radionuclide Therapy. Frontiers in Medicine. 2015;2:12.

35. Paillas S, Ladjohounlou R, Lozza C, Pichard A, Boudousq V, Jarlier M, et al. Localized Irradiation of Cell Membrane by Auger Electrons Is Cytotoxic Through Oxidative Stress-Mediated Nontargeted Effects. Antioxidants & Redox Signaling. 2016;25:467–84.

36. Kam WWY, Banati RB. Effects of ionizing radiation on mitochondria. Free Radical Biology and Medicine. 2013;65:607–19.

37. Prise KM, O'Sullivan JM. Radiation-induced bystander signalling in cancer therapy. Nature Reviews Cancer. 2009;9:351–60.

38. Karam J, Constanzo J, Pichard A, Gros L, Chopineau J, Morille M, et al. Rapid communication: insights into the role of extracellular vesicles during Auger radioimmunotherapy. International Journal of Radiation Biology. 2023;99:109–18.

39. Pouget JP, Navarro-Teulon I, Bardiès M, Chouin N, Cartron G, Pèlegrin A, et al. Clinical radioimmunotherapy-the role of radiobiology. Nature Reviews Clinical Oncology. 2011;8:720–34.

40. Baidoo KE, Yong K, Brechbiel MW. Molecular pathways: Targeted α - Particle radiation therapy. Clinical Cancer Research. 2013;19:530–7.

41. Gill MR, Falzone N, Du Y, Vallis KA. Targeted radionuclide therapy in combined-modality regimens. The Lancet Oncology. 2017;18:414-e423.

42. Cherry SR, Sorenson JA, Phelps ME. Modes of Radioactive Decay. Physics in Nuclear Medicine. 4th ed. Philadelphia: Elsevier; 2012. p. 19–30.

43. Howell R. Radiation spectra for Auger-electron emitting radionuclides: Report No.2 of AAPM Nuclear Medicine Task Group No.6. Medical Physics. 1992;19:1371–83.

44. Kassis AI, Adelstein SJ. Radiobiologic principles in radionuclide therapy. Journal of Nuclear Medicine. 2005;46:4–12.

45. Ku A, Facca VJ, Cai Z, Reilly RM. Auger electrons for cancer therapy – a review. EJNMMI Radiopharmacy and Chemistry. 2019;4:27.

46. Kassis AI. Molecular and cellular radiobiological effects of Auger emitting radionuclides. Radiation Protection Dosimetry. 2011;143:241–7.

47. Charlton D. E., Pomplun E., Booz J. Some Consequences of the Auger Effect: Fluorescence Yield, Charge Potential, and Energy Imparted. Radiation Research. 1987;111:553–64.

48. Carlson TA, White RM. Formation of Fragment Ions from CH3Te125 and C2H5Te125 Following the Nuclear Decays of CH_3I^{125} and $C_2H_5I^{125}$. The Journal of Chemical Physics. 1963;38:2930–4.

49. Krisch RE, Krasin F, Sauri CJ. DNA breakage, repair and lethality after ^{125}I decay in rec+ and recA strains of Escherichia coli. International Journal of Radiation Biology. 1976;29:37–50.

50. Lobachevsky PN, Martin RF. Iodine-125 decay in a synthetic oligodeoxynucleotide. II. The role of Auger electron irradiation compared to charge neutralization in DNA breakage. Radiation Research. 2000;153:271–8.

51. Lobachevsky PN, Martin RF. Iodine-125 decay in a synthetic oligodeoxynucleotide. I. Fragment size

distribution and evaluation of breakage probability. Radiation Research. 2000;153:263–70.

52. Bavelaar BM, Lee BQ, Gill MR, Falzone N, Vallis KA. Subcellular targeting of theranostic radionuclides. Frontiers in Pharmacology. 2018;9:996.

53. Barry L. Zaret, H. William Strauss, Neil D. Martin, Master Sergeant Harry P. Wells, Jr., Lieutenant Colonel M. D. Flamm J. Noninvasive Regional Myocardial Perfusion with Radioactive Potassium—Study of Patients at Rest, with Exercise and during Angina Pectoris. N Engl J Med. 1973;288:809–12.

54. Hurley PJ, Cooper M, Reba RC, Poggenburg KJ WHJ. 43KCl: A New Radiopharmaceutical for imaging the heart. Journal of Nuclear Medicine. 1971;12:516-519.

55. Martin ND, Zaret BL, McGowan RL, Wells HP, Flamm MD. Rubidium-81: A New Myocardial Scanning Agent. Radiology. 1974;111:651–6.

56. Love WD, Smith RO, Pulley PE. Mapping Myocardial Mass and Regional Coronary Blood Flow by External Monitoring of K-42 or Rb-86 Clearance. Journal of Nuclear Medicine. 1969;10:702–7.

57. Romhilt BDW, Adolph RJ, Sodd VJ, Levenson NI, August LS, Nishiyama H, et al. Cesium-129 Myocardial Scintigraphy to Detect Myocardial Infarction. Circulation. 1973;48:1242–51.

58. Carr E, Gleason G, Ch BE, Shaw J, Arbor A. The direct diagnosis of myocardial infarction by photoscanning after administration of cesium-131. American Heart Journal. 1964;5:627–36.

59. Zaret BL. Myocardial Imaging with Radioactive Potassium and Its Analogs. Progress in Cardiovascular Diseases. 1977;20:81–94.

60. Hesse B, Tägil K, Cuocolo A, Anagnostopoulos C, Bardies M, Bax J, et al. EANM/ESC procedural guidelines for myocardial perfusion imaging in nuclear cardiology. European Journal of Nuclear Medicine and Molecular Imaging. 2005;32:855–97.

61. McKillop JH. Thallium 201 Scintigraphy. The Western Journal of Medicine. 1980;133:23–46.

62. Pagnanelli RA, Basso DA. Myocardial perfusion imaging with 201Tl. Journal of Nuclear Medicine Technology. 2010;38:1–3.

63. Krasnow AZ, Collier BD, Isitman AT, Hellman RS, Peck DC. The clinical significance of unusual sites of thallium-201 uptake. Seminars in Nuclear Medicine. 1988;18:350–8.

64. Winchell HS. Mechanisms for localization of radiopharmaceuticals in neoplasms. Seminars in Nuclear Medicine. 1976;6:371–8.

65. McCall D, Zimmer LJ, Katz AM. Kinetics of thallium exchange in cultured rat myocardial cells.

Circulation Research. 1985;56:370–6.

66. Grunwald AM, Watson DD, Holzgrefe HH, Irving JF, Beller GA. Myocardial Thallium-201 Kinetics in Normal and Ischemic Myocardium. Circulation. 1981;64:610–8.

67. Schinkel AFL, Poldermans D, Elhendy A, Bax JJ. Assessment of myocardial viability in patients with heart failure. Journal of Nuclear Medicine. 2007;48:1135–46.

68. Jain D. Technetium-99m labeled myocardial perfusion imaging agents. Seminars in Nuclear Medicine. 1999;29:221–36.

69. Chatal JF, Rouzet F, Haddad F, Bourdeau C, Mathieu C, Guludec D Le. Story of rubidium-82 and advantages for myocardial perfusion PET imaging. Frontiers in Medicine. 2015;2:1–7.

70. Basara BE, Wallner R, Hakki A-H, Iskandrian, Abdulmassih. Extracardiac Accumulation of Thallium-201 in Pulmonary Carcinoma. The American Journal of Cardiology. 1984;53:358–9.

71. Tonami N, Hisada K. Clinical experience of tumor Imaging with Tl-201 chloride. Clinical Nuclear Medicine. 1977;2:75–81.

72. Salvatore M, Carratu L, Porta E. Thallium-201 as a positive indicator for lung neaoplasmas: preliminary experiments. Radiology. 1976;121:487–8.

73. Ito Y, Muranaka A, Harada T, Matsudo A, Yokobayashi T, Hideaki T. Experimental Study on Tumor Affinity of 201Tl-Chloride. European Journal of Nuclear Medicine. 1978;3:81–6.

74. Pauwels EKJ, McCready VR, Stoot JHMB, Deurzen DFP Van. The mechanism of accumulation of tumour-localising radiopharmaceuticals. European Journal of Nuclear Medicine. 1998;25:277–305.

75. Sehweil A, McKillop JH, Ziada G, Al-Sayed M, Abdel-Dayem H, Omar YT. The optimum time for tumour imaging with thallium-201. European Journal of Nuclear Medicine. 1988;13:527–9.

76. Hisada K, Tonami N, Miyamae T, Hiraki Y, Yamazaki T, Maeda T, et al. Clinical Evaluation of Tumor Imaging witl 201Tl Chloride. Radiology. 1978;129:497–500.

77. Sehweil AM, McKillop JH, Milroy R, Wilson R, Abdel-Dayem HM, Omar YT. Mechanism of 201Tl uptake in tumours. European Journal of Nuclear Medicine. 1989;15:376–9.

78. Sato O, Kawai A, Ozaki T, Kunisada T, Danura T, Inoue H. Value of thallium-201 scintigraphy in bone and soft tissue tumors. Journal of Orthopaedic Science. 1998;3:297–303.

79. Waxman AD, Eller D, Ashook G, Ramanna L, Brachman M, Heifetz L, et al. Comparison of gallium-67-citrate and thallium-201 scintigraphy in peripheral and intrathoracic lymphoma. Journal of Nuclear

Medicine. 1996;37:46–50.

80. MacManus MP, Hicks RJ, Ball DL, Ciavarella F, Binns D, Hogg A, et al. Imaging with F-18 FDG PET is superior to Tl-201 SPECT in the staging of non-small cell lung cancer for radical radiation therapy. Australasian Radiology. 2001;45:483–90.

81. Kim KT, Black KL, Marciano D, Mazziotta JC, Guze BH, Grafton S, et al. Thallium-201 SPECT imaging of brain tumors: Methods and results. Journal of Nuclear Medicine. 1990;31:965–9.

82. Gómez-Río M, Rodríguez-Fernández A, Ramos-Font C, López-Ramírez E, Llamas-Elvira JM. Diagnostic accuracy of ^{201}Thallium-SPECT and ^{18}F-FDG-PET in the clinical assessment of glioma recurrence. European Journal of Nuclear Medicine and Molecular Imaging. 2008;35:966–75.

83. Kurenkov N V., Lunev VP, Masterov VS, Shubin YN. Excitation functions for the formation of the neutron deficient nuclei ^{201}Tl, ^{201}Pb and 201Bi. Calculated and experimental data. Applied Radiation and Isotopes. 1995;46:29–37.

84. Bonardi M, Groppi F, Birattari C. A rapid improved method for gamma-spectrometric determination of ^{202}Tl impurities in [^{201}Tl]-labelled radiopharmaceuticals. Applied Radiation and Isotopes. 2002;57:647–55.

85. Tárkányi F, Ditrói F, Takács S, Hermanne A, Yamazaki H, Baba M, et al. Investigation of activation cross-section data of proton induced nuclear reactions on natTl to 42 MeV: review, new data and evaluation. Applied Radiation and Isotopes. 2013;77:103–9.

86. Cvjetko P, Cvjetko I, Pavlica M. Thallium toxicity in humans. Arhiv za Higijenu Rada i Toksikologiju. 2010;61:111–9.

87. Trtić TM, Čomor JJ. Extraction of thallium with butyl acetate. Separation Science and Technology. 1999;34:771–9.

88. Haji-Saeid M, Pillai MRA, Ruth TJ, Schlyer DJ, Van Den Winkel P, Vora M., et al. Cyclotron Produced Radionuclides: Principles and Practice. International Atomic Energy Agency. Vienna; 2008.

89. Hijnen NM, de Vries A, Blange R, Burdinski D, Grüll H. Synthesis and in vivo evaluation of ^{201}Tl(III)-DOTA complexes for applications in SPECT imaging. Nuclear Medicine and Biology. 2011;38:585–92.

90. Amiri A, Fatemi SJ, Fatemi SN. Removal of thallium by combining desferrioxamine and deferiprone chelators in rats. BioMetals. 2007;20:159–63.

91. Goldschmidt J, Wanger T, Engelhorn A, Friedrich H, Happel M, Ilango A, et al. High-resolution mapping of neuronal activity using the lipophilic thallium chelate complex TlDDC: Protocol and

validation of the method. NeuroImage. 2010;49:303–15.

92. Wanger T, Scheich H, Ohl FW, Goldschmidt J. The use of thallium diethyldithiocarbamate for mapping CNS potassium metabolism and neuronal activity: Tl^+-redistribution, Tl^+-kinetics and Tl^+-equilibrium distribution. Journal of Neurochemistry. 2012;122:106–14.

93. Bruine JF De, Royen EA Van, Vyth A, Jong JMBV De, Schoot JB Van Den. Thallium-201 Diethyldithiocarbamate: An Alternative to Iodine-123 N-Isopropyi-p-Iodoamphetamine. Journal of Nuclear Medicine. 1985;26:925–30.

94. Frei A, Rigby A, Yue TTC, Firth G, Ma MT, Long NJ. To chelate thallium (I) - synthesis and evaluation of Kryptofix-based chelators for ^{201}Tl. Dalton Transactions. 2022;51:9039–48.

95. Cullen DL, Meyer EF, Smith KM. Porphyrins and large metal ions. Crystal and molecular structure of 2,3,7,8,12,13,17,18-octaethylporphinatochlorothallium(III). Inorganic Chemistry. 1977;16:1179–86.

96. Lemon CM, Brothers PJ, Boitrel B. Porphyrin complexes of the period 6 main group and late transition metals. Dalton Transactions. 2011;40:6591. A

97. Fazaeli Y, Jalilian AR, Feizi S, Shadanpour N. Development of a radiothallium (III) labeld porphyrin complex as a potential imaging agent. ract. 2013;101:795–800.

98. Rigby A, Blower JE, Blower PJ, Terry SYA, Abbate V. Targeted Auger electron-emitter therapy: Radiochemical approaches for thallium-201 radiopharmaceuticals. Nuclear Medicine and Biology. 2021;98–99:1–7.

99. Rigby A, Firth G, Rivas C, Pham T, Kim J, Phanopoulos A, et al. Toward Bifunctional Chelators for Thallium-201 for Use in Nuclear Medicine. Bioconjugate Chemistry. 2022;33:1422–36.

100. Ramanna L, Waxman A, Binney G, Waxman S, Mirra J, Rosen G. Thallium-201 Scintigraphy in Bone Sarcoma: Comparison with Gallium-67 and Technetium- MDP in the Evaluation of Chemotherapeutic Response. Journal of Nuclear Medicine. 1990;31:567–72.

101. Suga K, Kume N, Orihashi N, Nishigauchi K, Uchisako H, Matsumoto T, et al. Difference in ^{201}Tl accumulation on single photon emission computed tomography in benign and malignant thoracic lesions. Nuclear Medicine Communication. 1993;14:1071–8.

102. Kawakami N, Kunisada T, Sato S, Morimoto Y, Tanaka M, Sasaki T, et al. Thallium-201 scintigraphy is an effective diagnostic modality to distinguish malignant from benign soft-tissue tumors. Clinical Nuclear Medicine. 2011;36:982–6.

103. Lebowitz E, Greene MW, Fairchild R, Bradley-Moore PR, Atkins HL, Ansari AN, et al. Thallium-201 for medical use. the Journal of Nuclear Medicine. 1975;16:151–6.

104. Cornelissen B, A Vallis K. Targeting the nucleus: an overview of Auger-electron radionuclide therapy. Current Drug Discovery Technologies. 2010;7:263–79.

105. Ku A, Facca VJ, Cai Z, Reilly RM. Auger electrons for cancer therapy – a review. EJNMMI Radiopharmacy and Chemistry. 2019;4:27.

106. Falzone N, Fernández-Varea JM, Flux G, Vallis KA. Monte Carlo evaluation of Auger electron-emitting theranostic radionuclides. Journal of Nuclear Medicine. Society of Nuclear Medicine Inc.; 2015;56:1441–6.

107. Kiess AP, Minn II, Chen Y, Hobbs R, Sgouros G, Mease RC, et al. Auger Radiopharmaceutical Therapy Targeting Prostate-Specific Membrane Antigen. Journal of Nuclear Medicine. 2015;56:1401–7.

108. Bodei L, Kassis AI, Adelstein SJ, Mariani G. Radionuclide Therapy with Iodine-125 and Other Auger-Electron-Emitting Radionuclides: Experimental Models and Clinical Applications. Cancer biotherapy & radiopharmaceuticals. 2003;18:861–77.

109. Pouget JP, Santoro L, Raymond L, Chouin N, Bardiès M, Bascoul-Mollevi C, et al. Cell membrane is a more sensitive target than cytoplasm to dense ionization produced by Auger electrons. Radiation Research. 2008;170:192–200.

110. Rao O V, Govelitz GF, Sastry KSR. Radiotoxicity of Thallium-201 in Mouse Testes: Inadequacy of Conventional Dosimetry. Journal of Nuclear Medicine. 1983;24:145–53.

111. Kassis AI, Adelstein SJ, Haydock C, Sastry KSR. Thallium-201: An experimental and a theoretical radiobiological approach to dosimetry. Journal of Nuclear Medicine. 1983;24:1164–75.

112. Pilatus U, Shim H, Artemov D, Davis D, van Zijl PCM, Glickson JD. Intracellular volume and apparent diffusion constants of perfused cancer cell cultures, as measured by NMR. Magnetic Resonance in Medicine. 1997;37:825–32.

113. Sattari I, Aslani G, Dehghan MK, Shirazi B, Shafie M, Shadanpour N, et al. Dependence of quality of thallium-201 on irradiation data. Iranian Journal of Radiation Research. 2003;1:51–4.

114. Ogawa H, Cornelius F, Hirata A, Toyoshima C. Sequential substitution of K^+ bound to Na^+,K^+-ATPase visualized by X-ray crystallography. Nature Communications. 2015;6:8004.

115. Thier SO. Potassium Physiology. The American Journal of Medicine. 1986;80:3–7.

116. Othman MFB, Mitry NR, Lewington VJ, Blower PJ, Terry SYA. Re-assessing gallium-67 as a therapeutic radionuclide. Nuclear Medicine and Biology. 2017;46:12–8.

117. Howell RW. Radiation spectra for Auger-electron emitting radionuclides: Report No. 2 of AAPM Nuclear Medicine Task Group No. 6. Medical Physics. 1992;19:1371–83.

118. Hoffman RS. Thallium toxicity and the role of Prussian blue in therapy. Toxicological Reviews. 2003;22:29–40.

119. Galván-Arzate S, Santamaría A. Thallium toxicity. Toxicology Letters. 1998;99:1–13.

120. Busquets MA, Estelrich J. Prussian blue nanoparticles: synthesis, surface modification, and biomedical applications. Drug Discovery Today. 2020;25:1431–43.

121. Buser H, Schwarzenbach D, Petter W, Ludi A. Crystal structure of Prussian blue: $Fe_4[Fe(CN)_6]_3*x[H_2O]$. Inorganic chemistry. 1977;16:2704–9.

122. Yang Y, Faustino PJ, Progar JJ, Brownell CR, Sadrieh N, May JC, et al. Quantitative determination of thallium binding to ferric hexacyanoferrate: Prussian blue. International Journal of Pharmaceutics. 2008;353:187–94.

123. Kravzov J, Rios C, Altagracia M, Monroy-Noyola A, López F. Relationship between physicochemical properties of Prussian blue and its efficacy as antidote against thallium poisoning. Journal of Applied Toxicology. 1993;13:213–6.

124. Catala L, Mallah T. Nanoparticles of Prussian blue analogs and related coordination polymers: From information storage to biomedical applications. Coordination Chemistry Reviews. 2017;346:32–61.

125. Du X, Hao X, Wang Z, Guan G. Electroactive ion exchange materials: Current status in synthesis, applications and future prospects. Journal of Materials Chemistry A. Royal Society of Chemistry; 2016;4:6236–58.

126. Song X, Song S, Wang D, Zhang H. Prussian Blue Analogs and Their Derived Nanomaterials for Electrochemical Energy Storage and Electrocatalysis. Small Methods. 2021;5:1–36.

127. Jiménez JR, Tricoire M, Garnier D, Chamoreau LM, Von Bardeleben J, Journaux Y, et al. A new $\{Fe_4Co_4\}$ soluble switchable nanomagnet encapsulating Cs+: enhancing the stability and redox flexibility and tuning the photomagnetic effect. Dalton Transactions. 2017;46:15549–57.

128. Ying S, Chen C, Wang J, Lu C, Liu T, Kong Y, et al. Synthesis and Applications of Prussian Blue and Its Analogues as Electrochemical Sensors. ChemPlusChem. 2021;86:1608–22.

129. Vokhmyanina D, Daboss E, Sharapova O, Mogilnikova M, Karyakin A. Single Printing Step Prussian Blue Bulk-Modified Transducers for Oxidase-Based Biosensors. Biosensors. 2023;13:250.

130. Wang SJ, Chen CS, Chen LC. Prussian blue nanoparticles as nanocargoes for delivering DNA drugs to cancer cells. Science and Technology of Advanced Materials. 2013;14:044405 (10pp).

131. Shokouhimehr M, Soehnlen ES, Hao J, Griswold M, Flask C, Fan X, et al. Dual purpose Prussian blue nanoparticles for cellular imaging and drug delivery: A new generation of T1-weighted MRI contrast and small molecule delivery agents. Journal of Materials Chemistry. 2010;20:5251–9.

132. Liang X, Deng Z, Jing L, Li X, Dai Z, Li C, et al. Prussian blue nanoparticles operate as a contrast agent for enhanced photoacoustic imaging. Chemical Communications. 2013;49:11029–31.

133. He H, Long M, Duan Y, Gu N. Prussian blue nanozymes: progress, challenges, and opportunities. Nanoscale. 2023;12818–39.

134. Lu L, Zhang C, Zou B, Wang Y. Hollow prussian blue nanospheres for photothermal/chemo-synergistic therapy. International Journal of Nanomedicine. 2020;15:5165–77.

135. Shi Y, van der Meel R, Chen X, Lammers T. The EPR effect and beyond: strategies to improve tumor targeting and cancer nanomedicine treatment efficacy. Theranostics. 2020;10:7921–4.

136. Perrier M, Busson M, Massasso G, Long J, Boudousq V, Pouget JP, et al. $^{201}Tl^{+}$-labelled Prussian blue nanoparticles as contrast agents for SPECT scintigraphy. Nanoscale. 2014;6:13425–9.

137. Szigeti K, Hegedus N, Rácz K, Horváth I, Veres DS, Szöllosi D, et al. Thallium Labeled Citrate -Coated Prussian Blue Nanoparticles as Potential Imaging Agent. Contrast Media and Molecular Imaging. 2018;2023604.

138. Maurin-Pasturel G, Rascol E, Busson M, Sevestre S, Lai-Kee-Him J, Bron P, et al. ^{201}Tl-labeled Prussian blue and Au@Prussian blue nanoprobes for SPEC-CT imaging: Influence of the size, shapeand coating on the biodistribution. Inorganic Chemistry Frontiers. 2017;4:1737–41.

139. Li X Da, Liang XL, Ma F, Jing LJ, Lin L, Yang YB, et al. Chitosan stabilized Prussian blue nanoparticles for photothermally enhanced gene delivery. Colloids and Surfaces B: Biointerfaces. 2014;123:629–38.

140. Osytek KM, Blower PJ, Costa IM, Smith GE, Abbate V, Terry SYA. In vitro proof of concept studies of radiotoxicity from Auger electron-emitter thallium-201. EJNMMI Research. 2021;11.

141. Sápi J, Kovács L, Drexler DA, Kocsis P, Gajári D, Sápi Z. Tumor volume estimation and quasi-continuous administration for most effective bevacizumab therapy. PLoS ONE. 2015;10:e0142190.

142. Fu G, Liu W, Li Y, Jin Y, Jiang L, Liang X, et al. Magnetic Prussian Blue Nanoparticles for Targeted Photothermal Therapy under Magnetic Resonance Imaging Guidance. Bioconjugate Chemistry. 2014;25:1655–63.

143. Queiroz MF, Melo KRT, Sabry DA, Sassaki GL, Rocha HAO. Does the use of chitosan contribute to oxalate kidney stone formation? Marine Drugs. 2015;13:141–58.

144. Chakraborty N, Jha D, Gautam HK, Roy I. Peroxidase-like behavior and photothermal effect of chitosan-coated Prussian-blue nanoparticles: Dual-modality antibacterial action with enhanced bioaffinity. Materials Advances. 2020;1:774–82.

145. Shokouhimehr M, Soehnlen ES, Khitrin A, Basu S, Huang SD. Biocompatible Prussian blue nanoparticles: Preparation, stability, cytotoxicity, and potential use as an MRI contrast agent. Inorganic Chemistry Communications. 2010;13:58–61.

146. Souza TGF, Ciminelli VST, Mohallem NDS. A comparison of TEM and DLS methods to characterize size distribution of ceramic nanoparticles. Journal of Physics: Conference Series. 2016;733:012039.

147. Busquets MA, Novella-Xicoy A, Guzmán V, Estelrich J. Facile synthesis of novel Prussian blue-lipid nanocomplexes. Molecules. 2019;24:4137.

148. Sabourian P, Yazdani G, Ashraf SS, Frounchi M, Mashayekhan S, Kiani S, et al. Effect of physico-chemical properties of nanoparticles on their intracellular uptake. International Journal of Molecular Sciences. 2020;21:8019–39.

149. Zhang S, Gao H, Bao G. Physical Principles of Nanoparticle Cellular Endocytosis. ACS Nano. 2015;9:8655–71.

150. Fröhlich E. The role of surface charge in cellular uptake and cytotoxicity of medical nanoparticles. International Journal of Nanomedicine. 2012;7:5577–91.

151. Agashe HB, Dutta T, Garg M, Jain NK. Investigations on the toxicological profile of functionalized fifth-generation poly(propylene imine) dendrimer. Journal of Pharmacy and Pharmacology. 2010;58:1491–8.

152. Chithrani BD, Ghazani AA, Chan WCW. Determining the size and shape dependence of gold nanoparticle uptake into mammalian cells. Nano Letters. 2006;6:662–8.

153. Blechinger J, Bauer AT, Torrano AA, Gorzelanny C, Bräuchle C, Schneider SW. Uptake kinetics and nanotoxicity of silica nanoparticles are cell type dependent. Small. 2013;9:3970–80.

154. Richard I, Thibault M, De Crescenzo G, Buschmann MD, Lavertu M. Ionization behavior of chitosan

and chitosan-DNA polyplexes indicate that chitosan has a similar capability to induce a proton-sponge effect as PEI. Biomacromolecules. 2013;14:1732–40.

155. Li WB, Friedland W, Jacob P, Panyutin IG, Paretzke HG. Simulation of ^{125}I decay in a synthetic oligodeoxynucleotide with normal and distorted geometry and the role of radiation and non-radiation actions. Radiation and Environmental Biophysics. 2004;43:23–33.

156. Faraggi M, Gardin I, de Labriolle-Vaylet C, Moretti JL, Bok BD. The influence of tracer localization on the electron dose rate delivered to the cell nucleus. Journal of nuclear medicine. 1994;35:113–9.

157. Falzone N, Fernandez-Varea JM, Flux G, Vallis KA. Monte Carlo Evaluation of Auger Electron-Emitting Theranostic Radionuclides. Journal of Nuclear Medicine. 2015;56:1441–6.

158. Reissig F, Mamat C, Steinbach J, Pietzsch HJ, Freudenberg R, Navarro-Retamal C, et al. Direct and Auger electron-induced, singleand double-strand breaks on plasmid DNA caused by ^{99}mTc-labeled pyrene derivatives and the effect of bonding distance. PLoS One. 2016;11:e0161973.

159. Balagurumoorthy P, Xu X, Wang K, Adelstein SJ, Kassis AI. Effect of distance between decaying 125 I and DNA on Auger-electron induced double-strand break yield. International Journal of Radiation Biology. 2012;88:998–1008.

160. Lee H, Riad A, Martorano P, Mansfield A, Samanta M, Batra V, et al. PARP-1-targeted Auger emitters display high-LET cytotoxic properties in vitro but show limited therapeutic utility in solid tumor models of human neuroblastoma. Journal of Nuclear Medicine. 2020;61:850–6.

161. Kassis AI, Fayad F, Kinsey BM, Sastry KSR, Taube RA, Adelstein SJ. Radiotoxicity of ^{125}I in mammalian cells. Radiation Research. 1987;111:305–18.

162. Sahu SK, Wen PYC, Foulon CF, Nagel JS, Black PM, Adelstein SJ, et al. Intrathecal 5-[^{125}I]Iodo-2'-Deoxyuridine in a Rat Model of Leptomeningeal Metastases. Journal of Nuclear Medicine. 1997;38:386–90.

163. Dahmen V, Kriehuber R. Cytotoxic effects and specific gene expression alterations induced by I-125-labeled triplex-forming oligonucleotides. International Journal of Radiation Biology. 2012;88:972–9.

164. Pirovano G, Jannetti SA, Carter LM, Sadique A, Kossatz S, Guru N, et al. Targeted brain tumor radiotherapy using an Auger emitter. Clinical Cancer Research. 2020;26:2871–81.

165. Reilly RM, Kiarash R, Cameron RG, Porlier N, Sandhu J, Hill RP, et al. ^{111}In-labeled EGF is selectively radiotoxic to human breast cancer cells overexpressing EGFR. Journal of Nuclear Medicine.

2000;41:429–38.

166. Bailey KE, Costantini DL, Cai Z, Scollard DA, Chen Z, Reilly RM, et al. Epidermal growth factor receptor inhibition modulates the nuclear localization and cytotoxicity of the Auger electron-emitting radiopharmaceutical ^{111}In-DTPA-human epidermal growth factor. Journal of Nuclear Medicine. 2007;48:1562–70.

167. Costantini DL, Chan C, Cai Z, Vallis KA, Reilly RM. 111In-labeled trastuzumab (Herceptin) modified with nuclear localization sequences (NLS): an Auger electron-emitting radiotherapeutic agent for HER2/neu-amplified breast cancer. Journal of Nuclear Medicine. 2007;48:1357–68.

168. Drescher D, Büchner T, Schrade P, Traub H, Werner S, Guttmann P, et al. Influence of Nuclear Localization Sequences on the Intracellular Fate of Gold Nanoparticles. ACS Nano. 2021;15:14838–49.

169. Pan L, He Q, Liu J, Chen Y, Ma M, Zhang L, et al. Nuclear-targeted drug delivery of TAT peptide-conjugated monodisperse mesoporous silica nanoparticles. Journal of the American Chemical Society. 2012;134:5722–5.

170. De La Fuente JM, Berry CC. TAT peptide as an efficient molecule to translocate gold nanoparticles into the cell nucleus. Bioconjugate Chemistry. 2005;16:1176–80.

171. Yu B, Wei H, He Q, Ferreira CA, Kutyreff CJ, Ni D, et al. Efficient Tumor and Mitochondria Uptake of 177 Lu-Porphyrin-PEG Nanocomplexes for Multimodal Imaging Guided Combination Therapy. Angewandte Chemie International Edition. 2018;57:218–22.

172. Paillas S, Ladjohounlou R, Lozza C, Pichard A, Boudousq V, Jarlier M, et al. Localized Irradiation of Cell Membrane by Auger Electrons Is Cytotoxic Through Oxidative Stress-Mediated Nontargeted Effects. Antioxidants and Redox Signaling. 2016;25:467–84.

173. Maucksch U, Runge R, Wunderlich G, Freudenberg R, Naumann A, Kotzerke J. Comparison of the radiotoxicity of the ^{99}mTc-labeled compounds ^{99}mTc-pertechnetate, ^{99}mTc-HMPAO and ^{99}mTc-MIBI. International Journal of Radiation Biology. 2016;92:698–706.

174. Britten JS, Blank M. Thallium activation of the (Na^+-K^+)-activated ATPase of rabbit kidney. Biochimica et Biophysica Acta. 1968;159:160–6.

175. Hoffman RS. Thallium toxicity and the role of Prussian blue in therapy. Toxicological Reviews. 2003;22:29–40.

176. Herman M, Bensch K. Light and electron microscopic studies of acute and chronic thallium intoxication in rats. Toxicology and Applied Pharmacology. 1967;10:199–222.

177. Eskandari MR, Mashayekhi V, Aslani M, Hosseini MJ. Toxicity of thallium on isolated rat liver mitochondria: The role of oxidative stress and MPT pore opening. Environmental Toxicology. 2015;30:232–41.

178. Rodríguez-Mercado JJ, Hernández-de la Cruz H, Felipe-Reyes M, Jaramillo-Cruz E, Altamirano-Lozano MA. Evaluation of cytogenetic and DNA damage caused by thallium(I) acetate in human blood cells. Environmental Toxicology. 2015;30:572–80.

179. Rodríguez-Mercado JJ, Altamirano-Lozano MA. Genetic toxicology of thallium: a review. Drug and Chemical Toxicology. 2013;36:369–83.

180. Sánchez-Chapul L, Santamaría A, Aschner M, Ke T, Tinkov AA, Túnez I, et al. Thallium-induced DNA damage, genetic, and epigenetic alterations. Frontiers in Genetics. 2023;14:1–10.

181. Villaverde MS, Hanzel CE, Verstraeten S V. In vitro interactions of thallium with components of the gluthathione-dependent antioxidant defence system. Free Radical Research. 2004;38:977–84.

182. Costa IM, Cheng J, Osytek KM, Imberti C, Terry SYA. Methods and techniques for in vitro subcellular localization of radiopharmaceuticals and radionuclides. Nuclear Medicine and Biology. 2021;98–99:18–29.

183. Sakurai H, Okamoto M, Hasegawa M, Satoh T, Oikawa M, Kamiya T, et al. Direct visualization and quantification of the anticancer agent, cis-diamminedichloro-platinum(II), in human lung cancer cells using in-air microparticle-induced X-ray emission analysis. Cancer Science. 2008;99:901–4.

184. Aghevlian S, Cai Z, Hedley D, Winnik MA, Reilly RM. Radioimmunotherapy of PANC-1 human pancreatic cancer xenografts in NOD/SCID or NRG mice with Panitumumab labeled with Auger electron emitting, ^{111}In or β-particle emitting, ^{177}Lu. European Journal of Nuclear Medicine and Molecular Imaging Radiopharmacy and Chemistry. 2020;5:22.

185. Man F, Lim L, Volpe A, Gabizon A, Shmeeda H, Draper B, et al. In Vivo PET Tracking of ^{89}Zr-Labeled Vγ9Vδ2 T Cells to Mouse Xenograft Breast Tumors Activated with Liposomal Alendronate. Molecular Therapy. 2019;27:219–29.

186. Pan L, Liu J, Shi J. Cancer cell nucleus-targeting nanocomposites for advanced tumor therapeutics. Chemical Society Reviews. 2018;47:6930–46.

187. Uemura T, Ohba M, Kitagawa S. Size and surface effects of prussian blue nanoparticles protected by organic polymers. Inorganic Chemistry. 2004;43:7339–45.

188. Shiba F, Nito M, Kawakita K, Okawa Y. Size control of monodisperse prussian blue nanoparticles

by enforced-nucleation and additional-growth procedures in a Citrate Reduction System. Particulate Science and Technology. 2015;33:671–6.

189. Feng K, Zhang J, Dong H, Li Z, Gu N, Ma M, et al. Prussian Blue Nanoparticles Having Various Sizes and Crystallinities for Multienzyme Catalysis and Magnetic Resonance Imaging. ACS Applied Nano Materials. 2021;4:5176–86.

190. Shokouhimehr M. Prussian Blue Nanoparticles and its Analogues as New-Generation T1-Weighted MRI Contrast Agents for Cellular Imaging. Kent State University; 2010.

191. Bonta M, Török S, Hegedus B, Döme B, Limbeck A. A comparison of sample preparation strategies for biological tissues and subsequent trace element analysis using LA-ICP-MS. Analytical and Bioanalytical Chemistry. 2017;409:1805–14.

192. Ladeira LCM, dos Santos EC, Valente GE, da Silva J, Santos TA, dos Santos Costa Maldonado IR. Could biological tissue preservation methods change chemical elements proportion measured by energy dispersive X-ray spectroscopy? Biological Trace Element Research. 2020;196:168–72.

193. Stewart TJ. Across the spectrum: integrating multidimensional metal analytics for in situ metallomic imaging. Metallomics. 2019;11:29–49.

194. Löhr K, Traub H, Wanka AJ, Panne U, Jakubowski N. Quantification of metals in single cells by LA-ICP-MS: Comparison of single spot analysis and imaging. Journal of Analytical Atomic Spectrometry. 2018;33:1579–87.

195. Tian H, Wucher A, Winograd N. Reducing the Matrix Effect in Organic Cluster SIMS Using Dynamic Reactive Ionization. Journal of the American Society for Mass Spectrometry. 2016;27:2014–24.

196. Van Malderen SJM, Van Acker T, Vanhaecke F. Sub-micrometer Nanosecond LA-ICP-MS Imaging at Pixel Acquisition Rates above 250 Hz via a Low-Dispersion Setup. Analytical Chemistry. 2020;92:5756–64.

197. Van Malderen SJM, Van Acker T, Laforce B, De Bruyne M, de Rycke R, Asaoka T, et al. Three-dimensional reconstruction of the distribution of elemental tags in single cells using laser ablation ICP-mass spectrometry via registration approaches. Analytical and bioanalytical chemistry. Analytical and Bioanalytical Chemistry; 2019;411:4849–59.

198. Westerhausen MT, Bishop DP, Dowd A, Wanagat J, Cole N, Doble PA. Super-Resolution Reconstruction for Two-and Three-Dimensional LA-ICP-MS Bioimaging. Analytical Chemistry. 2019;14886.

199. Jeynes JCG, Bailey MJ, Coley H, Kirkby KJ, Jeynes C. Microbeam PIXE analysis of platinum resistant and sensitive ovarian cancer cells. Nuclear Instruments and Methods in Physics Research, Section B: Beam Interactions with Materials and Atoms. Elsevier B.V.; 2010;268:2168–71.

200. Ma X, Fernández FM. Advances in mass spectrometry imaging for spatial cancer metabolomics. Mass Spectrometry Reviews. 2022;e21804.

201. Costa C, De Jesus J, Nikula C, Murta T, Grime GW, Palitsin V, et al. Exploring New Methods to Study and Moderate Proton Beam Damage for Multimodal Imaging on a Single Tissue Section. Journal of the American Society for Mass Spectrometry. 2022;33:2263–72.

202. Jia F, Zhao X, Zhao Y. Advancements in ToF-SIMS imaging for life sciences. Frontiers in Chemistry. 2023;11:1–15.

203. Scimeca M, Bischetti S, Lamsira HK, Bonfiglio R, Bonanno E. Energy dispersive X-ray (EDX) microanalysis: A powerful tool in biomedical research and diagnosis. European Journal of Histochemistry. 2018;62:89–99.

204. Ostrowski A, Nordmeyer D, Boreham A, Holzhausen C, Mundhenk L, Graf C, et al. Overview about the localization of nanoparticles in tissue and cellular context by different imaging techniques. Beilstein Journal of Nanotechnology. 2015;6:263–80.

205. Puncher MRB, Blower PJ. Radionuclide targeting and dosimetry at the microscopic level: the role of microautoradiography. European Journal of Nuclear Medicine. 1994;21:1347–65.

206. Julien-Schraermeyer S, Illing B, Tschulakow A, Taubitz T, Guezguez J, Burnet M, et al. Penetration, distribution, and elimination of remofuscin/soraprazan in Stargardt mouse eyes following a single intravitreal injection using pharmacokinetics and transmission electron microscopic autoradiography: Implication for the local treatment of Star. Pharmacology Research and Perspectives. 2020;8:1–10.

207. De Samber B, Niemiec MJ, Laforce B, Garrevoet J, Vergucht E, De Rycke R, et al. Probing Intracellular Element Concentration Changes during Neutrophil Extracellular Trap Formation Using Synchrotron Radiation Based X-Ray Fluorescence. PLoS ONE. 2016;11:e0165604.

208. Checchetto V, Teardo E, Carraretto L, Leanza L, Szabo I. Physiology of intracellular potassium channels: A unifying role as mediators of counterion fluxes? Biochimica et Biophysica Acta - Bioenergetics. 2016;1857:1258–66.

209. Jang SH, Byun JK, Jeon W Il, Choi SY, Park J, Lee BH, et al. Nuclear localization and functional characteristics of voltage-gated potassium channel Kv1.3. Journal of Biological Chemistry. 2015;290:12547–57.

210. Chen Y, Sánchez A, Rubio ME, Kohl T, Pardo LA, Stühmer W. Functional kv10.1 channels localize to the inner nuclear membrane. PLoS ONE. 2011;6.

211. Behzadi S, Serpooshan V, Tao W, Hamaly MA, Alkawareek MY, Dreaden EC, et al. Cellular uptake of nanoparticles: Journey inside the cell. Chemical Society Reviews. 2017;46:4218–44.

212. Wongrakpanich A, Geary SM, Joiner MLA, Anderson ME, Salem AK. Mitochondria-targeting particles. Nanomedicine. 2014;9:2531–43.

213. Frantz MC, Wipf P. Mitochondria as a target in treatment. Environmental and Molecular Mutagenesis. 2010;51:462–75.

214. Jalilian AR, Yari-Kamrani Y, Kamali-Dehghan M, Rajabifar S. Preparation and evaluation of [201Tl](III)-DTPA complex for cell labeling. Journal of Radioanalytical and Nuclear Chemistry. 2008;275:109–14.

215. Balali-Mood M, Doyle P, Kazantzis G, Kiilunen M, Malcolm H, Nordberg G, et al. Environmental health criteria 182: Thallium. World Health Organization. Geneva; 1996.

216. Othman MF bin, Verger E, Costa I, Tanapirakgul M, Cooper MS, Imberti C, et al. In vitro cytotoxicity of Auger electron-emitting [^{67}Ga]Ga-trastuzumab. Nuclear Medicine and Biology. 2020;80–81:57–64.

217. Gao C, Leyton J V, Schimmer AD, Minden M, Reilly RM. Auger electron-emitting ^{111}In-DTPA-NLS-CSL360 radioimmunoconjugates are cytotoxic to human acute myeloid leukemia (AML) cells displaying the CD123+/CD131- phenotype of leukemia stem cells. Applied Radiation and Isotopes. 2016;110:1–7.

218. Lam K, Scollard DA, Chan C, Levine MN, Reilly RM. Kit for the preparation of ^{111}In-labeled pertuzumab injection for imaging response of HER2-positive breast cancer to trastuzumab (Herceptin). Applied Radiation and Isotopes. 2015;95:135–42.

219. Senge MO, Ruhlandt-Senge K, Regli KJ, Smith KM. Synthesis and characterization of halogeno- and pseudo-halogeno-thallium(III) porphyrin complexes. Variation of the co-ordination geometry as a function of the axial ligand. Journal of the Chemical Society, Dalton Transactions. 1993;3519.

220. Lai JJ, Khademi S, Meyer EF, Cullen DL, Smith KM. Bis-thallium(I) porphyrin complexes. Journal of Porphyrins and Phthalocyanines. 2001;5:621–7.

221. Fazaeli Y, Jalilian AR, Feizi S, Shadanpour N. Development of a radiothallium (III) labeld porphyrin complex as a potential imaging agent. Radiochimica Acta. 2013;101:795–800.

222. Preihs C, Arambula JF, Magda D, Jeong H, Yoo D, Cheon J, et al. Recent Developments in

Texaphyrin Chemistry and Drug Discovery. Inorganic Chemistry. 2013;52:12184–92.

223. Keca JM, Zheng G. Texaphyrin: From molecule to nanoparticle. Coordination Chemistry Reviews. 2019;379:133–46.

224. Wei W-H, Wang Z, Mizuno T, Cortez C, Fu L, Sirisawad M, et al. New polyethyleneglycol-functionalized texaphyrins: synthesis and in vitro biological studies. Dalton Transactions. 2006;1934.

225. Thiabaud G, He G, Sen S, Shelton KA, Baze WB, Segura L, et al. Oxaliplatin Pt(IV) prodrugs conjugated to gadoliniumtexaphyrin as potential antitumor agents. Proceedings of the National Academy of Sciences of the United States of America. 2020;117:7021–9.

226. Keca JM, Valic MS, Cheng MHY, Jiang W, Overchuk M, Chen J, et al. Mixed and matched metallo-nanotexaphyrin for customizable biomedical imaging. Advanced Healthcare Materials. 2019;8:1–11.

227. Keca JM, Chen J, Overchuk M, Muhanna N, MacLaughlin CM, Jin CS, et al. Nanotexaphyrin: one-pot synthesis of a manganese texaphyrin-phospholipid nanoparticle for magnetic resonance imaging. Angewandte Chemie - International Edition. 2016;55:6187–91.

228. Sessler JL, Murai T, Lynch V, Cyr M. An “Expanded Porphyrin”: the synthesis and structure of a new aromatic pentadentate ligand. Journal of the American Chemical Society. 1988;110:5586–8.

229. Uusijärvi H, Bernhardt P, Ericsson T, Forssell-Aronsson E. Dosimetric characterization of radionuclides for systemic tumor therapy: Influence of particle range, photon emission, and subcellular distribution. Medical Physics. 2006;33:3260–9.

230. Wyszomirska A. Iodine-131 for therapy of thyroid diseases. Physical and biological basis. Nuclear Medicine Review. 2012;15:120–3.

231. Willowson K, Bailey D, Schembri G, Baldock C. CT-based quantitative SPECT for the radionuclide ^{201}TI: Experimental validation and a standardized uptake value for brain tumour patients. Cancer Imaging. 2012;12:31–40.

232. Press OW, Eary JF, Appelbaum FR, Martin PJ, Badger CC, Nelp WB, et al. Radiolabeled-Antibody Therapy of B-Cell Lymphoma with Autologous Bone Marrow Support. The New England journal of medicine. 1993;329:1219–1224.

EJNMMI Research

ORIGINAL RESEARCH

Open Access

In vitro proof of concept studies of radiotoxicity from Auger electron-emitter thallium-201

Katarzyna M. Osytek[1], Philip J. Blower[1], Ines M. Costa[1], Gareth E. Smith[2], Vincenzo Abbate[3*†] and Samantha Y. A. Terry[1*†]

Abstract

Background: Auger electron-emitting radionuclides have potential in targeted treatment of small tumors. Thallium-201 (^{201}Tl), a gamma-emitting radionuclide used in myocardial perfusion scintigraphy, decays by electron capture, releasing around 37 Auger and Coster–Kronig electrons per decay. However, its therapeutic and toxic effects in cancer cells remain largely unexplored. Here, we assess ^{201}Tl in vitro kinetics, radiotoxicity and potential for targeted molecular radionuclide therapy, and aim to test the hypothesis that ^{201}Tl is radiotoxic only when internalized.

Methods: Breast cancer MDA-MB-231 and prostate cancer DU145 cells were incubated with 200–8000 kBq/mL [^{201}Tl]TlCl. Potassium concentration varied between 0 and 25 mM to modulate cellular uptake of ^{201}Tl. Cell uptake and efflux rates of ^{201}Tl were measured by gamma counting. Clonogenic assays were used to assess cell survival after 90 min incubation with ^{201}Tl. Nuclear DNA damage was measured with γH2AX fluorescence imaging. Controls included untreated cells and cells treated with decayed [^{201}Tl]TlCl.

Results: ^{201}Tl uptake in both cell lines reached equilibrium within 90 min and washed out exponentially ($t_{1/2}$ 15 min) after the radioactive medium was exchanged for fresh medium. Cellular uptake of ^{201}Tl in DU145 cells ranged between 1.6 (25 mM potassium) and 25.9% (0 mM potassium). Colony formation by both cell lines decreased significantly as ^{201}Tl activity in cells increased, whereas ^{201}Tl excluded from cells by use of high potassium buffer caused no significant toxicity. Non-radioactive TlCl at comparable concentrations caused no toxicity. An estimated average ^{201}Tl intracellular activity of 0.29 Bq/cell (DU145 cells) and 0.18 Bq/cell (MDA-MB-231 cells) during 90 min exposure time caused 90% reduction in clonogenicity. ^{201}Tl at these levels caused on average 3.5–4.6 times more DNA damage per nucleus than control treatments.

Conclusions: ^{201}Tl reduces clonogenic survival and increases nuclear DNA damage only when internalized. These findings justify further development and evaluation of ^{201}Tl therapeutic radiopharmaceuticals.

Keywords: Auger electrons, ^{201}Tl, Thallium-201, Radiobiology, Targeted molecular radionuclide therapy

Background

Thallium-201 (^{201}Tl, $t_{1/2}$ = 73 h) is well-known in diagnostic nuclear medicine. By mimicking the biological behavior of potassium, it has played a major role in myocardial perfusion scintigraphy [1], until it was largely replaced by ^{99m}Tc labeled complexes [2]. ^{201}Tl has also been used for tumor imaging [3, 4], to evaluate chemotherapy responses [5] and tumor malignancy [6, 7].

*Correspondence: vincenzo.abbate@kcl.ac.uk; samantha.terry@kcl.ac.uk
†Vincenzo Abbate and Samantha Y. A. Terry have contributed equally to this work
[1] School of Biomedical Engineering and Imaging Sciences, King's College London, London, UK
[3] Department of Analytical, Environmental and Forensic Sciences, King's College London, London, UK
Full list of author information is available at the end of the article

However, because of low signal-to-noise ratio, significant tissue attenuation and high radiation absorbed dose [8], diagnostic use of ^{201}Tl has substantially diminished in recent years.

Apart from its gamma rays (135 keV—3%, 167 keV—10%) and X-rays (67–83 keV—94%) used in clinical imaging [9], ^{201}Tl decay by electron capture to stable mercury (^{201}Hg) also produces around 37 short-range Auger and Coster–Kronig electrons, one of the highest numbers among other Auger-electron emitters (Table 1) [10] with therapeutic potential. The average total energy of Auger and Coster–Kronig electrons per decay is calculated as 15.3 keV [10] and even though this is comparable to the energy of ^{125}I, its half-life is around 20 times shorter and hence more amenable to clinical use. Auger electron-emitters such as ^{111}In,^{125}I and ^{67}Ga (Table 1) [10], have already shown potential for targeted radionuclide therapy of cancer [11–13], especially when delivered close to sensitive cellular targets such as DNA and plasma membrane [10, 14, 15]. However, the therapeutic potential of ^{201}Tl has barely been studied, despite its potent shower of Auger electrons and good worldwide availability. Nearly 40 years ago, in the context of the safety of diagnostic use of ^{201}Tl, Rao et al. observed radiotoxic effects of ^{201}Tl in spermatogonial cells after intratesticular injection in a mouse model [16], and Kassis et al. compared the cellular kinetics and radiotoxicity of ^{201}Tl to those of β-emitters (^{42}K, ^{43}K and ^{86}Rb) in Chinese hamster lung fibroblasts [17]. Since then there has been little interest in ^{201}Tl radiobiology or radionuclide therapy.

In this preliminary evaluation of the potential of ^{201}Tl as a therapeutic radionuclide, we investigated the rate and extent of non-targeted ^{201}Tl uptake into cancer cells via potassium channels, such as the Na^+/K^+ pump (Fig. 1), and used this mechanism of accumulation to assess its radiotoxic effect in human cancer cells in vitro. The primary aim of this study was to measure the effect of internalized and non-internalized ^{201}Tl on clonogenic survival and DNA integrity in prostate and breast cancer cells. Non-targeted ^{201}TlCl was used in this study only to assess the radiotoxic potential of the radionuclide, and not to assess the potential of ^{201}TlCl itself. In contrast to other Auger electron-emitting electrons, such as ^{111}In or ^{67}Ga, no suitable chelators are available for ^{201}Tl and their development can be challenging due to its physical and chemical properties. A finding that ^{201}Tl has potential as a therapeutic radionuclide would stimulate development of effective thallium chelators for construction of targeted bioconjugates.

Methods

Cell culture consumables, unless specified, were purchased from Sigma-Aldrich, UK.

[^{201}Tl]TlCl in sterile 0.9% NaCl solution (360–560 MBq/5.8 mL) was obtained from Curium Pharma, UK; [^{201}Tl]TlCl specific radioactivity was greater than or equal to 3.7 MBq/μg of thallium and radiochemical purity was at least equal to 95% (as per [^{201}Tl]TlCl specification). [^{201}Tl]TlCl was used in all experiments without any preconditioning.

Cell culture

Human breast adenocarcinoma cells MDA-MB-231 (ATCC® HTB-26™) were cultured in Dulbecco's Modified Eagle Medium (DMEM, low glucose 1000 mg/L) and human prostate carcinoma cells DU145 (ATCC® HTB-81™) in RPMI-1640 medium. Both media were supplemented with 10% fetal bovine serum, 5% L-glutamine, penicillin (100 units) and 100 μg/mL streptomycin. Cultured cells were trypsinized and seeded at 250,000 cells per well in 24-well plates 16 h before each experiment and grown at 37 °C in a humidified 5% CO_2 atmosphere. During experiments, cells were kept in full medium or phosphate buffered saline (PBS; D8537) supplemented with $MgCl_2$ and $CaCl_2$ in concentrations equivalent to those found in media, or PBS without potassium (Alfa Aesar, J60465) supplemented as described above for PBS. KCl solutions were prepared by dissolving KCl (BDH Laboratory) in 0.9% NaCl. Concentrations of K^+ and Na^+ in PBS, PBS without K^+, RPMI and DMEM media are shown in Table 2.

Table 1 Characteristics of some of the Auger electron emitters [10]

	^{201}Tl	^{111}In	^{67}Ga	^{125}I
Half-life (days)	3.04	2.80	3.26	59.4
Number of Auger and Coster–Kronig electrons /decay	36.9	14.7	4.7	24.9
Auger and Coster–Kronig electrons energy per decay (keV)	15.3	6.8	6.3	12.2
Associated gamma emission (keV)	135.3; 167.4	171.3; 245.4	9.1; 9.3; 184; 209; 300; 393	3535

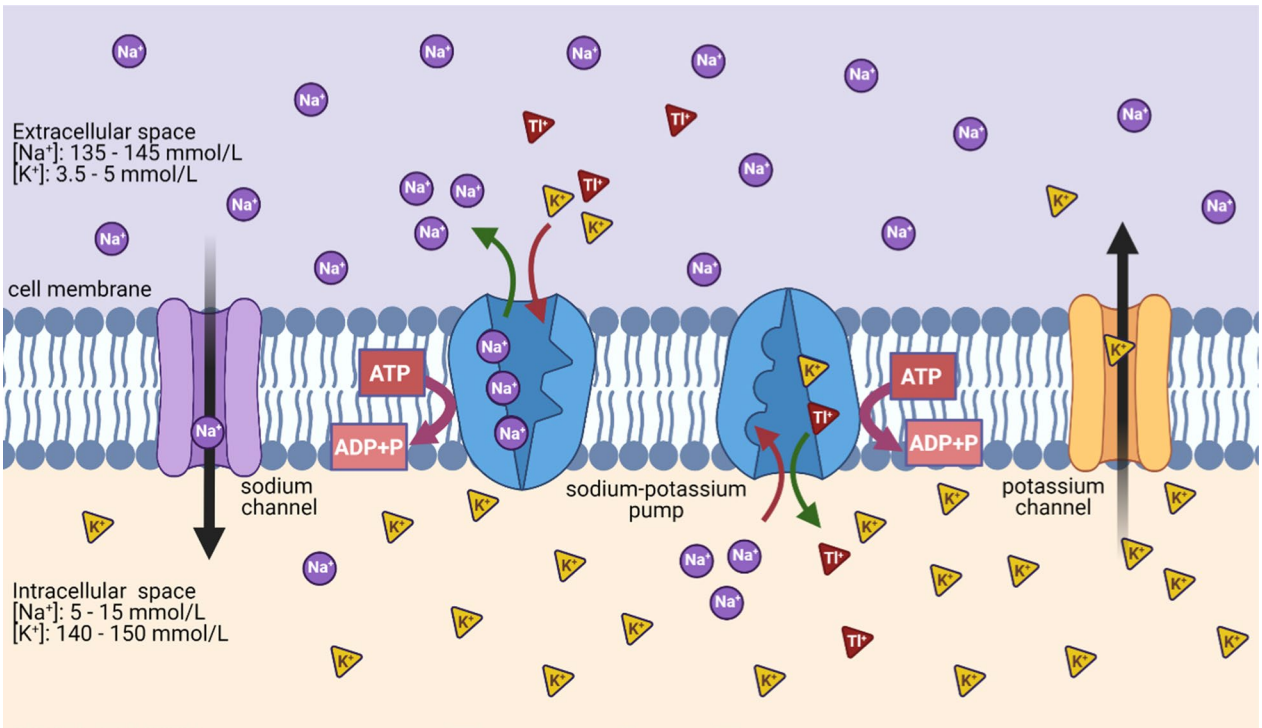

Fig. 1 Schematic representation of K^+, Na^+ and Tl^+ transport across cellular membranes. Sodium–potassium pump (Na^+/K^+-ATPase) transports K^+ ions inside and Na^+ ions outside a cell against their concentration gradient using energy released by the hydrolysis of ATP. Tl^+ ions, which mimic K^+ physiological behaviour, can be transported inside the cell via potassium channels, such as the sodium–potassium pump. Tl^+ transport mechanism outside the cell is currently unknown

Table 2 Concentration of potassium and sodium in incubation solutions used in experiments

Incubation solution	Concentration of K^+ (mmol/L)	Concentration of Na^+ (mmol/L)
Dulbecco's Modified Eagle Medium (DMEM)	5.3	155.0
RPMI-1640 medium	5.3	138.5
Phosphate buffer saline (PBS)	4.2	153.0
Phosphate buffer saline (PBS) without K^+	0	157.0

Concentration of potassium and sodium in incubation solutions used in experiments. To modulate ^{201}Tl uptake in cells, 0 mmol/L K^+ solutions were supplemented with KCl at a range of concentrations up to 25 mmol/L

Uptake and efflux assays

Fifteen minutes before each experiment the medium in each well was replaced by 200 µL fresh medium, PBS or PBS without K^+. Stock [^{201}Tl]TlCl was diluted with 0.9% NaCl to the required concentration (1–40 MBq/mL) and 50 µL (50–2000 kBq) was added to each well. Plates were incubated at 37 °C for a specified period. Then, the radioactive incubation solution was collected. Adherent cells were briefly washed thrice with PBS and lysed with 1 M NaOH for 15 min at room temperature (RT). Unbound radioactivity (incubation medium and PBS washings) and cell-bound radioactivity (lysate) were measured (counts per minute, CPM) with a CompuGamma CS1282 gamma counter.

To measure the rate of ^{201}Tl washout, cells were incubated at 37 °C for 90 min with 50 kBq (1 MBq/mL) ^{201}Tl in 250 µL medium (total), which was then removed. Adherent cells were washed briefly with 250 µL PBS and 250 µL of fresh non-radioactive medium was added to each well. Cells were incubated for various times (from 15 to 180 min) at 37 °C, after which medium was collected and cells washed and lysed as described above. A second method, to assess continuous complete ^{201}Tl efflux, involved repeated medium changes on the same

cells. In brief, after incubation with 50 kBq (1 MBq/mL) ^{201}Tl as above, replacing radioactive medium with fresh medium and allowing a further 15 min of efflux; medium was again removed, cells were washed once with PBS and fresh medium added. This process was repeated 4 times at intervals from 15 to 60 min. After 180 min cells were lysed and ^{201}Tl activity measured as described above, converting CPM to activity by means of a calibration curve (Additional file 1: Fig. S1). A nominal average intracellular volume of 1.6 pL for individual DU145 cells (as measured by diffusion NMR spectroscopy [18]) was used for intracellular-to-extracellular concentration ratio calculations.

^{203}Tl is a stable isotope used as a target material in the ^{201}Tl manufacturing process [19] and despite a rigorous purification process, some ^{203}Tl is still present in [^{201}Tl]TlCl solution (Additional file 1: Fig. S2 and Table S1). Inductively Coupled Plasma-Mass Spectrometry (ICP-MS) analysis was performed using a PerkinElmer NexION350D ICP-Mass Spectrometer to estimate ^{203}Tl concentrations in [^{201}Tl]TlCl decayed samples, using a calibration curve prepared as described in Additional file 1.

DNA damage

γH2AX assays were used to quantify DNA double-strand breaks (DSBs). Cells were seeded on coverslips coated with poly-L-lysine (50 μg/mL) placed in each well of a 24-well plate. Following a 90-min incubation with 50 μL (50–2000 kBq) of different ^{201}Tl activities (200–8000 kBq/mL), ^{203}Tl/^{201}Hg in equivalent concentrations, or ^{201}Tl (1000 kBq, 4000 kBq/mL) with added KCl (15 and 25 mM), medium was removed and coverslips were washed with PBS, fixed with 3.7% formalin in PBS, treated for 15 min with 0.5% Triton X-100® and 0.5% IGEPAL CA-630® solution, incubated with 1% goat serum/2% bovine serum albumin (BSA) in PBS for 1 h, washed with PBS, incubated overnight at 4 °C with mouse antiphospho-histone H2A.X monoclonal antibody (Merck, 1:1600 in 3% BSA), washed with 3% BSA in PBS and incubated with goat anti-mouse secondary fluorescent antibody Alexa Fluor®488 (Invitrogen, 1:500 in PBS) for 2 h at 4 °C. Hoechst 33,342 nuclei stain was added for 2 min at RT. Coverslips were washed twice with PBS and attached to microscope slides using 2.5% DABCO/Mowiol® (except for the experiment blocking ^{201}Tl uptake with KCl, where cells were stained and mounted with Prolong™ Gold Antifade Reagent with DAPI (Invitrogen)). Slides were stored at 4 °C. A TCS SP5 confocal microscope with Leica software was used to obtain fluorescent images and CellProfiler was used to quantify foci numbers per nucleus.

Cytotoxicity

^{201}Tl (50–2000 kBq, 200–8000 kBq/mL), ^{203}Tl/^{201}Hg in equivalent concentrations, or ^{201}Tl (1000 kBq, 4000 kBq/mL) with KCl (15 and 25 mM) was added to MDA-MB-231 or DU145 cells in 200 μL medium or potassium-free PBS. After 90 min, the radioactive incubation solution was removed, cells were washed three times with PBS, trypsinized, re-suspended in non-radioactive medium, seeded at 1000 cells/well in a 6-well plate and cultured for 8–10 days, changing medium every 2–3 days. Colonies were fixed and stained with 0.05% crystal violet in 50% methanol and counted manually with blinding, defining colonies as containing > 50 cells. All clonogenic assays were done alongside uptake assays to relate activity per cell with the surviving fraction.

Statistical analysis

Data were analysed in Excel Microsoft 2016 and GraphPad Prism 8, and expressed as mean ± SD. A nonparametric Mann–Whitney test for unpaired data was used to determine significance ($P < 0.05$). Each experiment was performed in triplicate or quadruplicate. Error bars represent standard deviations among independent experiments, except when $n = 1$ where the error is intra-experimental.

The intracellular activity was calculated comparing the gamma counter measurements (cpm) of the collected medium activity (with three PBS washes) to the lysate (NaOH) activity. The background count (BC) was subtracted from both values.

$$\text{Intracellular activity (\%)} = \frac{\text{lysate activity} - \text{BC}}{(\text{lysate activity} - \text{BC}) + (\text{collected medium activity} - \text{BC})} * 100$$

For the gamma counter measurements, fractions of the culture medium and lysate were taken (when needed) and then multiplied by the appropriate factor to obtain total values necessary for calculations.

The intracellular activity per cell was calculated by multiplying the activity added to each well (50–2000 kBq) by the measured intracellular activity (%) and divided by the number of cells per well counted right after the experiment.

$$\text{Intracellular activity per cell (Bq/cell)} = \frac{\text{activity added per well (Bq)} * \text{intracellular activity (\%)}}{\text{number of cells per well} * 100}$$

Figures were created with GraphPad Prism 8 and http://www.BioRender.com.

Results

^{201}Tl kinetics: uptake and efflux

In preliminary experiments in RPMI or DMEM medium (Table 2), cellular uptake of ^{201}Tl in both DU145 and MDA-MB-231 cells rose sharply up to 60 min and then plateaued (Fig. 2a and Additional file 1: Fig. S3a). The % uptake was independent of the activity used within the range examined (Fig. 2b, c) showing that the uptake mechanism was not saturable in this range. Based on these results: 90 min incubation time was chosen for radiobiological experiments. Efflux rate measurements were performed after 90 min 'loading' with 200 kBq/mL of ^{201}Tl in RPMI or DMEM medium. In both cell lines, when the radioactive medium was replaced by non-radioactive medium, ^{201}Tl bound by cells decreased exponentially with a half-life of around 15 min reaching

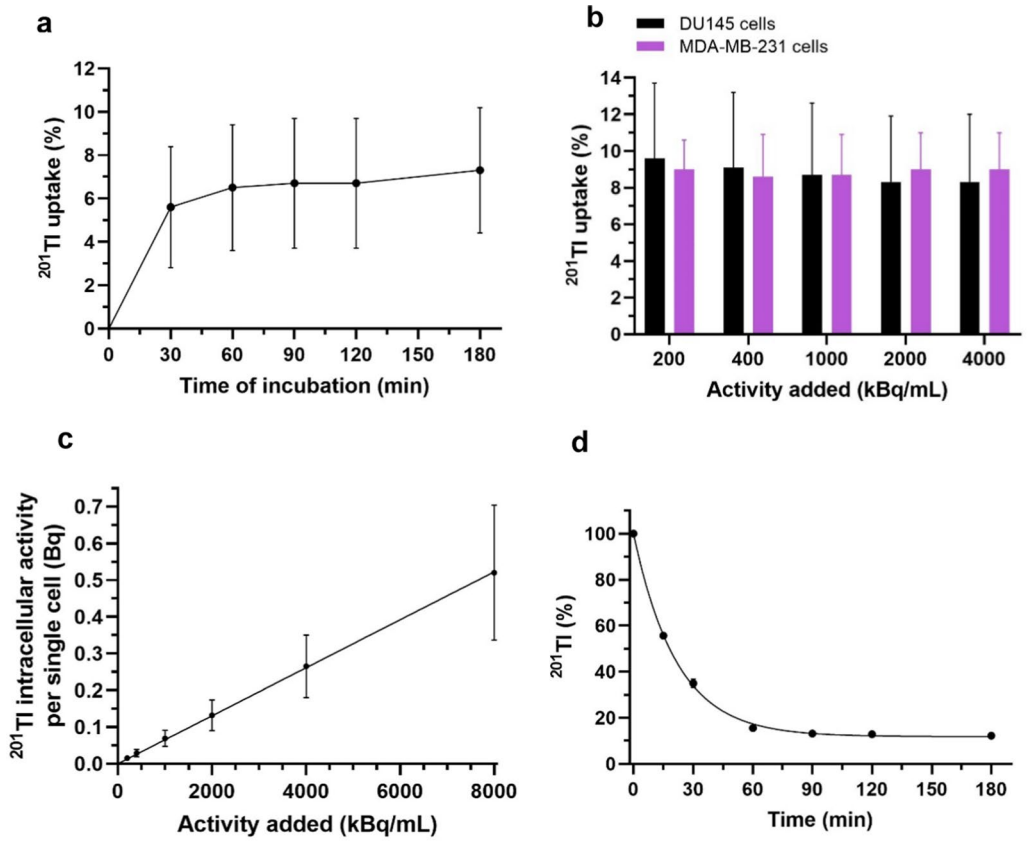

Fig. 2 ^{201}Tl kinetics. **a** Uptake of ^{201}Tl in DU145 cells ($n = 3$) after incubation with 200 kBq/mL [^{201}Tl]TlCl in medium. These results were used to determine the best incubation time for subsequent radiobiological experiments. **b** ^{201}Tl uptake in DU145 cells ($n = 3$) and MDA-MD-231 cells ($n = 2$) after 90 min incubation in medium with different activities of [^{201}Tl]TlCl. **c** ^{201}Tl intracellular activity per single cell (Bq) versus activity added (kBq/mL) in DU145 cells ($n = 3$) measured in medium. Graphs b and c show that the increasing activity of ^{201}Tl does not inhibit its cellular uptake, suggesting that saturation of uptake mechanisms is not reached at the activities used in this work. **d** Efflux of ^{201}Tl in DU145 ($n = 3$) cells. Plateau uptake from the preceding uptake assay is defined as 100% at time 0. Radioactive medium was replaced with non-radioactive and ^{201}Tl activity was measured over time. Data are presented as mean ± SD, done in triplicates; exponential regression line was fitted in d. Some error bars are smaller than the data symbols and hence not visible

a new equilibrium (Fig. 2d and Additional file 1: Fig. S3b) with the same intracellular-to-extracellular ratio of ^{201}Tl concentration. When medium was repeatedly refreshed, we again observed an exponential drop in the activity bound per cell, from 0.017 to 0.019 Bq at the beginning of the efflux experiment to approach 0 after 180 min (Additional file 1: Fig. S3c).

To modulate ^{201}Tl uptake into cells, cardiac glycosides digoxin and ouabain were evaluated but rejected because of their toxic effects on cells as described in Supplementary Material (Additional file 1: Fig. S4a and b) [20]. Instead, the effect of varying potassium concentration was evaluated. DU145 cells were incubated with 80 kBq/mL of ^{201}Tl for 90 min in PBS solution without potassium (Table 2) and supplemented with different concentrations of KCl rising to 50 mM. ^{201}Tl uptake decreased from 23.6 ± 0.6% in 0 mM potassium to 1.1 ± 0.1% in 50 mM potassium (Additional file 1: Fig. S4c). The potassium concentrations used showed no measurable baseline effects as measured by clonogenic assay or yH2AX imaging (see below), therefore variation of potassium concentration was adopted as the method of choice to modulate ^{201}Tl uptake.

^{201}Tl-induced nuclear DNA damage (yH2AX assay)

Results from three experiments on DU145 and MDA-MB-231 cells are shown in (Fig. 3a, Table 3). Cells treated with 4000 kBq/mL of ^{201}Tl showed a significantly higher average number of foci per nucleus (3.5 and 4.6 times for DU145 and MDA-MB-231 cells, respectively) than in the 0.9% NaCl-treated control ($P < 0.05$, Mann–Whitney test) (Additional file 1: Fig. S5a and b). Comparing the nuclear DNA damage in DU145 cells caused by 4000–8000 kBq/mL of ^{201}Tl to that caused by an equivalent volume of decayed [^{201}Tl]TlCl sample, we observed that only the radioactive component of the samples significantly increased the average number of foci per nucleus ($P < 0.05$, Mann–Whitney test) (Fig. 3b). The decayed sample caused no visible DNA damage compared to untreated controls (Fig. 3c) as expected, since thallium concentration is very low and other heavy metals (such as Hg decay product) were not detectable by ICP-MS (see Additional file 1: Fig. S2a and b and Table S1).

^{201}Tl radiotoxicity: clonogenic survival

Figure 4a presents clonogenic survival results for both cell lines incubated with various activities of ^{201}Tl for 90 min in RPMI or DMEM medium ([K^+] 5.3 mM). No reduction in surviving fractions was observed in cells treated with an equivalent volume of the decayed ^{201}Tl sample in DU145 cells (Fig. 4b). An estimated average ^{201}Tl intracellular activity per cell of 0.29 Bq (95% CI 0.18–0.49 Bq) for DU145 cells and 0.18 Bq (95% CI 0.10–0.39 Bq) for MDA-MB-231 cells (Fig. 4c, d) reduced clonogenic survival by at least 90% compared to untreated cells.

The impact of ^{201}Tl internalisation on clonogenic survival and nuclear DNA damage in DU145 cells

Varying potassium concentrations in the incubation solution above and below the physiological level (3.5–5 mM [21]) was adopted as a method to modulate ^{201}Tl uptake in cells, for the purpose of comparing the radiotoxicity of intracellular and extracellular ^{201}Tl. Applying this method, we used the yH2AX assay to compare the average number of foci per nucleus in DU145 cells with high ^{201}Tl uptake ([K^+] 0 mM, 25.9 ± 1.7% uptake, 181:1 intra:extra ratio) and low ^{201}Tl uptake ([K^+] 15 and 25 mM, 1.6 ± 0.4 and 2.2 ± 0.2% uptake respectively, 8:1 and 12:1 intra:extra ratio) after incubation with the same radioactive concentration (4,000 kBq/mL) of ^{201}Tl (Fig. 5a, b) and (Additional file 1: Table S2). We observed a significant reduction in the average number of foci per nucleus induced by ^{201}Tl—from 31.9 ± 5.2 at 0 mM K^+ to 8.8 ± 4.3 and 7.5 ± 5.0 at 15 and 25 mM potassium respectively ($P < 0.05$, Mann–Whitney test). In cells incubated with these K^+ concentrations without ^{201}Tl or non-radioactive Tl (NC1,3–4), there was no increase in foci per nucleus compared to cells incubated in standard RPMI medium ([K^+] 5.3 mM) (NC2). These results show that ^{201}Tl only induced DNA DSBs when internalized; extracellular ^{201}Tl showed no effect. A similar result emerged from clonogenic survival assays. Incubation of DU145 cells for 90 min with 4000 kBq/mL of ^{201}Tl (Fig. 5c) was lethal (no clonogenic survival) in 0 mM potassium medium, but 94.7 ± 3.9 to 98.6 ± 4.4% survival was found when ^{201}Tl uptake was suppressed with 15 or 25 mM KCl. Both extremes of potassium concentration showed no clonogenic toxicity in the absence of ^{201}Tl. Thus, preventing or reducing cellular uptake of the ^{201}Tl by increasing potassium concentration in the medium prevented both the DNA damage and clonogenic toxicity of ^{201}Tl.

Discussion

^{201}Tl is efficiently taken up by MDA-MB-231 cells and DU145 cells in standard incubation media ([K^+] 4.2–5.3 mM), achieving equilibrium at around 90 min with an estimated intracellular to extracellular ^{201}Tl concentration ratio (in DU145 cells) in the range 40:1–53:1 (Additional file 1: Table S2a and b) (very similar to literature estimates for K^+ ratios of 30:1–50:1 [16]). This ratio rises to 181:1 in potassium-free medium and collapses to 8:1 at elevated potassium levels (25 mM) (Additional file 1: Table S2c). These findings are consistent with the assumption that Tl^+ mimics potassium in a biological

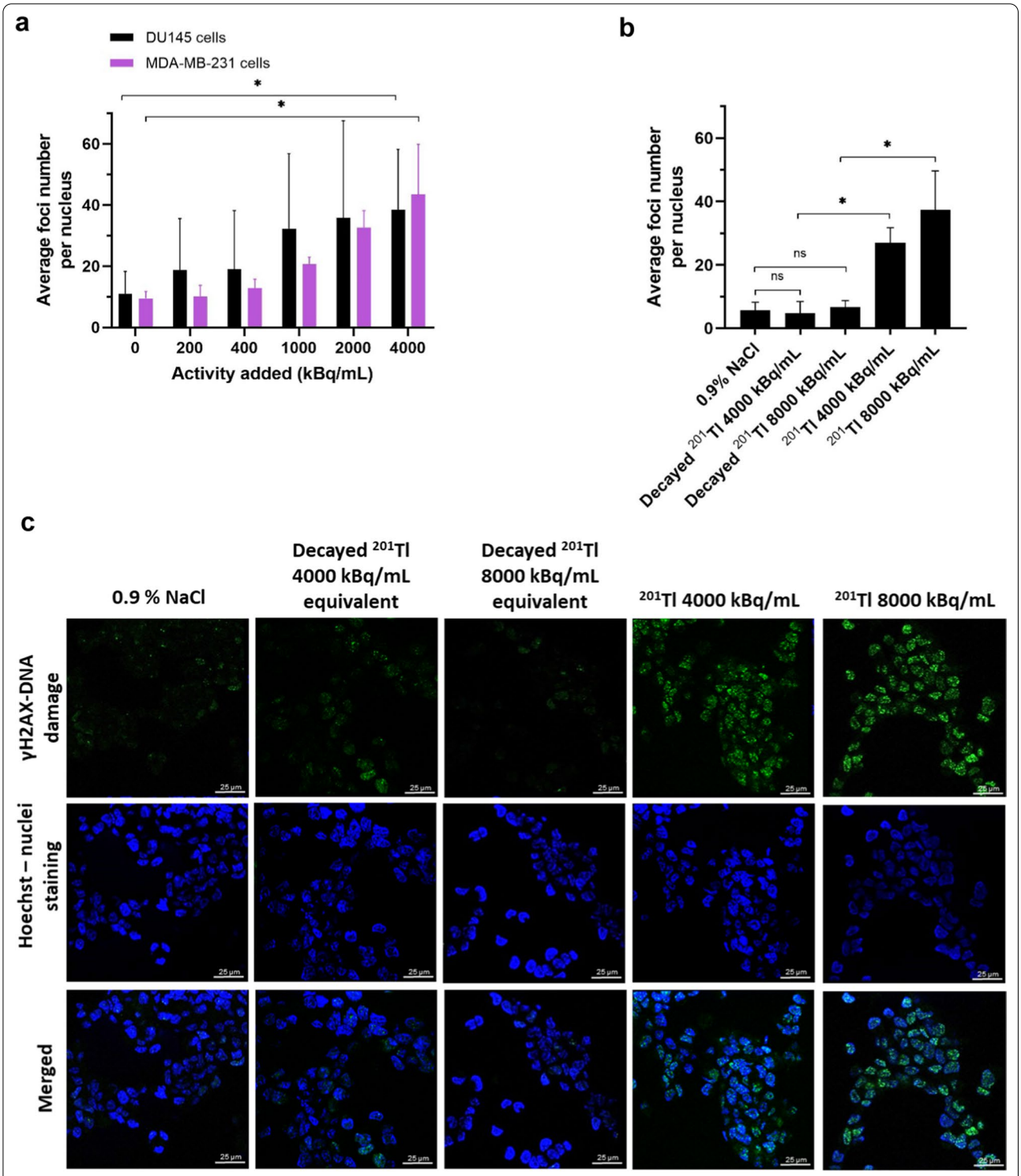

Fig. 3 ^{201}Tl radiotoxicity—nuclear DNA damage. Average number of foci per nucleus in DU145 cells and MDA-MD-231 cells after 90 min incubation **a** with [^{201}Tl]TlCl in medium **b** with 0.9% NaCl (negative control), an equivalent volume of [^{201}Tl]TlCl-decayed sample or [^{201}Tl]TlCl. A range of 26–72 nuclei per condition were analysed across all experiments; same settings were kept within the experiment. 3–9 pixel units were set as a typical diameter of foci. Bars represent mean ± SD, $n = 3$, * indicates $P < 0.05$, ns—not significant. **c** Exemplar confocal microscopy images (100×, field contain minimum 26 nuclei) of DU145 cells incubated for 90 min with 0.9% NaCl (negative control), an equivalent volume of [^{201}Tl]TlCl-decayed sample or [^{201}Tl]TlCl followed by immunofluorescence staining with green fluorescence for γH2AX (smart gain and smart offset were kept constant for all conditions in the experiment). Nuclear DNA is stained with Hoechst (blue). Scale bar—25 µm

Table 3. ^{201}Tl radiotoxicity—nuclear DNA damage

Activity of ^{201}Tl (kBq/mL)	Average number of foci per nucleus (±SD) DU145			Average number of foci per nucleus (±SD) MDA-MB-231		
0	3.5 ± 3.6	17.8 ± 18.3	11.9 ± 10.4	7.9 ± 10.3	8.6 ± 6.2	12.0 ± 10.9
100	5.2 ± 5	37.5 ± 25.2	13.3 ± 10.6	7.0 ± 5.3	9.4 ± 7.5	14.0 ± 13.1
200	4.4 ± 4.1	40.6 ± 33.7	12.0 ± 9.1	13.8 ± 8.0	9.5 ± 5.3	15.0 ± 7.2
400	16.2 ± 11.5	60.4 ± 34.9	19.9 ± 12.8	18.2 ± 9.4	22.7 ± 11.0	21.0 ± 12.2
1000	10.1 ± 6.2	71.2 ± 23.2	26.2 ± 18.1	30.9 ± 18.0	27.9 ± 17	38.8 ± 20.4
4000	28.6 ± 14.7	61.2 ± 27.8	25.3 ± 13.0	61.5 ± 28.0	29.6 ± 12.7	39.2 ± 21.5

Average number of foci per nucleus in DU145 cells and MDA-MD-231 cells after 90 min incubation with various activities of [^{201}Tl]TlCl in medium, and with 0.9% NaCl (0 kBq/mL) measured in three independent experiments

environment. ^{201}Tl efflux results showed exponential time-dependent efflux when the incubation medium was replaced by ^{201}Tl-free medium, returning to a new equilibrium with similar internal to external concentration ratio, suggesting that there is no significant irreversible binding mechanism for thallium ions inside cells in the short time scale of these experiments. The two efflux methods used confirmed that the chemical form

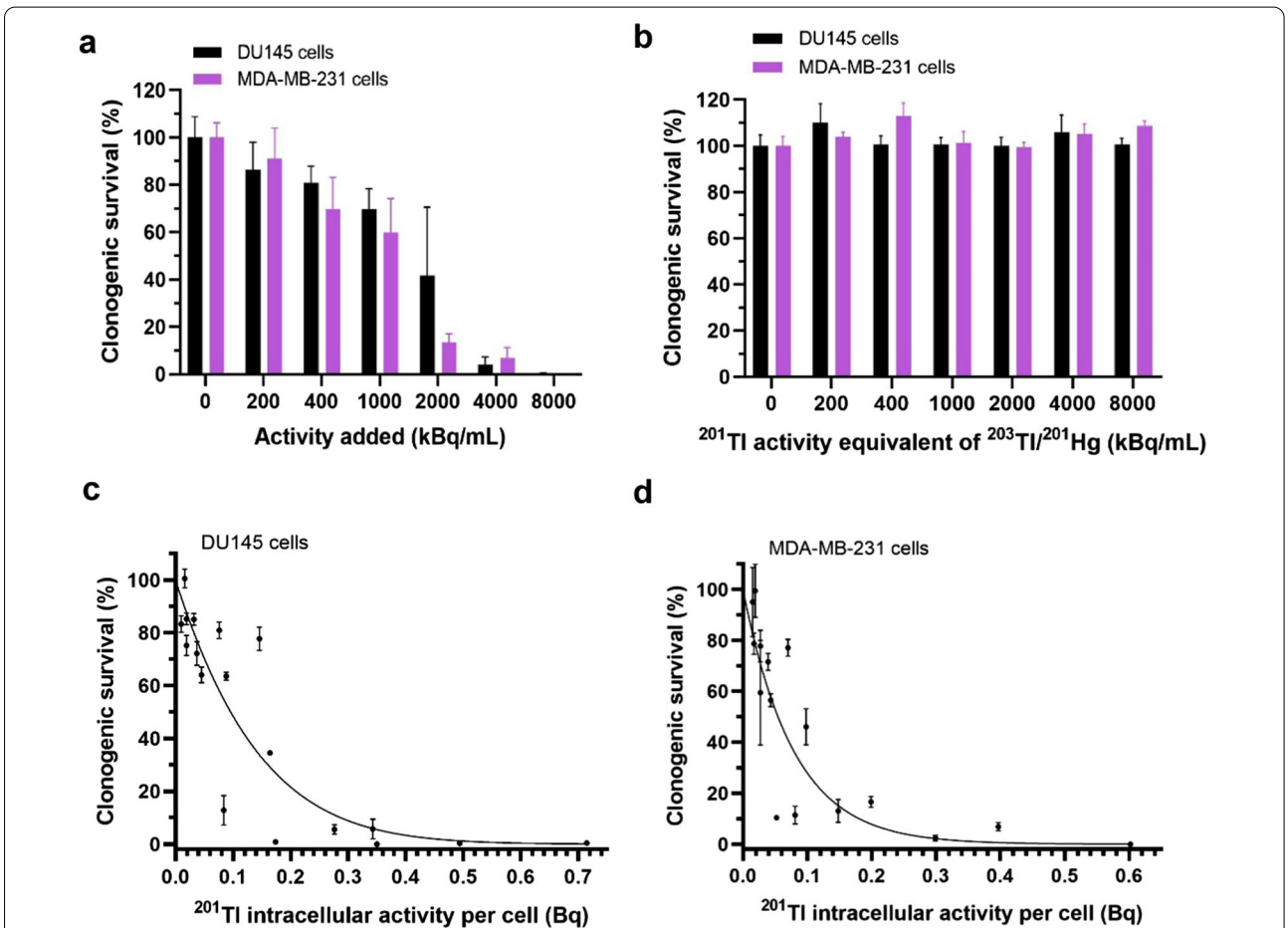

Fig. 4 ^{201}Tl radiotoxicity—clonogenic survival. **a** Clonogenic survival (%) in DU145 ($n = 3$) and MDA-MD-231 cells ($n = 3$ except 8000 kBq/mL where $n = 1$) after 90 min incubation with [^{201}Tl]TlCl in medium. **b** Clonogenic survival (%) measured in DU145 cells ($n = 3$) and MDA-MB-231 cells ($n = 1$) after 90 min incubation in medium with different concentrations of non-radioactive [^{201}Tl]TlCl decayed sample. **c** Clonogenic survivals (%) versus ^{201}Tl intracellular activity per single cell in DU145 cells ($n = 3$) and **d** MDA-MB-231 cells ($n = 3$). Linear quadratic survival model was fitted and calculated activity causing at least 90% reduction was 0.29 Bq for DU145 cells (95% CI 0.18–0.49) and 0.18 Bq for MDA-MB-231 (95% CI 0.10–0.39). Some error bars are smaller than the data points and not visible. Data are presented as mean ± SD, triplicates

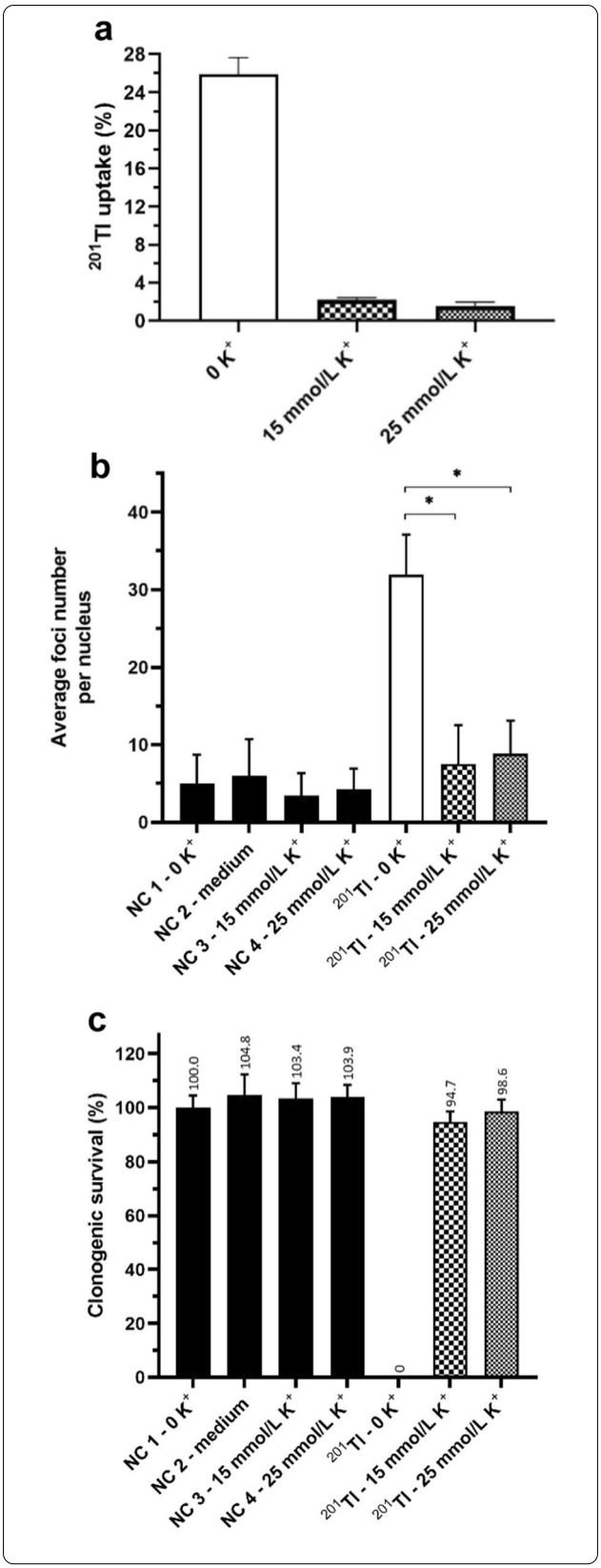

Fig. 5 ^{201}Tl radiotoxicity—internal vs external ^{201}Tl. **a** ^{201}Tl uptake in DU145 cells in PBS with different concentrations of K^+ (0–25 mM) after 90 min incubation with 4000 kBq/mL of [^{201}Tl]TlCl. **b** Average number of foci per nucleus and **c** clonogenic survival measured in DU145 cells after 90 min incubation with 4000 kBq/mL of [^{201}Tl]TlCl and 15 or 25 mmol/L KCl and various non-radioactive controls (NC1-4). Data are presented as mean ± SD, $n = 3$, triplicates, * indicates $P < 0.05$

of thallium is unchanged after entering the cell and the uptake mechanism is completely reversible, since the same ratios are preserved at every wash; and that only by the continuous efflux method can radioactivity be completely removed from the cells. Nevertheless, the high intracellular to extracellular concentration ratio achievable allowed evaluation of radiotoxicity of internalized ^{201}Tl without having a specific tumor-targeted uptake mechanism.

The radiotoxic effect of ^{201}Tl uptake in both cell lines was assessed by measuring clonogenic survival and the average number of DNA damage foci per nucleus. Treatment of both cell lines with ^{201}Tl in standard incubation media caused a substantial reduction in the surviving fraction compared to non-treated cells. Cells incubated with an equivalent volume of decayed [^{201}Tl]TlCl did not show this effect, indicating that the toxicity was solely due to the radioactivity. The average intracellular activity per cell required to achieve 90% reduction in clonogenicity over 90 min was estimated as 0.29 Bq (DU145) and 0.18 Bq (MDA-MB-231). These levels of exposure were accompanied by nuclear DNA damage measurable by the γH2AX assay, which showed a significant increase in the nuclear DNA DSBs caused by ^{201}Tl compared to negative controls. Larger standard deviations when measuring nuclear DNA damage could be linked to a heterogeneous uptake of ^{201}Tl among cells and/or its unequal subcellular distribution. Factors such as a different cell passage number or different cell cycle phases within the population, might explain large variation in results between experiments. Although nuclear DNA damage might be an important factor leading to a reduction in clonogenic survival, we cannot exclude ^{201}Tl impact on other susceptible cellular targets, such us cell membrane or mitochondria, both of which have been linked to the toxicity of other Auger electron-emitting radionuclides [22]. Currently, the precise sub-cellular localization of ^{201}Tl in cancer cells remains unknown.

In clonogenic survival studies on MDA-MB-231 cells we used ^{201}Tl activity of 8000 kBq/mL in one experiment only as the lower activities used were considered high enough to cause at least 90% reduction in

clonogenic survival necessary for the calculations and comparing with the other cell line. In toxicity control figures (Figs. 3b, 4b) showing that various components of decayed ^{201}Tl material are not affecting ^{201}Tl radiotoxicity, we aimed to use the maximum amount of the radioactive material (and its "cold" equivalent) to be able to observe the potential impact of non-radioactive thallium, if there was one. We therefore limited the number of experiments with higher ^{201}Tl activities (4000–8000 kBq/mL) to DU145 ($n=3$) only or $n=1$ for MDA-MB-231. This is justified by repeatedly observing no impact of low thallium concentrations on cell toxicity and our efforts to reduce radiation expose caused by the higher doses of gamma radiation.

Based on the subcellular range of Auger electrons (<1 μm) [11] and their typically low energy, we hypothesized that ^{201}Tl has to be internalized to exhibit its radiotoxic effect in cells and that the gamma and X-ray emissions do not contribute significantly to toxicity. To test this hypothesis, we needed a method to modulate ^{201}Tl cellular uptake from the medium. Na^+/K^+-pump inhibitors ouabain or digoxin, known to be effective in blocking potassium uptake [20], in our experiments caused substantial baseline cytotoxicity in tested cells. However, by varying the K^+ concentration in the incubation solution between 0 and 25 mM, we were able to achieve a range of ^{201}Tl uptake values from 25.9 (0.8 Bq/cell) to 1.6% (0.05 Bq/cell), corresponding to intracellular to extracellular concentration ratios in the range 8:1 to 181:1—a wider range than could be achieved with the cardiac glycosides—without affecting baseline clonogenic survival. When ^{201}Tl uptake in cells was substantially suppressed by high K^+ concentration in the medium, both the loss in clonogenic survival and the increase in DNA DSB caused by ^{201}Tl were completely suppressed. This suggests that ^{201}Tl needs to be transported inside cells to cause significant radiotoxicity. In the future, if ^{201}Tl can be successfully incorporated into a targeted radiopharmaceutical, an optimal dose for the radionuclide administration can be established to achieve an effective therapeutic effect. Furthermore, an impact of low energy gamma and X-ray emission on patients and carers should be investigated to assess feasibility of this treatment. The same principle would apply to any other Auger electron-emitting radiopharmaceutical.

The average of 0.18 Bq/cell for MDA-MB-231 and 0.29 Bq/cell for DU145 of intracellular ^{201}Tl required to achieve 90% reduction in clonogenicity over 90 min is equivalent to around 1000–1600 decays per cell. This is less than half the number of decays per cell calculated for ^{111}In and ^{67}Ga-oxine complexes (3240 and 3600 decays per cell, respectively, over 60-min incubation) required to obtain the same 90% reduction in clonogenicity in DU145 cells [23]. Although these experiments were not conducted under fully identical conditions, this result is consistent with the higher total energy and number of Auger and Coster–Kronig electrons per decay released by ^{201}Tl (15.3 keV, 37 electrons) compared to ^{111}In and ^{67}Ga (6.7 keV, 14.7 electrons and 6.3 keV, 4.7 electrons, respectively) [24]. Because ^{201}Tl effluxes quickly from the cell after the incubation period, whereas ^{111}In and ^{67}Ga do not, the nominal incubation time in the latter cases severely underestimates the actual exposure time, suggesting that ^{201}Tl has a much higher radiotoxic potential per Bq.

Our results are consistent with early work by Rao et al. and Kassis et al. [16, 17] addressing potential radiobiological risk associated with diagnostic use of ^{201}Tl, showing that decay of intracellular ^{201}Tl is toxic, reducing clonogenicity and inducing DNA DSBs. At the same time, ^{201}Tl decay presents little hazard to bystander cells that have not taken up the radionuclide. Although we have not compared this potency directly with other Auger electron-emitting radionuclides under consideration as radiotherapeutics, it appears that ^{201}Tl is more potent than ^{111}In and ^{67}Ga, consistent with the respective known number and energy of the emissions. Consequently, ^{201}Tl is an attractive candidate radionuclide for further research in targeted Auger electron-emitter therapy. In addressing this goal, it will be necessary to overcome several limitations of the present work. First, while we have shown that ^{201}Tl must be internalized to elicit significant radiotoxic effects, it is likely that different subcellular distributions will have greatly differing effects, since the range of the emitted electrons is much smaller than typical cell dimensions. Nothing is known about the subcellular distribution of ^{201}Tl in the cell lines investigated here, nor of ^{67}Ga and ^{111}In in similar studies [23]; indeed, in general the role of subcellular location of radionuclides in determining toxic effects is poorly understood. A radiopharmaceutical containing ^{201}Tl that is targeted both to cancer cells and to specific subcellular locations within them might be significantly more potent than [^{201}Tl]TlCl. Moreover, 'trapping' ^{201}Tl inside the cell will slow down its efflux and might further increase its radiotoxic potential. Despite the high potency, actualising therapeutic potential with ^{201}Tl is currently more challenging than with other potential Auger electron emitters (^{67}Ga, ^{111}In, ^{125}I etc.) because the chemistry required to incorporate ^{201}Tl into targeting molecules is underdeveloped—there are no satisfactory bifunctional chelators for thallium(I) or thallium(III). Here we have used physiological mimicry of potassium to achieve uptake in cells, but this has no specificity for cancer cells and probably has no specific targeting to subcellular structures.

Conclusion

^{201}Tl showed significant radiotoxicity, damaging nuclear DNA and reducing clonogenic survival when internalized in both cancer cell lines used in this study, and had no significant effect if not internalized. These results warrant further investigation of ^{201}Tl as a therapeutic radionuclide and the development of chelators to incorporate thallium into targeting molecules for specific delivery of ^{201}Tl to cancer cells.

Abbreviations

BC: Background count; BSA: Bovine serum albumin; CPM: Counts per minute; DMEM: Dulbecco's modified eagle medium; PBS: Phosphate buffered saline; RT: Room temperature.

Supplementary Information

The online version contains supplementary material available at https://doi.org/10.1186/s13550-021-00802-w.

Additional file 1. Additional results for In vitro proof of concept studies of radiotoxicity from Auger electron-emitter thallium-201.

Acknowledgements

We acknowledge the support received from King's College London Metallomics Facility with ICP-MS analysis funded by a Wellcome Multi-User Equipment Grant**.** Authors would like to thank Prof Robert Hider, Dr Elise Verger, Dr Francis Man, Jordan Cheng, and Alex Rigby for help and advice related to the project.

Authors' contributions

KO contributed to the conception of the experiments, designed the study, acquired, analysed and interpreted the data, and has drafted and revised the work. PB, ST, GS and VA conceived the project and significantly contributed to the conception and design of the experiments, analysis and interpretation of the data, and has substantially revisited the drafted manuscript. IC helped with the design and data interpretation. All authors substantially revised drafts. All authors have read and approved the final version of this manuscript, and have agreed both to be personally accountable for the author's own contributions and to ensure that questions related to the accuracy or integrity of any part of the work, even ones in which the author was not personally involved, are appropriately investigated, resolved, and the resolution documented in the literature.

Funding

This study received funding from UK Research and Innovation Medical Research Council Doctoral Training Partnership (MR/N013700/1), Theragnostics Ltd., Rosetrees Trust (M786), Engineering and Physical Sciences Research Council (EPSRC) (EP/S032789/1), Wellcome/EPSRC Centre for Medical Engineering (WT 203148/Z/16/Z), and Wellcome Trust. The research was also supported by the National Institute for Health Research (NIHR) Biomedical Research Centre at Guy's and St Thomas' NHS Foundation Trust and King's College London. The views expressed are those of the authors and not necessarily those of the NHS, the NIHR or the Department of Health. This research was funded in whole, or in part, by the Wellcome Trust [WT 203148/Z/16/Z]. For the purpose ofopen access, the author has applied a CC BY public copyright licence to any Author Accepted Manuscriptversion arising from this submission.

Availability of data and materials

The datasets generated and analysed during the current study are available from the corresponding author on reasonable request.

Declarations

Ethics approval and consent to participate

Not applicable.

Consent for publication

Not applicable.

Competing interests

GS was an employee of Theragnostics Ltd. at the time of this research. PJB is a member of the Theragnostics Advisory Board.

Author details

[1]School of Biomedical Engineering and Imaging Sciences, King's College London, London, UK. [2]Theragnostics Limited, 2 Arlington Square, Bracknell RG12 1WA, UK. [3]Department of Analytical, Environmental and Forensic Sciences, King's College London, London, UK.

Received: 16 March 2021 Accepted: 3 June 2021
Published online: 05 July 2021

References

1. McKillop JH. Thallium 201 Scintigraphy (Medical Progress). West J Med. 1980;133:23–46.
2. Jain D. Technetium-99m labeled myocardial perfusion imaging agents. Semin Nucl Med. 1999;29:221–36. https://doi.org/10.1016/S0001-2998(99)80012-9.
3. Krasnow AZ, Collier BD, Isitman AT, Hellman RS, Peck DC. The clinical significance of unusual sites of thallium-201 uptake. Semin Nucl Med. 1988;18:350–8. https://doi.org/10.1016/S0001-2998(88)80044-8.
4. Ito Y, Muranaka A, Harada T, Matsudo A, Yokobayashi T, Hideaki T. Experimental study on tumor affinity of ^{201}Tl—chloride. Eur J Nucl Med. 1978;3:81–6. https://doi.org/10.1007/BF00251628.
5. Ramanna L, Waxman A, Binney G, Waxman S, Mirra J, Rosen G. Thallium-201 scintigraphy in bone sarcoma: comparison with gallium-67 and technetium—MDP in the evaluation of chemotherapeutic response. J Nucl Med. 1990;31:567–72.
6. Suga K, Kume N, Orihashi N, Nishigauchi K, Uchisako H, Matsumoto T, et al. Difference in ^{201}Tl accumulation on single photon emission computed tomography in benign and malignant thoracic lesions. Nucl Med Commun. 1993;14:1071–8. https://doi.org/10.1097/00006231-199312000-00004.
7. Kawakami N, Kunisada T, Sato S, Morimoto Y, Tanaka M, Sasaki T, et al. Thallium-201 scintigraphy is an effective diagnostic modality to distinguish malignant from benign soft-tissue tumors. Clin Nucl Med. 2011;36:982–6. https://doi.org/10.1097/RLU.0b013e3182177407.
8. Hesse B, Tägil K, Cuocolo A, Anagnostopoulos C, Bardies M, Bax J, et al. EANM/ESC procedural guidelines for myocardial perfusion imaging in nuclear cardiology. Eur J Nucl Med Mol Imaging. 2005;32:855–97. https://doi.org/10.1007/s00259-005-1779-y.
9. Lebowitz E, Greene MW, Fairchild R, Bradley-Moore PR, Atkins HL, Ansari AN, et al. Thallium-201 for medical use. J Nucl Med. 1975;16:151–6.
10. Cornelissen B, Vallis KA. Targeting the nucleus: an overview of Auger-electron radionuclide therapy. Curr Drug Discov Technol. 2010;7:263–79. https://doi.org/10.2174/157016310793360657.
11. Ku A, Facca VJ, Cai Z, Reilly RM. Auger electrons for cancer therapy–a review. EJNMMI Radiopharm Chem. 2019;4:27. https://doi.org/10.1186/s41181-019-0075-2.

12. Falzone N, Fernández-Varea JM, Flux G, Vallis KA. Monte Carlo evaluation of Auger electron-emitting theranostic radionuclides. J Nucl Med. 2015;56:1441–6. https://doi.org/10.2967/jnumed.114.153502.
13. Kiess AP, Minn II, Chen Y, Hobbs R, Sgouros G, Mease RC, et al. Auger radiopharmaceutical therapy targeting prostate-specific membrane antigen. J Nucl Med. 2015;56:1401–7. https://doi.org/10.2967/jnumed.115.155929.
14. Bodei L, Kassis AI, Adelstein SJ, Mariani G. Radionuclide therapy with iodine-125 and other Auger-electron-emitting radionuclides: experimental models and clinical applications. Cancer Biother Radiopharm. 2003;18:861–77. https://doi.org/10.1089/108497803322702833.
15. Pouget JP, Santoro L, Raymond L, Chouin N, Bardiès M, Bascoul-Mollevi C, et al. Cell membrane is a more sensitive target than cytoplasm to dense ionization produced by Auger electrons. Radiat Res. 2008;170:192–200. https://doi.org/10.1667/RR1359.1.
16. Rao OV, Govelitz GF, Sastry KSR. Radiotoxicity of thallium-201 in mouse testes: inadequacy of conventional dosimetry. J Nucl Med. 1983;24:145–53.
17. Kassis AI, Adelstein SJ, Haydock C, Sastry KSR. Thallium-201: an experimental and a theoretical radiobiological approach to dosimetry. J Nucl Med. 1983;24:1164–75.
18. Pilatus U, Shim H, Artemov D, Davis D, van Zijl PCM, Glickson JD. Intracellular volume and apparent diffusion constants of perfused cancer cell cultures, as measured by NMR. Magn Reson Med. 1997;37:825–32. https://doi.org/10.1002/mrm.1910370605.
19. Sattari I, Aslani G, Dehghan MK, Shirazi B, Shafie M, Shadanpour N, et al. Dependence of quality of thallium-201 on irradiation data. Iran J Radiat Res. 2003;1:51–4.
20. Ogawa H, Cornelius F, Hirata A, Toyoshima C. Sequential substitution of K+ bound to Na+, K+-ATPase visualized by X-ray crystallography. Nat Commun. 2015;6:8004. https://doi.org/10.1038/ncomms9004.
21. Thier SO. Potassium Physiology. Am J Med. 1986;80:3–7.
22. Bavelaar BM, Lee BQ, Gill MR, Falzone N, Vallis KA. Subcellular targeting of theranostic radionuclides. Front Pharmacol. 2018;9:996. https://doi.org/10.3389/fphar.2018.00996.
23. Othman MFB, Mitry NR, Lewington VJ, Blower PJ, Terry SYA. Re-assessing gallium-67 as a therapeutic radionuclide. Nucl Med Biol. 2017;46:12–8. https://doi.org/10.1016/j.nucmedbio.2016.10.008.
24. Howell RW. Radiation spectra for Auger-electron emitting radionuclides: Report No. 2 of AAPM nuclear medicine task group No 6. Med Phys. 1992;19:1371–83. https://doi.org/10.1118/1.596927.

Publisher's Note